



UNIVERSIDAD
POLITECNICA
DE VALENCIA



PhD Dissertation

Analysis and Design of Antennas for Wireless Communications Using Modal Methods

Universidad Politécnica de Valencia
Departamento de Comunicaciones

Valencia, February 2008

Author:

Eva Antonino Daviu

Advisor:

Prof. Dr. Miguel Ferrando Bataller

To my parents.

To Pepe.

Agradecimientos

Después de tantos años de trabajo considero necesario plasmar aquí mi agradecimiento a todas aquellas personas que me han prestado su apoyo durante esta etapa.

En primer lugar, agradecer a mi director de tesis, Miguel Ferrando, la confianza depositada en mí desde el primer momento, así como su apoyo y dedicación durante estos años. Espero seguir trabajando con él durante mucho tiempo, y seguir aprendiendo día a día de sus inestimables conocimientos y experiencia.

En segundo lugar, agradecer a Alejandro Valero sus consejos y ayuda en muchos momentos de la tesis, sobre todo en los tiempos en que comenzaba y éramos muy pocos en el grupo de investigación. Agradecer también a Mariano Baquero y a Vicent M. Rodrigo su total disposición a ayudar cuando ha sido necesario.

A Marta Cabedo quiero agradecerle su ayuda, confianza y amistad durante estos años de trabajo. Muchas han sido las dificultades que hemos sobrellevado juntas y siempre la he considerado una gran compañera de equipo.

También quiero agradecer a José Ignacio Herranz su ayuda, compañerismo y amistad durante estos años de elaboración de la tesis.

Agradecer también al resto de miembros del Grupo de Radiación Electromagnética (los que están o han estado) su ayuda y amistad, haciendo que este trabajo no haya resultado tan duro gracias a ellos: Daniel Sánchez, Esperanza Alfonso, David González, Antonio Vila, Bernardo Bernardo, Felipe Vico, Fulvio Grassi y Michele Gallo. Agradecer también a Carlos A. Suárez su amistad, sus consejos y su ayuda durante la etapa que compartió con nosotros en la UPV.

Quiero agradecer especialmente a mis padres su apoyo incondicional durante estos años. Ellos me han enseñado siempre que todo lo que vale la pena requiere esfuerzo y dedicación, y que al final uno obtiene su recompensa. Sé que esta Tesis es tan importante para ellos como para mí. También quiero agradecer a mis hermanos, Jose, Vicente y Francisco, su ayuda y ánimos incondicionales.

Quisiera también mostrar mi agradecimiento a los miembros del Departamento de Antenas y modelado EM, de la empresa alemana IMST GmbH, con los que compartí cuatro meses de este trabajo. Agradecerle a Matthias Geissler el acogerme en la empresa y el permitirme disfrutar de un gran ambiente de trabajo y profesionalidad. Y muy especialmente, agradecer a Marta Martínez su ayuda y orientación

durante esos meses en la empresa, además de hacerme sentir como en casa durante el tiempo que estuve en Alemania. A ella y a su marido Ángel les debo los grandes momentos vividos en Düsseldorf.

Por último, quiero agradecerle a la persona que más cerca de mí ha estado durante estos años su apoyo, confianza, ánimo y paciencia infinita. ¡Muchas gracias Pepe por permitirme sobrellevar los momentos duros con energía y confianza y por estar ahí siempre dispuesto a apoyarme!

Acknowledgements

After all these years of hard work I think it is necessary to express my gratitude to those people that have given me their support over all these years.

First of all, I would like to thank my advisor, Miguel Ferrando, for all the confidence he placed on me from the very beginning, and for his support and dedication during these years. I expect to continue working with him for many years, and continue learning day after day from his huge knowledge and experience.

I would also like to thank Alejandro Valero for his valuable advices and help in some moments of the work, especially in the first years, when there were only a few people working in our research group. I also want to thank Mariano Baquero and Vicent M. Rodrigo for their complete willingness to help whenever it was necessary.

To Marta Cabedo I am deeply grateful for her help, trust and friendship during these years. We have been facing together complex problems concerning our research and I have always considered her an excellent team partner.

I would also like to thank Jose Ignacio Herranz for his help, support and friendship during these years of work.

I am also very grateful to all present and past members of the Electromagnetic Radiation Group of the Technical University of Valencia (UPV). Thanks to their help and friendship this work has not been so hard!: Daniel Sánchez, Esperanza Alfonso, David González, Antonio Vila, Bernardo Bernardo, Felipe Vico, Fulvio Grassi and Michele Gallo. I would also like to thank Carlos A. Suárez for his friendship, advice and support in the period he shared with us in UPV.

I especially want to show my gratitude to my parents, for his unconditional support during these years. They have always taught me that every important achievement in life needs of effort and dedication, what finally lead to success. I know the big significance this work has also for them. I also want to thank my brothers, Jose, Vicente and Francisco for their unconditional support and encouragement.

My thankfulness goes also to the members of the Department of Antennas and EM Modeling of IMST GmbH., with whom I shared some months of this work. I would like to thank Matthias Geissler for welcoming me in the firm and allowing me to enjoy a great work atmosphere and professionalism. And thanks especially for Marta Martinez for her help and orientation during those months in the company,

and also for making me feel at home during this period in Germany. To her and her husband Angel I want to thank the great moments enjoyed in Düsseldorf!

Finally, I want to thank the person who has been closest to me during all these years, for his support, trust, encouragement and infinite patience. Thank you from the heart, Pepe, for helping me to overcome the difficult moments with energy and confidence and for standing always by me!

Abstract

Design of antennas for wireless communication systems has attracted increasing interest during last years. The main objective of this Thesis is to propose a general design procedure of antennas for wireless communications systems, which provides a physical insight into the design process. To accomplish this objective, a method based on a modal decomposition of the current on the surface of the conducting structure will be proposed. Modes have the advantage to provide physical insight into the radiating behavior of the antenna, as well as useful information for the optimization of the antenna geometry and the selection of the optimum feeding mechanism and its location.

A review of different modal methods, as well as the most important parameters to deal with when working with modal solutions, will be made. A method to obtain closed-form expressions for the modal surface currents on open planar conducting objects will be investigated. As it will be discussed, planar objects with canonical shapes can be interpreted in most cases as a deformation of three-dimensional objects whose surfaces coincide with any of the curvilinear reference coordinate systems. Consequently, closed-form expressions for vector modes in a circular conducting disk and an infinite planar conducting strip will be obtained. These functions will be proposed to be used as entire-domain basis functions in more complex problems including these planar surfaces.

Current modes defined from vector wave functions are of complex nature, what sometimes makes them difficult to use for design purposes. In contrast, the Theory of Characteristic Modes provides a decomposition of the total current in the surface of any arbitrary conducting body in a set of real modes, whose radiation patterns are orthogonal over both the source region and the sphere at infinity.

The Thesis will apply the Theory of Characteristic Modes to antenna design. Investigations will mainly focus on the effect of the feeding configuration and location on the modal excitation. The objective is to provide final prototypes of antennas to be used in real wireless systems, so as to prove the utility of the proposed method in a real design process. The method will hence be applied to antennas for different applications: Wideband antennas, antennas for UWB systems, antennas for Multiple-Input Multiple-Output (MIMO) systems and antennas for handheld devices.

Resumen

El diseño de antenas para los nuevos sistemas de comunicaciones inalámbricas ha suscitado un creciente interés en los últimos años. El principal objetivo de esta Tesis Doctoral es la propuesta de un método general de diseño de antenas para sistemas de comunicaciones inalámbricas que proporcione una visión física del proceso de diseño. Para alcanzar este objetivo, se propone el uso de un método basado en la descomposición modal de la corriente en la superficie del cuerpo conductor. Los modos tienen la ventaja de proporcionar una visión más física del comportamiento radiante de la antena, así como información muy útil para la optimización de la geometría de la antena y para la selección del mecanismo óptimo de alimentación y su localización.

En la Tesis se realizará una revisión de los diferentes métodos modales disponibles, así como de los parámetros más importantes a tratar cuando se trabaja con soluciones modales. Además, se investigará un método para obtener expresiones cerradas para las corrientes superficiales en objetos conductores planos abiertos. Como se verá, los objetos planos con formas canónicas se pueden interpretar en muchas ocasiones como deformaciones de objetos tridimensionales cuyas superficies coinciden con las de algunos de los sistemas de coordenadas curvilíneas. De esta forma, se obtendrán expresiones cerradas para los modos vectoriales en un disco conductor circular y una tira plana infinita. Estas funciones se propondrán como funciones base de dominio completo en problemas más complejos que incluyan este tipo de superficies planas.

Los modos de corriente definidos a partir de las funciones de onda vectoriales son de naturaleza compleja, lo que dificulta en ocasiones su uso para el diseño de antenas. Por el contrario, la Teoría de los Modos Característicos proporciona una descomposición de la corriente total en la superficie de un cuerpo conductor de forma arbitraria en un conjunto de modos reales, cuyos diagramas de radiación son ortogonales sobre la región de la fuente y la esfera infinita.

La Tesis aplicará la Teoría de los Modos Característicos para el diseño de antenas. Las investigaciones se centrarán fundamentalmente en el efecto de la configuración de alimentación y su localización sobre la excitación de los modos. El objetivo es proporcionar prototipos finales de antenas para su uso en sistemas inalámbricos reales, para probar la utilidad del método propuesto en un proceso real de diseño. El método se aplicará a antenas para diversas aplicaciones: antenas de banda ancha, antenas para sistemas UWB, antenas para sistemas MIMO (*Multiple-Input Multiple-Output*) y antenas para terminales móviles.

Resum

El disseny d'antenes per als nous sistemes de comunicacions sense fil ha suscitat un creixent interès en els últims anys. El principal objectiu d'esta Tesi Doctoral és la proposta d'un mètode general de disseny d'antenes per a sistemes de comunicacions sense fil que proporcione una visió física del procés de disseny. Per a aconseguir este objectiu, es proposa l'ús d'un mètode basat en la descomposició modal del corrent en la superfície del cos conductor. Els modes tenen l'avantatge de proporcionar una visió més física del comportament radiant de l'antena, així com informació molt útil per a l'optimització de la geometria de l'antena i per a la selecció del mecanisme òptim d'alimentació i la seua localització.

En la Tesi es realitzarà una revisió dels diferents mètodes modals disponibles, així com dels paràmetres més importants a tractar quan es treballa amb solucions modals. A més, s'investigarà un mètode per a obtenir expressions tancades per als corrents superficials en objectes conductors plans oberts. Com es veurà, els objectes plans amb formes canòniques es poden interpretar moltes vegades com a deformacions d'objectes tridimensionals les superfícies dels quals coincideixen amb les d'alguns dels sistemes de coordenades curvilínies. D'esta manera, s'obtindran expressions tancades per als modes vectorials en un disc conductor circular i una tira plana infinita. Estes funcions es proposaran com a funcions base de domini complet en problemes més complexos que incloguen este tipus de superfícies planes.

Els modes de corrent definits a partir de les funcions d'onda vectorials són de naturalesa complexa, la qual cosa dificulta de vegades el seu ús per al disseny d'antenes. Al contrari, la Teoria dels Modes Característics proporciona una descomposició del corrent total en la superfície d'un cos conductor de forma arbitrària en un conjunt de modes reals, els diagrames de radiació del qual són ortogonals sobre la regió de la font i l'esfera infinita.

La Tesi aplicarà la Teoria dels Modes Característics per al disseny d'antenes. Les investigacions se centraran fonamentalment en l'efecte de la configuració d'alimentació i la seua localització sobre l'excitació dels modes. L'objectiu és proporcionar prototips finals d'antenes per al seu ús en sistemes sense fil reals, per a provar la utilitat del mètode proposat en un procés real de disseny. El mètode s'aplicarà a antenes per a diverses aplicacions: antenes de banda ampla, antenes per a sistemes UWB, antenes per a sistemes MIMO (Multiple-Input Multiple-Output) i antenes per a terminals mòbils.

Table of Contents

CHAPTER 1.	INTRODUCTION.....	1
CHAPTER 2.	VECTOR WAVE FUNCTIONS IN PERFECTLY CONDUCTING BODIES	7
2.1.	INTRODUCTION	7
2.2.	MODES IN A PERFECTLY CONDUCTING SPHERE	10
2.3.	MODES OF CURRENT IN A CIRCULAR DISK	17
2.4.	MODES IN AN INFINITE PLANAR STRIP	27
2.5.	CONCLUSIONS	41
CHAPTER 3.	INTERNAL AND EXTERNAL RESONANCES IN PERFECT CONDUCTORS	43
3.1.	INTRODUCTION	43
3.2.	INTERNAL RESONANCES IN CLOSED CONDUCTING STRUCTURES	44
3.3.	EXTERNAL RESONANCES IN CONDUCTING STRUCTURES	46
3.4.	REVIEW OF THE THEORY OF CHARACTERISTIC MODES	48
3.4.1.	<i>Mathematical formulation.....</i>	<i>48</i>
3.4.2.	<i>Physical significance of characteristic modes</i>	<i>52</i>
3.5.	RELATION BETWEEN CHARACTERISTIC MODES AND VECTOR WAVE FUNCTIONS ...	59
3.5.1.	<i>Analytic characteristic modes of the conducting sphere</i>	<i>59</i>
3.5.2.	<i>Closed-form characteristic modes of an infinite metallic strip</i>	<i>61</i>
3.6.	CONCLUSIONS	69
CHAPTER 4.	EXCITATION OF CHARACTERISTIC MODES.....	71
4.1.	INTRODUCTION	71
4.2.	EXCITATION OF MODES IN A CIRCULAR WIRE LOOP ANTENNA	72
4.2.1.	<i>Characteristic modes of a circular wire loop antenna.....</i>	<i>73</i>
4.2.2.	<i>Excitation of characteristic modes.....</i>	<i>77</i>
4.2.3.	<i>Reactive loading to control characteristic modes</i>	<i>88</i>
4.3.	MODAL EXCITATION IN PLANAR ANTENNAS.....	91
4.3.1.	<i>Characteristic modes in a rectangular conducting plate</i>	<i>92</i>
4.3.2.	<i>Excitation of a square planar monopole antenna</i>	<i>96</i>
4.3.3.	<i>Application of a double feed planar monopole antenna to MIMO systems</i>	<i>106</i>
4.3.4.	<i>Wideband antennas with polarization diversity</i>	<i>110</i>
4.4.	CONCLUSIONS	114

CHAPTER 5. MODAL ANALYSIS AND DESIGN OF WIDEBAND ANTENNAS WITH COUPLED RESONATORS.....	115
5.1. INTRODUCTION.....	115
5.2. MODAL ANALYSIS OF WIDEBAND PLANAR MONOPOLE ANTENNAS WITH EMBEDDED RESONATORS.....	118
5.3. CONTROL OF THE SLOT MODE EXCITATION.....	124
5.3.1. <i>Insertion of active devices to control the slot mode excitation.....</i>	<i>126</i>
5.3.2. <i>Results for the reconfigurable antenna prototype.....</i>	<i>129</i>
5.4. REACTIVE LOADING TO CONTROL THE SLOT MODE RESONANCE.....	132
5.4.1. <i>Results for the UWB tunable antenna prototype.....</i>	<i>134</i>
5.5. CONCLUSIONS.....	137
CHAPTER 6. DESIGN OF ANTENNAS FOR MOBILE TERMINALS USING THE PCB RESONANT MODES.....	139
6.1. INTRODUCTION.....	139
6.2. CHARACTERISTIC MODES OF A MOBILE HANDSET RECTANGULAR PCB.....	142
6.3. INVESTIGATIONS IN THE EXCITATION OF THE PCB CHARACTERISTIC MODES.....	143
6.3.1. <i>Experiments with coplanar resonant elements.....</i>	<i>143</i>
6.3.2. <i>Experiments with non-coplanar coupling elements.....</i>	<i>155</i>
6.4. WIDEBAND FEEDING OF THE MOBILE HANDSET PCB.....	165
6.5. DOUBLE FOLDED PCB ANTENNA.....	172
6.6. NOTCHED RADIATING GROUND PLANE.....	179
6.6.1. <i>Characteristic modes of a double-notched radiating ground plane.....</i>	<i>180</i>
6.6.2. <i>Modal excitation of a double-notched radiating ground plane.....</i>	<i>182</i>
6.7. CONCLUSIONS.....	192
CHAPTER 7. CONCLUSIONS AND FURTHER WORK.....	195
7.1. CONCLUSIONS.....	195
7.2. FURTHER WORK.....	198
REFERENCES.....	201
APPENDIX A COORDINATE SYSTEMS.....	215
A.1. SPHERICAL COORDINATE SYSTEM.....	215
A.2. OBLATE SPHEROIDAL COORDINATE SYSTEM.....	215
A.2.1. <i>Spheroidal scalar wave functions.....</i>	<i>217</i>
A.3. ELLIPTICAL-CYLINDRICAL COORDINATE SYSTEM.....	219
A.3.1. <i>Helmholtz equation in elliptic coordinates.....</i>	<i>221</i>
RELATED PUBLICATIONS.....	229
OTHER PUBLICATIONS.....	234

Chapter 1

Introduction

“A good beginning makes a good end.”

Louis L'Amour

Design of antennas for wireless communication systems has attracted increasing interest during last years. In the last decade, the number of wireless communications standards has rapidly increased, due to the miniaturization and cost reduction of wireless terminals as well as the spread of novel services very attractive for the users. In addition to analog and digital cellular-based services, broadband technologies such as third generation cellular and ultrawideband (UWB) systems, as well as wireless LAN standards and Bluetooth technology, have emerged. Figure 1.1 summarizes the operating bands of all these different wireless communications standards, where it can be observed the large portion of available RF spectrum reserved for these systems [1]. Obviously, the inclusion of multiple technologies in wireless devices will significantly increase their functionality.

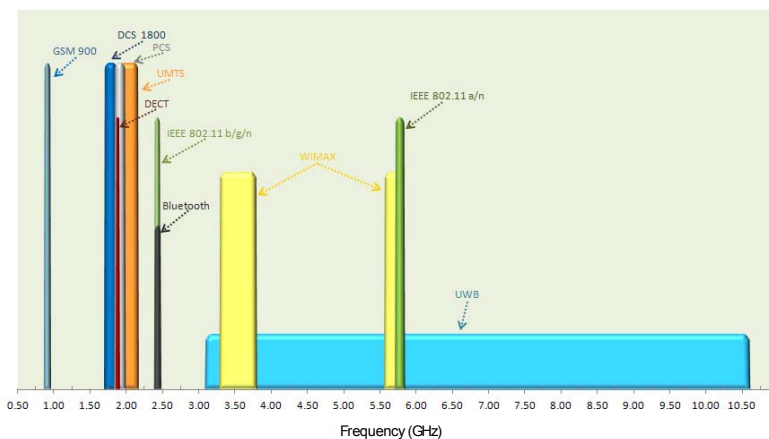


Figure 1.1 Operating bands of different wireless communications standards.

Therefore, the proliferation of wireless communication services spurs on the need for compact antennas capable of providing good performance while operating at a broad frequency range, since it would be very attractive to cover all emergent standards using a single antenna. Present-day research in this field focuses on designing wide-band or multiband antennas which cover all the desired frequencies, while retaining good radiation characteristics and reducing the space required for the antenna.

Although many antennas have been presented in the literature, which provide a satisfactory performance with a relative small size, general guidelines for the design and development of antennas for these systems are scarce [2][3]. Most of the time, design is dominated by the experience of the designer, who usually employs some kind of Computer Assisted Design (CAD) tool to develop the antenna, and a final design is mostly reached using cut-and-try methods. Neither physical insight into the antenna performance nor guidelines for the design, which would be useful for the future, are thus provided.

In last years, automatic optimization design tools based in different heuristic algorithms, such as genetic algorithms [4][5], particle-swarm optimization [6][7], simulated annealing [5][6] or neuronal networks [8], among others, have become increasingly popular for antenna design problems. Although this design strategy usually provides a good solution for a specific problem, general design guidelines can not usually be extracted from the solution adopted, since physical insight into the problem is not gained at all. If a modification of the structure in some direction is required, a new execution of the automatic algorithm is in most cases necessary.

Therefore, due to the lack of general design procedures detected in the literature, the main objective of this Thesis is to propose a general method for the design of antennas for wireless communications systems, which provides a physical insight into the design process. To accomplish this objective, a method based on a modal decomposition of the current on the surface of the conducting structure will be proposed. Modes have the advantage to provide physical insight into the radiating behavior of the antenna, as well as useful information for the optimization of the antenna geometry and the selection of the optimum feeding mechanism and its location.

Modal analysis has been traditionally applied to the study of electromagnetic fields inside closed conductors (such as waveguides or cavities), and also in radiation and scattering problems concerning canonical geometries [9]-[11]. Some of the most important concepts and properties regarding these modes will be revisited in further chapters. Recently, a modal-based numerical method formulated forty years ago has become very popular in antenna analysis. This is the Singularity

Expansion Method (SEM), based on the expansion of the current in its complex natural resonances in the Laplace domain [12]. So far, the information provided by these complex modes has only been used for analysis and modeling of antennas, and not for design purposes, probably due to the added difficulty of dealing with modes of complex nature. A brief description of this method will be provided in a later chapter.

The Thesis is divided in two parts: First, a review of different modal methods as well as the most important parameters to deal with when working with modal solutions will be made. In addition, a method to obtain closed-form expressions for the modal surface currents on open planar conducting objects will be investigated in this first part. As it will be discussed in later chapters, planar objects with canonical shapes can be interpreted in most cases as a deformation of three-dimensional objects whose surfaces coincide with any of the curvilinear reference coordinate systems. Consequently, closed-form expressions for vector modes in a circular conducting disk and an infinite planar conducting strip can be obtained following the proposed approach. Moreover, these functions may be used as entire-domain basis functions in more complex problems including these planar surfaces.

Current modes defined from vector wave functions are of complex nature, what sometimes makes them difficult to use for design purposes. In contrast, the Theory of Characteristic Modes, defined originally by Garbacz [13][14] and refined later by Harrington and Mautz [15][16], provides a decomposition of the total current in the surface of any arbitrary conducting body in a set of real modes, whose radiation patterns are orthogonal over both the source region and the sphere at infinity. In the first part of the Thesis, the mathematical foundations and interpretation of characteristic modes and their associate eigenvalues will be revisited. Moreover, a connection with vector wave functions will be established, showing the similarities between them.

In the second part, the Thesis will focus on the application of the Theory of Characteristic Modes to antenna design. This Thesis builds on the work developed in [17], where the Theory of Characteristic Modes was applied for the analysis of a wide variety of structures, and the physical interpretation of the information provided by these modes was established. In the present work, investigations will mainly focus on the effect of the feeding configuration and location on the modal excitation. Moreover, the objective is to provide final prototypes of antennas to be used in real wireless systems, so as to prove the utility of the proposed method in a real design process. The proposed design method will hence be applied to antennas for different applications: Wideband antennas, antennas for UWB systems, antennas for Multiple-Input Multiple-Output (MIMO) systems and antennas for

handheld devices. In each chapter, state of the art of the antenna technology for a specific application will be revisited.

This Thesis has been developed in the Electromagnetic Radiation Group (GRE) of the Institute of Telecommunications and Multimedia Applications (iTEAM) of the Technical University of Valencia (UPV). The work has partly been financially supported by FPU grant AP2002-2622, from the Spanish Ministry of Education and Science. Moreover, different parts of the work included in this Thesis have been carried out within the framework of different projects:

- Project "Antennas for UMTS base-stations" (TIC2001-2364-C03-02), supported by the Spanish Ministry of Science and Technology.
- Project "Distributed mobile networks for multi-user Communications, MI-MONET" (TEC2004-04866-C04-01), supported by the Spanish Ministry of Education and Science.
- Project "Wideband and multiband antennas for mobile platforms, WI-MANT" (TEC2007-66698-C04-03/TCM), supported by the Spanish Ministry of Education and Science.
- COST Action/Network 284 on "Innovative Antennas for Emerging Terrestrial & Space-based Applications".
- COST IC0603 on "Antenna Systems & Sensors for Information Society Technologies (ASSIST)".
- ACE (Antennas Center of Excellence) network, within activities A2.2 on "Small Antennas", A2.3 on "Wideband and Multiband Antennas" and A3.1 on "Training and Education".

Besides, part of this Thesis was developed at the Department of Antennas & EM Modeling of IMST GmbH., a German research company very experienced in the design and development of antennas for mobile terminals and satellite applications. The aim of this collaboration was to connect research in the field of antenna design for mobile terminals with more practical aspects, in order to provide design methodologies and results according to market requirements. Moreover, IMST experience with active elements and with manufacturing and measurement procedures was very valuable in some of the prototypes presented in this dissertation.

The dissertation is structured in seven chapters, including this introductory chapter, as follows:

In chapter 2, vector wave functions or modes for some canonical conducting structures will be revisited. These modes form an orthonormal set in which to expand the total field, and have an associated current distribution over the conducting object. First, modes of a perfectly conducting sphere and their properties will be revisited, as they have long been used in electromagnetic problems. As planar

antennas are more commonly used in wireless communications applications, a method to obtain closed-form expressions for the modes on some planar structures such a circular disk or an infinite conducting strip will be obtained. Complex current modes over these structures, in which the total current can be expanded, will be presented graphically.

In chapter 3, similar modes to those presented in chapter 2 will be obtained by means of the Theory of Characteristic Modes, proposed by Garbacz [13][14] and refined by Harrington and Mautz [15][16]. The advantage of using these modes instead of traditional vector wave functions is mainly their real nature and orthogonal properties over the source region, what facilitates the treatment of these modes in an antenna design problem. The mathematical foundations of the Theory of Characteristic Modes and the physical interpretation of the eigenvalue associated to each mode will be revisited in this chapter. Closed-form expressions for the characteristic modes of planar antennas investigated in the previous chapter will be obtained, and comparison with the traditional vector wave functions for the surface current expansion will be presented. This will help to understand the physical interpretation of the radiation mechanisms of a conducting structure.

In chapter 4, the problem of the excitation of characteristic modes will be investigated. After the analysis and interpretation of the properties associated to the characteristic modes of a structure, the next step in the antenna design process will consist in selecting the optimum feeding configuration and location. The modal excitation problem will be first investigated using a simple structure, such a wire loop antenna. The dependence of the modal excitation on the sources location and the symmetries imposed in the structure will be studied. Then, excitation of a more complex structure, such as a planar monopole antenna, will be investigated in depth. Based on the information provided by characteristic modes, a novel feeding mechanism for this type of structures will be proposed. A prototype of the novel antenna will be fabricated and measurements will be provided, in order to validate the proposed design. Moreover, based on the previous design, a MIMO antenna will be proposed and measurements in a real MIMO system performed.

In chapter 5, characteristic modes will be used to analyze wideband antennas with narrowband coupled resonators. Actually, resonators embedded into the geometry of a planar monopole antenna will be studied, since many antennas based on this configuration have been experimentally proposed in recent years. For the first time, a modal study of this type of structures will be carried out, which will physically explain the performance of the antenna. Planar monopole antennas with embedded narrowband resonators have recently been used as wideband antennas with band-notched behavior. The physical knowledge of the behavior of the antenna and its combination with the potentiality of active devices, will lead to pro-

pose novel planar monopole antennas, where the excitation of the embedded resonator can be controlled electronically. This will obviously increase the functionality of the antenna to a great extent. Moreover, electronically controlled reactive loading can also be used to tune the resonance of the coupled structure. Prototypes will be provided again to verify the proposed designs. Furthermore, time-domain measurements for UWB antennas including active devices will be presented for the first time ever.

In chapter 6, modal analysis will be applied to the design of antennas for mobile terminals based on the radiation of its Printed Circuit Board (PCB). This design philosophy of antennas for mobile terminals has become very popular in the last years, and hence knowledge of the PCB characteristic modes will be proven extraordinarily useful for this design perspective. Characteristic modes of a typical rectangular PCB used in mobile handsets will be first presented, and then the excitation of the different modes will be investigated using a wide variety of feeding configurations. From these investigations, general design guidelines will be provided for this type of antennas. Finally, antennas for other devices, including PCMCIA cards and mobile terminals such a PDAs, based also on the use of a radiating ground plane, will be studied, and different feeding mechanisms will be investigated.

Finally, in chapter 7 conclusions of the work will be presented, and some guidelines for further work will be proposed.

Chapter 2

Vector wave functions in perfectly conducting bodies

“Philosophy is written in this grand book - I mean the Universe - which stands continually open to our gaze, but it cannot be understood unless one first learns to comprehend the language and interpret the characters in which it is written. It is written in the language of Mathematics, and its characters are triangles, circles and other geometrical figures, without which it is humanly impossible to understand a single word of it.”

Galileo Galilei

2.1. Introduction

The field radiated or scattered by a perfectly conducting body can be expressed as a superposition of vector wave functions or modes. Traditionally these vector field modes have been used in radiation and scattering problems when canonical geometries are considered [9][10]. If a source-free, linear, homogeneous and isotropic region is considered, all vectors characterizing the electromagnetic field (field vectors \vec{E} , \vec{B} , \vec{D} and \vec{H}) satisfy the same *vector wave equation*:

$$\nabla^2 \vec{C} + k^2 \vec{C} = 0 \quad (2.1)$$

where \vec{C} denotes any such vector. Solutions of equation (2.1) are called *vector wave functions*. As these functions form a complete set, they are the building blocks for the modal expansion of electromagnetic fields [9][11].

An arbitrary electromagnetic field can be then resolved into partial fields, each of them derivable from a purely scalar function satisfying the wave equation. In this case, the problem is reduced to solve the scalar wave equation (Helmholtz equation), which is separable in eleven distinct coordinate systems [11], summarized in table 2.1. Thus, if scalar function ψ is a solution of the scalar Helmholtz equation

$$\nabla^2 \psi + k^2 \psi = 0 \quad (2.2)$$

it is possible to construct three independent vector solutions of (2.1) as follows:

$$\vec{L} = \nabla \psi, \quad \vec{M} = \nabla \times (\hat{u} \cdot \psi), \quad \vec{N} = \frac{1}{k} \nabla \times \vec{M} \quad (2.3)$$

where \hat{u} is a constant unit vector such as \hat{x} , \hat{y} and \hat{z} , or the position vector \hat{r} . Hence, if \vec{C} is placed equal to \vec{L} , \vec{M} or \vec{N} , equation (2.1) will be satisfied [11]. The vector functions \vec{L} , \vec{M} and \vec{N} have certain properties that follow from their definitions:

$$\begin{aligned} \nabla \times \vec{L} &= 0 \\ \nabla \cdot \vec{M} &= 0 \\ \nabla \cdot \vec{N} &= 0 \end{aligned} \quad (2.4)$$

that is, \vec{L} is an irrotational vector function, whereas \vec{M} and \vec{N} are solenoidal functions. To each solution ψ_n of the scalar equation (2.2) there are three vector solutions \vec{L}_n , \vec{M}_n and \vec{N}_n of the associated equation (2.1). Therefore, any arbitrary wave function can be represented as a linear combination of these vector wave functions.

When considering a perfectly conducting object whose surface coincides with any of these eleven coordinate systems where the scalar wave function is separable, analytical expressions for the vector wave functions can be obtained. The field radiated or scattered by this body can thus be expressed as a superposition of those wave functions. Moreover, each field mode has an associated current distribution over the surface of the conducting body, which is responsible for the modal field properties. The knowledge of the properties of the vector wave fields, as well as those of the associated surface current modes may be used to improve the radiating behavior of the conducting structure.

It must be emphasized that these wave functions are independent of the excitation or source of the problem, as they have been calculated in source-free conditions. Although these modes have traditionally been used in radiation and scattering problems, this Thesis will mainly be focused on the surface current modes on the conducting object. The aim is using them as an initial step in an antenna design process, subsequently selecting the optimum feeding configuration to excite those modes with more interesting properties, in terms of either their bandwidth or their radiated field.

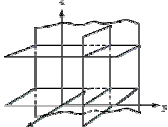
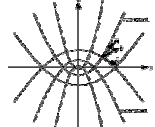
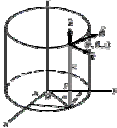
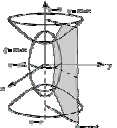
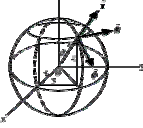

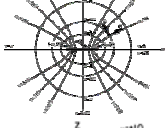
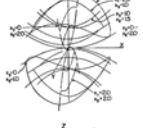
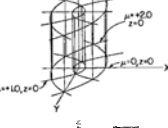
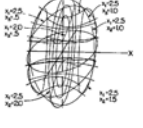

Coordinate System (ξ_1, ξ_2, ξ_3)	Vector Wave Equation Separable?		Coordinate System (ξ_1, ξ_2, ξ_3)	Vector Wave Equation Separable?	
Rectangular (x, y, z)	Yes		Parabolic (u, v, θ)	No	
Circular Cylinder (ρ, ϕ, z)	Yes		Prolate Spheroidal (η, ξ, ϕ)	No	
Spherical (r, ϕ, θ)	Yes		Oblate Spheroidal (η, ξ, ϕ)	No	
Elliptic Cylinder (η, ξ, z)	Yes		Paraboloidal (λ, μ, ν)	No	
Parabolic Cylinder (u, v, z)	Yes		Ellipsoidal (ξ, η, ζ)	No	
Conical (λ, μ, ν)	Yes				

Table 2.1. Characteristics of the eleven different separable three-dimensional coordinates for the scalar wave equation [18].

In this chapter, vector wave functions for five different perfectly conducting bodies will be derived analytically. The study will extend from a simple well-known structure such as the perfectly conducting sphere to more complicated but much practical planar structures, such as the circular disk and the planar strip. The objective of this study is twofold: on the one hand, closed-form expressions for the current modes in the structures will be derived, which could be used in certain problems to accelerate the computation of impedance matrices; on the other hand, properties of these modes will be analyzed, in order to improve the design of planar antennas and provide some design guidelines. Additionally, the possibility of analyzing planar

structures by degeneration or deformation of three-dimensional bodies, whose surface coincides with any of the eleven coordinate systems, will be considered.

Afterwards, the suitability of these vector wave functions for antenna design will be discussed. As discussed later, another type of modes (called characteristic modes, which were initially defined by Garbacz [13][14]), will be proven to be more suitable for design purposes, due to their real nature. In the next chapter, properties of characteristic modes will be discussed, emphasizing their similarities to those of the traditionally used vector wave functions. Connections between the vector wave functions of the structure analyzed in this chapter and their characteristic modes will be established in the following chapter.

2.2. Modes in a perfectly conducting sphere

The conducting sphere is a very well-known structure, whose modal properties have been widely analyzed in the literature [9]-[11]. In this section, a short review of the most interesting properties of the vector wave functions associated to this structure will be reviewed.

Thus, let us consider a source-free, linear, homogeneous and isotropic region. If a perfectly conducting sphere of radius a is considered, the wave equation associated to the fields radiated or scattered by the sphere is separable if a spherical coordinate system is used. Traditional definition of spherical coordinates can be found in Appendix A. In this case, a set of spherical wave functions or modes TM (Transverse Magnetic) and TE (Transverse Electric) to r can be defined, in which the total field can be expanded.

For the TM to r case, the magnetic and electric vector wave functions can be expressed, respectively, by [9]:

$$\vec{H}_{mn}^{TM\ e,o} = r \cdot h_n^{(2)}(kr) \left[\hat{\theta} \cdot \frac{P_n^m(\cos\theta)}{\sin\theta} \cdot \begin{Bmatrix} -\sin m\phi \\ \cos m\phi \end{Bmatrix} \cdot m - \hat{\phi} \cdot \frac{\partial P_n^m(\cos\theta)}{\partial\theta} \cdot \begin{Bmatrix} \cos m\phi \\ \sin m\phi \end{Bmatrix} \right] \quad (2.5)$$

$$\begin{aligned}
 \vec{E}_{mn}^{TM\ e,o} &= \frac{1}{j\omega\epsilon} \nabla \times \vec{H}_{mn}^{TM\ e,o} = \\
 &= \frac{1}{j\omega\epsilon} \cdot \frac{1}{r} \left[\hat{\phi} \cdot \frac{\partial [kr \cdot h_n^{(2)}(kr)]}{\partial r} \cdot \frac{P_n^m(\cos\theta)}{\sin\theta} \cdot \left\{ \begin{array}{l} -\sin m\phi \\ \cos m\phi \end{array} \right\} \cdot m + \right. \\
 &\quad \left. + \hat{\theta} \cdot \frac{\partial [kr \cdot h_n^{(2)}(kr)]}{\partial r} \cdot \frac{\partial P_n^m(\cos\theta)}{\partial \theta} \cdot \left\{ \begin{array}{l} \cos m\phi \\ \sin m\phi \end{array} \right\} \right] \\
 &\quad \left[\hat{r} \cdot \frac{1}{\sin\theta} \cdot r \cdot h_n^{(2)}(kr) \cdot \left[\frac{\partial}{\partial \theta} \left[\frac{-\partial P_n^m(\cos\theta)}{\partial \theta} \sin\theta \right] \cdot \left\{ \begin{array}{l} \cos m\phi \\ \sin m\phi \end{array} \right\} + \right. \right. \\
 &\quad \left. \left. + \frac{P_n^m(\cos\theta) \cdot m}{\sin\theta} \cdot \left\{ \begin{array}{l} \cos m\phi \\ \sin m\phi \end{array} \right\} \right] \right] \quad (2.6)
 \end{aligned}$$

where $n = 1, 2, 3, \dots$; $m = 0, 1, 2, \dots, n$, and subscript e, o denote even and odd modes associated to $\cos m\phi$ and $\sin m\phi$, respectively. Moreover, $P_n^m(\cos\theta)$ are the associated Legendre functions of the first kind, and $h_n^{(2)}(kr)$ are the spherical Hankel functions of the second kind, which represent outward traveling waves.

In the dual case, the set of field modes TE to r is given by:

$$\vec{E}_{mn}^{TE\ e,o} = -\nabla \times \hat{r} (F_r)_{mn}^{e,o} = k \cdot h_n^{(2)}(kr) \cdot \left[\hat{\phi} \cdot \frac{\partial P_n^m(\cos\theta)}{\partial \theta} \cdot \left\{ \begin{array}{l} \cos m\phi \\ \sin m\phi \end{array} \right\} - \right. \\
 \left. - \hat{\theta} \cdot \frac{P_n^m(\cos\theta)}{\sin\theta} \cdot \left\{ \begin{array}{l} -\sin m\phi \\ \cos m\phi \end{array} \right\} \cdot m \right] \quad (2.7)$$

$$\begin{aligned}
 \vec{H}_{mn}^{TE\ e,o} &= -\frac{1}{j\omega\mu} \nabla \times \vec{E}_{mn}^{TE\ e,o} = \\
 &= -\frac{1}{j\omega\mu} \cdot \frac{1}{r} \cdot \frac{\partial [kr \cdot h_n^{(2)}(kr)]}{\partial r} \cdot \left[\hat{\theta} \cdot \frac{\partial P_n^m(\cos\theta)}{\partial \theta} \cdot \left\{ \begin{array}{l} \cos m\phi \\ \sin m\phi \end{array} \right\} + \right. \\
 &\quad \left. + \hat{\phi} \cdot \frac{P_n^m(\cos\theta)}{\sin\theta} \cdot \left\{ \begin{array}{l} -\sin m\phi \\ \cos m\phi \end{array} \right\} \cdot m \right] \quad (2.8)
 \end{aligned}$$

The set of TM plus TE modes is complete, and hence a summation of them can be used to represent an arbitrary field in a source-free region. Moreover, each mode can be characterized by a single radially directed wave impedance expressed by [9]:

$$Z_n^{TM} = \frac{E_\theta^{TM}}{H_\phi^{TM}} = j\eta \frac{h_n^{(2)'}(kr)}{h_n^{(2)}(kr)}; \quad Z_n^{TE} = \frac{E_\theta^{TE}}{H_\phi^{TE}} = -j\eta \frac{h_n^{(2)}(kr)}{h_n^{(2)'}(kr)} \quad (2.9)$$

The behavior of the spherical Hankel functions of the second kind $h_n^{(2)}(kr) = j_n(kr) - i \cdot n_n(kr)$ shows that for arguments $kr < n$, the imaginary parts of spherical Hankel functions and their derivatives become large in magnitude. Hence, these wave impedances become predominantly reactive when $kr < n$ and predominantly resistive when $kr > n$. Figure 2.1 illustrates this behavior by showing X_n/R_n , where $Z_n = R_n + jX_n$, for the first five TM and TE modes. Thereby the value $kr = n$ (independent of the mode number m) may be considered as a point of frequency cut-off [9].

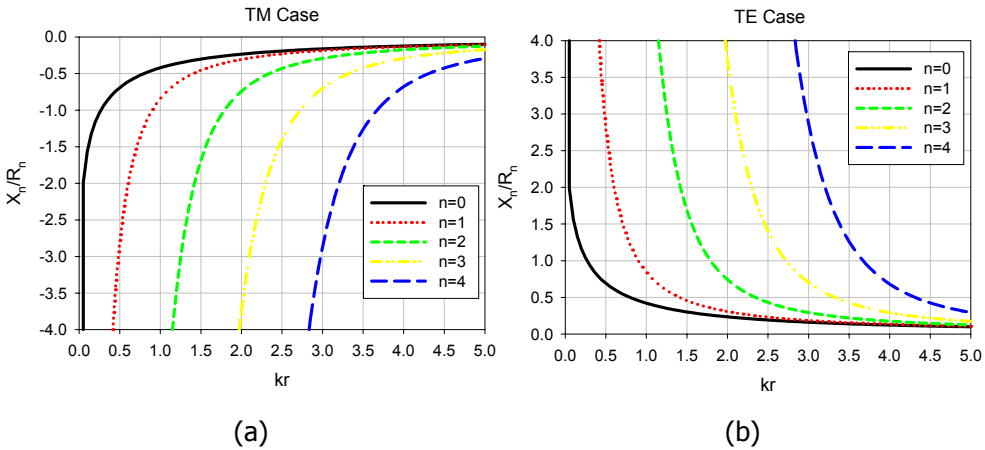


Figure 2.1 Ratios of wave reactance to wave resistance: (a) For the TM spherical modes; (b) For the TE spherical modes.

In addition, an equivalent circuit for the TM_{mn} and TE_{mn} modes can be proposed [19], based on the recurrence relations of Bessel functions, which clearly shows that, for fixed r , the higher the mode number n , the lower the power transmitted by a spherical mode. Moreover, a quality factor Q_n for modes of order n can be defined, which is a quantitative measure of its bandwidth. This quality factor is defined as [9]:

$$Q_n = \begin{cases} \frac{2\omega\bar{W}_e}{\bar{W}_{rad}} & \bar{W}_e > \bar{W}_m \\ \frac{2\omega\bar{W}_m}{\bar{W}_{rad}} & \bar{W}_m > \bar{W}_e \end{cases} \quad (2.10)$$

where \bar{W}_e and \bar{W}_m are the average stored electric and magnetic energies of the mode, and \bar{W}_{rad} is the radiated power. In the TM waves $\bar{W}_e > \bar{W}_m$, while in the TE waves $\bar{W}_m > \bar{W}_e$. However, due to the duality of TM and TE modes, their associated Q's are equivalent [9].

Furthermore, associated to these TM and TE modal fields, a set of current modes in the surface of the conducting sphere of radius a can be obtained as following:

$$\begin{aligned} \vec{J}_{S,mn}^{TM\ e,o} &= \hat{n} \times \vec{H}_{mn}^{TM\ e,o} \Big|_{r=a} = \hat{r} \times \vec{H}_{mn}^{TM\ e,o} \Big|_{r=a} = \\ &= ka \cdot h_n^{(2)}(ka) \left[\hat{\phi} \cdot \frac{P_n^m(\cos\theta)}{\sin\theta} \cdot \begin{Bmatrix} -\sin m\phi \\ \cos m\phi \end{Bmatrix} \cdot m + \hat{\theta} \cdot \frac{\partial P_n^m(\cos\theta)}{\partial\theta} \cdot \begin{Bmatrix} \cos m\phi \\ \sin m\phi \end{Bmatrix} \right] \end{aligned} \quad (2.11)$$

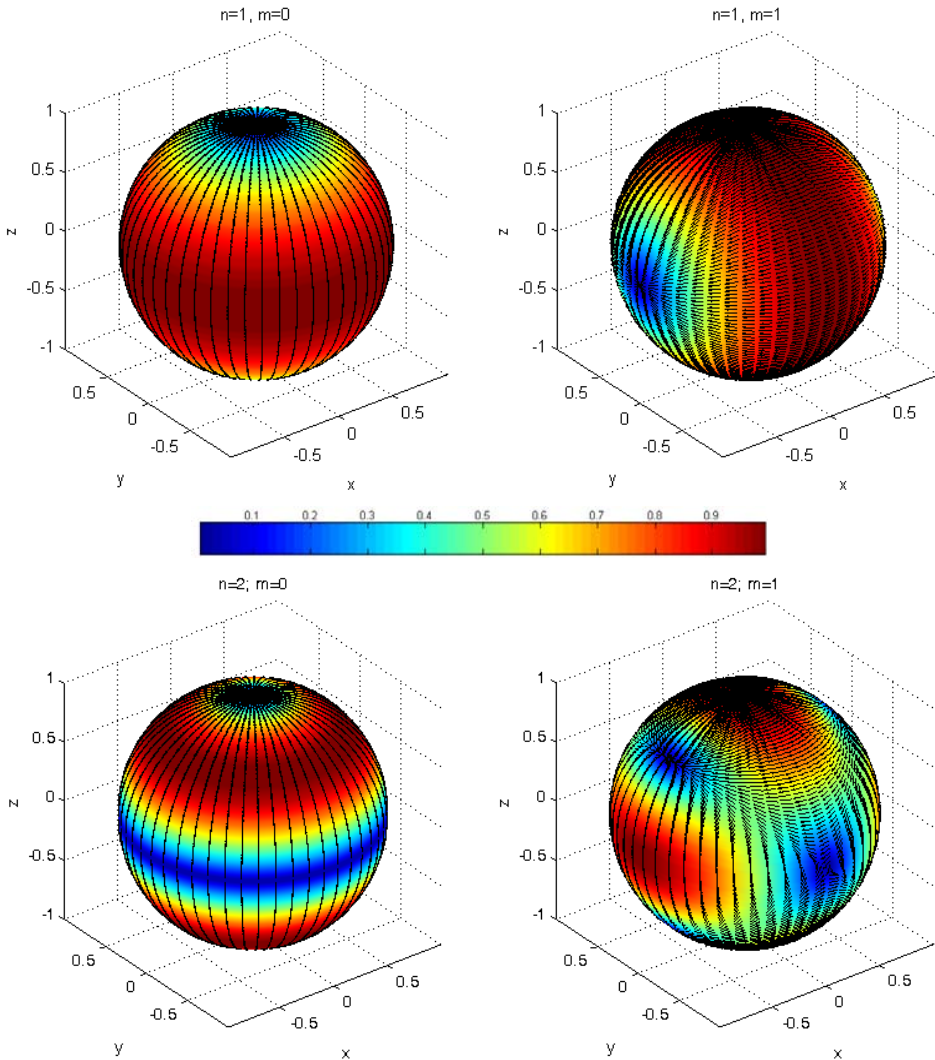
$$\begin{aligned} \vec{J}_{S,mn}^{TE\ e,o} &= \hat{n} \times \vec{H}_{mn}^{TE\ e,o} \Big|_{r=a} = \hat{r} \times \vec{H}_{mn}^{TE\ e,o} \Big|_{r=a} = \\ &= \frac{1}{j\omega\mu} \cdot \frac{1}{a} \cdot \frac{\partial [kr \cdot h_n^{(2)}(kr)]}{\partial r} \cdot \left[\begin{array}{l} \hat{\theta} \cdot \frac{P_n^m(\cos\theta)}{\sin\theta} \cdot \begin{Bmatrix} -\sin m\phi \\ \cos m\phi \end{Bmatrix} \cdot m - \\ -\hat{\phi} \cdot \frac{\partial P_n^m(\cos\theta)}{\partial\theta} \cdot \begin{Bmatrix} \cos m\phi \\ \sin m\phi \end{Bmatrix} \end{array} \right] \end{aligned} \quad (2.12)$$

where $\vec{J}_{S,mn}^{TM\ e,o}$, $\vec{J}_{S,mn}^{TE\ e,o}$ represents the surface current modes on the sphere of radius a for the TM and TE case, respectively. As observed, these current modes are complex, as a result of the complex nature of the spherical Hankel function of the second kind.

In Figure 2.2, some of the normalized TM even vector current modes are depicted, for different values of m and n . Colors in the figure represent absolute values of the modal current, whereas arrows represent its vector nature. Only the real part of the modal current has been represented for the vectors in the figure, since the distribution for imaginary vector currents is very similar. As observed in the figure, index m is associated to the number of azimuthal variations, while index n is

associated to the total number of variations (both in elevation and azimuth) of the current distribution. Thus, for instance, current mode with $n=1, m=0$ exhibits one variation in θ and no variation in ϕ , while presenting only vector components in $\hat{\theta}$ direction, as shown in the figure. In consequence, the higher the index n of the mode, the higher number of variations the mode will exhibit.

These modal current distributions are therefore associated to the field modes of the same index m and n , given by equations (2.5) and (2.6).



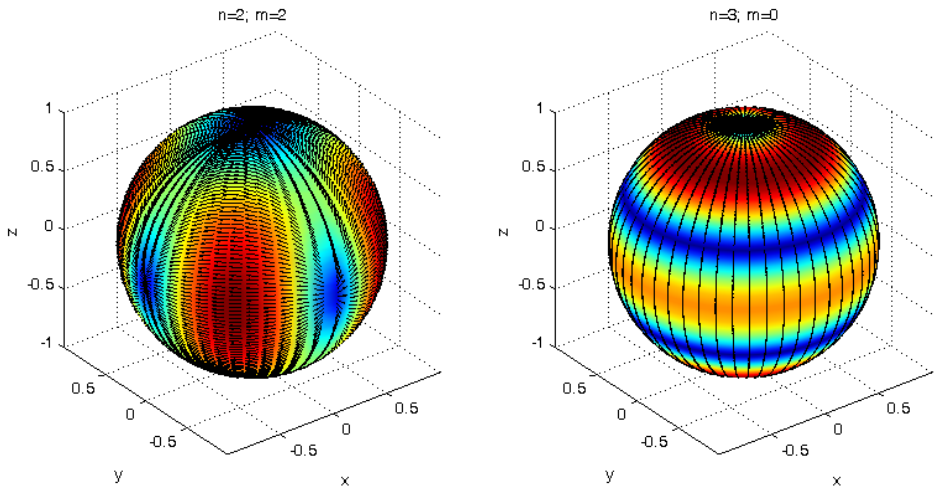
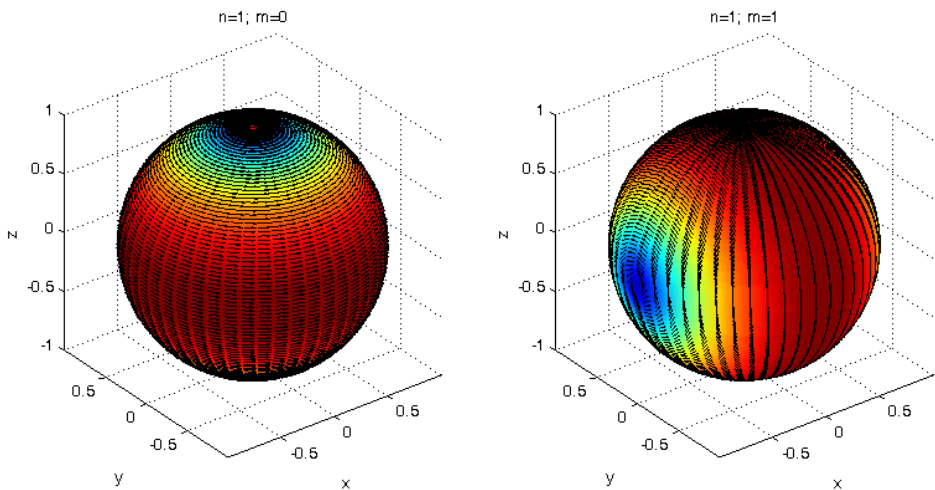


Figure 2.2 Normalized real part of the current distribution of even modes on the surface of a sphere of radius $a = 0.16\lambda$, associated to the set of field modes TM to r , for different values of m and n .

For the TE case, different current distributions are associated to the field modes, as observed in Figure 2.3. The significance of indexes is the same as in the TM case. For instance, even current mode with $n=1, m=0$ exhibits also one variation in θ and no variation in ϕ , but in this case it only has vector components in $\hat{\theta}$ direction.



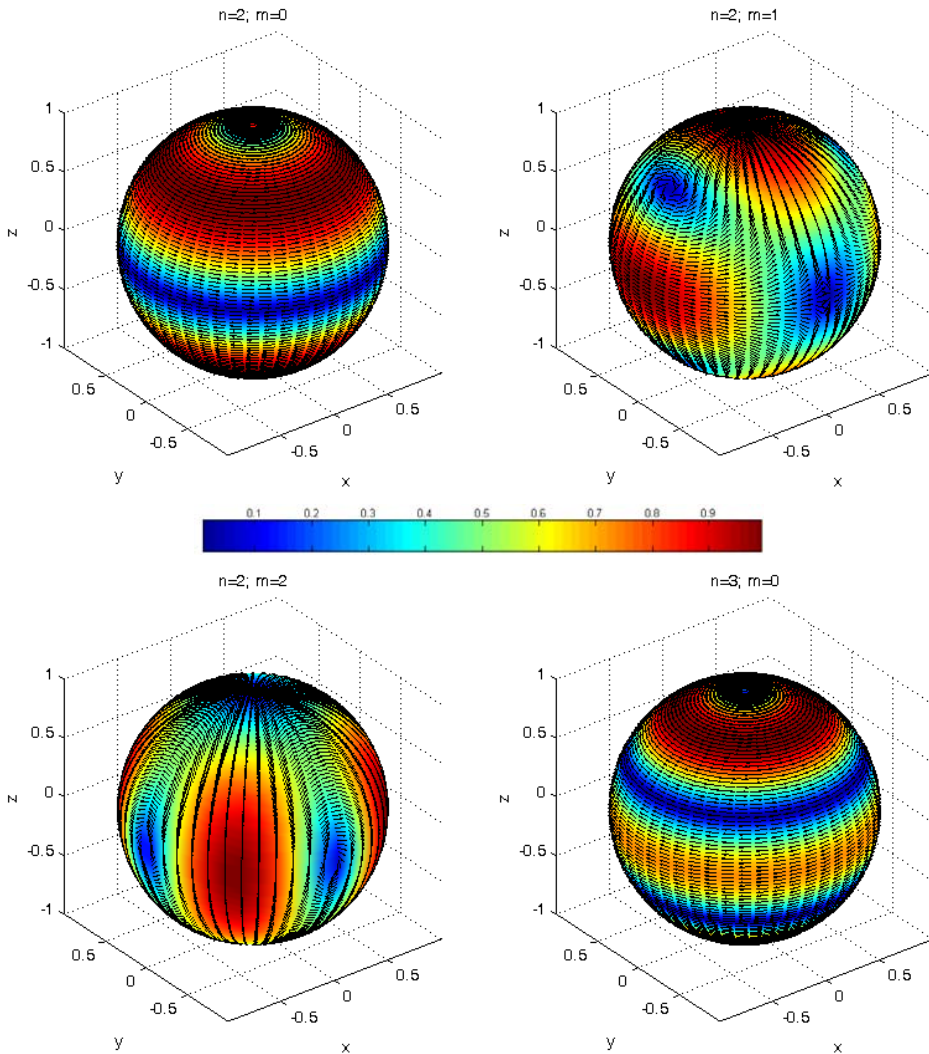


Figure 2.3 Normalized real part of the current distribution of even modes on the surface of a sphere of radius $a = 0.16\lambda$, associated to the set of field modes TE to r , for different values of m and n .

Knowledge of the modal current distributions or eigencurrents in the surface of a sphere, which are responsible of each modal field, is important in order to determine the most appropriate location of sources in the structure for exciting a specific mode. As already discussed, each mode is characterized by a modal impedance and a quality factor, which determine its radiating behavior and bandwidth. A

detailed analysis of the properties of the modal currents on the sphere can be proposed as a previous step to excite the structure, in order to improve the behavior of the antenna.

Next sections will be focused on the analysis of modal properties in planar structures. Vector wave functions will be analyzed for a circular disk and a planar strip, as these are common geometries employed for wireless communication antennas.

2.3. Modes of current in a circular disk

In order to extract the modal current distribution of planar objects, such as a circular disk, an analytical approach can consist in analyzing the current modes of a more general structure, which degenerates to the planar structure in a limit case, as commented in [10]. This will be the adopted approach for the circular conducting disk: Firstly, vector wave functions of a perfectly conducting spheroid will be presented and modal current distributions will be computed. Then, the height of the spheroid will be progressively reduced, tending to the limit case in which the spheroid derives into a circular disk, and hence the modal currents for this planar structure will be obtained.

In order to compute the modal currents of a perfectly conducting spheroid, the vector wave equation should be solved in spheroidal coordinates. Spheroidal coordinates are formed by rotating the two dimensional elliptic coordinate system about the major or minor axes of the ellipses. In the former case, the prolate spheroidal coordinate system is derived, whereas in the latter case, the oblate spheroidal system is obtained. In any of both coordinate systems, a circular disk can be obtained in the limit case. Consequently, they are equally valid to analyze the proposed structure, but only one of them must be chosen to avoid unnecessary redundancy in this section. The oblate spheroidal system has finally been the choice, but the prolate spheroidal system could have been selected as well.

In both spheroidal systems, any point of space is defined by three values (ξ, η, ϕ) , where $-1 \leq \eta \leq 1$, $0 \leq \xi < \infty$, $0 \leq \phi \leq 2\pi$, as shown in Figure 2.4. In Appendix A, section A2, a more detailed description of the oblate spheroidal coordinate system is provided.

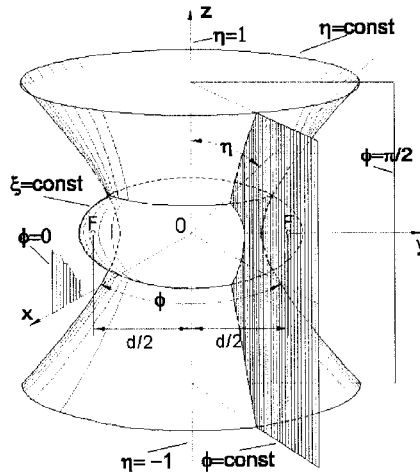


Figure 2.4 Oblate spheroidal coordinate system [20].

In this coordinate system, the determination of spheroidal vector wave functions which solve the vector wave equation results more difficult than in the spherical case, since the wave equation is not separable in spheroidal coordinates [21]. As shown in Table 2.1, there are only six coordinate systems that support orthogonal vector wave solutions (rectangular, circular-cylinder, elliptic-cylinder, parabolic-cylinder, spherical, and conical coordinate systems), but the spheroidal system is not included among them [18]. Nevertheless, since spheroidal coordinates are included in the eleven basic coordinate systems that support solutions to the scalar Helmholtz equation in three dimensions, wave functions can be obtained by expressing the quantities in equation (2.3) in spheroidal coordinates [20].

Solutions of the scalar Helmholtz equation in spheroidal coordinates can be expressed as:

$$\psi_{mn}^{e,o} = S_{mn}(-ic, \eta) \cdot R_{mn}^{(i)}(-ic, i\xi) \cdot \begin{cases} \cos m\phi \\ \sin m\phi \end{cases} \quad (2.13)$$

where three independent functions are found:

- (1) the angular spheroidal function $S_{mn}(-ic, \eta)$,
- (2) the radial spheroidal function $R_{mn}^{(i)}(-ic, i\xi)$,
- (3) sine and cosine functions.

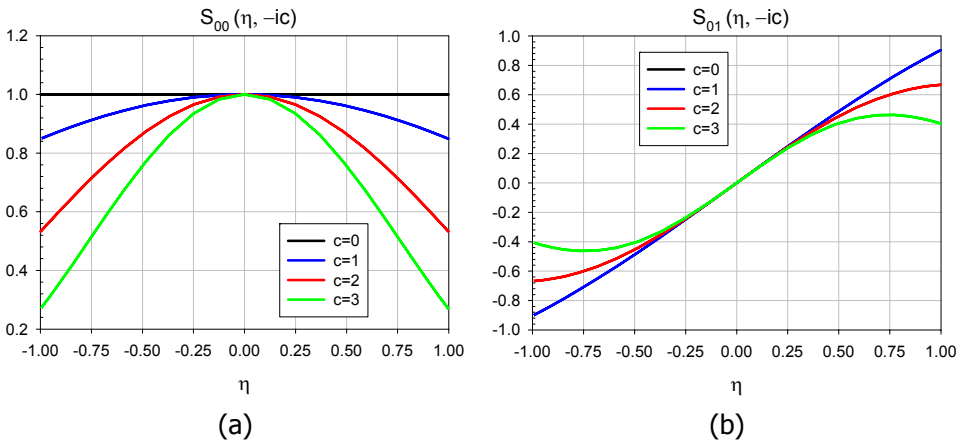
In general, the angular and radial functions in spheroidal coordinates are the generalization of Legendre functions and spherical Bessel functions, respectively, in spherical polar coordinates [20]. Appendix A contains a detailed description of these functions, including their expansion in series of Legendre and Bessel functions.

Computation of spheroidal radial or angular functions results computationally intensive, since it requires an eigenvalue computation with forward and backward recursion formulations. In [22], an optimized Fortran code is provided to compute these special functions, whereas [23] provides tabulated results for the functions evaluated with different parameters, which have been proven very useful to test results.

Moreover radial and angular functions also depend on the dimensionless parameter c , defined by:

$$c = \frac{1}{2}kd = \pi \frac{d}{\lambda} \quad (2.14)$$

where λ is the wavelength corresponding to the wave number k , and d is the focal distance (see Figure 2.4). Therefore, spheroidal functions also depend on geometrical parameters such as the focal distance. For the sake of illustration, spheroidal angular functions $S_{nm}(-ic, \eta)$ vs. η have been plotted in Figure 2.5, for different values of parameter c . On the one hand, as $c \rightarrow 0$ the angular functions collapse to Legendre functions of the first kind, with the same m and n values. Consequently, for a small value of the c parameter, the spheroid can be approximated to a sphere, with a more than acceptable precision.



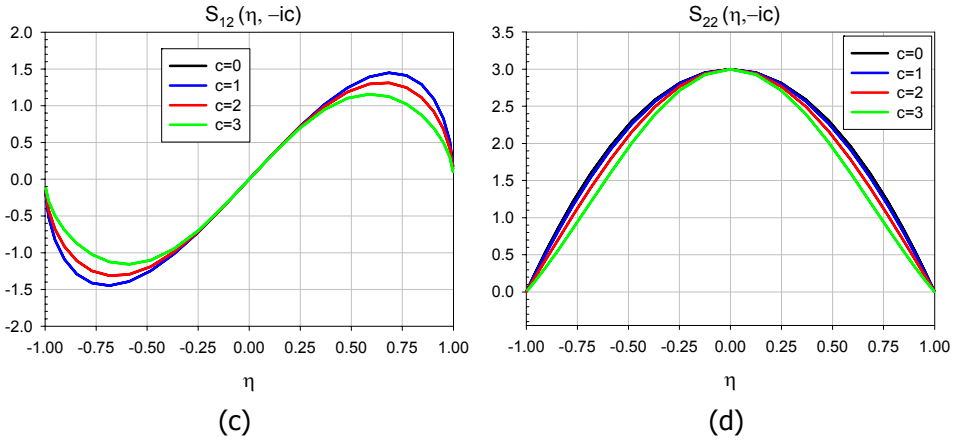


Figure 2.5 Spheroidal angular functions for oblate coordinates, for different values of parameter c : (a) $S_{00}(-ic, \eta)$; (b) $S_{01}(-ic, \eta)$; (c) $S_{12}(-ic, \eta)$; (d) $S_{22}(-ic, \eta)$.

On the other hand, radial functions $R_{mn}^{(i)}(-ic, i\xi)$ are usually expanded in a basis of spherical Bessel functions (see Appendix A). Plots of these functions can be found in [24].

As previously mentioned, once the scalar wave equation has been resolved in oblate spheroidal coordinates, vector wave functions can be obtained by using equation (2.3) and setting \hat{u} equal to the position vector \hat{r} , resulting in the following expression in spheroidal coordinates:

$$\hat{r} = -\frac{1}{2}d\eta\sqrt{\frac{1-\eta^2}{\xi^2+\eta^2}} \cdot \hat{\eta} + \frac{1}{2}d\xi\sqrt{\frac{\xi^2+1}{\xi^2+\eta^2}} \cdot \hat{\xi} \quad (2.15)$$

Therefore, the resulting spheroidal vector wave functions can be written as [20]:

$$\begin{aligned}
 \vec{M}_{mn}^{r e, o}(c; \eta, \xi, \phi) &= \nabla \times (\hat{r} \cdot \psi_{mn}) = \frac{m \cdot \xi}{\left(\sqrt{(\xi^2 + \eta^2)}(1 - \eta^2) \right)} \cdot S_{mn} \cdot R_{mn}^{(4)} \cdot \begin{Bmatrix} \sin(m\phi) \\ -\cos(m\phi) \end{Bmatrix} \cdot \hat{\eta} + \\
 &+ \frac{m \cdot \eta}{\left(\sqrt{(\xi^2 + \eta^2)}(\xi^2 + 1) \right)} \cdot S_{mn} \cdot R_{mn}^{(4)} \cdot \begin{Bmatrix} \sin(m\phi) \\ -\cos(m\phi) \end{Bmatrix} \cdot \hat{\xi} + \\
 &+ \frac{\sqrt{(\xi^2 + 1)}(1 - \eta^2)}{(\xi^2 + \eta^2)} \left[\xi \frac{\partial S_{mn}}{\partial \eta} \cdot R_{mn}^{(4)} + \eta S_{mn} \frac{\partial R_{mn}^{(4)}}{\partial \xi} \right] \cdot \begin{Bmatrix} \cos(m\phi) \\ \sin(m\phi) \end{Bmatrix} \cdot \hat{\phi}
 \end{aligned} \tag{2.16}$$

$$\begin{aligned}
 \vec{N}_{mn}^{r e, o}(c; \eta, \xi, \phi) &= \frac{1}{k} \nabla \times \nabla \times (\hat{r} \cdot \psi_{mn}) = \\
 &= \frac{\sqrt{\xi^2 + 1}}{kd \sqrt{\xi^2 + \eta^2}} \left[\frac{m^2 \xi S_{mn} R_{mn}^{(4)}}{(\xi^2 + 1)(1 - \eta^2)} - \frac{\partial}{\partial \eta} \left(\frac{1 - \eta^2}{(\xi^2 + \eta^2)} \left[\eta S_{mn} \frac{\partial R_{mn}^{(4)}}{\partial \xi} + \xi R_{mn}^{(4)} \frac{\partial S_{mn}}{\partial \eta} \right] \right) \right] \cdot \begin{Bmatrix} \cos(m\phi) \\ \sin(m\phi) \end{Bmatrix} \cdot \hat{\xi} \\
 &+ \frac{\sqrt{1 - \eta^2}}{kd \sqrt{\xi^2 + \eta^2}} \left[\frac{\partial}{\partial \xi} \left(\frac{(\xi^2 + 1)}{(\xi^2 + \eta^2)} \left[\eta S_{mn} \frac{\partial R_{mn}^{(4)}}{\partial \xi} + \xi R_{mn}^{(4)} \frac{\partial S_{mn}}{\partial \eta} \right] \right) - \frac{m^2 \eta S_{mn} R_{mn}^{(4)}}{(\xi^2 + 1)(1 - \eta^2)} \right] \cdot \begin{Bmatrix} \cos(m\phi) \\ \sin(m\phi) \end{Bmatrix} \cdot \hat{\eta} - \\
 &- \frac{m \sqrt{(\xi^2 + 1)}(1 - \eta^2)}{kd (\xi^2 + \eta^2)} \left[\frac{S_{mn}}{(1 - \eta^2)} \frac{\partial \xi R_{mn}^{(4)}}{\partial \xi} - \frac{R_{mn}^{(4)}}{(\xi^2 + 1)} \frac{\partial (\eta S_{mn})}{\partial \eta} \right] \cdot \begin{Bmatrix} -\sin(m\phi) \\ \cos(m\phi) \end{Bmatrix} \cdot \hat{\phi}
 \end{aligned} \tag{2.17}$$

where $\vec{M}_{mn}^{r e, o}$ and $\vec{N}_{mn}^{r e, o}$ would correspond to the TM and TE wave functions with respect to the position vector \vec{r} , respectively [25], and the dependence of $R_{mn}^{(4)}$ and S_{mn} with respect to $(-ic; \eta, i\xi)$ has been omitted for brevity. By using these functions, any field can be expressed as:

$$\begin{cases} \vec{E}(c; \eta, \xi, \phi) = \sum_{n=1}^{\infty} \sum_{m=-n}^n \left(\alpha_{mn} \vec{M}_{mn}^{r e, o} + \beta_{mn} \vec{N}_{mn}^{r e, o} \right) \\ \vec{H}(c; \eta, \xi, \phi) = \sum_{n=1}^{\infty} \sum_{m=-n}^n \left(\alpha_{mn} \vec{N}_{mn}^{r e, o} + \beta_{mn} \vec{M}_{mn}^{r e, o} \right) \end{cases} \tag{2.18}$$

These spheroidal vector wave functions have recently been used for the calculation of closed-form eigenfrequencies in spheroidal cavities [26], for the improvement of

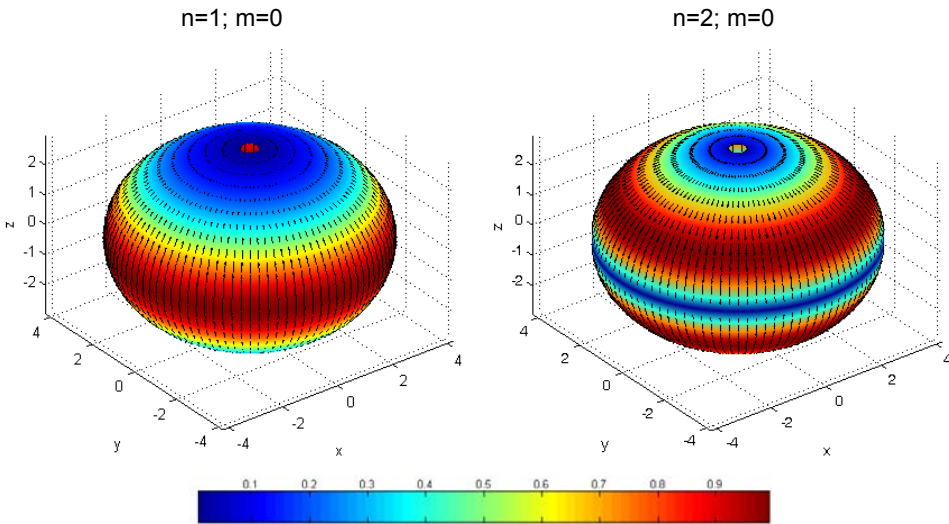
near-field to far-field transformation in both linear and planar structures [27] and for the analysis of the input impedance of a prolate-spheroidal monopole antenna fed by a magnetic frill [28].

For the TM case, the vector current modes can be expressed, for instance, as:

$$\begin{aligned} \vec{J}_{S,mm}^{TM e,o}(c;\eta,\xi,\phi) = & \frac{m \cdot \xi}{\left(\sqrt{(\xi^2 + \eta^2)(1 - \eta^2)}\right)} \cdot S_{mn} \cdot R_{mn}^{(4)} \cdot \begin{Bmatrix} \sin(m\phi) \\ -\cos(m\phi) \end{Bmatrix} \cdot \hat{\phi} - \\ & - \frac{\sqrt{(\xi^2 + 1)(1 - \eta^2)}}{(\xi^2 + \eta^2)} \left[\xi \frac{\partial S_{mn}}{\partial \eta} \cdot R_{mn}^{(4)} + \eta S_{mn} \frac{\partial R_{mn}^{(3)}}{\partial \xi} \right] \cdot \begin{Bmatrix} \cos(m\phi) \\ \sin(m\phi) \end{Bmatrix} \cdot \hat{\eta} \end{aligned} \quad (2.19)$$

where the dependence of $R_{mn}^{(4)}$ and S_{mn} with respect to $(-ic;\eta,i\xi)$ has been omitted for brevity.

This set of modes has been computed for an spheroid of radius $\xi = 1$, a focal distance $d = 6$ and parameter $c = 1$. Some of the TM even modal current distributions are shown in Figure 2.6, for different values of m and n .



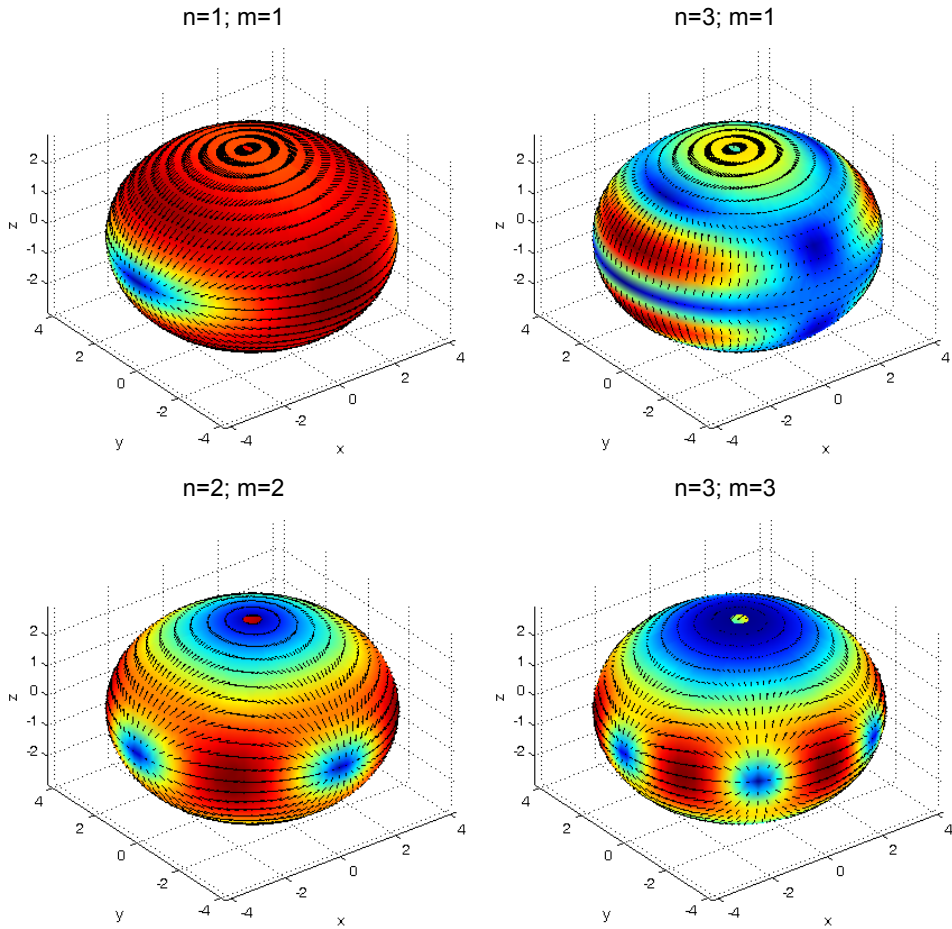


Figure 2.6 Normalized real part of the current distribution of even vector modes on the surface of an oblate spheroid of $\xi = 1$, focal distance $d = 6$ and $c = 1$, associated to the set of field modes TM to r , for different values of m and n .

As in the conducting sphere, colors in the figure represent absolute values of the even modal current, whereas arrows represent its vectorial orientation. Only the real part of the vector modal current has been represented in the figure, but imaginary vector currents will present nonetheless a similar behavior. As observed, current modes have similar distributions to those of the spherical modes, for the same m and n .

For the TE case, vector current modes present similar distributions to the spherical case. For brevity, these current modes have not been included here.

Once vector wave functions for the current have been obtained for the conducting oblate spheroid, analytical expressions for the current modes in a planar circular disk can be extracted by deforming the spheroid and tending to the limit case $\xi = 0$. As shown in Figure 2.7, when $\xi \rightarrow 0$ the oblate spheroid degenerates in a circular disk.

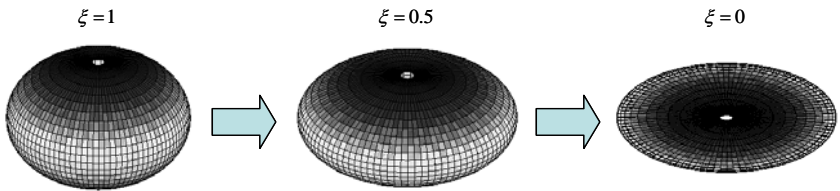
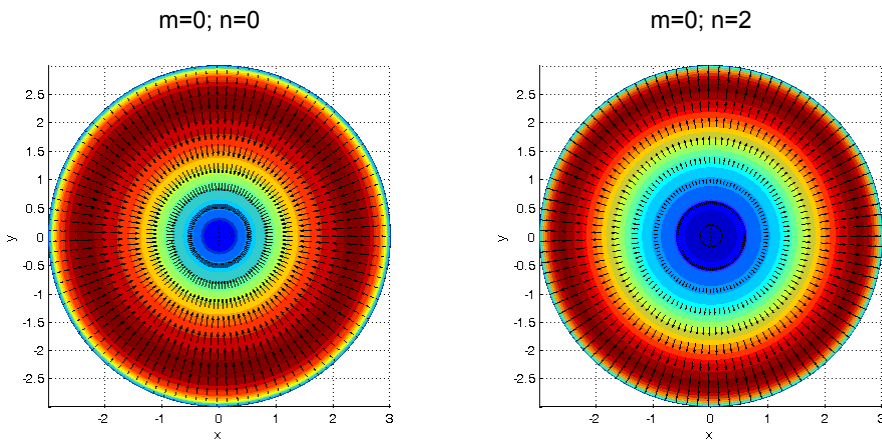


Figure 2.7 Circular disk as a derivation of the oblate spheroid when $\xi \rightarrow 0$.

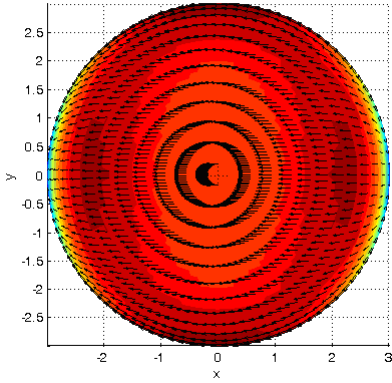
Therefore, modal currents TM to r in the surface of the conducting disk can be then expressed as follows:

$$\vec{J}_{S,mm}^{TM e,o}(c;\eta,\xi=0,\phi) = \hat{\eta} \cdot \frac{-\sqrt{(1-\eta^2)}}{\eta} \cdot S_{mm}(-ic;\eta) \cdot \left. \frac{\partial R_{mm}^{(4)}(-ic,i\xi)}{\partial \xi} \right|_{\xi=0} \cdot \begin{cases} \cos(m\phi) \\ \sin(m\phi) \end{cases} \quad (2.20)$$

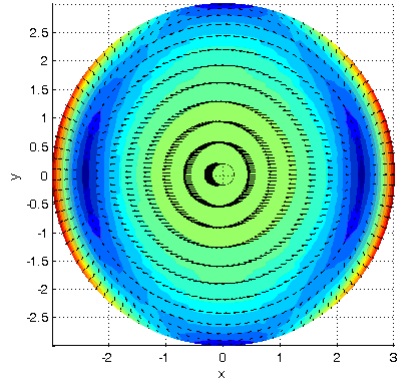
Figure 2.8 shows these vector current modes for the TM case.



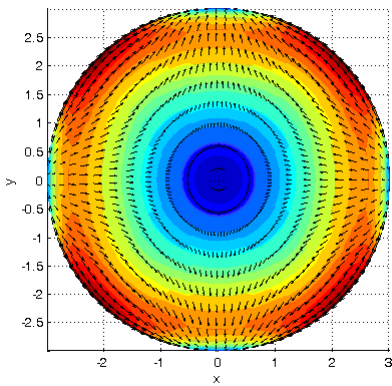
$m=1; n=1$



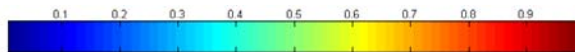
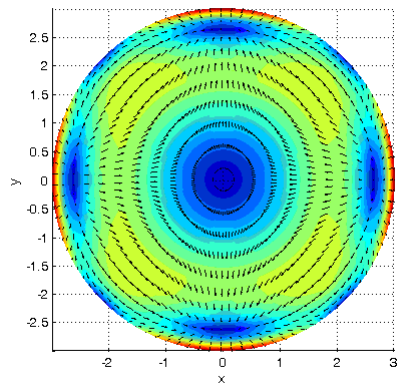
$m=1; n=2$



$m=2; n=2$



$m=2; n=3$



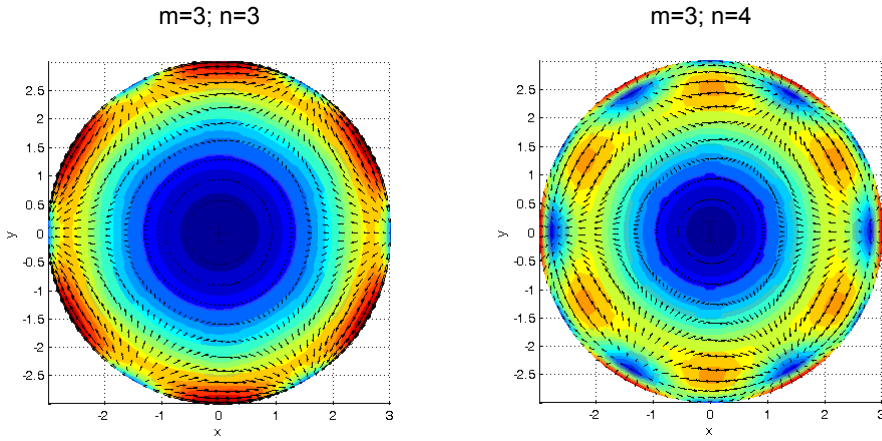
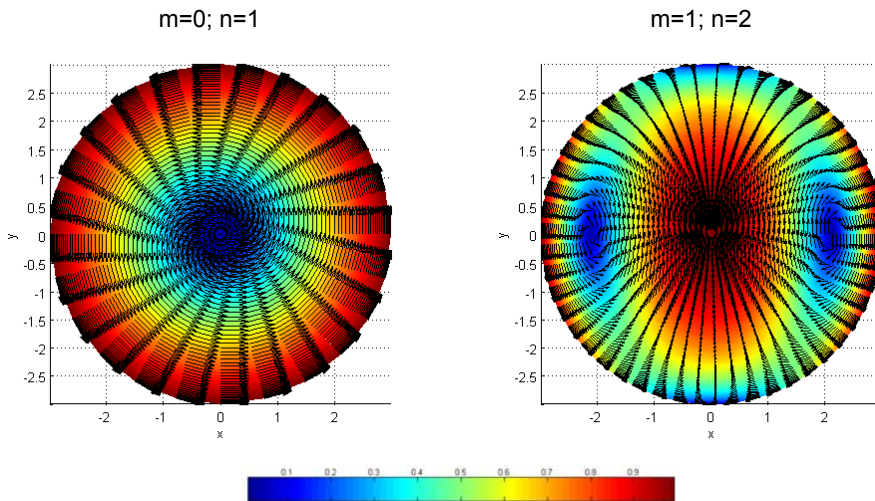


Figure 2.8 Normalized real part of the current distribution of even vector modes on the surface of a circular disk, associated to the set of field modes TM to r , for different values of m and n .

For the TE case, current modes are shown in Figure 2.9. As observed, in this case the current describes loops in the surface of the circular disk.



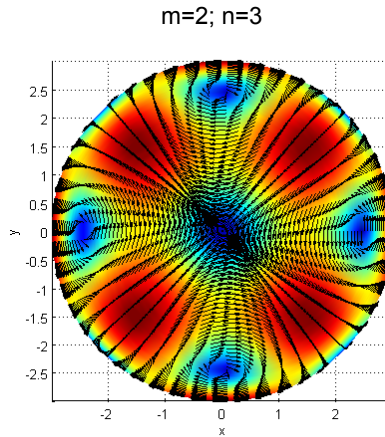


Figure 2.9 Normalized real part of the current distribution of even vector modes on the surface of a circular disk, associated to the set of field modes TE to r , for different values of m and n .

2.4. Modes in an infinite planar strip

In order to find the vector wave functions of an infinite planar strip, a similar approach to that of the previous section can be adopted. In this case, the infinite planar strip can be analyzed as one of the limit cases of an infinite elliptic cylinder. Therefore, vector wave functions of a perfectly conducting elliptic cylinder will be first computed. Afterwards, the elliptic cylinder will be deformed, tending to the limit case in which it derives into a planar strip. The modal currents for the resulting planar structure will hence be obtained.

In order to find the vector wave functions of an infinite elliptic cylinder, a solution of the vector wave equation in elliptical-cylindrical coordinates must be obtained. The elliptical-cylindrical coordinate system (Figure 2.10) is very similar to the spheroidal system, although with the main difference that in this case coordinate z replaces coordinate ϕ . Therefore, any point of space can be defined by three values (ξ, η, z) , with $\xi \in [0, \infty)$, $\eta \in [0, 2\pi)$ and $z \in (-\infty, \infty)$. Detailed information about this coordinate system can be found in Appendix A, section A3.

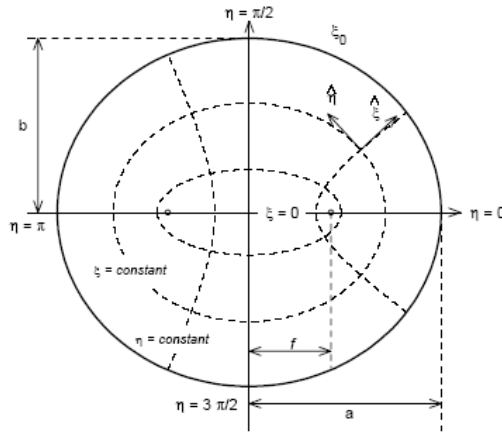


Figure 2.10 Elliptic coordinate system [29].

Since the vector wave equation is separable in this coordinate system, orthogonal elliptical vector wave functions, which are solution of the vector wave equation, can be obtained straightforwardly in this case [21].

The scalar Helmholtz equation in elliptic coordinates can be solved by the method of separation of variables (see Appendix A), and hence the general solution can be expressed as:

$$\psi_m^{e,o}(\xi, \eta, z; s) = \begin{cases} Se_m(\eta; s) \cdot Re_m(\xi; s) \cdot \exp(\pm ik_z z) \\ So_m(\eta; s) \cdot Ro_m(\xi; s) \cdot \exp(\pm ik_z z) \end{cases} \quad (2.21)$$

where three independent functions, with very similar properties as those presented before for the spheroidal vector wave equation, are found [30]:

- (1) the angular Mathieu functions $Se_m(\eta; s), So_m(\eta; s)$
- (2) the radial Mathieu functions $Re_m^{(i)}(\xi; s), Ro_m^{(i)}(\xi; s)$
- (3) the exponential function $\exp(\pm ik_z z)$

Angular Mathieu functions $Se_m(\eta; s)$ and $So_m(\eta; s)$ are real periodic functions which can be expressed by Fourier series, as shown in equations (A.3-13)-(A.3-16) of Appendix A. Functions $Se_m(\eta; s)$ represent cosine-elliptic functions which are

even about $\eta = 0$, whereas $So_m(\eta; s)$ represent sine-elliptic functions, which are odd functions.

Figure 2.11 graphically represents functions $Se_m(\eta; s)$ and $So_m(\eta; s)$ with $s = 1$ for different values of m . As portrayed by the figure, the number of oscillations of these functions increases with the value of m . Moreover, it is shown that angular functions $Se_m(\eta; s)$ present symmetry about $\eta = 90^\circ$ for m even, and antisymmetry for m odd. Besides, odd angular functions $So_m(\eta; s)$ are symmetric about $\eta = 90^\circ$ for m odd, and antisymmetric for m even.

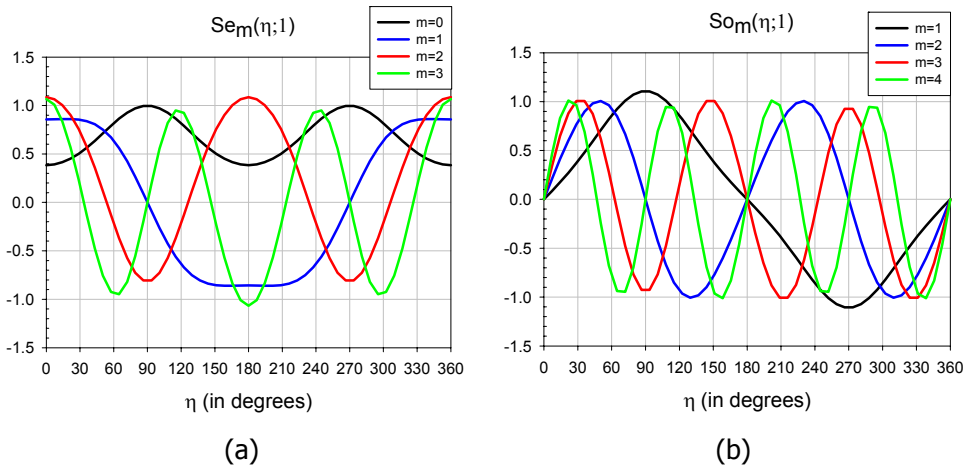


Figure 2.11 Plots of angular Mathieu functions for different values of m : (a) $Se_m(\eta; s = 1)$ vs. η (in degrees); (b) $So_m(\eta; s = 1)$ vs. η (in degrees).

In addition, angular functions $Se_m(\eta; s)$ and $So_m(\eta; s)$ also depend on the dimensionless parameter s , which is related to the transverse propagation constant k_t and the semifocal distance f by

$$s = \frac{f^2}{4} k_t^2 \quad (2.22)$$

Therefore, angular Mathieu functions also depend on geometrical parameters, such as the focal distance. This fact can be observed in Figure 2.12, where angular

Mathieu functions with $m = 1$ are depicted for different values of s . The curves with $s = 0$ reduce to the trigonometric functions $\cos(m\eta)$ and $\sin(m\eta)$.

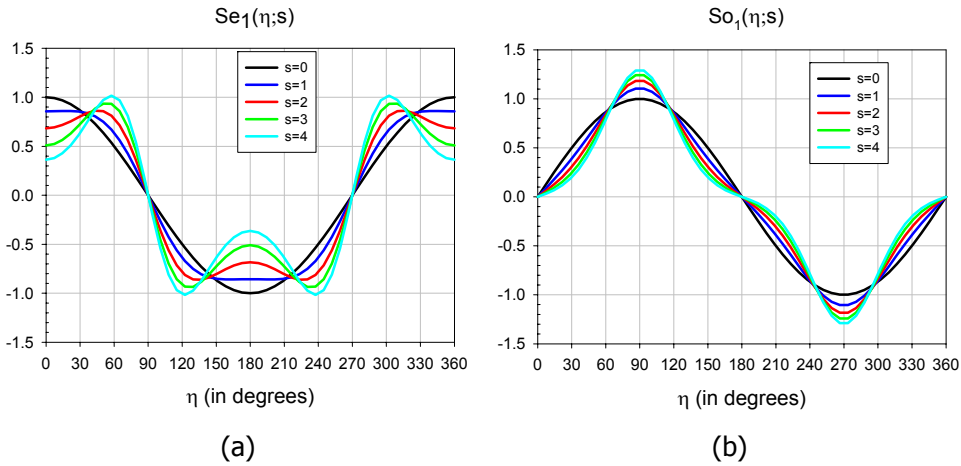


Figure 2.12 Plots of angular Mathieu functions vs. η (in degrees) for different values of s : (a) $Se_m(\eta; s)$; (b) $So_m(\eta; s)$

Moreover, radial Mathieu functions $Re_m^{(i)}(\xi; s)$ and $Ro_m^{(i)}(\xi; s)$ play a similar role in elliptic coordinates as the Bessel functions in circular-cylindrical coordinates. In order to provide an overview of the complete family of Radial Mathieu functions, Table 2.2 shows a general classification of these functions. In addition, Appendix A provides a detailed definition of Radial Mathieu functions and their series expansion in terms of Bessel functions [29].

Radial Mathieu Functions:	First Kind:	$Re_m^{(1)}(\xi; s)$	$Ro_m^{(1)}(\xi; s)$	
	$s > 0$	Second Kind:	$Re_m^{(2)}(\xi; s)$	$Ro_m^{(2)}(\xi; s)$
	Mathieu-Hankel:	$Re_m^{(3),(4)} = Re_m^{(1)} \pm j Re_m^{(2)}$	$Ro_m^{(3),(4)} = Ro_m^{(1)} \pm j Ro_m^{(2)}$	
	$s < 0$	First Kind:	$Ie_m^{(1)}(\xi; -s)$	$Io_m^{(1)}(\xi; -s)$
	Second Kind:	$Ke_m^{(1)}(\xi; -s)$	$Ko_m^{(1)}(\xi; -s)$	

Table 2.2. Classification of the Radial Mathieu functions [29].

Figure 2.13 shows the behavior of different Radial Mathieu Functions for several values of m . With these plots, it is possible to compare the even and odd versions of the first and second kind of Radial Mathieu Functions. It must be noted that the slope of even functions of the first kind always vanish at $\xi \neq 0$, whereas the odd functions vanish at $\xi = 0$. In Figure 2.13 (c) and (d), it can be observed that Radial Mathieu Functions of the second kind are finite at the origin of coordinates.

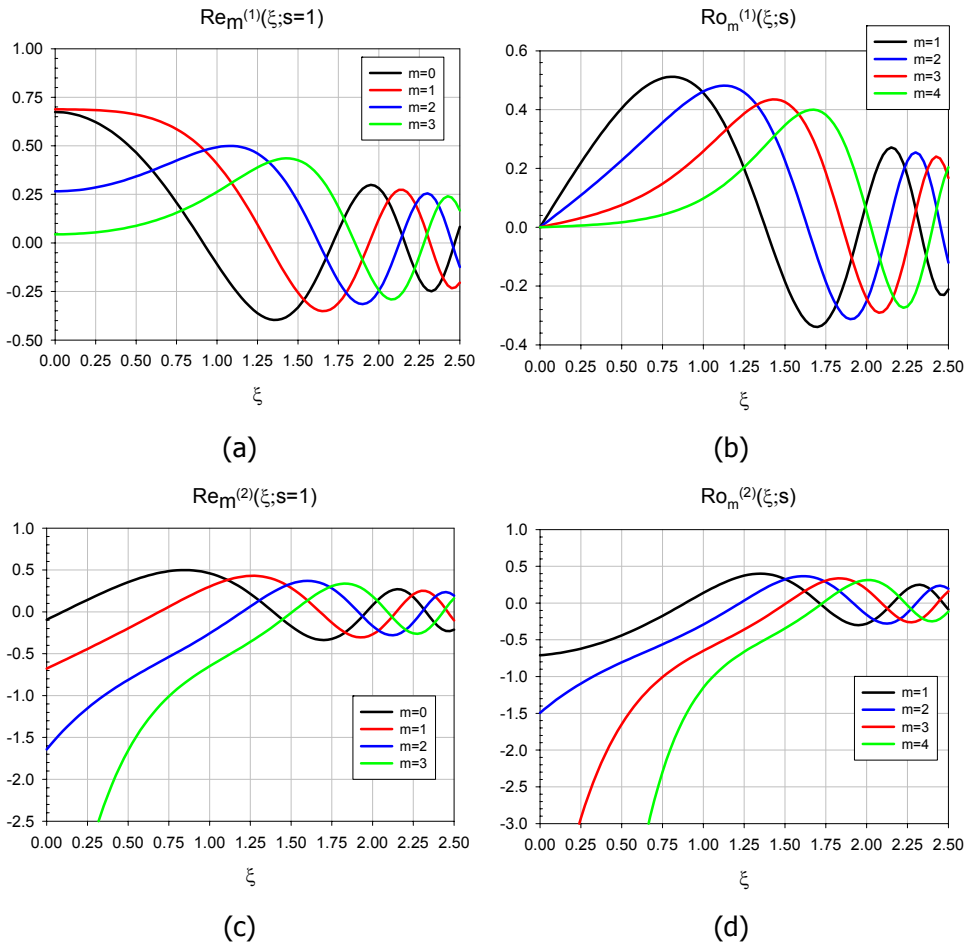


Figure 2.13 Plots of radial Mathieu functions vs. ξ for different values of m :
 (a) $Re_m^{(1)}(\xi; s)$; (b) $Ro_m^{(1)}(\xi; s)$; (c) $Re_m^{(2)}(\xi; s)$; (d) $Ro_m^{(2)}(\xi; s)$

In Figure 2.14 the behavior of several Radial Mathieu Functions is shown for a variety of values of s . As observed, the higher the value of s , the higher the number of oscillations the Radial Mathieu Functions present. For smaller values of s , the initial values of $Re_1^{(2)}$ and $Ro_1^{(2)}$ become more negative.

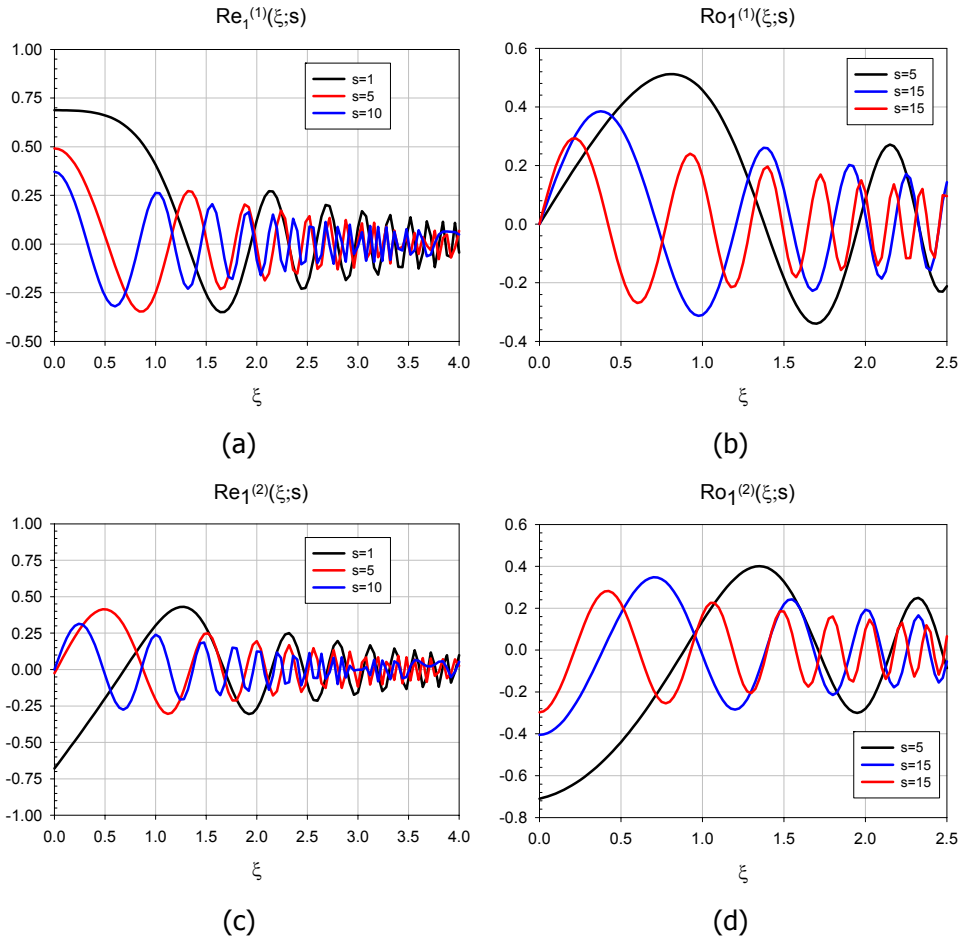


Figure 2.14 Plots of radial Mathieu functions of first order vs. ξ for different values of s : (a) $Re_1^{(1)}(\xi; s)$; (b) $Ro_1^{(1)}(\xi; s)$; (c) $Re_1^{(2)}(\xi; s)$; (d) $Ro_1^{(2)}(\xi; s)$

Once the scalar solutions of the Helmholtz equation have been obtained in elliptical coordinates, resolution of the vector wave equation is rather straightforward. As discussed before, solutions of the vector wave equation in elliptic-cylinder coordi-

nates can be obtained if terms of the transverse electric (TE) and transverse-magnetic (TM) with respect to z scalar parts.

Therefore, a field TM to z can be obtained by letting

$$\vec{A} = \hat{z} \cdot \psi \quad (2.23)$$

where \vec{A} is the magnetic vector potential [9], ψ is the solution of the scalar wave function given by equation (2.21), and the electric and magnetic fields are expanded in terms of \vec{A} :

$$\vec{H}^{TM} = \nabla \times \vec{A} \quad (2.24)$$

$$\vec{E}^{TM} = -j\omega\mu\vec{A} + \frac{1}{j\omega\varepsilon} \nabla(\nabla \cdot \vec{A}) = \frac{1}{j\omega\varepsilon} \nabla \times \vec{H}^{TM} \quad (2.25)$$

In elliptic coordinates this expansion yields:

$$\begin{aligned} E_\xi &= \frac{1}{j\omega\varepsilon} \cdot \frac{1}{h} \cdot \frac{\partial\psi}{\partial\xi\partial z} & H_\xi &= \frac{1}{h} \cdot \frac{\partial\psi}{\partial\eta} \\ E_\eta &= \frac{1}{j\omega\varepsilon} \cdot \frac{1}{h} \cdot \frac{\partial\psi}{\partial\eta\partial z} & H_\eta &= -\frac{1}{h} \cdot \frac{\partial\psi}{\partial\xi} \\ E_z &= j\omega\mu\psi + \frac{1}{j\omega\varepsilon} \cdot \frac{\partial^2\psi}{\partial z^2} & H_z &= 0 \end{aligned} \quad (2.26)$$

where $h = f\sqrt{\cosh^2 \xi - \cos^2 \eta}$.

Consequently, the vector current modes in the surface of an infinite elliptic cylinder of radius $\xi = \xi_0$ can be obtained as:

$$\begin{aligned} \vec{J}_m^{TM e.o}(\xi = \xi_0) &= \hat{\xi} \times \vec{H}_m^{TM} \Big|_{\xi=\xi_0} = -\hat{z} \cdot \frac{1}{h} \cdot \frac{\partial\psi}{\partial\xi} \Big|_{\xi=\xi_0} = \\ &= -\hat{z} \cdot \frac{1}{h_{\xi=\xi_0}} \left\{ \begin{aligned} &Se_m(\eta; s) \cdot Re_m^{(4)'}(\xi = \xi_0; s) \cdot \exp(\pm ik_z z) \\ &So_m(\eta; s) \cdot Ro_m^{(4)'}(\xi = \xi_0; s) \cdot \exp(\pm ik_z z) \end{aligned} \right\} \end{aligned} \quad (2.27)$$

where $h_{\xi=\xi_0} = f\sqrt{\cosh^2 \xi_0 - \cos^2 \eta}$ and the prime in $\text{Re}_m^{(4)'}$ and $\text{Ro}_m^{(4)'}$ denotes the derivative of $\text{Re}_m^{(4)}$ and $\text{Ro}_m^{(4)}$ with respect to ξ .

If an infinite elliptic cylinder with uniform current in z direction is considered, TM vector current wave functions can be expressed as:

$$\vec{J}_m^{TM e,o}(\xi = \xi_0) = -\hat{z} \cdot \frac{1}{f\sqrt{\cosh^2 \xi_0 - \cos^2 \eta}} \left\{ \begin{array}{l} \text{Se}_m(\eta; s) \cdot \text{Re}_m^{(4)' }(\xi = \xi_0; s) \\ \text{So}_m(\eta; s) \cdot \text{Ro}_m^{(4)' }(\xi = \xi_0; s) \end{array} \right\} \quad (2.28)$$

Furthermore, in the limit case $\xi = \xi_0 \rightarrow 0$, the infinite elliptic cylinder degenerates into an infinite planar strip, as depicted in Figure 2.15. It must be emphasized that in this particular case the semifocal distance f coincides with half of the strip width ($W/2$).

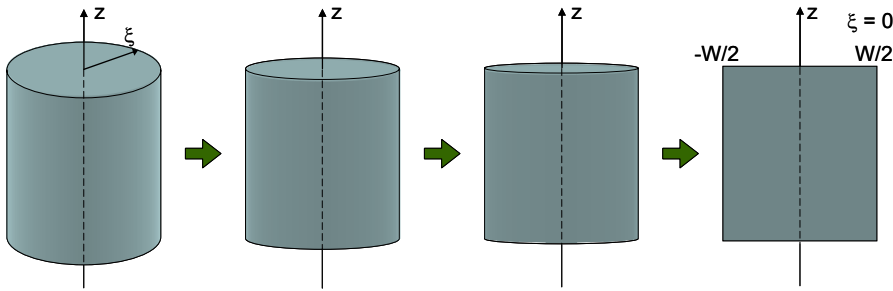


Figure 2.15 Limit case where an infinite elliptic cylinder degenerates into an infinite planar strip ($\xi \rightarrow 0$).

Hence, analytical expressions for the vector current modes of an infinite planar strip can be obtained by particularizing equation (2.28) for the case $\xi = \xi_0 = 0$:

$$\vec{J}_m^{TM e,o}(\xi = 0) = -\hat{z} \cdot \frac{1}{W/2 \cdot \sqrt{1 - \cos^2 \eta}} \left\{ \begin{array}{l} \text{Se}_m(\eta; s) \cdot \text{Re}_m^{(4)' } (0; s) \\ \text{So}_m(\eta; s) \cdot \text{Ro}_m^{(4)' } (0; s) \end{array} \right\} \quad (2.29)$$

In $\xi = 0$, $\text{Re}_m^{(1)' } (0; s) = 0$, and hence $\text{Re}_m^{(4)' } (0; s) = -i \text{Re}_m^{(2)' } (0; s)$. Therefore:

$$\vec{J}_m^{TM e,o}(\xi = 0) = -\hat{z} \cdot \frac{1}{W/2 \cdot \sqrt{1 - \cos^2 \eta}} \left\{ \begin{array}{l} \text{Se}_m(\eta; s) \cdot [-i \text{Re}_m^{(2)' } (0; s)] \\ \text{So}_m(\eta; s) \cdot [\text{Ro}_m^{(1)' } (0; s) - i \text{Ro}_m^{(2)' } (0; s)] \end{array} \right\} \quad (2.30)$$

As the current modes are uniform in z , the variation along the transversal coordinate η of even and odd modes on the surface of the strip has been represented in Figure 2.16 and Figure 2.17, respectively. In these plots, the coordinate η varies from 0° to 360° , with the range from 0° to 180° corresponding to one side of the strip and the range from 180° to 360° relating to the opposite side. Edges of the strip are hence located at $\eta = 0^\circ/360^\circ$ and $\eta = 180^\circ$, whereas the center of the strip is located at $\eta = 90^\circ/270^\circ$. For better understanding, a schematic of the strip and the current flow has also been depicted in the figures, with the side of the strip to which current is associated standing out. Note that these TM currents flow in \hat{z} direction.

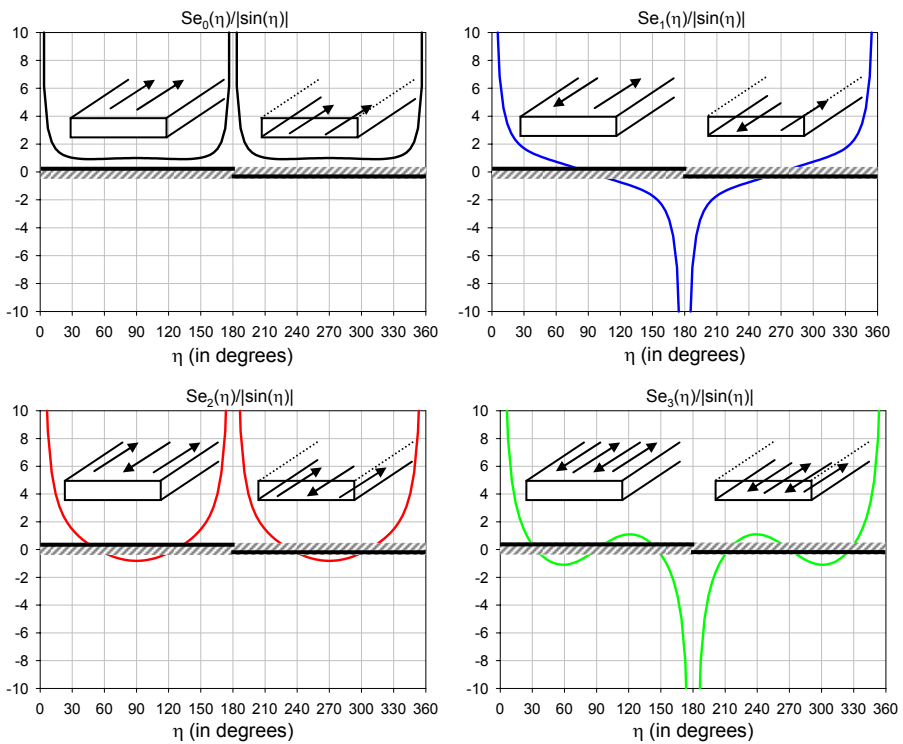


Figure 2.16 Variation along the transversal coordinate η of the current distribution for the TM even vector current modes of an infinite planar strip of width $=0.64\lambda$.

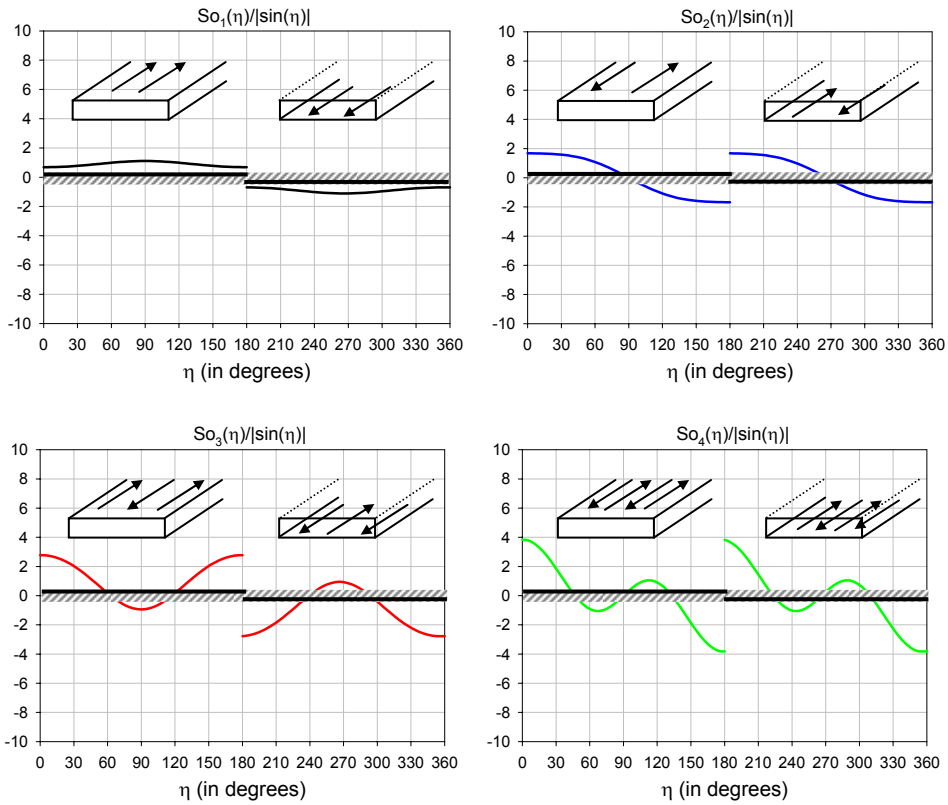


Figure 2.17 Variation along the transversal coordinate η of the current distribution for the TM odd vector current modes of an infinite planar strip of width= 0.64λ .

On the one hand, a singular behavior is observed for the even modes $Se_m(\eta; s)/\sqrt{1-\cos^2(\eta)}$, at the two edges of the strip ($\eta = 0^\circ/360^\circ$ and $\eta = 180^\circ$). Consequently, even modes represent currents flowing in the same direction in the front and back side of the strip, and hence they could be identified as antenna modes, making an analogy with the well-known modes of a folded dipole. On the other hand, odd modes $So_m(\eta; s)/\sqrt{1-\cos^2(\eta)}$ flow in opposite direction in the front and back side of the planar strip, and hence they could be identified as transmission line modes. Obviously, the radiation behavior of antenna modes will be better than that of transmission line modes, since contributions to the radiating field on both sides of the strip do not cancel each other in the former case.

Moreover, fields associated to the TE to z case can be obtained by letting the electric vector potential [9] be:

$$\vec{F} = \hat{z} \cdot \psi \quad (2.31)$$

where ψ is the solution of the scalar wave function, given by equation (2.21), and the electric and magnetic fields are expanded in terms of \vec{F} :

$$\vec{E}^{TE} = -\nabla \times \vec{F} \quad (2.32)$$

$$\vec{H}^{TE} = -j\omega\epsilon\vec{F} + \frac{1}{j\omega\mu} \nabla(\nabla \cdot \vec{F}) \quad (2.33)$$

In elliptic coordinates this expansion yields:

$$\begin{aligned} E_\xi &= \frac{1}{h} \cdot \frac{\partial \psi}{\partial \eta} & H_\xi &= \frac{1}{j\omega\mu} \cdot \frac{1}{h} \cdot \frac{\partial^2 \psi}{\partial \xi \partial z} \\ E_\eta &= -\frac{1}{h} \cdot \frac{\partial \psi}{\partial \xi} & H_\eta &= \frac{1}{j\omega\mu} \cdot \frac{1}{h} \cdot \frac{\partial^2 \psi}{\partial \eta \partial z} \\ E_z &= 0 & H_z &= j\omega\epsilon\psi + \frac{1}{j\omega\mu} \cdot \frac{\partial^2 \psi}{\partial z^2} \end{aligned} \quad (2.34)$$

where $h = f \sqrt{\cosh^2 \xi - \cos^2 \eta}$.

As in the TM case, if an infinite elliptic cylinder of radius $\xi = \xi_0$ with uniform fields in z is considered, the vector current modes in the surface of an infinite elliptic cylinder of radius $\xi = \xi_0$ can be derived as:

$$\begin{aligned} \vec{J}_m^{TE e,0}(\xi = \xi_0) &= \hat{\xi} \times \vec{H}_m^{TE} \Big|_{\xi=\xi_0} = -\hat{\eta} \cdot j\omega\epsilon\psi \Big|_{\xi=\xi_0} = \\ &= -\hat{\eta} \cdot j\omega\epsilon \left\{ \begin{aligned} &S e_m(\eta; s) \cdot \text{Re}_m^{(4)}(\xi = \xi_0; s) \\ &S o_m(\eta; s) \cdot \text{Ro}_m^{(4)}(\xi = \xi_0; s) \end{aligned} \right\} \end{aligned} \quad (2.35)$$

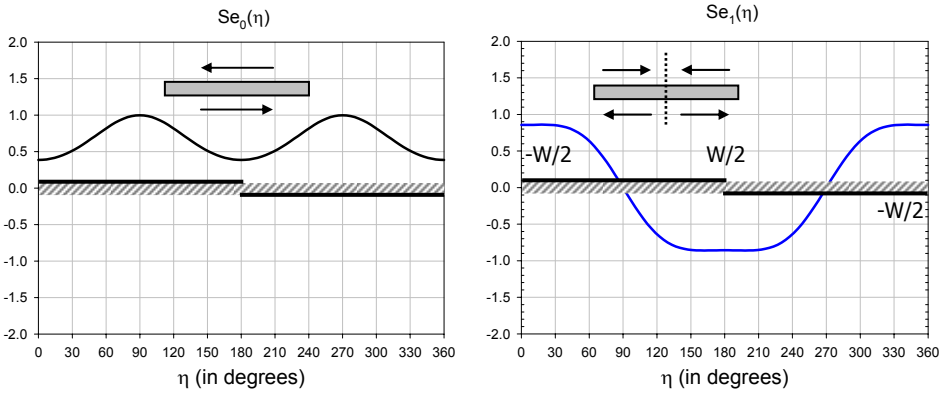
Therefore, for the case of the planar strip ($\xi = \xi_0 = 0$) the current distribution will be:

$$\vec{J}_m^{TE_{e,o}}(\xi=0) = -\hat{\eta} \cdot j\omega\epsilon \begin{Bmatrix} Se_m(\eta; s) \cdot Re_m^{(4)}(\xi=0; s) \\ So_m(\eta; s) \cdot Ro_m^{(4)}(\xi=0; s) \end{Bmatrix} \quad (2.36)$$

In $\xi=0$, $Ro_m^{(1)}(0; s) = 0$ (see Figure 2.13), and hence $Ro_m^{(4)}(0; s) = -iRe_m^{(2)}(0; s)$. Then:

$$\vec{J}_m^{TE_{e,o}}(\xi=0) = -\hat{\eta} \cdot j\omega\epsilon \begin{Bmatrix} Se_m(\eta; s) \cdot [Re_m^{(1)}(0; s) - jRe_m^{(2)}(0; s)] \\ So_m(\eta; s) \cdot [-jRo_m^{(2)}(0; s)] \end{Bmatrix} \quad (2.37)$$

The variation along the transversal coordinate η of even and odd modes on the surface of the strip has been represented in Figure 2.18 and Figure 2.19, respectively. On the one hand, even modes Se_m represent current modes flowing in opposite direction in the front and back side of the planar strip (transmission line modes). On the other hand, odd modes So_m flow in the same direction in the front and back side of the strip (antenna modes), presenting a null of current at the edges of the strip. It must be noted that TE current modes flow in the transversal direction $\hat{\eta}$.



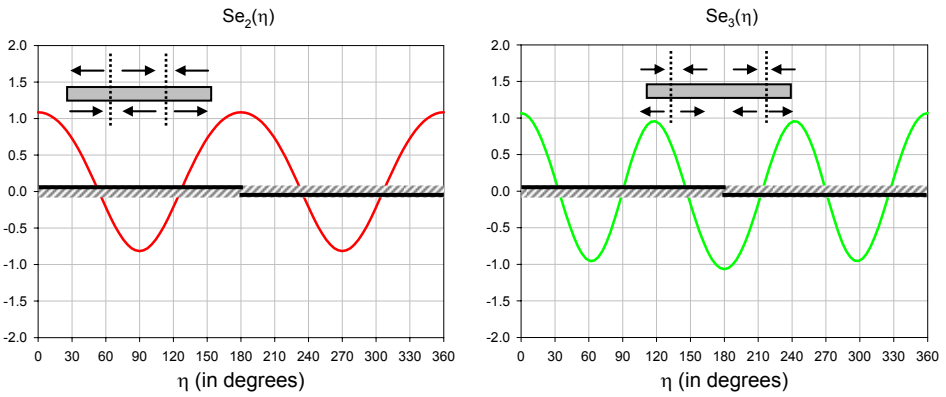


Figure 2.18 Variation along coordinate η of the current distribution for the TE even vector current modes of an infinite planar strip of width= 0.64λ .

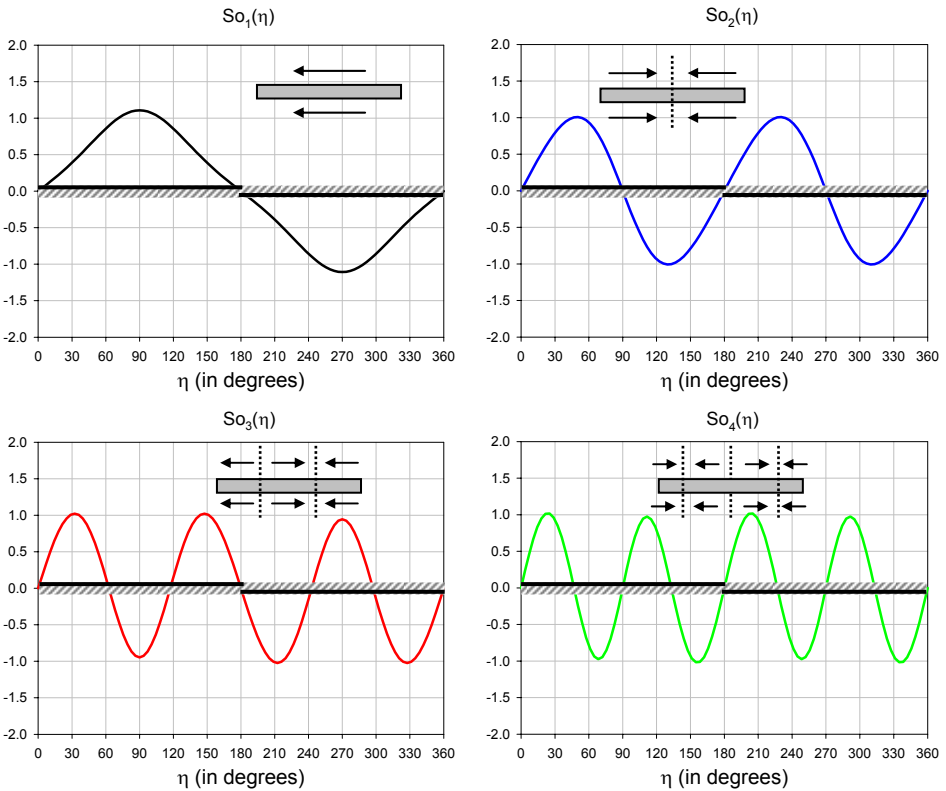


Figure 2.19 Variation along coordinate η of the current distribution for the TE odd vector current modes of an infinite planar strip of width= 0.64λ .

As in the spherical and spheroidal modes, each mode of the infinite strip can be characterized by a radially directed wave impedance, which gives information about the reactive or resistive behavior of the mode. The wave impedance for the TM and TE cases can be expressed as:

$$Z_m^{TM} = -\frac{E_z^{TM}}{H_\eta^{TM}} = j\omega\mu h \left\{ \begin{array}{l} \frac{\text{Re}_m^{(4)}(\xi; s)}{\text{Re}_m^{(4)'(\xi; s)}} \\ \frac{\text{Ro}_m^{(4)}(\xi; s)}{\text{Ro}_m^{(4)'(\xi; s)}} \end{array} \right\}; \quad Z_m^{TE} = \frac{E_\eta^{TE}}{H_z^{TE}} = -\frac{1}{h} \cdot \frac{1}{j\omega\epsilon} \cdot \left\{ \begin{array}{l} \frac{\text{Re}_m^{(4)'(\xi; s)}(\xi; s)}{\text{Re}_m^{(4)}(\xi; s)} \\ \frac{\text{Ro}_m^{(4)'(\xi; s)}(\xi; s)}{\text{Ro}_m^{(4)}(\xi; s)} \end{array} \right\} \quad (2.38)$$

Figure 2.20 shows the ratio X_m/R_m where $Z_m = R_m + jX_m$, for the first six TM and TE even modes, as a function of the argument ξ and for $s = 0.01$. For odd modes the behavior of the wave impedance is similar. In Figure 2.21, the ratio of wave reactance to wave resistance versus ξ is plotted for different values of m and s . As observed, when parameter s increases, the semifocal distance also increases and the resistive part of a given mode m become large for the same argument ξ .

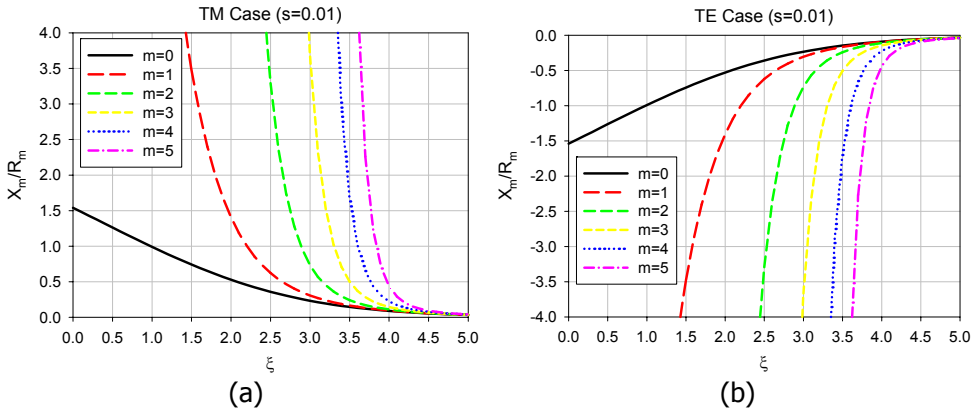


Figure 2.20 Ratios of wave reactance to wave resistance vs. ξ : (a) For the TM even modes; (b) For the TE even modes.

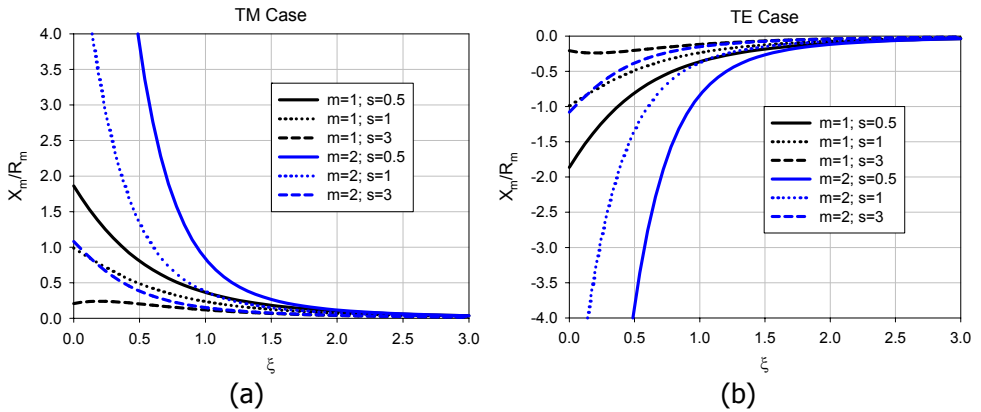


Figure 2.21 Ratios of wave reactance to wave resistance vs. ξ , for different values of n and s : (a) TM even case; (b) TE even case.

These modes can be used to approximate the current in the surface of the planar strip, using the analytic expressions given in equations (2.30) and (2.37). Moreover, the knowledge of the modal current distributions provides an idea about the optimal location of each source to excite modes with a specific distribution, radiation pattern and radiating bandwidth.

2.5. Conclusions

In the present chapter, vector wave functions for different structures have been revisited. Vector wave functions have traditionally been used to expand the total field radiated or scattered by a conducting body. It has been shown that each vector wave function or mode is characterized by a field distribution, produced by some current distribution over the surface of the conducting body.

Moreover, it has been established that vector wave functions can be calculated in eleven different basic coordinate systems. Although the vector wave equation is only separable in six of them, derivation of vector wave functions for the other five systems can also be obtained. Throughout the chapter, several planar structures have been analyzed as a limit case of a structure whose surface coincides with some of these coordinates systems. In this manner, a closed-form expression for the field and current modes can be obtained, which can in turn be used as a basis to improve the design.

Thus, closed-form expressions for the modal current in perfectly conducting bodies, including a sphere, a circular disk and an infinite planar strip, have been obtained. The conducting disk has been analyzed as a limit case of an oblate spheroid, whereas the planar strip has been studied as a degeneration of an infinite cylinder with elliptical section. Analytic expressions of the current modes not only assist in a further numerical analysis of problems including these structures, but also provide physical insight into the behavior of the structures under an external excitation source.

Chapter 3

Internal and external resonances in perfect conductors

"Man is the interpreter of nature, science the right interpretation"

William Whewell

3.1. Introduction

In the previous chapter, vector wave functions of diverse conducting structures whose surface coincides with some of the curvilinear reference coordinate systems were revisited. Surface current distributions associated to these modes were also presented for some perfectly conducting bodies: a sphere, a circular disk and an infinite planar strip. Closed-form expressions for their current modes were established, and the modes were represented graphically. Moreover, the possibility of using the modal current distribution associated to each mode and its properties was suggested as an initial step of the antenna design process.

Vector wave functions can be used to study electromagnetic problems regarding the external and internal regions of the conductor. In closed conductors, the electromagnetic problem inside the structure has been addressed by several authors for many types of cavities [9][31]. In contrast, the study of the electromagnetic problem in the external region has been treated as a radiation or scattering problem [9][11]. Moreover, radiation in open conductors can be considered as a particular case of the external radiation of a closed conducting structure, where dimensions of the internal region tend to zero. This is the approach followed in the previous chapter. In addition to the previous discussions, in the beginning of this chapter, some important definitions associated to internal and external resonances will be reviewed.

Furthermore, the current modes obtained in the previous chapter are complex functions, what introduces a higher degree of complication for their use in the antenna design process. The Theory of Characteristic Modes, however, provides real current modes, which can be more easily treated and numerically computed. In the present chapter, a brief review of this theory and physical interpretation of the most important parameters will be presented.

Finally, characteristic modes for some of the structures analyzed in the previous chapter will be computed. Thus, similarities between vector wave functions and characteristic modes will be illustrated for the cases of a metallic sphere and an infinite planar strip.

3.2. Internal resonances in closed conducting structures

The theory of internal resonances in closed structures or cavities has been investigated for many years. This section intends to revisit some interesting concepts of resonances in cavities, which will be connected with the theory of resonances in open structures.

In the loss-free case, electromagnetic fields can exist within a source-free region enclosed by a perfect conductor [9]. These fields must satisfy the vector wave equation (2.1), together with the boundary conditions imposed by the cavity, i.e. tangential components of the electric field must be zero over its walls. These fields can exist only at specific frequencies, which are called *resonant frequencies*, and which comprise a discrete set of values. When losses are present, a source must exist to sustain oscillations.

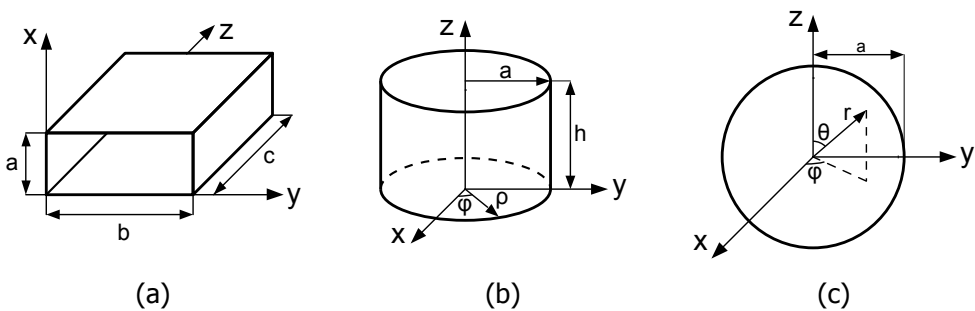


Figure 3.1 (a)Rectangular; (b) circular and (c) spherical cavity.

Table 3.1, summarizes elementary wave functions, from which all the possible solutions or modes for the rectangular, circular and spherical cavity (shown in

Figure 3.1) can be derived [9]. Therefore, solutions of electric and magnetic field modes can be derived, both for the TM and TE cases. In the table, solutions are for $m = 0, 1, 2, \dots$; $n = 0, 1, 2, \dots$; $p = 1, 2, 3, \dots$; except for $m = n = 0$, in the rectangular cavity; for $n = 0, 1, 2, \dots$; $p = 1, 2, 3, \dots$ and $q = 1, 2, 3, \dots$, in the circular cavity, where x_{np} and x'_{np} are the zeros of Bessel functions $J_n(x)$ and $J'_n(x')$, respectively; and for $m = 0, 1, 2, \dots$; $n = 0, 1, 2, \dots$; $p = 1, 2, 3, \dots$ in the spherical cavity, where u_{np} and u'_{np} are zeros of the spherical Bessel function $\hat{J}_n(u)$ and $\hat{J}'_n(u')$ [9].

	TM case	TE case
Rectangular cavity	$\psi_{mnp}^{TM} = \sin\left(\frac{m\pi x}{a}\right) \sin\left(\frac{n\pi y}{b}\right) \cos\left(\frac{p\pi z}{c}\right)$	$\psi_{mnp}^{TE} = \cos\left(\frac{m\pi x}{a}\right) \cos\left(\frac{n\pi y}{b}\right) \sin\left(\frac{p\pi z}{c}\right)$
Circular cavity	$\psi_{npq}^{TM} = J_n\left(\frac{x_{np}\rho}{a}\right) \begin{cases} \sin n\phi \\ \cos n\phi \end{cases} \cos\left(\frac{q\pi}{h} z\right)$	$\psi_{npq}^{TE} = J_n\left(\frac{x'_{np}\rho}{a}\right) \begin{cases} \sin n\phi \\ \cos n\phi \end{cases} \sin\left(\frac{q\pi}{h} z\right)$
Spherical cavity	$\psi_{mnp}^{TM} = \hat{J}_n\left(u'_{np} \frac{r}{a}\right) P_n^m(\cos\theta) \begin{cases} \cos m\phi \\ \sin m\phi \end{cases}$	$\psi_{mnp}^{TE} = \hat{J}_n\left(u_{np} \frac{r}{a}\right) P_n^m(\cos\theta) \begin{cases} \cos m\phi \\ \sin m\phi \end{cases}$

Table 3.1. Elementary wave functions for the derivation of electromagnetic field solutions inside the cavity, both for the TM and TE case.

As observed, all modes in the cavities are *standing waves*, since their phase is independent of z in the rectangular and circular cavity, and independent of ϕ in the spherical case. The resonant frequency f_r of these modes is given in table 3.2. Moreover, each mode has associated a field pattern (field lines) inside the cavity.

	TM case	TE case
Rectangular cavity	$(f_r)_{mnp} = \frac{1}{2\sqrt{\epsilon\mu}} \sqrt{\left(\frac{m}{a}\right)^2 + \left(\frac{n}{b}\right)^2 + \left(\frac{p}{c}\right)^2}$	$(f_r)_{mnp} = \frac{1}{2\sqrt{\epsilon\mu}} \sqrt{\left(\frac{m}{a}\right)^2 + \left(\frac{n}{b}\right)^2 + \left(\frac{p}{c}\right)^2}$
Circular cavity	$(f_r)_{npq}^{TM} = \frac{1}{2\pi a\sqrt{\epsilon\mu}} \sqrt{x_{np}^2 + \left(\frac{q\pi a}{h}\right)^2}$	$(f_r)_{npq}^{TE} = \frac{1}{2\pi a\sqrt{\epsilon\mu}} \sqrt{x'_{np}{}^2 + \left(\frac{q\pi a}{h}\right)^2}$
Spherical cavity	$(f_r)_{mnp}^{TM} = \frac{u'_{np}}{2\pi a\sqrt{\epsilon\mu}}$	$(f_r)_{mnp}^{TE} = \frac{u_{np}}{2\pi a\sqrt{\epsilon\mu}}$

Table 3.2. Resonant frequency for electromagnetic modes inside the cavity, both for the TM and TE case.

3.3. External resonances in conducting structures

In closed conducting or dielectric bodies, external resonant modes also exist, which are defined as those field patterns that can exist in the absence of sources [32]. For a perfectly conducting sphere of radius a , for instance, the external resonances for a TE mode occur when the condition

$$h_n^{(2)}(ka) = 0 \quad (3.1)$$

is satisfied, since it makes the tangential TE field given by equation (2.7) to meet the boundary conditions over the surface of the sphere. Equally, for the TM case, the following condition must be fulfilled, as derived from equation (2.6):

$$\left. \frac{\partial [r h_n^{(2)}(kr)]}{\partial r} \right|_{r=a} = 0 \quad (3.2)$$

Due to the behavior of Hankel functions of second kind, these conditions can only be satisfied for complex values of k . Thus, for instance, the $n=1$ mode of the conducting sphere presents a resonance at $ka = \pm 0.86 + j0.5$ [32]. A complex value of ka leads to a time factor $e^{j\omega t}$ of the form $e^{\alpha t} e^{j\beta t}$, where α must be negative in order to take radiation losses into account.

These complex natural resonances are characteristic of the shape and composition of the body. When an incident wave over the conducting object is swept in frequency, the various modes of the body resonate successively, producing – for instance – peaks in the radar cross section that may serve to identify the nature of the object. These complex natural resonances have been analyzed numerically and measured for a number of conducting and dielectric bodies [33]-[35], thereby obtaining complex natural resonance signatures for each of them [36].

A sophisticated method to extract these complex resonances is the Singularity Expansion Method (SEM), proposed in 1971 by Baum [12]. This method establishes that the late-time scattered or radiated fields can be represented in time-domain by a series of damped sinusoidal oscillations, whose frequencies depend only on the geometry and material of the scatterer, and not on the nature of the incident fields. Each damped sinusoid corresponds to a complex pole in the Laplace domain (s plane), and hence the basic concept behind the method is to express the solution in the complex frequency plane in terms of its singularities or poles.

To locate the resonances of objects with arbitrary shape, numerical techniques such as the Method of Moments [37] in the Laplace domain can be used. Thereby the following matrix system is obtained:

$$\bar{\bar{Z}}(s) \cdot \bar{I}(s) = \bar{V}(s) \quad (3.3)$$

where the various modes are characterized by vectors \bar{M}_n satisfying:

$$\bar{\bar{Z}}(s_n) \cdot \bar{I}(s_n) = \bar{\bar{Z}}(s_n) \cdot \bar{M}(s_n) = 0 \quad (3.4)$$

and where the complex resonances s_n are obtained by solving

$$\det \left\{ \bar{\bar{Z}}(s_n) \right\} = 0 \quad (3.5)$$

Therefore, the SEM approximation of the current over the conducting object takes the form:

$$\bar{I}(s) = \sum_{n=1}^{\infty} \frac{\eta_n \cdot M_n}{s - s_n} + F_e(s) \quad (3.6)$$

where η_n are the mode amplitudes or coupling coefficients and $F_e(s)$ is an entire domain function.

Although SEM was mathematically formulated forty years ago, the method has become very popular in the last decade, as numerical techniques have improved very much their computational efficiency. Among other applications, SEM has been successfully applied to the determination of natural poles in order to characterize and identify conducting targets [38], to the analysis of resonance and quality factor of antenna and scattering systems [39][40] and to antenna modeling in the frequency and time domains [41]. Moreover, some papers have dealt with computation of the natural surface current modes on perfectly conducting objects [42]-[44]. However, information about the distribution of the natural current modes and their properties has not been employed for antenna design so far, due to the added difficulty of dealing with modes of complex nature.

Nevertheless, an alternative modal theory which defines a complete set of real resonant modes for a conducting body was defined by Garbacz in 1968 [13][14]. He showed that similar modes to those defined in chapter 2 can be defined for conducting bodies of arbitrary shape, and he addressed this problem by diagonalizing the scattering matrix. This led him to the conclusions that these mode currents are real and that the tangential electric mode field exhibits a constant phase over the surface of the body. However, a general method for the determination of these

real modes was not available until 1971, when Harrington and Mautz approached this problem by diagonalizing the operator which relates the current to the tangential electric field on the conducting body [15][16].

With the determination of the characteristic modes of a conducting body and its properties, valuable information for antenna design can be obtained. Since these modes are real, information about their current distribution can be more easily handled. In the next section, a review of the mathematical foundations of the Theory of Characteristic Modes and the definition of some interesting parameters will be carried out. Numerical analysis and physical interpretation of characteristic modes in several structures has been performed in [17], yet short examples will be shown here for better understanding. Finally, in a further step these modes will be connected with the general vector wave functions defined in chapter 2, through the analytical extraction of the characteristic modes of both the sphere and the infinite planar strip.

3.4. Review of the Theory of Characteristic Modes

3.4.1. Mathematical formulation

Let us consider one or more conducting bodies, defined by the surface S , and an impressed electric field \vec{E}^i . An operator equation for the current \vec{J} on S is [37]

$$\left[L(\vec{J}) - \vec{E}^i \right]_{\text{tan}} = 0 \quad (3.7)$$

where the subscript denotes the tangential components on S . The operator defined in equation (3.7) is defined by

$$L(\vec{J}) = j\omega\vec{A}(\vec{J}) + \nabla\Phi(\vec{J}) \quad (3.8)$$

$$\vec{A}(\vec{J}) = \mu \iint_S \vec{J}(r') \psi(r, r') dS' \quad (3.9)$$

$$\Phi(\vec{J}) = \frac{-1}{j\omega\epsilon} \iint_S \nabla' \cdot \vec{J}(r') \psi(r, r') dS' \quad (3.10)$$

$$\psi(r, r') = \frac{e^{-jk|r-r'|}}{4\pi|r-r'|} \quad (3.11)$$

where r is a field point, r' a source point, and ϵ, μ and k the permittivity, permeability and wavenumber, respectively, of free space. Physically, $-L(\vec{J})$ gives the electric intensity at any point of space due to the current \vec{J} on S . Therefore, the operator L has the dimensions of impedance:

$$Z(\vec{J}) = [L(\vec{J})]_{\text{tan}} \quad (3.12)$$

This impedance operator $Z = R + jX$ is a symmetric but not Hermitian operator, but since Z is symmetric, its Hermitian parts R and X are real symmetric operators.

Then, considering the following weighted eigenvalue equation [15]:

$$Z(\vec{J}_n) = \nu_n R(\vec{J}_n) \quad (3.13)$$

where ν_n are eigenvalues and \vec{J}_n are eigenfunctions, we have that R is a weight operator which diagonalize Z and gives orthogonality of the radiation patterns. From equation (3.13) it can be written

$$(R + jX)(\vec{J}_n) = \nu_n R(\vec{J}_n) \quad (3.14)$$

and letting

$$\nu_n = 1 + j\lambda_n \quad (3.15)$$

the common term in (3.14) can be cancelled to obtain

$$X(\vec{J}_n) = \lambda_n R(\vec{J}_n) \quad (3.16)$$

Since R and X are real symmetric operators, all eigenvalues λ_n and eigenfunctions \vec{J}_n are real. Moreover, the eigenvectors \vec{J}_n satisfy the following orthogonality conditions:

$$\begin{aligned}
\langle J_m, R(J_n) \rangle &= \langle J_m^*, R(J_n) \rangle = 0 \\
\langle J_m, X(J_n) \rangle &= \langle J_m^*, X(J_n) \rangle = 0 \\
\langle J_m, Z(J_n) \rangle &= \langle J_m^*, Z(J_n) \rangle = 0
\end{aligned} \tag{3.17}$$

when $m \neq n$. The choice of $\{J_n\}$ as basis functions simultaneously leads to diagonal matrix representations of R , X , and Z . These real functions J_n are therefore the **characteristic currents** or **eigencurrents** on the surface of the conducting body defined by S , which only depend on its shape and size, and are independent of any specific source or excitation.

Moreover, each eigencurrent J_n is normalized to radiate unit power:

$$\langle J_n^*, R(J_n) \rangle = 1 \tag{3.18}$$

As these eigencurrents are associated to external resonances, they can be so normalized for radiation problems. Therefore, when normalizing according to (3.18), the orthogonality relationships (3.17) can be combined with (3.18) to yield

$$\begin{aligned}
\langle J_m, R(J_n) \rangle &= \langle J_m^*, R(J_n) \rangle = \delta_{mn} \\
\langle J_m, X(J_n) \rangle &= \langle J_m^*, X(J_n) \rangle = \lambda_n \delta_{mn} \\
\langle J_m, Z(J_n) \rangle &= \langle J_m^*, Z(J_n) \rangle = (1 + j\lambda_n) \delta_{mn}
\end{aligned} \tag{3.19}$$

where δ_{mn} is the Kronecker delta.

To numerically compute the characteristic modes of an arbitrary conducting body, equation (3.16) needs to be reduced to matrix form, by means of the Method of Moments and the Galerkin formulation [16]

$$[X] \vec{J}_n = \lambda_n [R] \vec{J}_n \tag{3.20}$$

Afterwards, eigenvectors \vec{J}_n and eigenvalues λ_n of the object can be obtained by solving the generalized eigenproblem of (3.20) with standard algorithms.

Characteristic modes form a complete set of solutions, and hence the total current on the surface of a conducting body can be expressed as a linear superposition of these mode currents:

$$\vec{J} = \sum_n b_n \vec{J}_n \quad (3.21)$$

where b_n are the coefficients of the expansion. If characteristic modes are used as both expansion and testing functions of the Method of Moments and since they diagonalize the generalized impedance matrix Z , it is straightforward to derive the expansion coefficients b_n :

$$b_n = \frac{\langle \vec{J}_n, \vec{E}^i \rangle}{1 + j\lambda_n} = \frac{\oiint_S \vec{J}_n \cdot \vec{E}^i \cdot dS}{1 + j\lambda_n} = \frac{V_n^i}{1 + j\lambda_n} \quad (3.22)$$

where V_n^i is called the **modal excitation coefficient** [15], as it indicates the degree of coupling between the excitation and the characteristic mode.

Therefore, the modal solution for the current on S is:

$$\vec{J} = \sum_n \frac{V_n^i}{1 + j\lambda_n} \vec{J}_n \quad (3.23)$$

Moreover, each characteristic current \vec{J}_n produces an electric field, which is called **characteristic field** or **eigenfield** [15]. From equation (3.7), characteristic fields can be derived and expressed as:

$$E_n(\vec{J}_n) = Z(\vec{J}_n) = R(\vec{J}_n) + jX(\vec{J}_n) = R(\vec{J}_n)(1 + j\lambda_n) \quad (3.24)$$

Then, it is clear from (3.24) that characteristic electric fields are equiphase. If the body S is of finite extent, and if S' is chosen to be the sphere at infinity (S_∞), equation (3.27) provides the orthogonality relationships for radiation patterns and fields:

$$\frac{1}{\eta} \oiint_{S'} \vec{E}_m \cdot \vec{E}_n^* dS = \delta_{mn} \quad (3.25)$$

On S_∞ the characteristic fields are of the form of outward travelling waves, with the form

$$\vec{E}_n = -j\omega\mu \frac{e^{-jkr}}{4\pi r} \vec{F}_n(\theta, \phi) \quad (3.26)$$

where (θ, ϕ) are the angular coordinates of position on S_∞ , and \vec{F}_n is called the **characteristic pattern** or **eigenpattern**, corresponding to the eigencurrent \vec{J}_n .

Furthermore, orthogonality relationships for characteristic electric fields can be reached from characteristic currents by means of the complex Poynting theorem [9], as follows:

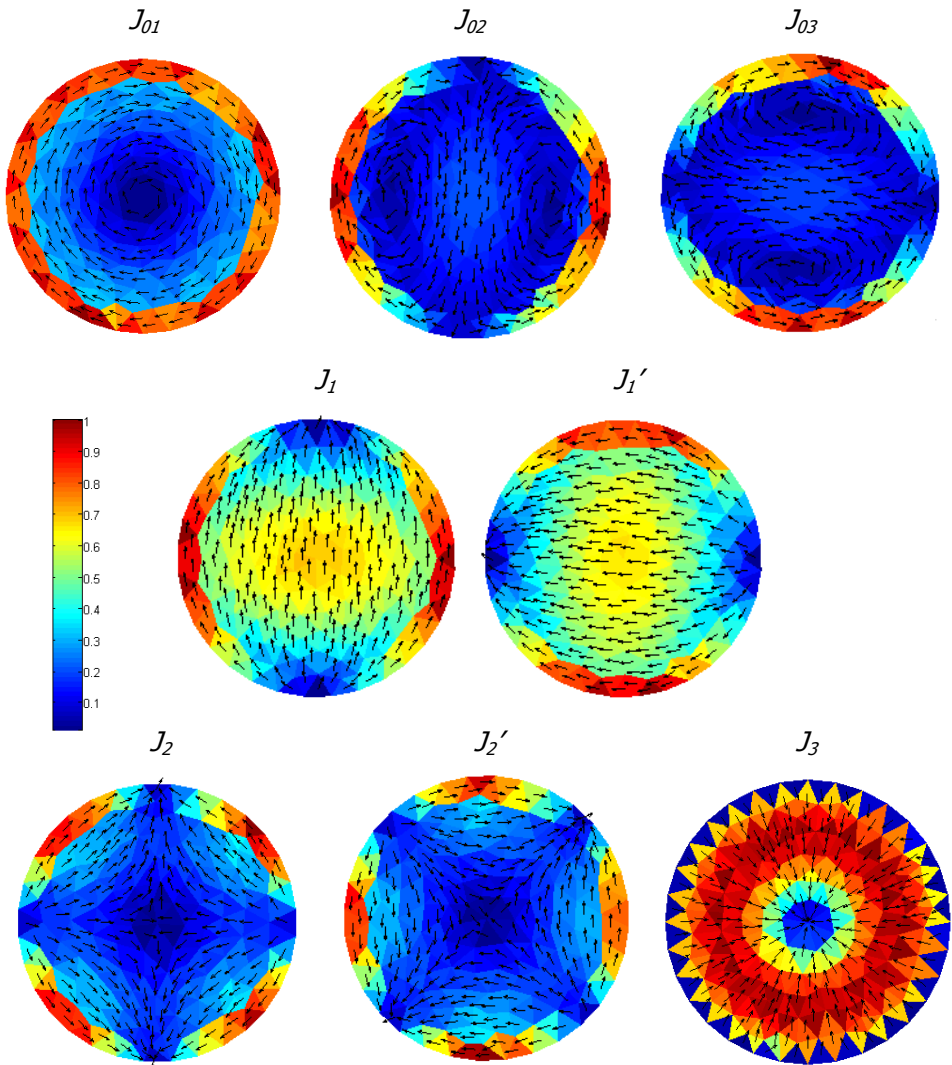
$$\begin{aligned} P(J_m, J_n) &= \langle J_m^*, ZJ_n \rangle = \langle J_m^*, RJ_n \rangle + j \langle J_m^*, XJ_n \rangle \\ &= \oiint_{S'} \vec{E}_m \times \vec{H}_n^* ds + j\omega \iiint_{\tau'} (\mu \vec{H}_m \cdot \vec{H}_n^* - \varepsilon \vec{E}_m \cdot \vec{E}_n^*) d\tau \quad (3.27) \\ &= (1 + j\lambda_n) \delta_{mn} \end{aligned}$$

3.4.2. Physical significance of characteristic modes

From the mathematical formulation it is clear that the characteristic modes of any arbitrarily shaped conducting body can be extracted through application of equation (3.20). Thereby a complete set of real eigenvectors \vec{J}_n or characteristic modes are obtained, which are the real currents on the surface of the conducting body that depend only on its shape and size, and are independent of any specific source or excitation. Associated to the eigencurrents, a set of real eigenvalues λ_n is also obtained, which provides information about the physical behavior of characteristic modes and determine the relative dominance of each mode.

For the sake of illustration, let us compute the characteristic modes of a perfectly conducting circular plate with 40 mm of diameter and infinitesimal thickness, in free space, and then establish the physical interpretation of the associated eigenvalues. A much more comprehensive analysis and interpretation of characteristic modes for several structures can be found in [17], covering from simple wire structures to three dimensional conducting objects.

Figure 3.2 shows the normalized current distribution of the lower order characteristic modes of the circular plate at 6 GHz, which is the resonant frequency of the first characteristic mode.



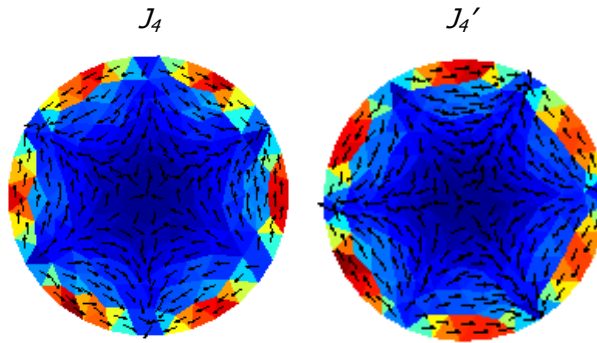


Figure 3.2 Normalized current distribution at 6 GHz of the characteristic currents of a circular plate in free space.

As observed, each characteristic mode presents a particular current distribution over the surface of the plate. Thus, mode J_{01} presents a current distribution that forms a loop in the structure, while modes J_{02} and J_{03} present two loops. Moreover, modes J_1 and J_1' exhibit vertical and horizontal current distributions, respectively. These two modes are degenerated modes, since they present the same resonant frequency, as discussed later. Throughout this Thesis, modes denoted with a single quotation mark refer to degenerated modes.

Finally, higher order modes J_2 , J_2' , J_4 and J_4' present an increasing number of nulls in the edge of the circular plate, whereas mode J_3 presents no variation in the angular dimension of the plate, with all vector currents being directed towards the centre of the plate, where a null is located. Although these current distributions are altered if the geometry is changed, the general pattern of the eigencurrents is preserved for any shape of the plate [45].

As it can be seen, the current distribution associated to the characteristic modes of the circular plate is very similar to that of the vector wave functions shown in chapter 2 for the circular disk. In Table 3.3, the correspondence between the vector wave functions and the characteristic modes with the same current distribution is depicted. The degenerated characteristic modes have not been plotted, but they correspond to the same m and n of the vector wave function, though using the alternate trigonometric function (see equation 2.20 in chapter 2). As observed, modes which forms loops on the structure are associated to TE fields.

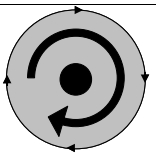
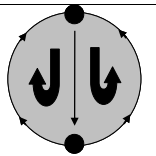
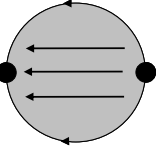
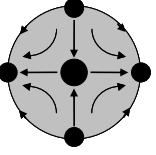
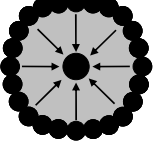
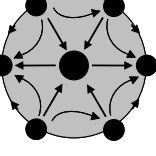
Current Distribution	Circular disk vector wave function	Charact. Mode	Current Distribution	Circular disk vector wave function	Charact. Mode
	TE ($m=0; n=1$)	J_{01}		TE ($m=1; n=2$)	J_{02}
	TM ($m=1; n=1$)	$J_{1'}$		TM ($m=2; n=2$)	J_2
	TM ($m=0; n=0$)	J_3		TM ($m=3; n=3$)	$J_{4'}$

Table 3.3. Comparison of the characteristic modes and the vector wave functions of a circular disk.

As commented in [17], the easiest way to understand how the magnitude of eigenvalues is related to the radiation of modes is analyzing the complex power balance yielded by equation (3.27). From this equation it is observed that, as commented, the power radiated by modes is normalized to unit value, whereas reactive power is proportional to the magnitude of the eigenvalues.

The eigenvalues λ_n range from $-\infty$ to $+\infty$. When the eigenvalue is $\lambda_n = 0$, the mode resonates, being called an *externally resonant mode*. Hence, those modes with smallest eigenvalues (in absolute value) are the most important for radiation and scattering problems, when excited. Additionally, the sign of the eigenvalue determines whether the mode contributes to store magnetic energy ($\lambda_n > 0$) or electric energy ($\lambda_n < 0$). The modes corresponding to the internal cavity resonances for the conducting surface would have $|\lambda_n| = \infty$, and do not enter into radiation and scattering problems.

Figure 3.3 shows the variation with frequency of the eigenvalues λ_n associated to the characteristic modes shown before. Therein it is observed that eigenvalues for

modes J_{01} , J_{02} and J_{03} are positive for all frequencies, and never reach the resonance condition $\lambda_n = 0$. Thus, these modes whose current distribution forms loops in the structure are special non-resonant modes, and they always exhibit an inductive behavior. The rest of the modes start however being capacitive ($\lambda_n < 0$) at lower frequencies, then they resonate ($\lambda_n = 0$) at a certain frequency and afterwards they keep a small positive value. Hence, for instance, modes J_1 and J_1' (degenerated modes) resonate at 6 GHz; modes J_2 and J_2' resonate at 9 GHz and the rest of the modes achieve the resonance condition at higher frequencies.

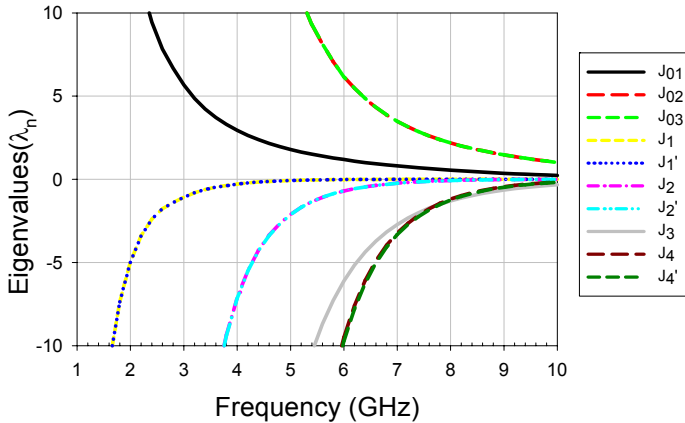


Figure 3.3 Variation in frequency of the eigenvalues λ_n associated to the characteristic modes plotted in Figure 3.2.

Here, it is important to note that the real nature of eigenvalues allows for an easier determination of the resonant frequencies of the modes, simply by analyzing their variation with frequency. In this case then is not necessary to search the complex frequency plane for roots of the determinant of the Z matrix.

In practice, another representation is preferred for the eigenvalues, so as to determine the resonant frequency of the modes and their natural behaviour. This representation is based on the definition of a **characteristic angle** associated to each mode. This parameter is defined as:

$$\alpha_n = 180^\circ - \tan^{-1}(\lambda_n) \tag{3.28}$$

and it physically describes the phase difference between the eigencurrent J_n and its associated characteristic field E_n .

Figure 3.4 represents the variation with frequency of the characteristic angle associated to the characteristic currents of the circular plate. In this case, the resonance of the mode occurs when the characteristic angle is equal to 180° , as in this case $\lambda_n = 0$. Therefore, when the characteristic angle is close to 180° (near resonance) the mode will be a good radiator, whereas the mode is mainly storing energy when its characteristic angle is near 90° or 270° . Thus, the variation of the characteristic angle with frequency provides qualitative information about the radiation bandwidth of the mode.

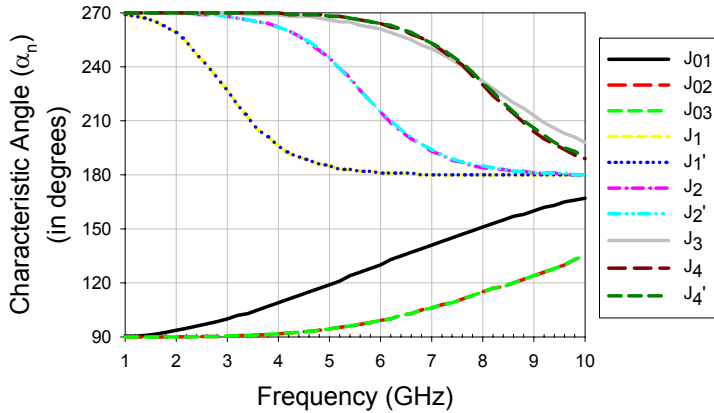
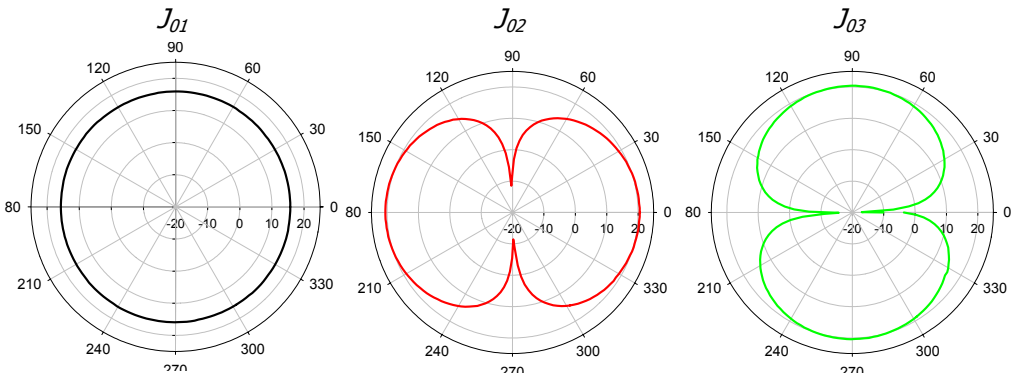


Figure 3.4 Variation in frequency of the characteristic angles α_n (in degrees) associated to the characteristic modes plotted in Figure 3.2.

Furthermore, it has been established that each characteristic current produces a characteristic field, which describes a specific radiation pattern. For the circular disk, the characteristic pattern associated to each one of the previous modes is depicted in Figure 3.5.



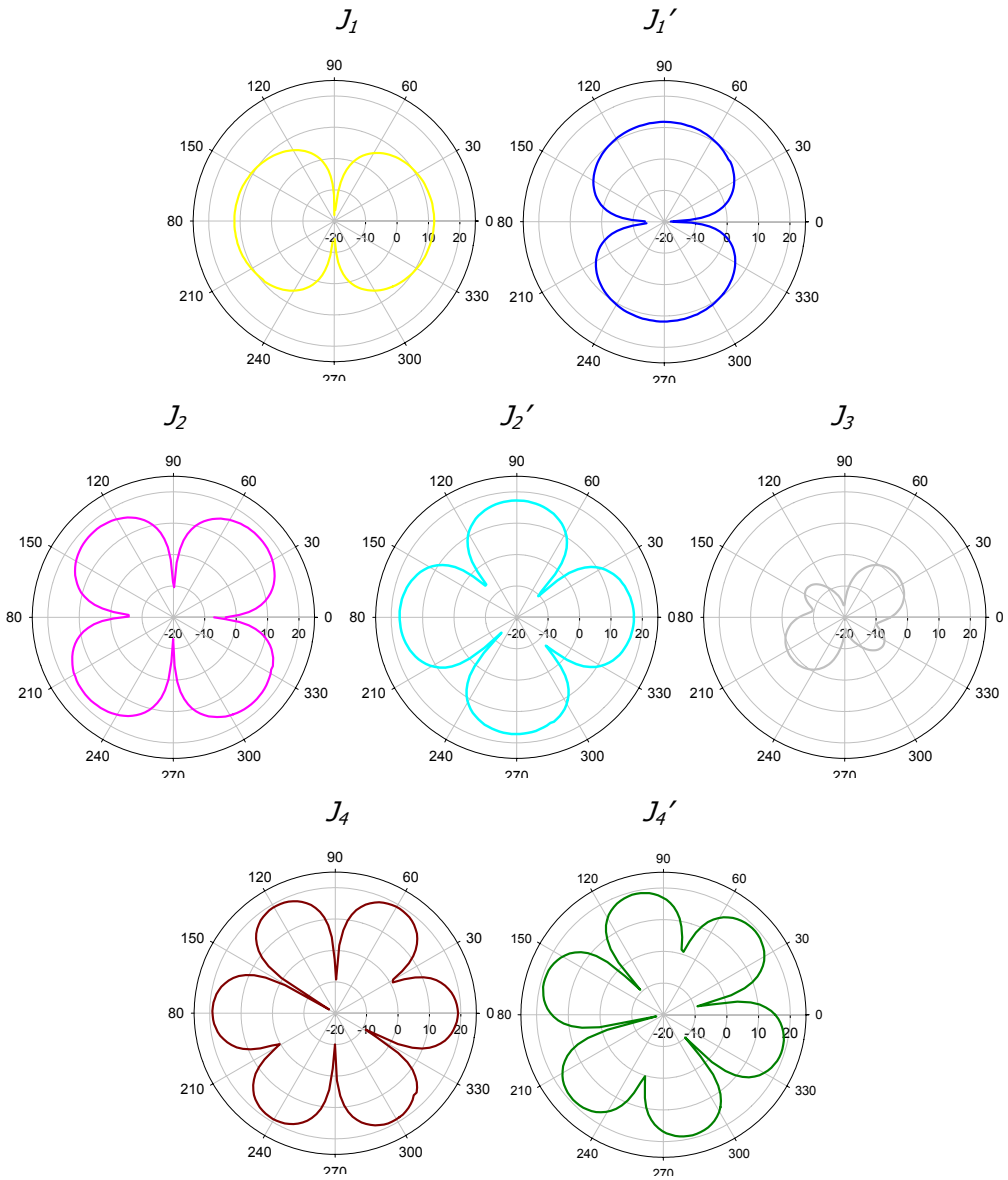


Figure 3.5 Radiation patterns associated to the modes depicted in Figure 3.2.

3.5. Relation between characteristic modes and vector wave functions

In chapter 2, natural vector current modes were analytically extracted for some structures, in which the wave equation was separable. These vector wave functions and the associated currents were of complex nature, what made them more difficult to handle for design and optimization of the conducting structures. Then, in the present chapter, another kind of current modes has been introduced, which are numerically computed for any arbitrary structure by the application of the Theory of Characteristic Modes.

Now, this section tries to establish the relationship between these two types of modal functions, since despite the benefits provided by characteristic modes, traditional vector wave functions are generally more widely known and usual in electromagnetic books. Therefore, characteristic modes for the sphere and the infinite planar strip will be derived, and connection between the analytical expressions of both types of functions will be established.

3.5.1. Analytic characteristic modes of the conducting sphere

In [14], Garbacz extracted the analytical expression for the characteristic modes of a conducting sphere of radius a , both for the TM and for the TE case. These expressions read as follows:

$$\begin{aligned} \bar{\mathbf{j}}_{mn}^{TM e,o} &= \frac{1}{k\sqrt{Z_0}} \frac{1}{a^2 [ka \cdot j_n(ka)]'} \sqrt{\frac{\epsilon_m}{4\pi} \cdot \frac{2n+1}{n(n+1)} \cdot \frac{(n-m)!}{(n+m)!}} \\ &\cdot \left[\hat{\phi} \cdot \frac{P_n^m(\cos\theta)}{\sin\theta} \cdot \begin{Bmatrix} -\sin m\phi \\ \cos m\phi \end{Bmatrix} \cdot m + \hat{\theta} \cdot \frac{\partial P_n^m(\cos\theta)}{\partial\theta} \cdot \begin{Bmatrix} \cos m\phi \\ \sin m\phi \end{Bmatrix} \right] \end{aligned} \quad (3.29)$$

$$\begin{aligned} \bar{\mathbf{j}}_{mn}^{TE e,o} &= \frac{1}{k\sqrt{Z_0}} \frac{1}{a^2 j_n(ka)} \sqrt{\frac{\epsilon_m}{4\pi} \cdot \frac{2n+1}{n(n+1)} \cdot \frac{(n-m)!}{(n+m)!}} \\ &\cdot \left[\hat{\theta} \cdot \frac{P_n^m(\cos\theta)}{\sin\theta} \cdot \begin{Bmatrix} -\sin m\phi \\ \cos m\phi \end{Bmatrix} \cdot m - \hat{\phi} \cdot \frac{\partial P_n^m(\cos\theta)}{\partial\theta} \cdot \begin{Bmatrix} \cos m\phi \\ \sin m\phi \end{Bmatrix} \right] \end{aligned} \quad (3.30)$$

where $n \geq 1$ and $m \leq n$, subscript e, o denote even and odd modes associated to $\cos m\phi$ and $\sin m\phi$, respectively, and ε_m is $\varepsilon_m = 1$ for $m = 0$, and $\varepsilon_m = 2$ for $m \neq 0$.

As observed, the analytic expressions for characteristic modes in the sphere are very similar to those of equations (2.11) and (2.12). In fact, the variation with (ϕ, θ) of the current modes in the surface of the sphere is exactly the same, both for the TM and for the TE case. This fact was also appreciated when comparing the vector wave functions of the circular disk and the characteristic modes of the circular plate.

The only difference between both modal functions is the amplitude term that multiplies the real term containing the vector variation in (ϕ, θ) . In fact, this amplitude term includes the complex behaviour in the vector wave functions (as it is the only complex term appearing in the expression of these functions), whereas it is real for the characteristic modes, as it accounts for the equiphase radiated fields. Moreover the amplitude term in the characteristic modes includes a normalization term, forcing each mode to radiate unit power, as established when defining the characteristic modes.

Associated to each characteristic current of the conducting sphere, a set of TM and TE eigenvalues exist, which reads as follows [14]:

$$\lambda_n^{TM} = - \frac{\partial/\partial r [kr \cdot n_n(kr)]|_{r=a}}{\partial/\partial r [kr \cdot j_n(kr)]|_{r=a}} \quad (3.31)$$

$$\lambda_{mn}^{TE} = - \frac{n_n(ka)}{j_n(ka)} \quad (3.32)$$

These eigenvalues make the modal fields in the surface of the sphere to be the same in both sets of modes. For instance, for the TM case, the tangential field in the surface of the conducting sphere of radius a produced by characteristic modes will be expressed as:

$$\vec{E}_{\tan mn}^{TM e,o}(r=a) = \frac{\partial [kr \cdot h_n^{(2)}(k)]}{\partial r} \Big|_{r=a} \cdot \left[\begin{array}{l} \hat{\phi} \cdot \frac{P_n^m(\cos \theta)}{\sin \theta} \cdot \begin{Bmatrix} -\sin m\phi \\ \cos m\phi \end{Bmatrix} \cdot m + \\ + \hat{\theta} \cdot \frac{\partial P_n^m(\cos \theta)}{\partial \theta} \cdot \begin{Bmatrix} \cos m\phi \\ \sin m\phi \end{Bmatrix} \end{array} \right] \quad (3.33)$$

As observed, equation (3.33) is practically the same as the tangential field particularized in $r = a$ produced by the vector wave functions in equation (2.6).

Figure 3.6 shows the characteristic angle variation with frequency associated to the first three characteristic modes of a conducting sphere of radius $a = 0.1 \text{ m}$. As observed, due to the oscillatory behavior of spherical Bessel functions of first and second kind and their derivatives, the characteristic angle takes periodical values between 90° and 270° with frequency. These curves represent the phase of the tangential electric field associated to the different eigenmodes on the surface of the sphere. As commented before, resonances occur at frequencies when the characteristic angles are equal to zero. In such case, the tangential field produced by the mode on the sphere is of real nature (radiating field).

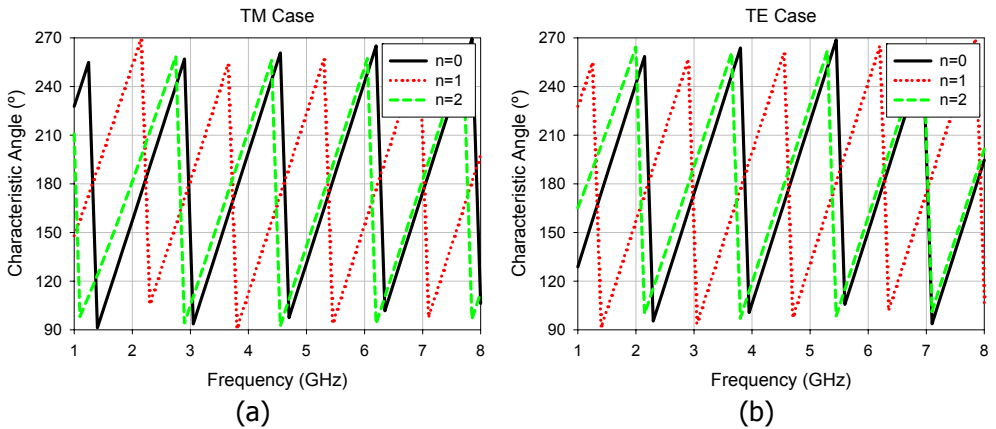


Figure 3.6 Variation in frequency of the characteristic angles associated to the first three characteristic modes of a conducting sphere of radius $a = 0.1 \text{ m}$:

(a) For the TM case; (b) For the TE case.

3.5.2. Closed-form characteristic modes of an infinite metallic strip

Some references have been found in the literature, which express the interest of computing characteristic modes for an infinite slot in a conducting plane [46]-[48], since these modes can be used as basis functions for more complex, non-separable geometries as well as for the investigation of slot-line discontinuities. In [46] and [47] the problem is numerically approached for both the TE and the TM case, and approximate analytical expressions are obtained only for the narrow strip

case. In this particular case, expansion of characteristic modes in terms of a few Chebyshev polynomials is proposed.

Nevertheless, exact analytical expressions for the characteristic modes of the infinite slot can be extracted, if the problem is addressed from the perspective used in chapter 2, section 2.4. By means of the Babinet principle, the problem of the slot in the conducting plane can be considered as equivalent to the problem of an infinite strip in free space. Therefore, as proposed in section 2.4, it is possible to cope with this problem by studying the particular case of a conducting elliptic cylinder that degenerates in the limit ($\xi \rightarrow 0$) into a planar strip.

In [49], characteristic modes for a conducting elliptic cylinder were analytically derived, but only for the TM case. In this case, the two-dimensional Green's function can be expressed in terms of elliptic harmonics as follows [18]:

$$H_0^{(2)}(kR) = 4 \left\{ \begin{aligned} & \sum_{m=0}^{\infty} \frac{Se_m(\eta'; s)}{N_m^{(e)}(s)} \cdot Se_m(\eta'; s) \cdot Re_m^{(1)}(\xi'; s) \cdot Re_m^{(4)}(\xi; s) + \\ & + \sum_{m=1}^{\infty} \frac{So_m(\eta'; s)}{N_m^{(o)}(s)} \cdot So_m(\eta'; s) \cdot Ro_m^{(1)}(\xi'; s) \cdot Ro_m^{(4)}(\xi; s) \end{aligned} \right. \quad (3.34)$$

where R is the distance between the observation point (η, ξ) and the source point (η', ξ') , and

$$N_m^{(e)}(s) = \int_0^{2\pi} [Se_m(\eta; s)]^2 \cdot d\eta; \quad N_m^{(o)}(s) = \int_0^{2\pi} [So_m(\eta; s)]^2 \cdot d\eta \quad (3.35)$$

If the Galerkin Method of Moments is applied, the following elements Z_{qn} in the generalized impedance matrix are obtained for the TM case:

$$\begin{aligned}
 Z_{qn}^{TM} = j\omega\mu \cdot \sum_{m=0}^{\infty} & \left[\frac{1}{Ne_m} \cdot \text{Re}_m^{(1)}(\xi'; s) \cdot \text{Re}_m^{(4)}(\xi; s) \cdot \right. \\
 & \left. \cdot \int_{\nu=0}^{2\pi} J_q(\eta) \cdot Se_m(\eta; s) \cdot h_\eta \cdot d\eta \cdot \int_{\nu'=0}^{2\pi} J_n(\eta') \cdot Se_m(\eta'; s) \cdot h_{\eta'} \cdot d\eta' \right] + \\
 + j\omega\mu \cdot \sum_{m=1}^{\infty} & \left[\frac{1}{No_m} \cdot \text{Ro}_m^{(1)}(\xi'; s) \cdot \text{Ro}_m^{(4)}(\xi; s) \cdot \right. \\
 & \left. \cdot \int_{\nu=0}^{2\pi} J_q(\eta) \cdot So_m(\eta; s) \cdot h_\eta \cdot d\eta \cdot \int_{\nu'=0}^{2\pi} J_n(\eta') \cdot So_m(\eta'; s) \cdot h_{\eta'} \cdot d\eta' \right]
 \end{aligned} \quad (3.36)$$

Herein, it can be easily observed that if the following functions are chosen as expansion and testing functions:

$$\vec{J}_n^{TM}(\eta) = \hat{z} \cdot \begin{Bmatrix} \frac{Se_n(\eta; s)}{h_\eta} \\ So_n(\eta; s) \\ \frac{So_n(\eta; s)}{h_\eta} \end{Bmatrix} \quad (3.37)$$

diagonalization of the impedance matrix Z of the conducting elliptic cylinder is obtained. Therefore, in the planar strip ($\xi \rightarrow 0$) the characteristic modes for the TM case will read as:

$$\vec{J}_n^{TM}(\eta) = \hat{z} \cdot \begin{Bmatrix} \frac{Se_n(\eta; s)}{h_\eta} \\ So_n(\eta; s) \\ \frac{So_n(\eta; s)}{h_\eta} \end{Bmatrix} = \hat{z} \cdot \begin{Bmatrix} \frac{Se_n(\eta; s)}{W/2 \cdot \sqrt{1 - \cos^2 \eta}} \\ So_n(\eta; s) \\ \frac{So_n(\eta; s)}{W/2 \cdot \sqrt{1 - \cos^2 \eta}} \end{Bmatrix} \quad (3.38)$$

As in the case of the sphere, it can be seen that these characteristic modes present the same variation as that of equation (2.30) in chapter 2, for the TM vector current wave functions, although for real modal currents in this case.

Moreover, when $\xi = \xi' = 0$, radiation of odd modes in equation (3.38) is zero, since $Ro_m^{(1)}(\xi' = 0; s) = 0$ in equation (3.36). Therefore, in the case of the conducting

strip of zero thickness, characteristic modes will only appear in even modes

$$\frac{Se_n(\eta; s)}{W/2 \cdot \sqrt{1 - \cos^2 \eta}}$$

for the TM case.

Thus, Figure 3.7 represents some of the characteristic modes of a conducting strip of width $W = \lambda$ versus x / λ (being $x = W/2 \cos \eta$), for the TM case (TE case in the slot), computed using [50]. These waveforms coincide with those numerically calculated for the TE case of a slot in a conducting plane, provided in [46].

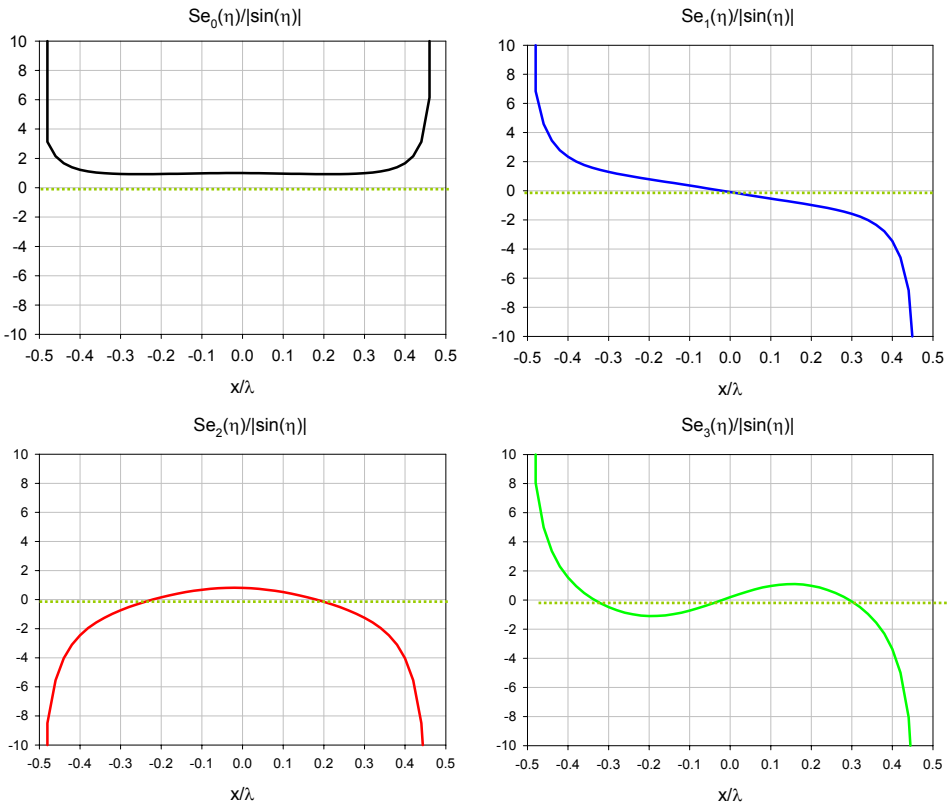


Figure 3.7 Characteristic modes in the TM case of a conducting strip of width $W = \lambda$.

Moreover, by means of the application of equation (3.16) closed-form expressions for the TM eigenvalues associated to the conducting strip of zero thickness can be derived:

$$\lambda_n^{TM}(s) = -\frac{\text{Re}_m^{(2)}(\xi=0; s)}{\text{Re}_m^{(1)}(\xi=0; s)} \quad (3.39)$$

For the TE case, no closed-form expressions have been found in the literature for the characteristic modes, since in this case the elements of the impedance matrix of a perfectly conducting elliptic cylinder become more complicated:

$$\begin{aligned} Z_{qn}^{TE} = & j\omega\mu \sum_{m=0}^{\infty} \text{Re}_m^{(1)}(0) \cdot \text{Re}_m^{(4)}(0) \int_{\eta} J_q(\eta) \cdot \text{Se}_m(\eta) \cdot h_{\eta} \cdot d\eta \cdot \int_{\eta'} J_n(\eta') \cdot \text{Se}_m(\eta') \cdot h_{\eta'} \cdot d\eta' \\ & - \frac{1}{j\omega\varepsilon} \sum_{m=0}^{\infty} \text{Re}_m^{(1)}(\xi, 0) \cdot \text{Re}_m^{(4)}(\xi, 0) \int_{\eta} J_q(\eta) \cdot \frac{\partial \text{Se}_m(\eta)}{\partial \eta} \cdot d\eta \cdot \\ & \cdot \left[\int_{\eta'} \text{Se}_m(\eta') \cdot \left[\frac{\partial J_n(\eta')}{\partial \eta'} + J_n(\eta') \cdot \frac{\cos \eta'}{\sin \eta'} \right] \cdot d\eta' \right] + \\ & + j\omega\mu \sum_{m=0}^{\infty} \text{Ro}_m^{(1)}(0) \cdot \text{Ro}_m^{(4)}(0) \int_{\eta} J_q(\eta) \cdot \text{So}_m(\eta) \cdot h_{\eta} \cdot d\eta \cdot \int_{\eta'} J_n(\eta') \cdot \text{So}_m(\eta') \cdot h_{\eta'} \cdot d\eta' - \\ & - \frac{1}{j\omega\varepsilon} \sum_{m=0}^{\infty} \text{Ro}_m^{(1)}(\xi, 0) \cdot \text{Ro}_m^{(4)}(\xi, 0) \int_{\eta} J_q(\eta) \cdot \frac{\partial \text{So}_m(\eta)}{\partial \eta} \cdot d\eta \cdot \\ & \cdot \left[\int_{\eta'} \text{So}_m(\eta') \cdot \left[\frac{\partial J_n(\eta')}{\partial \eta'} + J_n(\eta') \cdot \frac{\cos \eta'}{\sin \eta'} \right] \cdot d\eta' \right] \end{aligned} \quad (3.40)$$

Nevertheless, by analyzing the scattering problem instead of the radiation problem, it is easier to find the solutions for the characteristic modes. Therefore, for the TE case, the characteristic modes of the infinite strip ($\xi = \xi' = 0$) will be given by:

$$\vec{J}_n^{TE}(\eta) = \hat{\eta} \cdot \text{So}_n(\eta; s) \quad (3.41)$$

These modes are depicted in Figure 3.8 for a conducting strip of width $W = \lambda$ versus x/λ , for the TE case (or for the TM case in the slot, as a result of the duality of these two problems). These waveforms coincide with those calculated numerically for the TM case of a slot in a conducting plane, provided in [47].

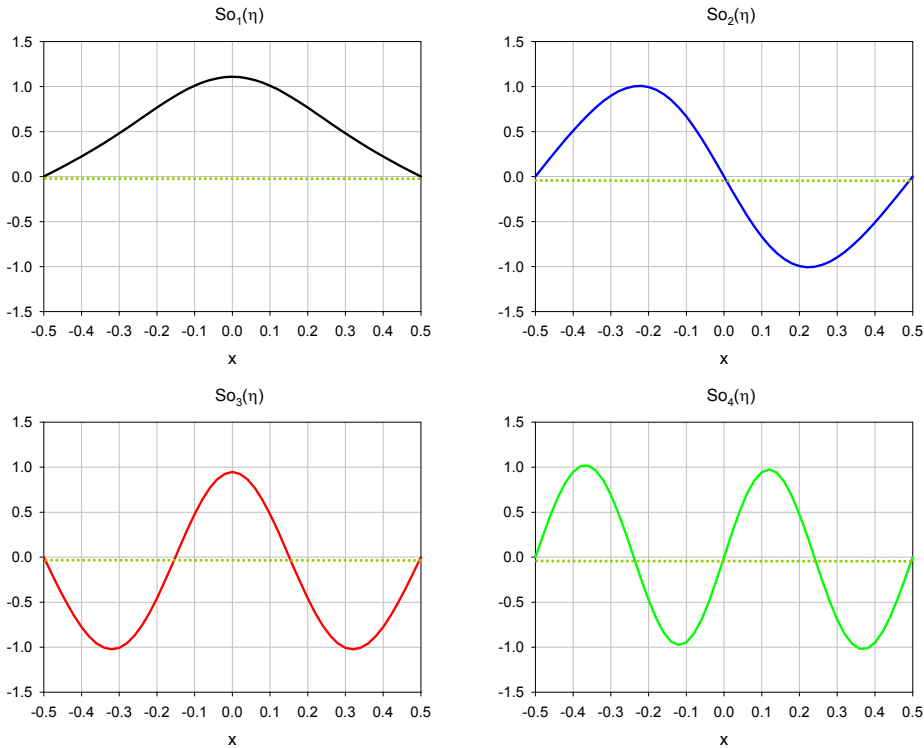


Figure 3.8 Characteristic modes in the TE case of a conducting strip of width $W = \lambda$.

Moreover, the eigenvalues for the TE case will be as follows:

$$\lambda_n^{TE}(s) = -\frac{RO_n^{(2)' }(\xi = 0; s)}{RO_n^{(1)' }(\xi = 0; s)} \tag{3.42}$$

Table 3.4 shows the eigenvalues obtained with equations (3.39) and (3.42) for an infinite slot of width $W = \lambda$ in a conducting plane. These values agree almost perfectly with those provided in [51], which were computed numerically. The characteristic angles associated to eigenvalues of equation (3.42) have been plotted in Figure 3.9, according to the definition provided by equation (3.28). In this figure, a strip of width $W = 0.1 m$ has been considered, plotting then the characteristic angle variation versus frequency. As observed, for the infinite slot, characteristic angles associated to TE modes are positive, (i.e. they are capacitive modes), whereas angles associated to TM modes are negative (i.e. they are inductive).

Mode	$\lambda_n^{TM} (s)$	$\lambda_n^{TE} (s)$
1	0.021288	-0.022393
2	0.304117	-0.5165278
3	1.464597	-7.963271
4	9.593173	-161.079222
5	163.759022	-5199.742994
6	5202.224245	-251476.151297

Table 3.4. Eigenvalues associated to the characteristic modes of a conducting strip of width $W = \lambda$, both for the TM and the TE case.

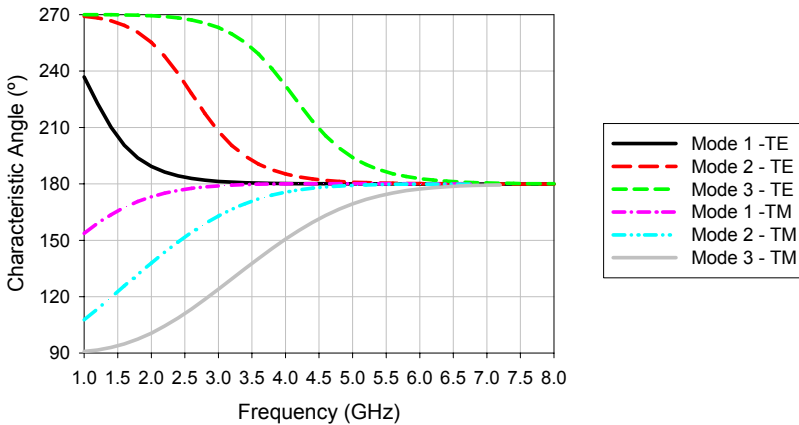


Figure 3.9 Characteristic angle vs. frequency associated to the characteristic modes of an infinite slot of width $W = 0.1 m$, both for the TE and TM cases.

In Figure 3.7 and Figure 3.8, it can be observed that these characteristic modes resemble very much the entire domain basis functions traditionally used to expand the current in a microstrip patch or a rectangular plate/slot. In these cases, the longitudinal current J_z is usually expanded in terms of Chebyshev polynomials of the first kind, with a singularity to account for the edge condition, whereas the transversal current J_x is expanded in terms of Chebyshev polynomials of the second kind, and a function that accounts for nulls at the edges [23][52], as follows:

$$J_q^z(x) = (2 - \delta_{q0}) \cdot \frac{2}{W\pi} \cdot \frac{T_q(2x/W)}{\sqrt{1 - (2x/W)^2}} \quad (3.43)$$

$$J_p^x(x) = \frac{4}{W\pi} \cdot j \cdot U_p(2x/W) \cdot \sqrt{1 - (2x/W)^2} \quad (3.44)$$

where $T_q(\cdot)$ and $U_p(\cdot)$ denotes the Chebyshev polynomials of the first and the second kind, respectively, and $J_q^z(x)$ and $J_p^x(x)$ represent the entire domain basis functions for the expansion of the current J_z and J_x , respectively.

Characteristic modes given by equations (3.37) and (3.41) are actually a generalization of those functions shown in equations (3.43) and (3.44). If the expansion of the angular Mathieu functions in terms of trigonometric functions is considered, as shown in Appendix A, it is possible to write:

$$Se_n(\eta; s) = \sum_p A_p^n \cos(p\eta) \quad (3.45)$$

$$So_n(\eta; s) = \sum_p B_p^n \sin(p\eta) \quad (3.46)$$

and taking into account that Chebyshev polynomials of the first kind and the second kind are defined through the following identities [23]:

$$T_n(\cos \theta) = \cos(n\theta) \quad (3.47)$$

$$U_n(\cos \theta) = \frac{\sin[(n+1)\theta]}{\sin \theta} \quad (3.48)$$

equations (3.45) and (3.46) can be written, respectively, as

$$Se_n(\eta; s) = \sum_p A_p^n \cdot T_p(\cos \eta) \quad (3.49)$$

$$So_n(\eta; s) = \sum_p B_p^n \cdot U_{p-1}(\cos \eta) \sin(\eta) \quad (3.50)$$

If the following relation between Cartesian and elliptical coordinates is considered:

$$x = \frac{W}{2} \cos \eta \quad (3.51)$$

then characteristic modes for the TM and TE cases can be written, respectively, as:

$$\vec{J}_n^{TM}(\eta) = \hat{z} \cdot \frac{S e_n(\eta; s)}{W/2 \cdot \sqrt{1 - \cos^2 \eta}} = \hat{z} \cdot \frac{\sum_p A_p^n \cdot T_p(2x/W)}{W/2 \cdot \sqrt{1 - (2x/W)^2}} \quad (3.52)$$

$$\vec{J}_n^{TE}(\eta) = \hat{x} \cdot S o_n(\eta; s) = \hat{x} \cdot \sum_p B_p^n \cdot U_n(2x/W) \sqrt{1 - (2x/W)^2} \quad (3.53)$$

As observed, characteristic modes can hence be considered a general case of the approximation of the current by Chebyshev polynomials. The provided closed-forms of characteristic modes may therefore be used as frequency dependent basis functions in geometries where rectangular contours are included, similarly to those proposed in [53].

3.6. Conclusions

In the present chapter, the Theory of Characteristic Modes has been revisited, as it provides real modes of current, which are easier to deal with in a design problem. Properties of these modes have been reviewed, and the physical interpretation of the information provided by the characteristic angle associated to each mode has been summarized. It has been seen that each mode, except loop modes, resonates at a certain frequency, where the associated eigenvalue takes a zero value. These resonances correspond to external resonances of the structure. Moreover, the variation of the eigenvalue or the characteristic angle versus frequency provides very interesting information about the radiating behavior of the mode.

The information about resonance and radiating bandwidth provided by characteristic modes can be used as an initial step in an antenna design process, where the geometry of the radiating structure can be optimized. As characteristic modes are obtained in absence of sources, the next step may consist in selecting an optimum feeding configuration to excite those modes with more appealing properties. The real current distribution associated to each mode will assist in selecting the optimum feeding location. This will be discussed in next chapter.

Furthermore, a connection between characteristic modes and traditional vector wave functions, obtained in the previous chapter, has been established. It has

been shown that both types of modes present very similar properties, except for the real nature of characteristic modes. Besides, closed-form expressions for the characteristic modes of an infinite planar strip have been presented for the first time, both for the TM and TE case. The provided characteristic functions could be used as entire-domain basis functions in problems including rectangular surfaces, since it has been demonstrated that they are a generalization of the traditionally used Chebyshev polynomials. Moreover, as the proposed functions are frequency dependent, they can be used to accelerate the convergence to the solution of these problems when a broad frequency range is considered.

Chapter 4

Excitation of Characteristic Modes

“Research is to see what everybody else has seen, and to think what nobody else has thought”

Albert Szent-Györgi

4.1. Introduction

In the previous chapter, characteristic modes of a conducting body were introduced as the real currents on the surface of the conducting structure depending only on its shape and size, which are independent of any specific source or excitation. Due to their real nature, it was concluded that these modal currents are the most suitable vector functions to deal with in order to address an antenna design problem from a modal perspective.

Associated to the characteristic currents, a set of real eigenvalues λ_n is also obtained, which provides valuable information about the physical behavior of the structure. By analyzing the variation of the eigenvalues with frequency, the resonant frequency and the radiating bandwidth of each mode can be determined. Consequently, the initial step in an antenna design process involves analyzing the characteristic modes of a specific radiating structure and identifying their properties. As these modes are calculated in the absence of excitation, the next step consists in selecting the optimum feed configuration in order to excite those modes with more appealing properties [54].

Excitation of current modes in open structures or antennas is very similar to the well-known problem of excitation of cavities in microwave networks. Thus, it is known that in the cavity shown in Figure 4.1, a complete set of orthogonal modes can be defined, which satisfy the field equations and boundary conditions in the cavity, in absence of sources. When electric sources are applied to the cavity, the total field \vec{E} can be then expressed as [9]:

$$\vec{E} = \sum_n \frac{j\omega \vec{E}_n}{\omega^2 - \omega_n^2} \iiint \vec{J} \cdot \vec{E}_n^* \cdot dV$$

where \vec{E}_n is a field mode vector, ω_n is the resonant frequency (eigenvalue) associated to the mode, \vec{J} is the electric source applied and V is the volume containing the cavity. As observed, this expression is very similar to the expansion of the total current in the surface of the conducting body in terms of characteristic modes, which was given by equation (3.23). In both expressions, the significance of each mode is determined by the coupling between the source and the mode, as well as the associated eigenvalue. Therefore, an interesting analogy exists between the excitation of modes in microwave cavities and in antennas.

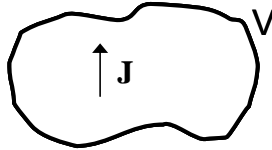


Figure 4.1 A cavity containing electric sources.

In the present chapter the problem of the excitation of characteristic modes in radiating structures will be addressed for different cases. Initially, modal excitation will be analyzed in a very simple structure, such a wire loop antenna, and different feeding configurations will be studied in order to illustrate their impact on the antenna performance. Afterwards, modal excitation will be investigated for more complex structures, such as planar antennas, and innovative designs of wideband antennas based on the use of multiple feeding points will be presented.

4.2. Excitation of modes in a circular wire loop antenna

Let us begin with the analysis of the excitation of characteristic modes in a simple structure, such as a circular wire loop antenna with radius $a=114.5$ mm. The geometry of the loop, which is placed in the XY plane, is shown in Figure 4.2. The wire is assumed to be a loss-free conductor.

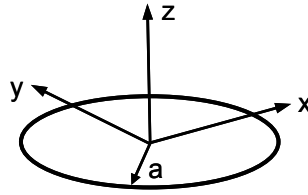


Figure 4.2 Wire circular loop of radius $a=114.5$ mm and wire diameter $d=1$ mm.

Characteristic modes of this structure have already been computed in [17], where their properties have also been analyzed. This section will be focused mainly on the analysis of the excitation of these modes. However, for the sake of understanding, the waveforms of these modes and their properties will be concisely reviewed in advance.

4.2.1. Characteristic modes of a circular wire loop antenna

As shown in [17], the characteristic modes of a circular loop are simple sinusoidal functions given by:

$$\vec{J}_n^{e,o}(\phi) = \hat{\phi} \cdot \begin{cases} \cos n\phi \\ \sin n\phi \end{cases} \quad (4.54)$$

for $n = 0, 1, 2, \dots$. Figure 4.3 shows the waveforms for the first six characteristic modes of the loop in free space, whose current distribution has been represented schematically in Figure 4.4. In this figure, black circles represent the location of the nulls of current along the structure. As expected, the first two modes, J_1 and J_2 exhibit two current nulls at $\phi = \pm 90^\circ$ and at $\phi = (0^\circ; 180^\circ)$, respectively. Modes J_3 and J_4 are higher order modes with four current nulls. Nulls of mode J_3 are at $\phi = (\pm 45^\circ; \pm 135^\circ)$, whereas nulls of mode J_4 are at $\phi = (0^\circ; 90^\circ; 180^\circ; 270^\circ)$. Mode J_5 and successive higher order modes exhibit an increasing number of nulls. There also exists mode J_0 that presents uniform current distribution along the loop.

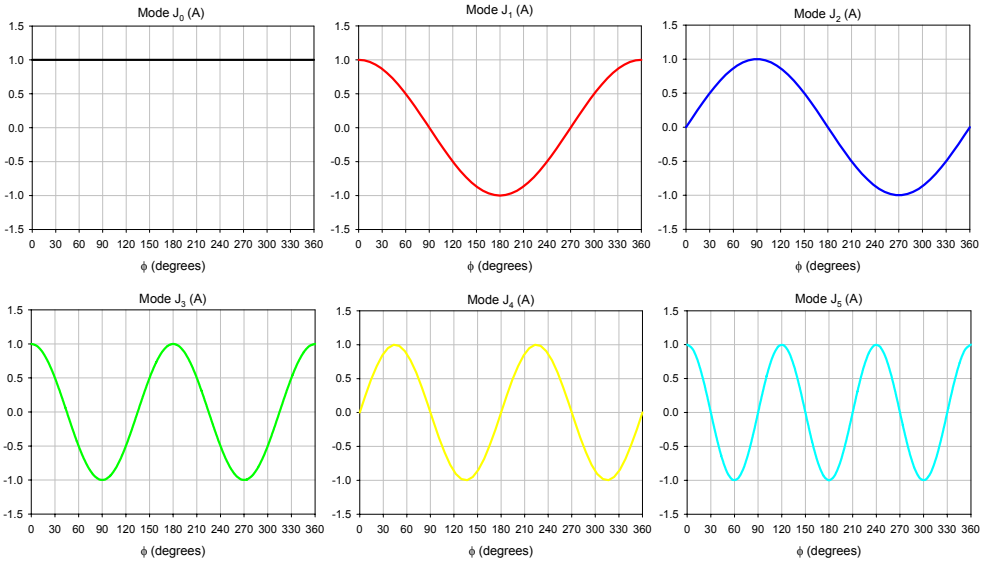


Figure 4.3 Normalized current distribution over the wire loop antenna for the first six characteristic modes, at first resonance ($f = 440$ MHz)

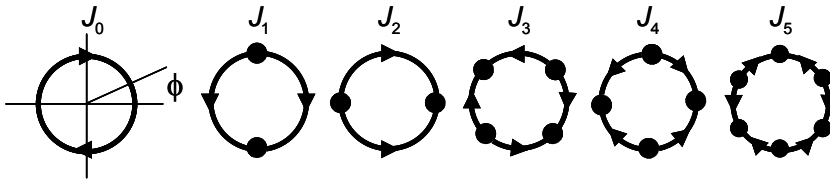


Figure 4.4 Diagrams of the modal current distributions in the wire loop antenna at first resonance (black dots refer to nulls of current).

Additionally, the characteristic angle associated to each eigenmode has been represented in Figure 4.5. As commented in chapter 3, characteristic modes which forms loops in the structure, like the mode J_0 , are special modes that do not resonate and present pure inductive behavior. This fact can be observed in Figure 4.5, where it is patent that mode J_0 never achieves the resonance condition ($\alpha_n = 180^\circ$), since the characteristic angle remains in the inductive region at all frequencies. Due to the symmetry of revolution of the structure, the rest of the modes resonate in pairs. In the frequency range under study, there are two pairs of degenerated modes with identical resonant frequency, J_1 - J_2 and J_3 - J_4 . The first pair of degenerated modes resonates at 440 MHz, when the perimeter of the loop

is approximately λ , whereas the second pair resonates at 860 MHz, when the perimeter of the loop is 2λ . At the remaining frequencies, degenerated modes present the same characteristic angle curve, as shown in Figure 4.5.

Furthermore, in Figure 4.3 and Figure 4.4 it is observed that degenerated modes present exactly the same current distribution, although with a 90° or 45° phase difference for the case of modes J_1 and J_2 and modes J_3 and J_4 , respectively. These differences are also patent in the radiation patterns associated to the eigenfields, which are depicted in Figure 4.6. According to the figure, only mode J_0 exhibits an omnidirectional radiation pattern in the XY plane.

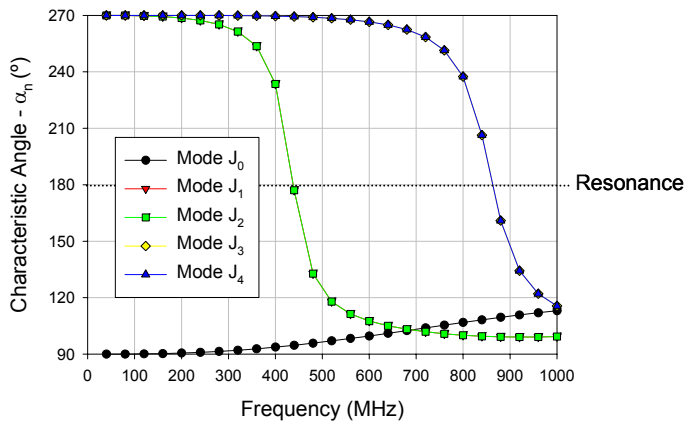


Figure 4.5 Variation with frequency of the characteristic angle associated to the eigenmodes shown in Figure 4.3.

Moreover, as discussed in chapter 3, information about the radiation bandwidth of the modes can be extracted from the curves plotted in Figure 4.5. Thus, the nearer to 180° the characteristic angle is over the frequency range, the wider bandwidth the mode presents. In this case, it is observed that modes do not present very wideband radiating properties, as expected for a wire structure, and hence the excitation of modes in this structure would only make sense for narrowband applications. In [17], the quality factor for each mode is provided, confirming their narrowband behavior.

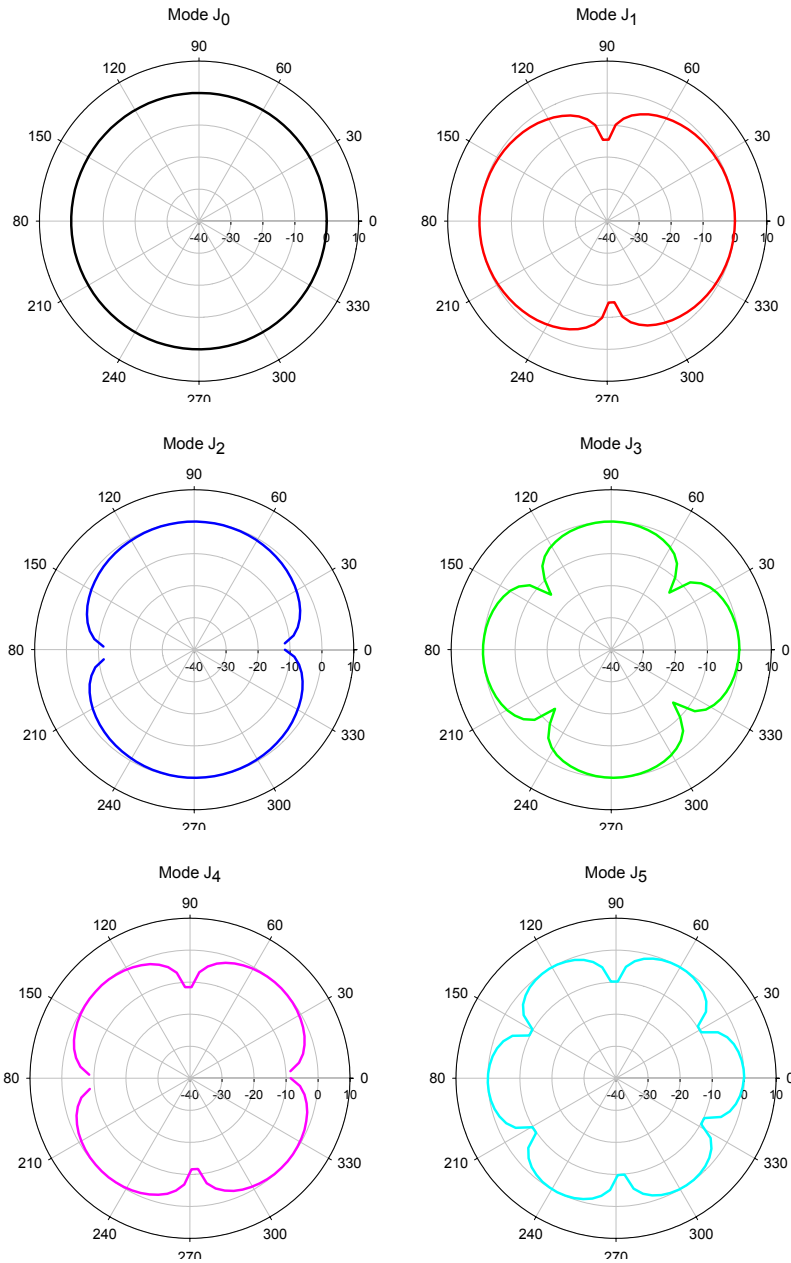


Figure 4.6 Radiation patterns in dB in XY plane ($\theta=90^\circ$) associated to the eigenmodes shown in Figure 4.3.

4.2.2. Excitation of characteristic modes

Once the current distribution exhibited by the characteristic modes of a circular loop has been reviewed, we will proceed with the excitation of these modes.

As commented in chapter 3, the total current distribution in the surface of the conducting structure can be expressed as a superposition of the characteristic modes by means of equation (3.23), where the contribution of each mode to the total current depends on:

- the magnitude of the eigenvalue λ_n associated to the characteristic current, being more significant those modes with lower eigenvalue;
- the degree of coupling between the source and the characteristic mode, which is given by the modal excitation coefficient defined by equation (3.22).

Therefore, the location of the source within the loop is crucial to obtain a proper coupling and hence excite the desired modes within the structure. In next sections, the impact of the location of the source on the antenna behaviour will be analyzed, and different feeding configurations will be studied.

In order to quantify the contribution of each mode, the input admittance Y_{in} of the antenna will be computed. For a voltage excitation of 1 V, the input admittance of the antenna can be easily calculated, as it is the total current given by equation (3.23) sampled at the feeding point P [17]:

$$Y_{in} = \frac{J(P)}{1} = \sum_n \frac{V_n^i}{1 + j\lambda_n} J_n(P) \quad (4.55)$$

This input admittance can be expressed in terms of the complex admittances of each mode (Y_n), as follows [17]:

$$Y_{in} = \sum_n Y_n = \sum_n G_n + jB_n = \sum_n \left(\frac{V_n^i \cdot J_n(P)}{1 + \lambda_n^2} - j \frac{V_n^i \cdot J_n(P) \cdot \lambda_n}{1 + \lambda_n^2} \right) \quad (4.56)$$

Therefore, it is possible to analyze the contribution of each mode by means of its modal admittance, as discussed later.

4.2.2.1. Excitation of the wire loop with a single source

Let us investigate the excitation of the characteristic modes over the structure, when locating a single source at different points along the geometry.

When a voltage gap source is placed at $\phi=0^\circ$, the modal admittances versus frequency depicted in Figure 4.7 are obtained, both for the real and imaginary parts. The total admittance calculated at the input port (Y_{in}) has been also represented in the figure, so as to facilitate the identification of the contribution of each mode to the total input admittance. As expected, the location of the source enhances the coupling to those modes whose amplitude is significant at the feed point (modes J_0 , J_1 and J_3 , in this case), while modes that present nulls of current in that point will not be excited (modes J_2 and J_4).

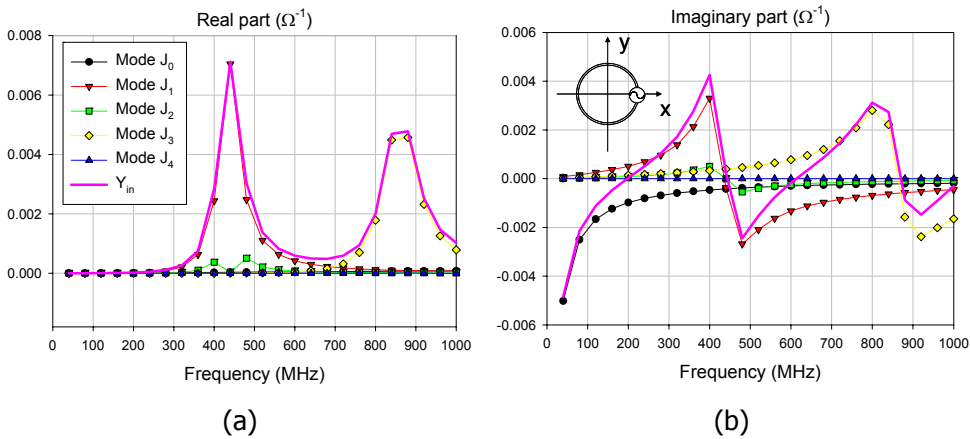


Figure 4.7 Contribution of the modal admittances Y_n to the input admittance Y_{in} when a voltage source is located at $\phi=0^\circ$. (a) Real part; (b) Imaginary part. Legend is common to both plots.

In Figure 4.7 the inductive behaviour of mode J_0 can also be noticed, since its contribution is only appreciated in the imaginary part of the input admittance. Moreover, as the different modes present narrow bandwidth, contribution of each one is only significant in the proximity of its resonant frequency. The contribution of the different modes is also patent in the radiation pattern of the structure. Figure 4.8 depicts the radiation pattern in the XY plane at three different frequencies within the analyzed range. By comparing with the eigenpatterns shown in Figure 4.6, it can be seen that the radiation pattern at 175 MHz is mainly due to mode J_0 , and the amplitude is small because this mode has not resonated. At 425 MHz the amplitude of the radiated field increases, since mode J_1 is near its reso-

nant frequency and the radiation pattern is hence due to this mode. Finally, near the second resonance of the structure, the radiation pattern corresponds to that exhibited by mode J_3 .

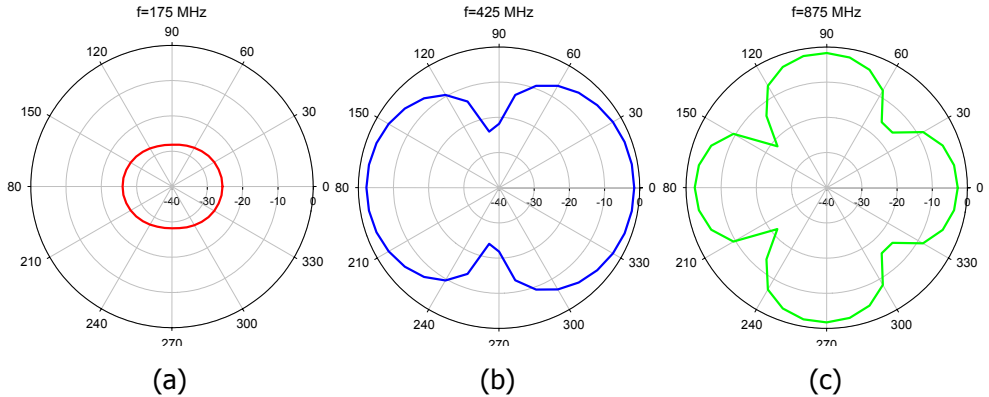


Figure 4.8 E_ϕ radiation pattern in the XY plane, for the wire circular loop antenna with a voltage source located at $\phi=0^\circ$, at three different frequencies: (a) 175 MHz; (b) 425 MHz; (c) 875 MHz.

Alternatively, if the voltage gap source is located at $\phi=90^\circ$, modes having no nulls of current at this position will be excited, i.e. modes J_0 , J_2 and J_3 . This fact can be observed clearly in Figure 4.9, where the modal admittances as well as the total input admittance have been represented.

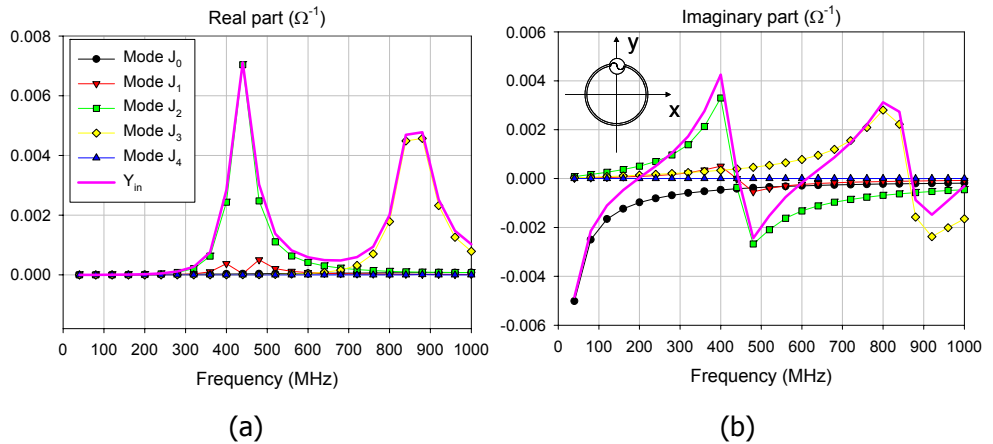


Figure 4.9 Contribution of the modal admittances Y_n to the input admittance Y_{in} when a voltage source is located at $\phi=90^\circ$. (a) Real part; (b) Imaginary part. Legend is common to both plots.

Although in this case mode J_2 is excited instead of mode J_1 , it can be observed in Figure 4.7 and Figure 4.9 that the total input admittance has not changed at all. This is due to the fact that modes J_1 and J_2 are degenerated modes, and they present the same radiating behavior, as portrayed by their characteristic angle curves in Figure 4.5. The excitation of one mode or the other affects mainly the total current distribution over the loop in the proximity of their resonant frequency ($f=440$ MHz), and hence the radiation pattern, which is represented in Figure 4.10 for three different frequencies. By comparing with the previous case, when exciting mode J_1 or mode J_2 two different and orthogonal radiation patterns will be obtained near the resonant frequency of the mode (440 MHz).

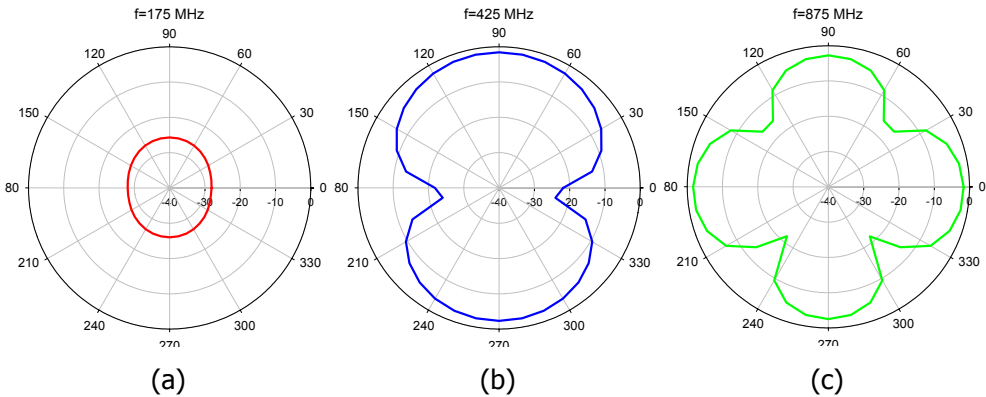


Figure 4.10 E_ϕ radiation pattern in the XY plane, for the wire circular loop antenna with a voltage source located at $\phi=90^\circ$, at three different frequencies: (a) 175 MHz; (b) 425 MHz; (c) 875 MHz.

Finally, if it is desired to avoid mode J_3 and excite mode J_4 , the voltage gap source should be placed in a point where a low current level of mode J_3 is present. In this case, $\phi=45^\circ$ would be a good location for the feeding point, as derived from the modal current distributions shown in Figure 4.3. Figure 4.11 shows once again the contribution of each mode to the total input admittance when $\phi=45^\circ$ is selected as the feeding point. As desired, mode J_3 is now prevented from excitation, while modes J_0 , J_1 , J_2 and J_4 are excited. It is also noticed in Figure 4.11 that degenerated modes J_1 and J_2 are equally excited at their resonant frequency, implying that the radiated power is divided between these two orthogonal modes at 440 MHz.

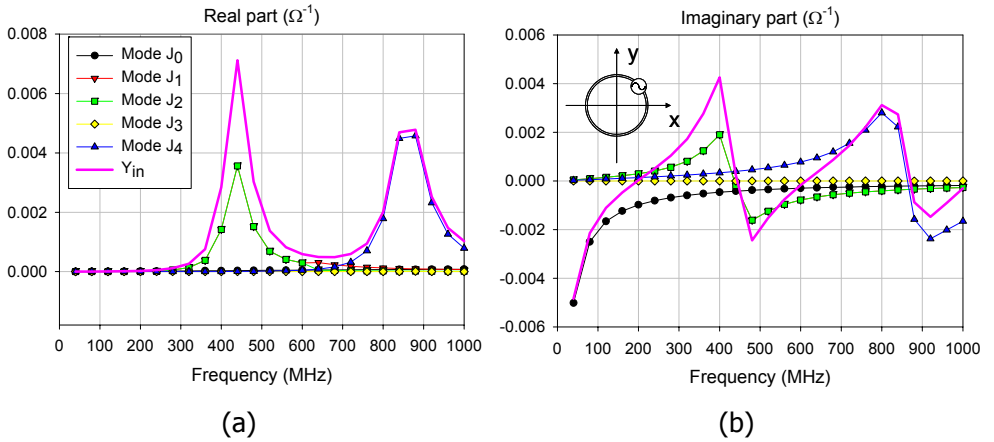


Figure 4.11 Contribution of the modal admittances Y_n to the input admittance Y_{in} when a voltage source is located at $\phi=45^\circ$. (a) Real part; (b) Imaginary part. Legend is common to both plots.

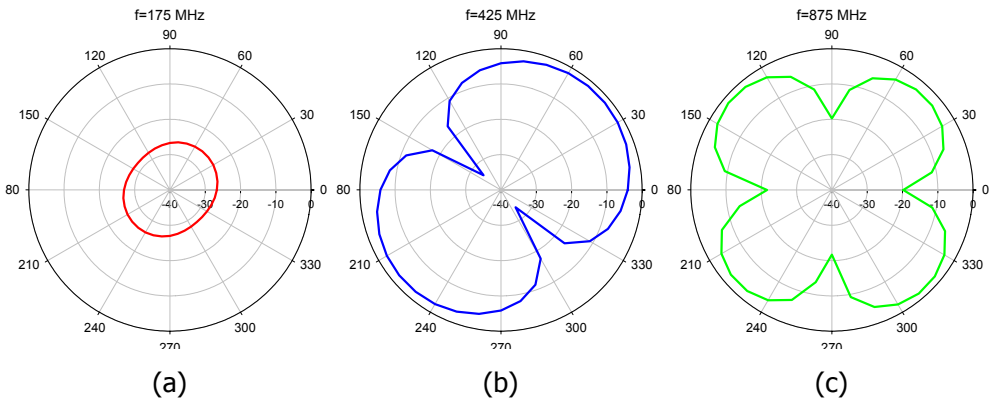


Figure 4.12 E_ϕ radiation pattern in the XY plane, for the wire circular loop antenna with a voltage source located at $\phi=45^\circ$, at three different frequencies: (a) 175 MHz; (b) 425 MHz; (c) 875 MHz.

Moreover, the radiation patterns for this case are shown in Figure 4.12, for three different frequencies. As observed, at 425 MHz the radiation pattern is due to the combination of the modes J_1 and J_2 , whereas at 875 MHz the radiation pattern is that of mode J_4 , as expected.

It has been observed that for the three feeding cases ($\phi=0^\circ$, $\phi=90^\circ$ and $\phi=45^\circ$), the input admittance is the same, whichever the modes excited. This is due to the fact that in every case, excited modes belong to a degenerated pair. Figure 4.13 shows the resulting input impedance for the circular loop with one feeding source. In the figure, it is possible to identify the resonances and anti-resonances of the structure defined according to [55], which -as shown- are linked to the excitation of characteristic modes. As observed, resonances of the structure are those associated to the modes ($f=440$ MHz for the first mode, and $f=860$ MHz for the second mode), whereas anti-resonances are caused by the transition from a mode that has already resonated to the next one that will start resonating when the frequency increases. Therefore, if the transition from one mode to the next resonant mode is abrupt, strong anti-resonances appear, which lead to high values of resistance, thereby decreasing the impedance bandwidth of the structure. This fact can be observed in the zoom plot of the input impedance in Figure 4.13b, where two strong anti-resonances occur at 170 MHz and 880 MHz.

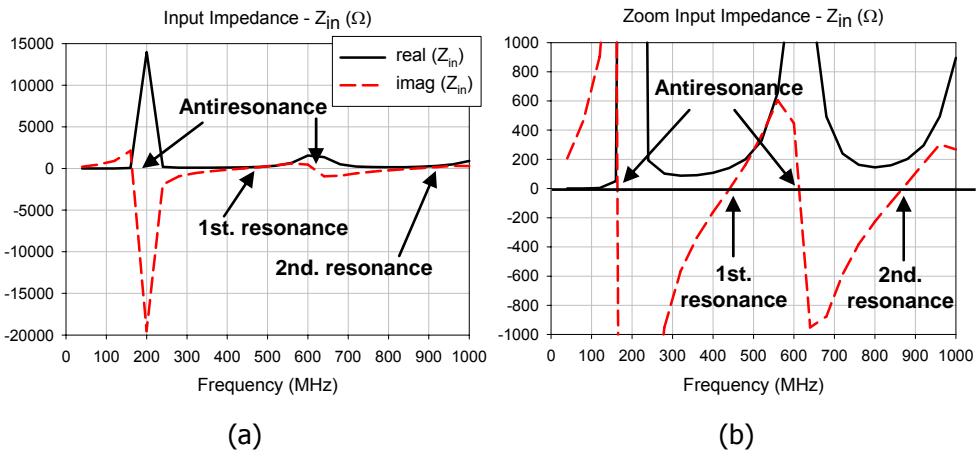


Figure 4.13 (a) Total input impedance for the wire circular loop antenna, excited at $\phi=0^\circ$, $\phi=90^\circ$ or $\phi=45^\circ$; (b) Zoom of the input impedance curve. Legend is common to both plots.

Therefore, the examples provided in this section clearly point out the importance of the feeding position for the excitation of characteristic modes. The coupling between the voltage source and the modal current at the feeding location strongly determines the significance of the mode on the radiating behavior of the antenna.

So far the effect of the placement of one single source within the structure has been analyzed. However, by taking into account the symmetry properties exhibited by the wire loop modes (Figure 4.4), it may be assumed that a more precise con-

trol on the excitation of characteristic modes could be gained if more than one excitation port was properly located in the structure. Next section is aimed at investigating this aspect.

4.2.2.2. Excitation of the wire loop with multiple sources

In previous section, it has been observed that when locating a single source anywhere along the wire structure, excitation of multiple modes is forced, when a wide frequency range is considered. Moreover, due to the current distribution exhibited by mode J_0 , its presence is unavoidable if only one source is used to excite the antenna. Hence its inductive behavior is always present in the input impedance.

The use of multiple sources in the antenna allows though to prevent the excitation of higher order modes in the structure, as well as the excitation of mode J_0 , if a proper arrangement of the feeding sources is carried out. When multiple sources are used to excite the structure, different phases can be applied to these sources in order to gain control of the modal excitation, by means of the application of symmetry conditions over the structure that excited modes have to meet.

Thus, if two voltage gap sources are placed at $\phi=0^\circ$ and $\phi=180^\circ$ with the same amplitude and phase, excitation of odd modes with respect to the y-axis will be imposed. Figure 4.14 shows the contribution of each mode to the total admittance, computed at each port.

As observed, by means of the symmetry conditions imposed in the structure by the arrangement of the sources, only mode J_1 is excited in the frequency range considered. Excitation of modes J_0 and J_3 , which appeared formerly when using a single port at either 0° or 90° , is now prevented. Additionally, the radiation pattern in the XY plane is depicted in Figure 4.15, for three different frequencies. In contrast to the previous cases, the radiation pattern of mode J_1 is present in a wider frequency range. However, the next higher order mode starts to appear at 875 MHz, as portrayed by the figure.

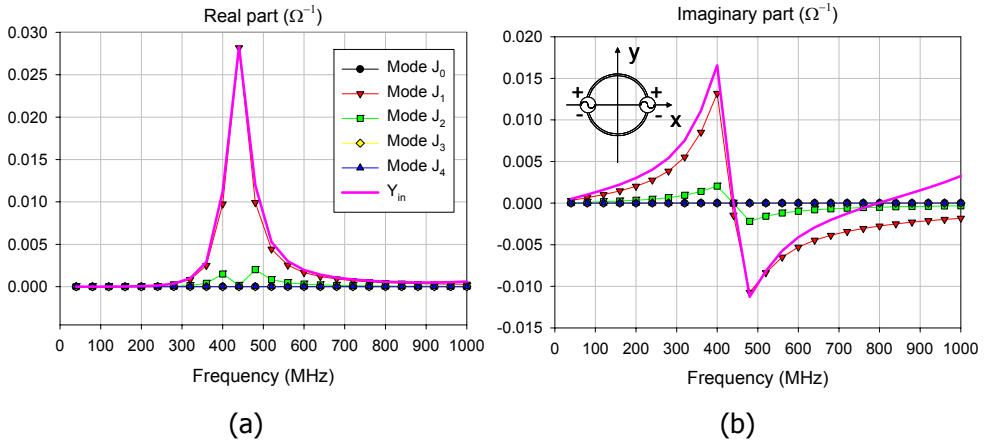


Figure 4.14 Contribution of the modal admittances Y_n to the input admittance Y_{in} when two voltage sources with the same phase are located at $\phi=(0^\circ;180^\circ)$: (a) Real part; (b) Imaginary part. Legend is common to both plots.

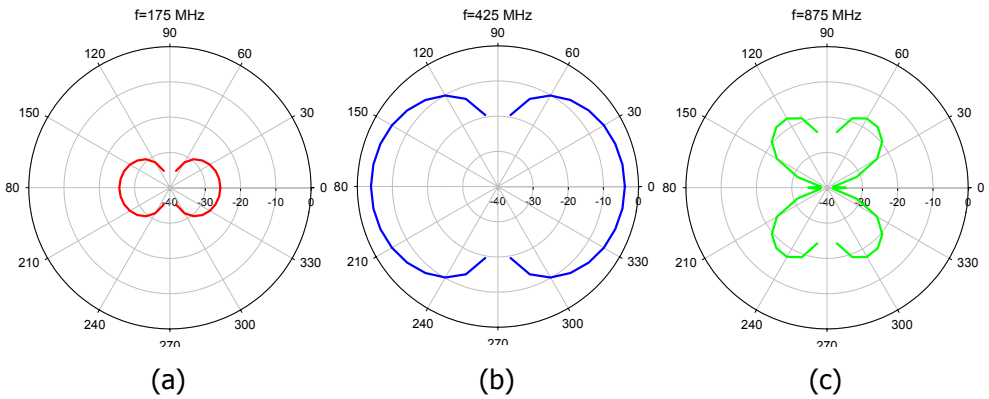


Figure 4.15 E_ϕ radiation pattern in the XY plane, for the wire circular loop antenna with two voltage sources located at $\phi=0^\circ$ and $\phi=180^\circ$, at three different frequencies: (a) 175 MHz; (b) 425 MHz; (c) 875 MHz.

The excitation of a single mode over a wide frequency range in the structure is especially interesting when dealing with modes having higher radiating bandwidth, since the presence of a second mode can provoke a strong anti-resonance that can degrade the bandwidth of the excited structure. In the present case, as the modes are narrowband, slight improvement of the matching bandwidth is observed. This will be shown later.

In case the two feeding sources are located at the same position as in the previous case, but fed with an opposite phase, the result obtained is shown Figure 4.16. In this case, even symmetry with respect to y-axis is imposed over the structure, and hence modes J_0 and J_4 are now excited within the frequency range considered. Again, the radiation pattern in the XY plane at three different frequencies is shown in Figure 4.17, where it is clearly visible that the eigenpattern of mode J_0 remains as the dominant contribution at lower frequencies.

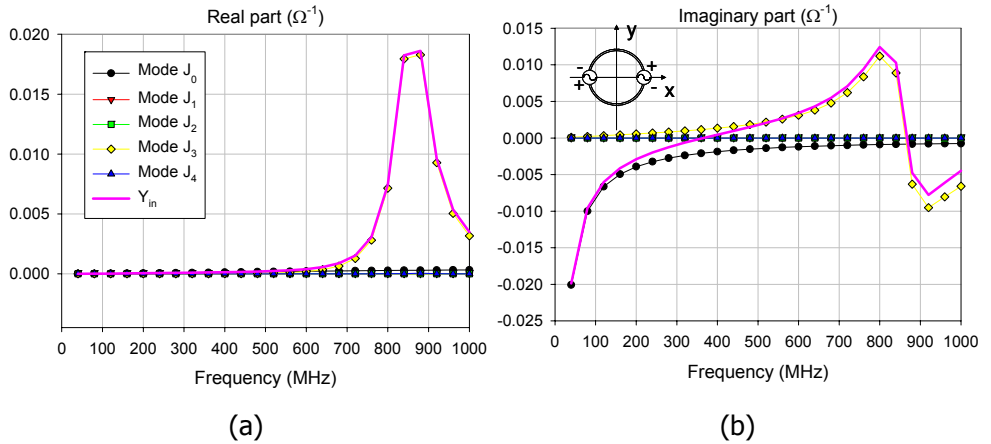


Figure 4.16 Contribution of the modal admittances Y_n to the input admittance Y_{in} when two voltage sources are located at $\phi=(0^\circ;180^\circ)$ with opposite phases: (a) Real part; (b) Imaginary part. Legend is common to both plots.

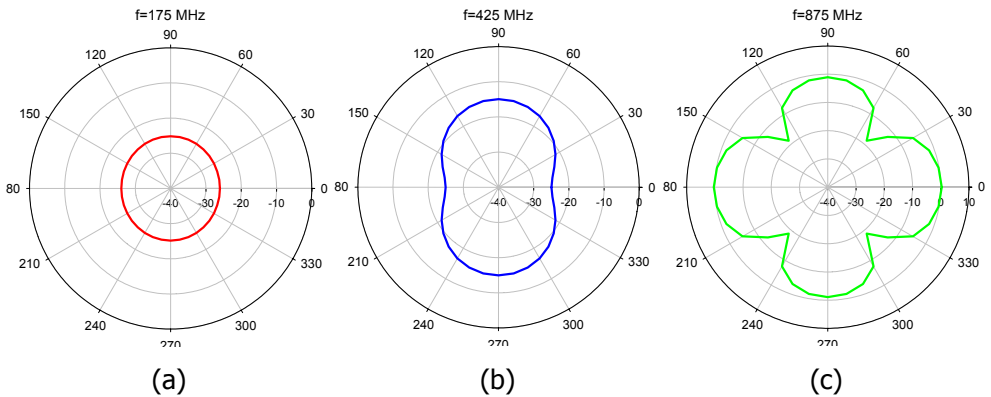


Figure 4.17 E_ϕ radiation pattern in the XY plane, for the wire circular loop antenna with two voltage sources located at $\phi=0^\circ$ and $\phi=180^\circ$, at three different frequencies: (a) 175 MHz; (b) 425 MHz; (c) 875 MHz.

As commented previously, the excitation of a single mode over a wide frequency range in the structure can improve the impedance bandwidth obtained. This fact is especially interesting when dealing with modes having higher bandwidth. In the present case, where narrowband modes exist, only a slight improvement in the impedance bandwidth is obtained. This can be observed in Figure 4.18, where the return loss of the circular loop antenna is represented for a single feed (at $\phi=0^\circ$, $\phi=90^\circ$ or $\phi=45^\circ$), for two feeds with the same phase and for two feeds with opposite phase.

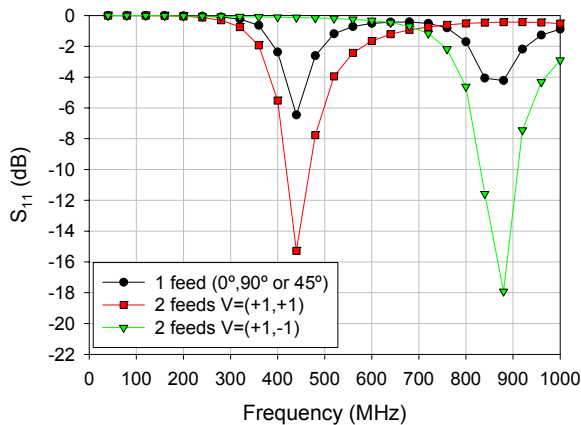


Figure 4.18 Return loss for the circular loop antenna shown in Figure 4.2, when using a single feed and two feeds with the same or opposite phases.

As observed, the impedance bandwidth is improved when exciting only a single mode, since the impedance matching is mainly degraded by the abruptness of anti-resonances occurring during the transitions from an inductive mode, which has already resonated, to a capacitive mode, which is the next to resonate. In general, the distance between two consecutive resonances is critical for good matching, as it determines the location of the anti-resonance that results from the transition from one mode to the next one.

Figure 4.19 plots the input impedance for the case of a single feed and two feeds with the same amplitude and phase. Here it can clearly be seen that for the case with two sources feeding, the input impedance near the resonant frequency of mode J_1 stays more stable than in the case of a single feed. In this latter case, the transition from mode J_1 to mode J_3 creates a strong anti-resonance that enormously increases the impedance level and degrades the impedance bandwidth.

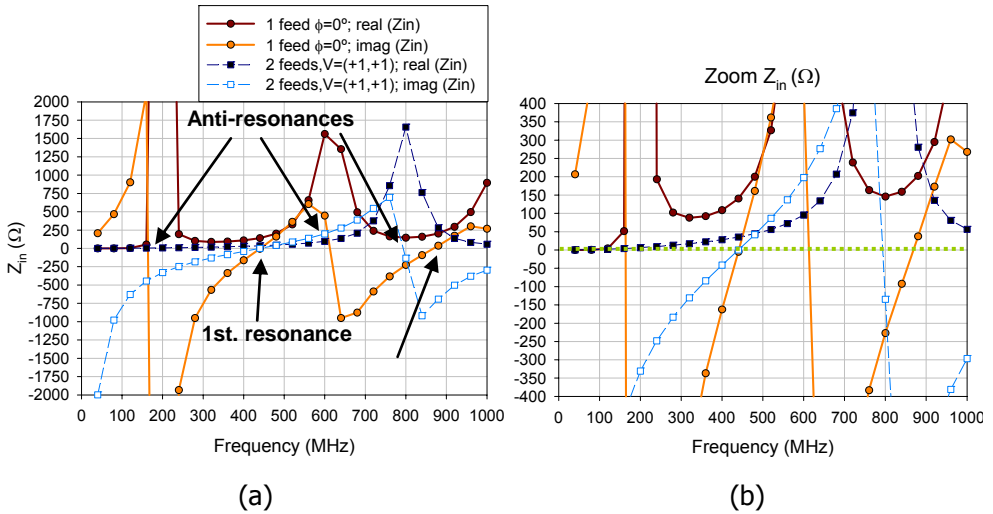


Figure 4.19 (a) Input impedance for the circular loop with one single feed located at $\phi=0^\circ$ and with two feeds located at $\phi=(0^\circ, 180^\circ)$ with the same amplitude and phase; (b) Zoom of the input impedance. Legend is common to both plots.

Finally, even more control on the modal excitation can be gained, by increasing the number of feeding points and selecting different phases for the ports. For instance, if four feeding points are located at $\phi=(0^\circ, 90^\circ, 180^\circ, 270^\circ)$ in the circular loop, as depicted in Figure 4.20, it is possible to impose different symmetry conditions by controlling the phases of the sources. Table 4.1 summarizes the different modes excited in the loop depending on the phases imposed, as well as the polarization obtained. For the sake of brevity, the table reflects the cases where at least two sources have amplitude equal to one. Some of the previously analyzed configurations are also reflected in Table 4.1.

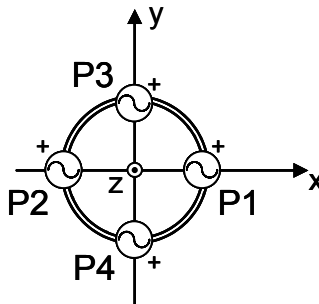


Figure 4.20 Wire circular loop with four feeding ports located at $\phi=(0^\circ, 90^\circ, 180^\circ, 270^\circ)$.

P1	P2	P3	P4	Excited Modes	Polarization
$1_{\angle 0^\circ}$	$1_{\angle 0^\circ}$	$1_{\angle 0^\circ}$	$1_{\angle 0^\circ}$	J_1, J_2	Linear
$1_{\angle 0^\circ}$	$1_{\angle 0^\circ}$	$1_{\angle 180^\circ}$	$1_{\angle 180^\circ}$	J_1, J_2	Linear
$1_{\angle 0^\circ}$	$1_{\angle 180^\circ}$	$1_{\angle 0^\circ}$	$1_{\angle 180^\circ}$	J_3	Linear
$1_{\angle 0^\circ}$	$1_{\angle 180^\circ}$	$1_{\angle 180^\circ}$	$1_{\angle 0^\circ}$	J_0	Linear
$1_{\angle 0^\circ}$	$1_{\angle 0^\circ}$	0	0	J_1, J_5	Linear
0	0	$1_{\angle 0^\circ}$	$1_{\angle 0^\circ}$	J_2, J_6	Linear
$1_{\angle 0^\circ}$	$1_{\angle 180^\circ}$	0	0	J_0, J_3	Linear
0	0	$1_{\angle 0^\circ}$	$1_{\angle 180^\circ}$	J_0, J_3	Linear
$1_{\angle 0^\circ}$	$1_{\angle 0^\circ}$	$1_{\angle 90^\circ}$	$1_{\angle 90^\circ}$	J_1, J_2	RHCP
$1_{\angle 90^\circ}$	$1_{\angle 90^\circ}$	$1_{\angle 0^\circ}$	$1_{\angle 0^\circ}$	J_1, J_2	LHCP

Table 4.1. Modes excited in the circular loop antenna shown in Figure 4.20, when different phases are imposed at the input ports (z is considered the direction of propagation).

Therefore, by adequately adjusting the phases of the feeding sources, different modes will be excited in the wire loop antenna. As discussed previously, the resulting radiation patterns will change depending on the excited modes. Consequently, and due to the orthogonality of the radiation patterns of characteristic modes, this multimode antenna could be a good candidate to be employed in Multiple-Input Multiple-Output (MIMO) applications. It is well known that MIMO systems offer high spectral efficiencies through space time coding and spatial multiplexing techniques, which permit these systems to obtain higher capacity rates compared to conventional systems [56]. Generally, MIMO systems employ multiple antennas at both ends of a wireless link, what requires an extra volume and could be troublesome for modern compact handsets. Therefore, more compact solutions based on the use of a multimode antenna (as the one shown here) are an attractive alternative [57][58].

4.2.3. Reactive loading to control characteristic modes

In [59] and [60], Harrington proposes the use of reactive loading, together with the Theory of Characteristic Modes, to control the radiation and scattering of conducting bodies. Thus, any desired characteristic mode can be resonated by reactive loads to make it the dominant mode current of the body at a certain frequency,

and therefore, if no other mode is near resonance, the radiation pattern becomes nearly the same as that of the resonated current [59]. Therefore, control over the resonance of the characteristic modes can easily be gained by reactive loading the conducting structure.

As stated in [17], the use of reactive loads in the structure does not alter the mathematical properties of characteristic modes, i.e., eigencurrents and eigenvalues remain real and orthogonality relationships of characteristic modes also remain unchanged.

Consequently, by properly using discrete loads over the structure, the resonant frequency of specific modes can be changed, while minimizing the effect over the rest of the modes. For the sake of illustration, let us insert two discrete loads of value $Z=j450 \Omega$ over the wire circular loop studied in the previous sections. The loads will be placed symmetrically at $\phi=\pm 90^\circ$ in order to preserve the symmetry of the structure, and a single feeding will be used at $\phi=0^\circ$, as depicted in Figure 4.21.

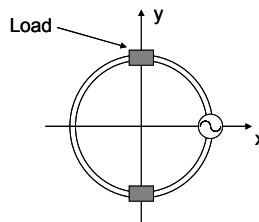


Figure 4.21 Wire circular loop antenna with two loads located at $\phi=\pm 90^\circ$.

Similarly as for excitation, the placement of loads over the structure will not affect those modes whose amplitude is low at the location of the loads. Therefore, if the two loads are placed at $\phi=\pm 90^\circ$, they will only affect the resonant frequency of modes J_2 and J_3 , within the range of frequencies previously considered. This can be observed in Figure 4.22, where the characteristic angle variation with frequency for the characteristic modes of the loaded structure is shown. As seen in the figure, the insertion of loads at $\phi=\pm 90^\circ$ shifts down the resonant frequency of modes J_2 and J_3 , while slightly reducing their bandwidth, whereas the rest of modes remain unmodified.

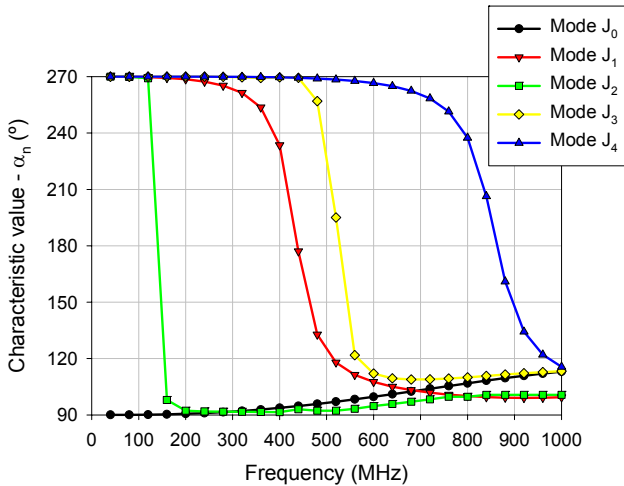


Figure 4.22 Variation with frequency of the characteristic angle associated to the eigenmodes of the structure shown in Figure 4.21.

As the resonant frequency of mode J_2 decreases, reactive loading can be used as a technique to compact the antenna, as proposed in [61]. Moreover, this can also be used to increase the impedance bandwidth of the structure, by locating the resonant frequency of one mode close to the resonant frequency of another one. This happens in the present case with modes J_1 and J_3 , whose resonant frequencies are very close to each other, as shown in Figure 4.22. The impedance bandwidth of the structure can hence be increased by combining the resonances of these two modes, as carried out also in [62]. Additionally, circular polarization can be provided by using reactive loading and a single source, if one mode of a degenerated pair is properly shifted to achieve a 90° phase difference with the other one, and both are excited with the same amplitude. The procedure is explained in detail in [17], and extensive use of this technique for obtaining circular polarization has recently been applied to annular slot antennas [63][64].

In the last decades, other applications have also benefited from the use of reactive loading [65]-[67]. In next chapter, however, a new application will be proposed which is based on the use of reactive loading to control the resonant mode of a slot embedded in a wideband structure. This will allow to vastly increase the functionality of the antenna, especially in case electronic control is provided.

4.3. Modal excitation in planar antennas

In this section, modal excitation in more complex structures, such as planar antennas, will be investigated, and novel designs based on the use of multiple feeding configurations will be presented, in order to obtain antennas with both wideband behavior and polarization agility.

Planar antennas, such as microstrip, printed antennas or planar monopoles have attracted much interest during the last decade, due to their attractive features of low profile, small size, ease of fabrication and conformability to mounting hosts [2]. Moreover, due to the rapid growth of wireless communications, compact and broadband design techniques for planar antennas have focused much attention from antenna researchers in recent years.

Planar structures in free space exhibit much wider radiation bandwidth than wire antennas [68]. Therefore, with an efficient excitation of the radiating modes associated to the planar structure, wideband behavior can be obtained. The present section is focused on modal excitation for a specific type of planar antennas: the planar monopoles. In chapter 6, investigations concerning the excitation of modes in other planar structures will be performed.

Planar monopoles are well-known antennas that have long been used in mobile communications, due to their wide impedance bandwidth, omnidirectional radiation pattern, compact and simple structure, low cost and ease of construction. Several planar monopole geometries providing wide impedance bandwidth, such as circular, elliptical, square, rectangular, hexagonal and pentagonal, have been proposed by different authors [69]-[75]. Some of these geometries are shown in Figure 4.23.

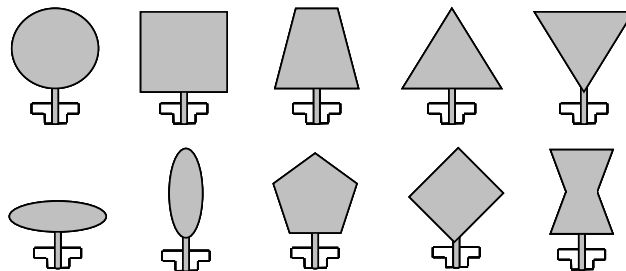


Figure 4.23 Different geometries for planar monopole antennas.

Among all of these configurations, the circular monopole and the elliptical monopole fed along the major axis were reported to yield maximum bandwidth [72]. However, in [70] it has been shown that, although the square monopole provides smaller bandwidth than the circular monopole, its radiation pattern suffers less degradation within the impedance bandwidth. Diverse slight modifications of the geometry of the square planar monopole antenna have been proposed in the literature, in order to increase its impedance bandwidth. They consist mainly in adding a shorting pin, using an off-centered feeding or employing diverse bevel angles on one or both sides of the base [76]-[78].

Although experimental results are widely provided in the references, an in-depth analysis explaining the behavior of such antennas can not be found in the literature. An analysis based on the Theory of Characteristic Modes provides deep physical insight into the behavior of this kind of antennas. Moreover, using these modes it can be demonstrated that with a proper feeding configuration, the impedance bandwidth of the square monopole can be hugely increased, being comparable to that provided by the circular monopole, while also improving polarization purity.

In the following section, characteristic modes associated to a rectangular plate in free space will be revisited [17], in order to identify the modes with more interesting properties to be excited when considering a square planar monopole. Subsequently, different experiments regarding the feeding will be carried out.

4.3.1. Characteristic modes in a rectangular conducting plate

In [17], the characteristic modes of a rectangular conducting plate of width $W=40$ mm and length $L=60$ mm, in free space, were presented. Figure 4.24 illustrates the current distribution of the first six characteristic modes at the first resonance ($f=2.3$ GHz), where all currents have been normalized to its maximum value in order to facilitate comparison. For a better understanding, Figure 4.25 additionally yields the current schematics for these six current modes. As observed, eigenvector J_0 forms a closed loop over the plate and it can be identified as one of the non-resonating modes, of inductive nature. Eigenvectors J_1 and J_2 , which are characterized by horizontal and vertical currents respectively, are the most frequently used modes in patch antenna applications, while the rest of eigenvectors, J_3 , J_4 and J_5 , are higher order modes that might be taken into consideration only at higher frequencies. Radiation patterns associated to each mode are provided in Figure 4.26.

Observe that these modes exhibit current distributions similar to those presented in chapter 3 for a conducting strip, i.e. singularities at the longer sides of the plate

for the longitudinal mode J_1 and nulls of current for the transversal mode J_2 , with nulls appearing for higher order modes. Nevertheless, since the strip has finite length in this case, longitudinal and transversal currents are coupled and they are not exactly the same as those of the infinite strip. Nonetheless, the higher the aspect ratio (L/W) of the rectangular plate, the closer current distributions will be to those presented in chapter 3 for the infinite metallic strip.

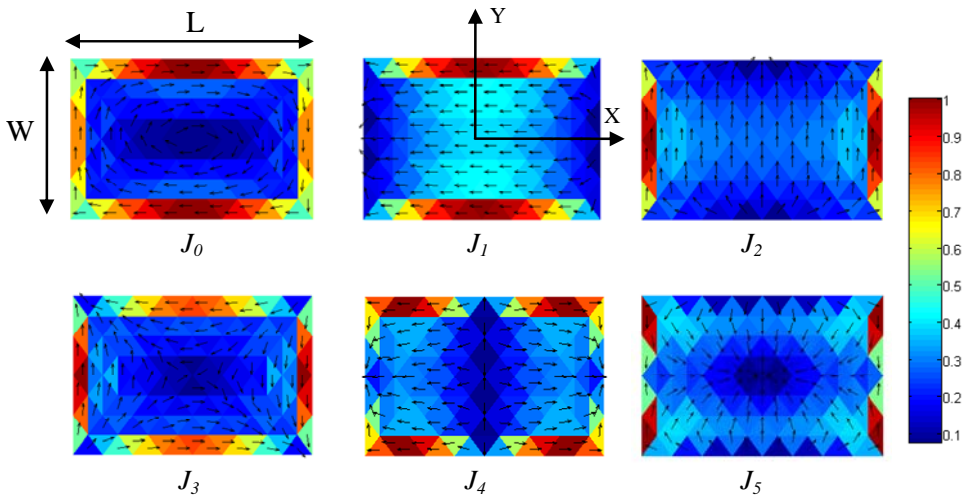


Figure 4.24 Normalized current distribution at first resonance ($f = 2.3$ GHz) of the eigenvectors J_n of a rectangular plate of width $W=40$ mm and length $L= 60$ mm.

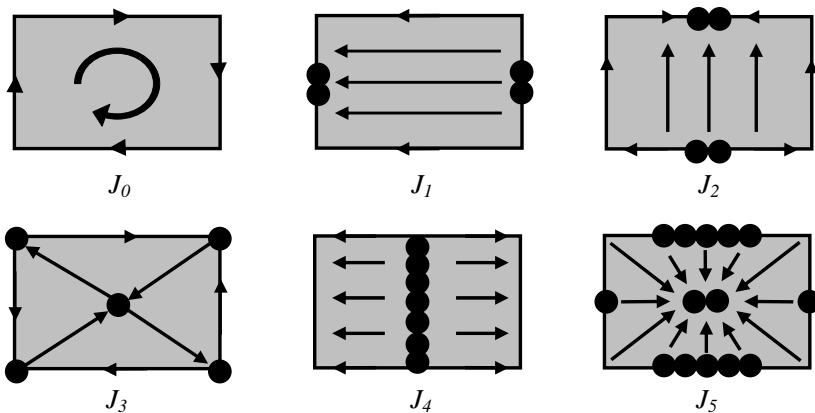


Figure 4.25 Current diagrams of the six characteristic modes shown in Figure 4.24 (black dots refer to nulls of current).

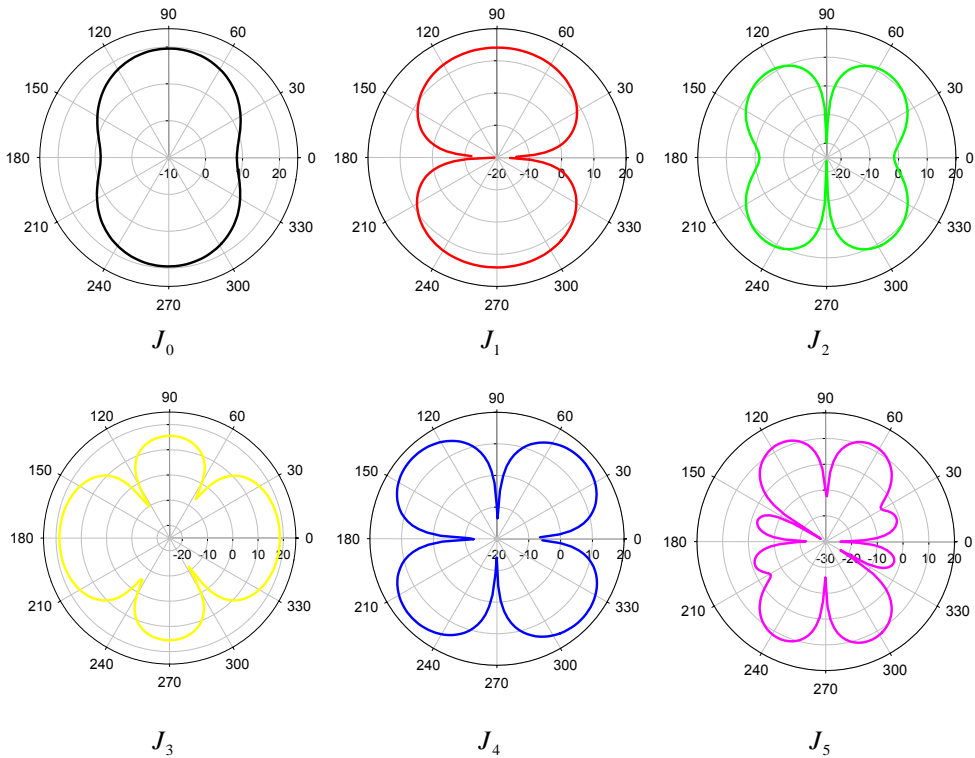


Figure 4.26 Radiation pattern in the XY plane of the modal electric fields $E_{\phi,n}$ at 4 GHz, produced by the characteristic modes J_n depicted in Figure 4.24.

It is worth noting that eigenvectors presented in Figure 4.24 have been computed in free space. The presence of a ground plane below the plate would not significantly alter their current distribution, but it would affect their resonance and radiating bandwidth [79]. It must also be noted that due to dependency of eigenvectors upon frequency, if a structure is to be analyzed in a different frequency range, modes need to be recalculated at every frequency [80].

Figure 4.27 presents the variation with frequency of the characteristic angle α_n associated to the six current modes of the rectangular plate presented before. Table 4.2 shows the resonant frequency corresponding to each mode, which is obtained when the characteristic angle is $\alpha_n = 180^\circ$. The special nature of the non-resonant inductive mode J_0 can be appreciated in the figure.

	Mode J_1	Mode J_2	Mode J_3	Mode J_4	Mode J_5
f_r (GHz)	2.3	4.9	4.1	5.6	9.9

Table 4.2. Resonant frequency (f_r) for each of the characteristic modes of the rectangular plate, in free space.

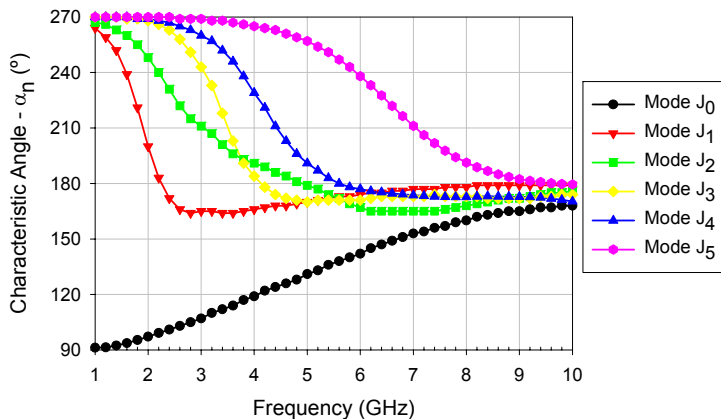


Figure 4.27 Characteristic angle variation with frequency for the current modes of a rectangular plate of width $W=40$ mm and length $L=60$ mm, in free space.

As stated before, all modes exhibit broad radiating bandwidth, since their characteristic angle curves are close to 180° in a wide frequency range after resonance, in contrast with the wire loop antenna, where the characteristic modes exhibited narrowband behaviour. In this case, the impedance bandwidth of the antenna at the input port will depend not only on the wideband behaviour of each mode, but also on the transition from one mode to the other. Note that when a frequency sweep is carried out, excited modes resonate successively, so a feeding mechanism that properly combines the excitation of the modes and the transition from one mode to another is necessary for wideband matching.

In the next section, the excitation of a square planar monopole antenna will be analyzed for diverse feeding configurations.

4.3.2. Excitation of a square planar monopole antenna

Let us consider a square planar monopole analyzed from an image theory point of view. As shown in Figure 4.28(a) the monopole can be modeled as a planar plate with two narrow slits that account for the feeding gap. In this case, the geometry of the antenna is not exactly the same as that of a rectangular plate, whose characteristic modes have been shown to exhibit wideband radiating properties. Indeed, these slits at the center of the rectangular plate force the current to meander around them, leading to a decrease of the resonant frequency, but the strong horizontal component of the current degrades the polarization and bandwidth of the antenna. This effect is well-known from microstrip antenna design, where current meandering is a technique widely used to obtain compact antennas [3].

This assessment is verified by Figure 4.28, which illustrates the current distribution of the vertical current mode at resonance for a rectangular plate of dimensions 85 mm x 40 mm, with and without slits. The vertical current mode of the slitted structure resonates at 1.3 GHz, and presents horizontal current flow near the slits, while the vertical current mode of the complete rectangular plate resonates at a higher frequency, 1.6 GHz, and displays pure vertical currents. Moreover, currents in the rectangular plate are noticeably more intense than in the slitted version, for the same color scale.

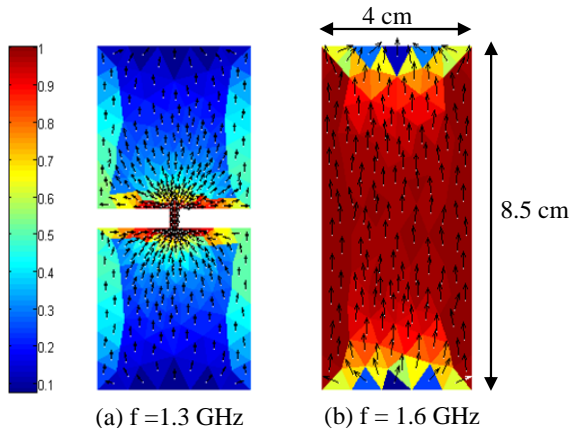


Figure 4.28 Normalized current distribution at resonance of the vertical current mode of a rectangular plate of dimensions 8.5 cm x 4 cm: (a) With slits, (b) Without slits.

In Figure 4.29 the plots of the characteristic angle versus frequency for each structure are represented. These curves demonstrate that the vertical current mode of the rectangular plate offers broader radiating bandwidth than in the slitted plate,

since its associated characteristic angle stands near 180° in a wider frequency range. Moreover, these results imply that the bandwidth performance of the square monopole would improve if a feeding configuration capable of enforcing intense vertical currents in the structure while diminishing horizontal currents in the base of the monopole is applied.

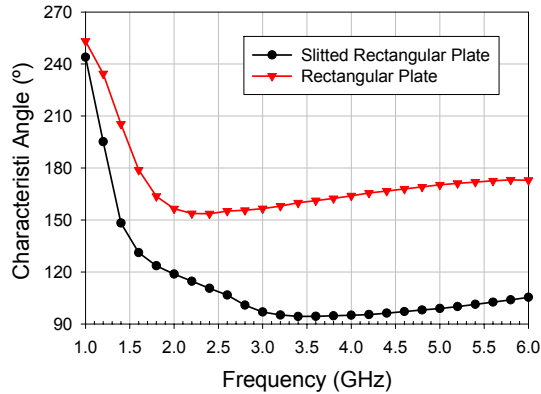


Figure 4.29 Characteristic angle versus frequency curves obtained for the rectangular plates presented in Figure 4.28.

Therefore, in order to reinforce the excitation of the vertical current mode J_1 in the structure, two excitation points (instead of a single one) can be placed symmetrically in the base of the monopole, as depicted in Figure 4.30(a). Once again, the geometry of the structure is modified, but since it is closely similar to the rectangular plate, the characteristic angle associated to the vertical current mode exhibits improved behavior compared to the slitted rectangular plate. This can be observed in Figure 4.30(b), where the characteristic angle vs. frequency of the vertical mode J_1 is represented for all three structures. In contrast, the properties of horizontal mode J_2 will be the same in the three structures, since its current distribution is not disturbed by the insertion of the slits [81]. However, the grade of excitation of this mode will differ depending on the feeding configuration employed, as it will be seen next.

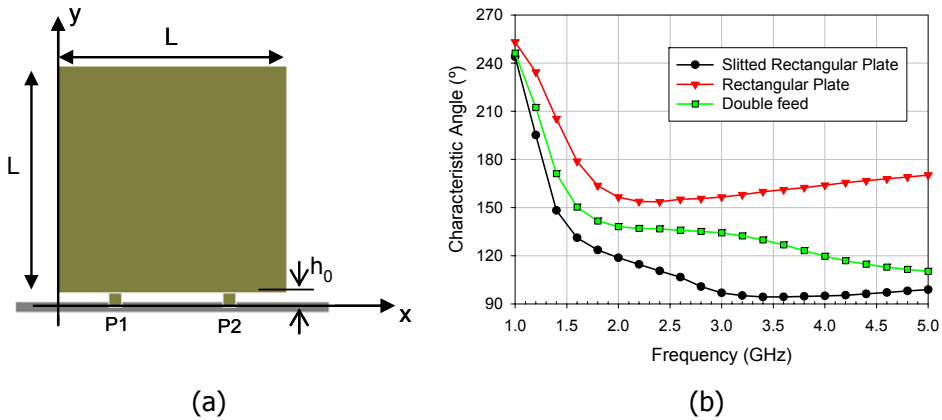


Figure 4.30 (a) Geometry of the square planar monopole with two strips at its base that account for the ports ($L=40$ mm; $h_0=2.5$ mm); (b) Comparison of the characteristic angle vs. frequency of the vertical mode J_z for the three structures.

Figure 4.31 shows a comparison of the absolute value of the total current in the surface of the planar monopole at 2 GHz, when a double feeding and a single feeding configuration are used, for cuts at $y=h_0+2$ mm and $y=h_0+4.5$ mm. These current distributions have been obtained with the electromagnetic simulation software CST Microwave Studio™. As observed, the horizontal component of the total current (J_x) is diminished when a double feed configuration is used, especially at the central part of the monopole, where a null is forced. As long as the current flows far enough from the excitation points ($y=h_0+4.5$ mm), it can be observed that the horizontal component (J_x) has significantly decreased at the centre of the monopole, whereas the vertical component (J_y) shows a much uniform distribution over the surface of the monopole, as desired for the vertical mode excitation. A similar behaviour is obtained for other frequencies.

In the figure, the singularity of the current at the excitation points can also be noticed. It is observed that component J_y presents a peak of current at the position of the feeding points, that decreases rapidly when coordinate y increases, due to the fact that evanescent modes created at the feeding point discontinuity almost disappear after a small distance from the excitation points.

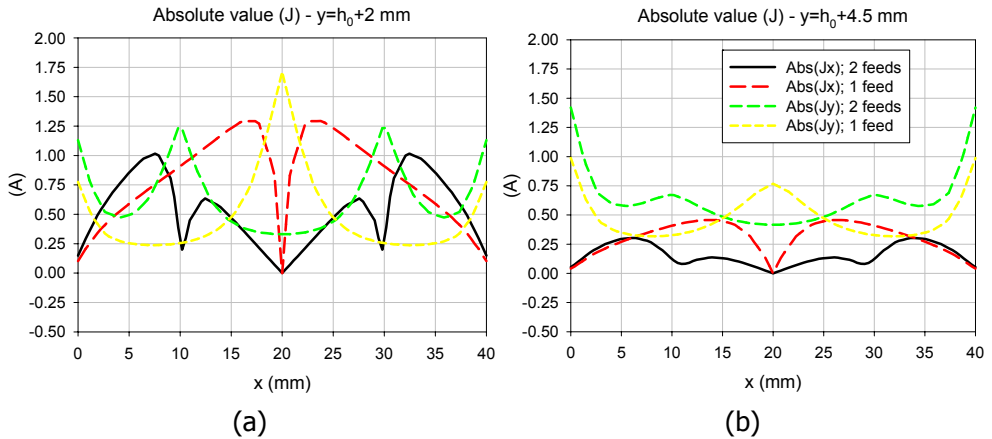


Figure 4.31 Comparison of the absolute value of the total current distribution vectors on the surface of the square planar monopole antenna, excited at one and two points of its base, for cuts at (a) $y=h_0+2$ mm; (b) $y=h_0+4.5$ mm. Frequency is 2 GHz.

Furthermore, the current distribution of the first four characteristic modes of this structure is also represented at first resonance ($f=1.3$ GHz) in Figure 4.32. As expected, the modal current distributions in the square planar monopole with two feeding ports are very similar to those of the rectangular plate previously shown.

Moreover, Figure 4.33 shows the contribution of the modal admittances to the total input admittance, for the square planar monopole antenna excited at two points symmetrically distributed in its base. As it can be noticed in the figure, through the use of the two feeding points, vertical current mode J_1 is strongly excited over the structure for a wide frequency range, what does not occur in other square planar monopoles such as the ones with a single feed, with an off-centred feed or with a shorting pin. A detailed modal excitation study of this kind of monopoles can be found in [17] and [82]. At 3.7 GHz, mode J_3 resonates and also contributes to radiation in the structure, whereas modes J_0 and J_2 are not excited at all within the whole frequency range.

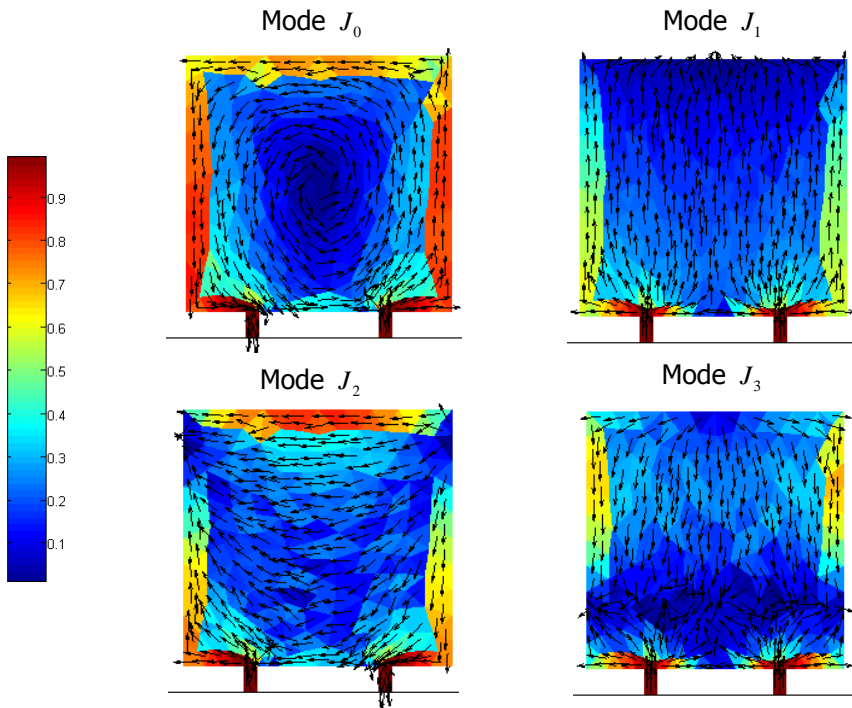


Figure 4.32 Normalized current distribution at first resonance ($f = 1.3$ GHz) of the first four eigenvectors J_n of the square planar monopole shown in Figure 4.30(a).

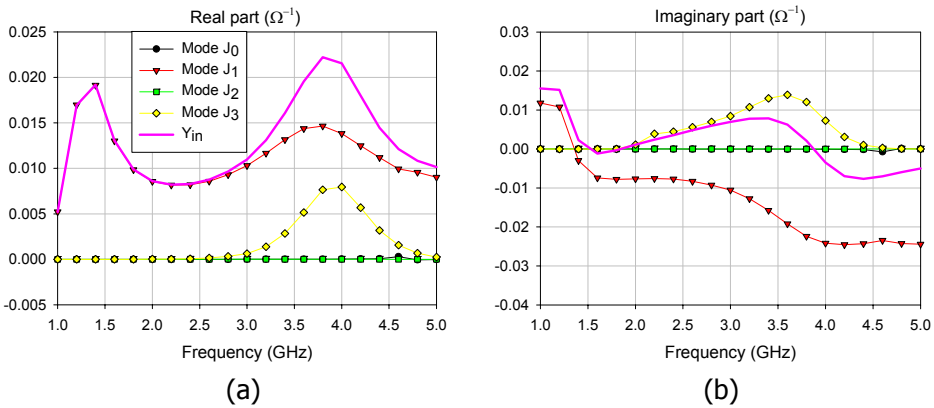


Figure 4.33 Contribution of the modal admittances Y_n to the input admittance Y_{in} for the double-fed square planar monopole. Legend is common to both plots.

These modal admittances have been obtained at each port of the structure. Due to the symmetrical distribution and equal phase of the two ports, the same admittances are obtained at each one, i.e. $Y_{in1} = Y_{in2}$. Furthermore, the input impedance vs. frequency computed at each input port is depicted in Figure 4.34(a). It can be noticed that input impedance values do not suffer strong variations within the considered frequency range, hence leading to a very high impedance bandwidth. In Figure 4.34(b) the return loss calculated for two different reference values of characteristic impedance is plotted. It can be seen that the impedance at the input ports is better matched for a value of $100\ \Omega$ than for $50\ \Omega$, hence yielding a high impedance bandwidth. Therefore, if a $50\ \Omega$ cable is used to feed the antenna, a wideband matching network should be implemented to obtain high impedance bandwidth and to take the most of the characteristic modes performance.

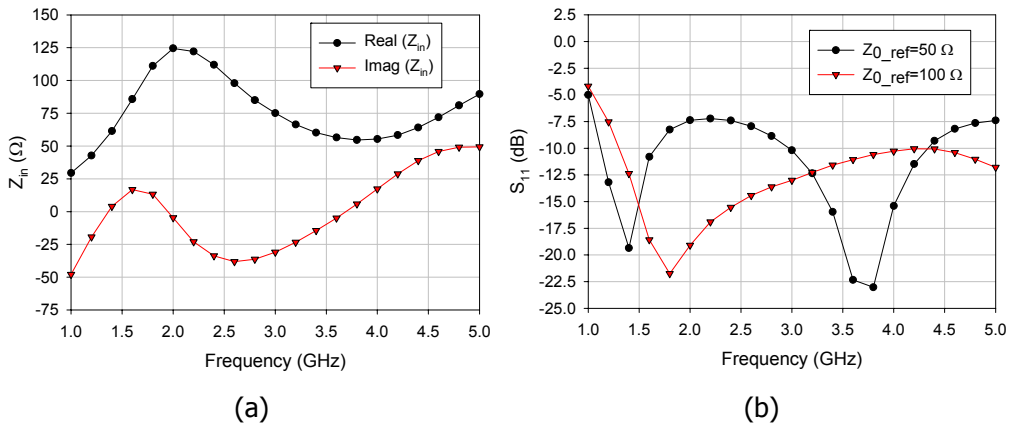


Figure 4.34 (a) Input impedance at each port of the double-fed square planar monopole antenna; (b) Return loss obtained for different values of reference impedance.

Since planar monopole antennas are usually fed by means of a single port, a feeding network has to be implemented in order to properly excite the antenna at the two ports, implementing also a wideband matching for the $100\ \Omega$ impedance of each input port.

4.3.2.1. Practical implementation of the double feed mechanism

In order to excite the structure with a single port, a feeding network has to be implemented, which must properly excite the monopole at the two symmetrical points at its base. Moreover, the feeding network must provide wideband imped-

ance matching to the $100\ \Omega$ impedance presented by the structure at both excitation points, in order to provide wideband behavior.

Therefore, a simple microstrip power divider can be used to feed the planar monopole. As the divider network is aimed at supplying power at two points of the same antenna, it is only necessary to take into account the bandwidth of the S_{11} and S_{12}/S_{13} parameters of the structure. Moreover, the characteristic impedance of the output ports is $100\ \Omega$, as required by the antenna. Figure 4.35 shows the geometry of the proposed feeding network, which is located at $0.76\ \text{mm}$ over a $100 \times 100\ \text{mm}^2$ ground plane. Its S-parameters, simulated with electromagnetic simulation package Zeland IE3D™, are shown in Figure 4.36. As observed, S_{11} remains below $-10\ \text{dB}$ for a wide frequency range, whereas S_{12}/S_{13} is also approximately $-3\ \text{dB}$ within a high bandwidth, as desired. Therefore, taking into account these parameters, wideband behavior can be considered for the proposed feeding network.

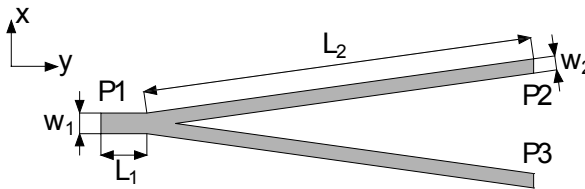


Figure 4.35 Geometry of the proposed feeding network.

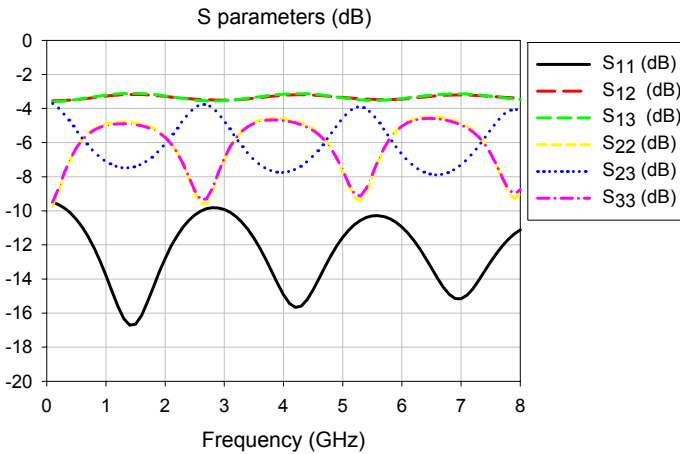
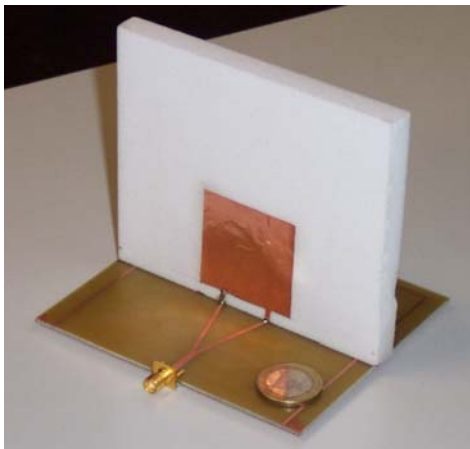


Figure 4.36 Simulated S-parameters of the feeding network.

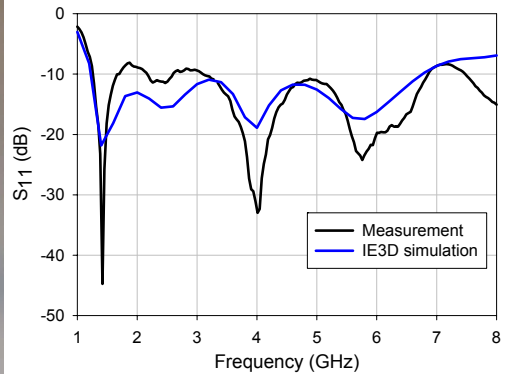
4.3.2.2. Results for the proposed antenna

Afterwards, a prototype of the antenna with the proposed feeding network has been fabricated and measured [83]. Figure 4.37(a) shows the prototype of the square planar monopole antenna with double feed, and Figure 4.37(b) depicts its simulated and measured return loss, showing a good agreement between them. As desired, very large bandwidth behavior is obtained with the proposed antenna.

Figure 4.38 compares the measured voltage standing wave ratio (VSWR) of the double-fed square monopole with that of a single-fed square monopole of the same dimensions. As it was expected from the previous discussion, when using a double-feed configuration the impedance bandwidth of the square monopole is notably improved.



(a)



(b)

Figure 4.37 (a) Prototype of the square monopole with double feed; (b) Comparison of simulated and measured results for the return loss referred to 50Ω , of the antenna prototype.

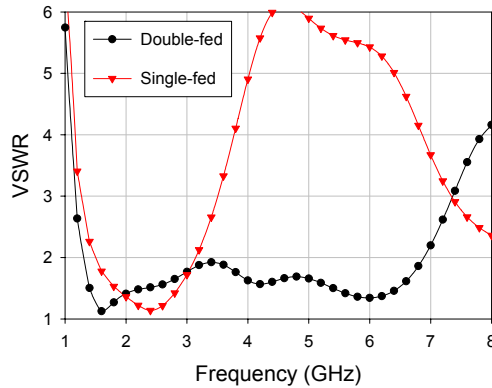


Figure 4.38 Comparison of the VSWR referred to 50Ω of a double-fed square monopole and a single-fed square monopole of the same dimension.

Moreover, for the sake of comparison, Figure 4.39 illustrates the radiation patterns in the XY plane for the square planar monopole antenna with double feed (SPMDF) and for a circular planar monopole (CM) with the same area and a feed gap of 1 mm, at three different frequencies. The feed gap chosen for the circular monopole was found to yield the maximum impedance bandwidth for these dimensions. It can be observed that, owing to the use of the double symmetrical feeding in the square planar monopole antenna, the cross-polar component (horizontal component) of the radiation pattern decreases when compared to that of the circular monopole antenna, for all frequencies. This is due to the fact that the symmetrical feeding configuration used causes the excitation of the vertical current mode of the structure, while preventing other modes (e.g. horizontal and asymmetrical current modes) from being excited.

Furthermore, other techniques, such as the insertion of bevels at the base of the monopole [76], can be combined with the use of the double feed in order to further increase the impedance bandwidth of the antenna. The addition of bevels on the lower corners of the square planar monopole reduces even further the horizontal current at the base of the monopole, and hence increased bandwidth can be obtained. Figure 4.40(a) shows the geometry of the antenna when applying the beveling technique. As observed in Figure 4.40(b) the bandwidth achieved with the combination of both techniques is highly increased.

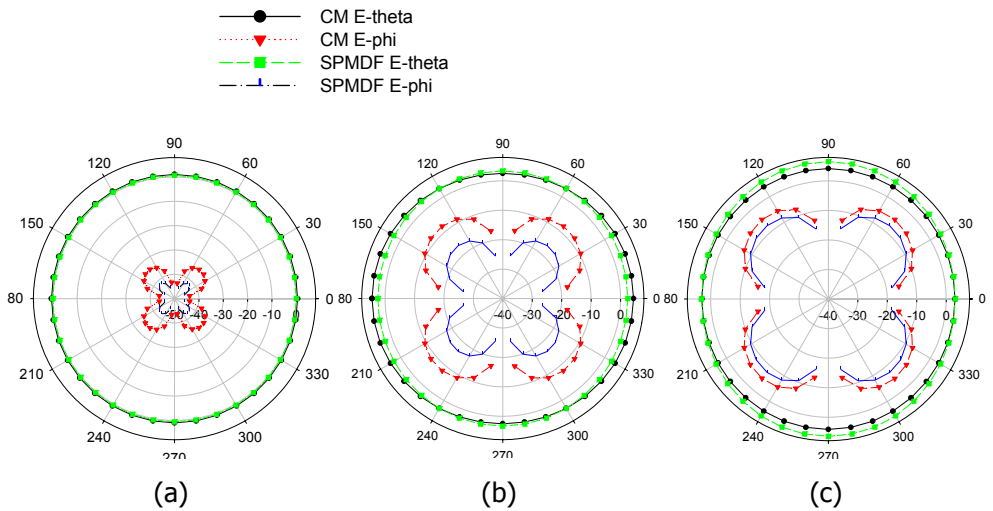


Figure 4.39 Radiation patterns in XY plane for the double feed square planar monopole and circular monopole antennas at (a) 2 GHz; (b) 4 GHz and (c) 6 GHz.

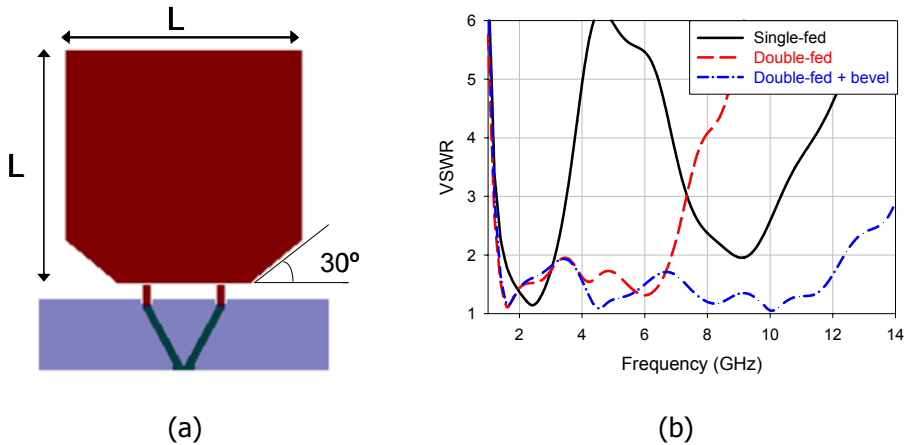


Figure 4.40 (a) Geometry of the square monopole with double feed and bevels ($L=40$ mm); (b) Comparison of measured VSWR referred to 50Ω for the antenna with a single feed, double feed and double feed with bevels.

Consequently, all the results presented in this section demonstrate the advantage of using the multiple feeding technique in square planar monopole antennas. The

use of this technique has been carefully reasoned, by means of the analysis of the characteristic modes of a rectangular plate. Other techniques for bandwidth enhancement proposed in the literature for this kind of antennas rarely justify the physical basis, being limited to the presentation of diverse experiments, and hence hindering the establishment of general design guidelines. The multiple feeding technique, proposed for the first time for this type of antennas, has been published in [83], and many authors have taken into account these design guidelines for the design of planar antennas [84]-[104].

Moreover, the multiple feeding technique can be used in other types of planar antennas, for instance to obtain polarization diversity or antennas for MIMO applications. This will be discussed in next sections.

4.3.3. Application of a double feed planar monopole antenna to MIMO systems

Deriving from the double feed planar monopole antenna presented in the previous section, a compact antenna for Multiple-Input Multiple-Output (MIMO) applications can be proposed.

As commented in section 4.2.2.2, the problem in modern compact handsets is that the volume required by multiple antennas usually needed in MIMO systems is often too large for this kind of terminals. To solve this problem, compact solutions are required, which can consist in the use of multimode antennas that have been shown to provide a channel capacity comparable to that of an array [57][58]. A different approach to reduce the overall size resides in using compact integrated diversity antennas, similar to the one described in [105]. This antenna effectively incorporates two antennas into one, and uses two isolated feed ports to provide diversity signals.

Based on this latter technique, a compact MIMO antenna can be derived from the double feed square planar monopole presented in the previous section [106][107]. However, since both feeding ports are desired to work independently, good isolation between ports and low envelope cross correlation are required. Figure 4.41 shows the geometry of the proposed MIMO antenna. As observed, it is very similar to the geometry of the antenna presented in the previous section, but in this case, the feeding network has been eliminated since the two ports are now fed independently. Moreover, a slit has been inserted between both ports of the antenna, in order to reduce the coupling between them. The dimensions of the antenna have been optimized to operate at 2.45 GHz, and the location and size of both ports have been adjusted to match the typical 50 Ω impedance.

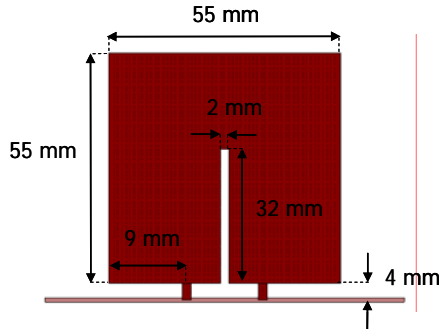


Figure 4.41 Geometry of the compact MIMO square planar monopole with two independent feeds.

Subsequently, a prototype of the antenna was fabricated and the S-parameters measured. Comparison of simulated and measured S-parameters is depicted in Figure 4.42, showing a very good agreement. As observed, the structure is matched in a range of frequencies of about 1 GHz, while the parameter S_{12} stays under -20 dB in most of this frequency range, reaching a minimum value under -35 dB at the design frequency. Therefore, isolation between ports is achieved.

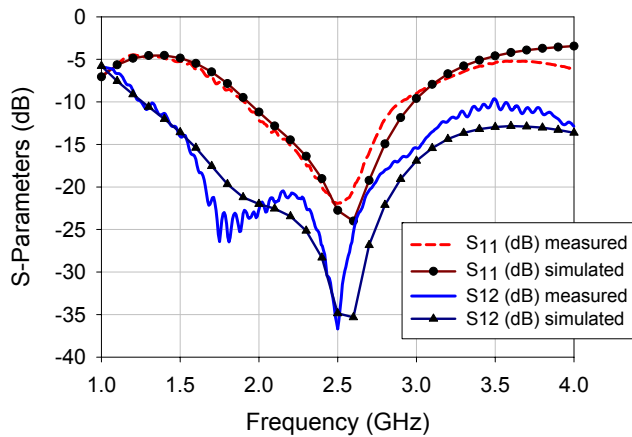


Figure 4.42 Geometry of the compact MIMO square monopole with two feeds.

Moreover, the envelope correlation was calculated by means of S-parameters, as described in [108]. Figure 4.43 shows that the prototype provides correlation values that remain below 0.02 within the whole band of interest.

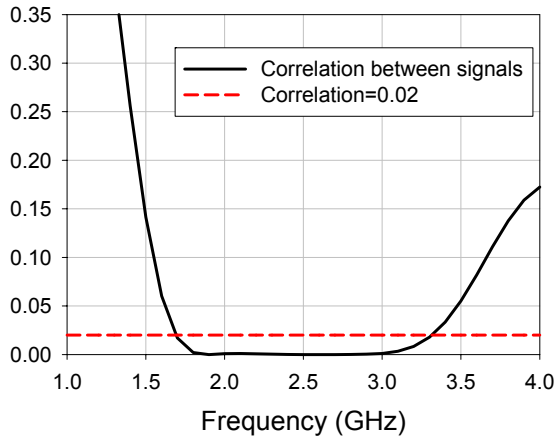


Figure 4.43 Correlation values obtained from the prototype.

To verify the suitability of this new MIMO design, the antenna was measured from 2 GHz to 3 GHz at the Technical University of Cartagena. A MIMO channel sounder based on a multiport network analyzer and a fast switch was used in order to measure the frequency response in an indoor environment [109]. A SIMO (Single-Input Multiple-Output) system was implemented, using a Cisco Aironet omnidirectional mast mount antenna (AIR-ANT2506) with 5 dBi gain as the transmitter, and the proposed two port planar monopole antenna as the receiver. The distance between the transmitter and the receiver was fixed to 3 m. Measurements were taken for a total of 1601 frequencies, with an intermediate frequency of 1 KHz. During the measurements, the lab was empty except for the system under measurement. Consequently, the channel has been supposed quasi-static.

The performance of different SIMO systems, with two vertical Cisco Aironet monopoles at reception using different spacing was studied. Figure 4.44 shows the relative power measured by each receiving antenna (two in this case), for the two port monopole, and for the two Cisco monopoles with different spacing. As observed, in every SIMO system, the received power by each antenna is similar. Obviously, as the Cisco monopoles present higher gain than the planar monopole, they receive higher power. It can also be noted that a higher power is received at the WiFi band (around 2.45 GHz) as the monopoles are tuned at those frequencies.

Figure 4.45 shows the correlation for the two antennas at reception for this environment. In general, the correlation decreases when the distance between the two receiving antennas increases. As observed, the behavior of the planar monopole

resembles that of the two Cisco monopoles at $\lambda/2$. Thus, the two port planar monopole could be considered approximately equivalent to the two vertical Cisco monopoles separated $\lambda/2$.

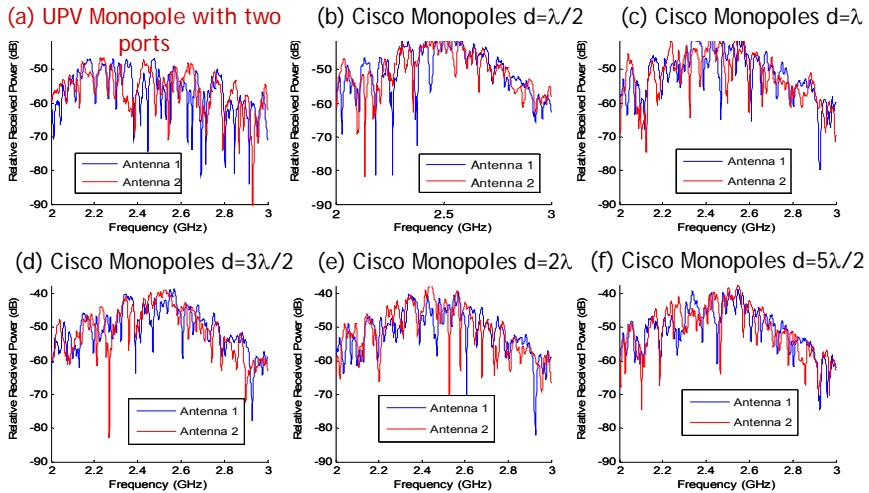


Figure 4.44 Power measured by each receiving antenna, for the two port planar monopole, and for the two vertical Cisco monopoles with different spacing.

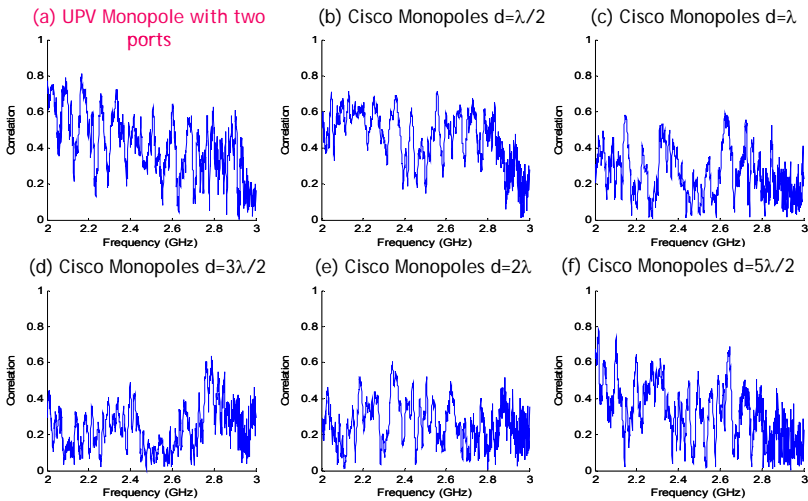


Figure 4.45 Correlation for the two antennas at reception, for the two port planar monopole, and for the two vertical Cisco monopoles with different spacing.

4.3.4. Wideband antennas with polarization diversity

The use of multiple feeding points to improve the polarization properties of an antenna can also be extended to other geometries. Therefore, the use of multiple excitations enables not only the improvement of the impedance bandwidth, but also the design of antennas with diverse polarizations, as far as the proper modes are coupled.

Thus, a four port antenna consisting of four circular plates and four feeding points can be proposed as a wideband multi-polarized antenna. The geometry of the structure is shown in Figure 4.46. By properly combining the amplitude and phases of the voltage generators at each port, different polarizations can be obtained for the antenna. The idea was already presented in section 4.2.2.2 for a wire loop antenna, where results for the excited modes and the polarization obtained for different amplitude and phase combinations of the sources were summarized in Table 4.1. Different combinations lead to diverse polarizations for the planar structure, obtaining a higher bandwidth than in the wire loop.

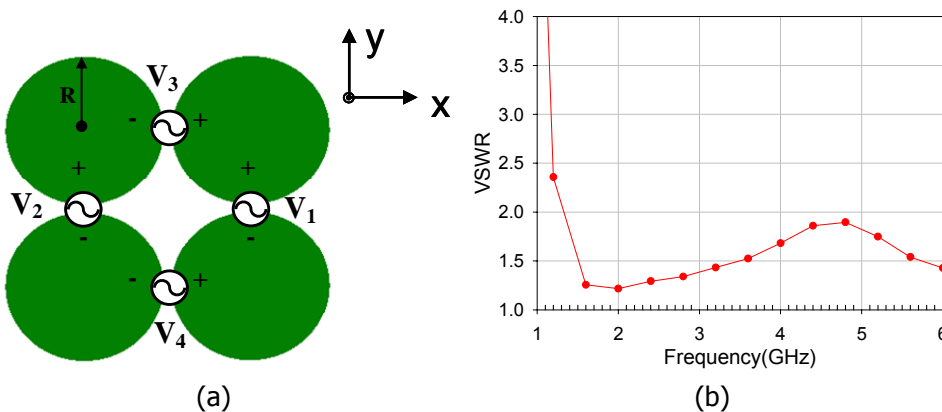


Figure 4.46 (a) Four circular plate antenna with dual polarization ($R=22.568$ mm); (b) VSWR referred to 50Ω .

Therefore, if symmetrical voltages V_1 and V_2 are applied in Figure 4.46, a vertical current distribution is generated (as shown in Figure 4.47a, where the total current distribution is depicted) and an electrical field with linear vertical polarization is radiated. In the same manner, when voltages V_3 and V_4 are applied, horizontal polarization operation is obtained (see Figure 4.47b). Finally, when the same amplitude and phase is applied to all the voltage sources in the antenna, a linear polarization of 45° is obtained, as a combination of the vertical and the horizontal

current modes excited (Figure 4.47c). Moreover, left-handed or right-handed circular polarization can be achieved if a phase difference of $+90^\circ$ or -90° is produced between sources V_1 (V_2) and V_3 (V_4), respectively, as shown in Table 4.1. Therefore, by adequately activating the four feedings, polarization agility can be obtained for the antenna.

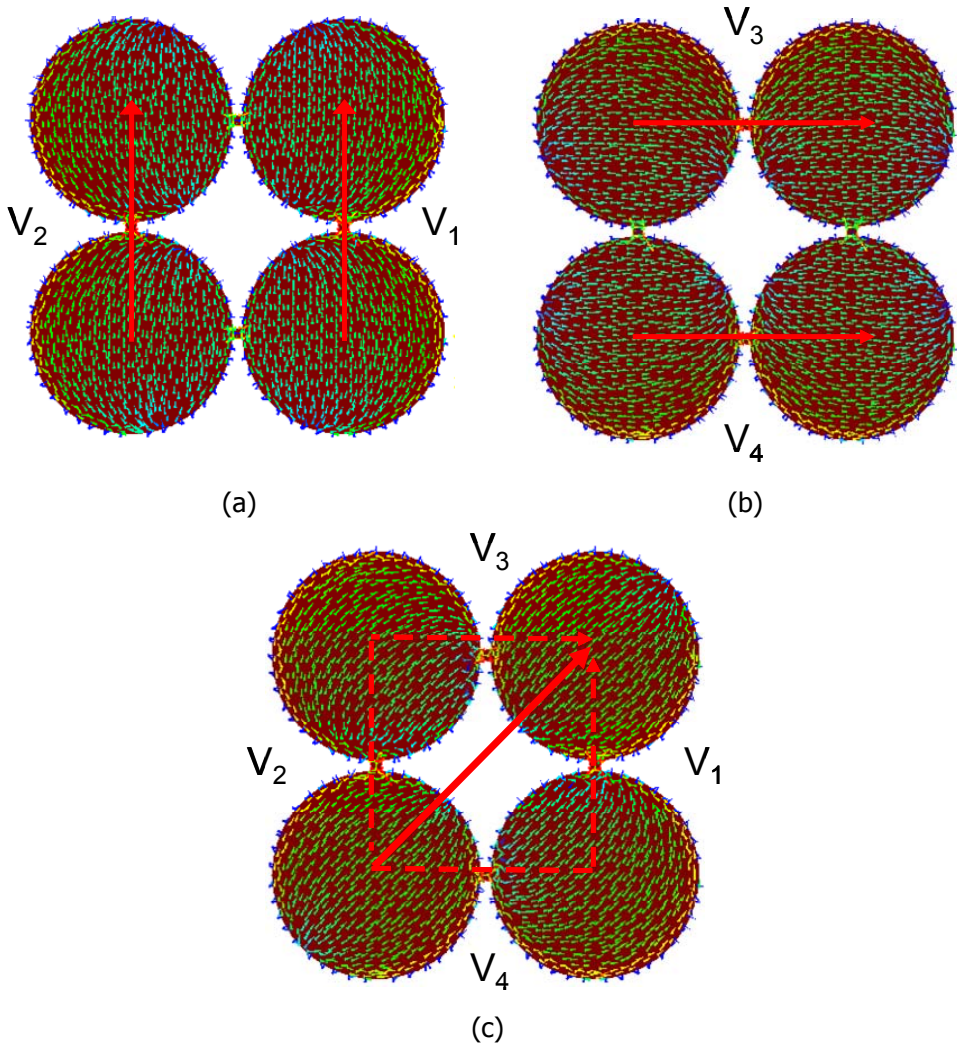


Figure 4.47 (a) Current distribution obtained with IE3D for different feeding configurations, at 2 GHz: (a) vertical polarization; (b) horizontal polarization; (c) 45° polarization.

The voltage standing wave ratio (VSWR) referred to 50Ω for the antenna excited with parallel voltages V_1 - V_2 or V_3 - V_4 and computed with commercial software Zealand IE3D™ is shown in Figure 4.46(b). As observed, an impedance bandwidth ratio higher than 4.6:1 is provided by this antenna. In Figure 4.48, the radiation pattern computed with IE3D at different frequencies for the antenna with vertical linear polarization is represented. The figure shows that some degradation in the radiation pattern occurs at higher frequencies (5 GHz approximately), due to the excitation of higher order modes.

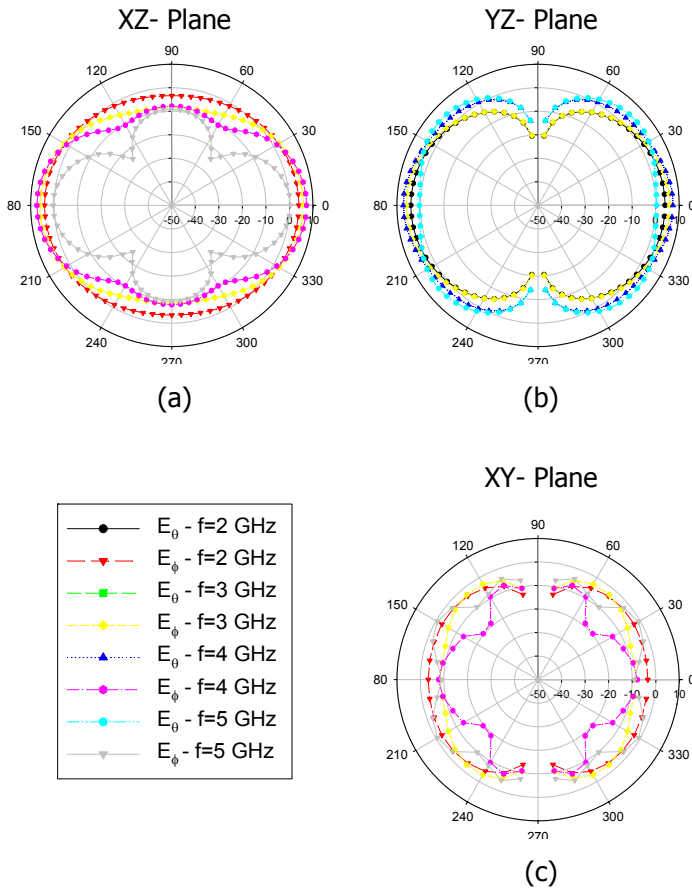


Figure 4.48 Radiation pattern at different frequencies within the operating bandwidth for vertical polarization in the (a) XZ plane; (b) YZ plane and (c) XY plane.

A comprehensive study of characteristic modes associated to the structure shown in Figure 4.46 is provided in [17]. From this study, it can be inferred that characteristic modes of the structure composed by four circular plates can easily be obtained as the different combinations of the characteristic modes of a single circular plate, what highly facilitates the computation of modes in identical coupled structures.

Other shapes for the planar structure can be proposed to decrease the lowest frequency of the operating band. For instance, a petal-shaped geometry with four feeding points can be used [110], as depicted in Figure 4.49(a). By means of the feeding configuration employed (a detail of the feeding is illustrated in the figure), the same performance as that of the double circular dipole previously discussed can be obtained. As observed in Figure 4.49(b), an impedance bandwidth from 800 MHz up to 6.8 GHz is achieved for a VSWR < 2. Radiation patterns similar to that of the four circular plates are obtained.

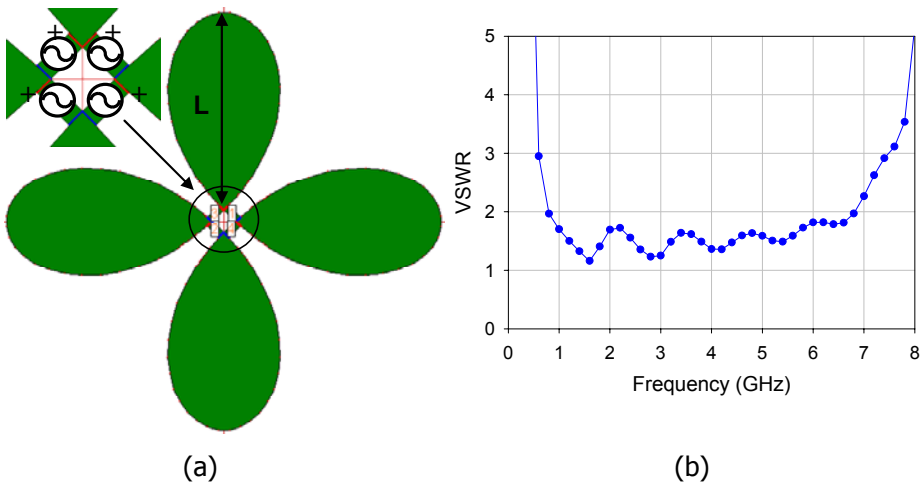


Figure 4.49 (a) Petal-shaped antenna with dual polarization ($L=110.31$ mm); (b) VSWR referred to 50Ω .

Therefore, it can be concluded that multiple feedings can also be used to gain control over the polarization of the antenna. By properly combining the amplitude and phase of the sources, a wideband antenna with diverse polarizations can be obtained. Information about a possible practical implementation of the feeding mechanism can be found in [111][112].

4.4. Conclusions

In the present chapter the excitation of characteristic modes in radiating structures has been investigated. Once the characteristic modes of a conducting structure have been analyzed, the next step in the design process should consist in deciding the location and configuration of the feeding mechanism, in order to properly excite those modes with more appealing properties.

Therefore, the modal excitation in a simple wire antenna has initially been investigated. It has been shown that the location of the source is critical to determine the significance of each mode in the radiating behaviour of the excited structure. Moreover, it has been demonstrated that by means of multiple sources, a more precise control over the modal excitation can be gained, as different mode symmetries over the structure can be imposed by the sources.

Afterwards, modal excitation in more complex structures, such as planar antennas, has been studied. It has been established that for a square planar monopole antenna usage of a double feeding mechanism can extremely improve the antenna performance, since the excitation of the wideband vertical current mode is reinforced. Later, a practical implementation of the feeding mechanism has been proposed and a prototype fabricated. Measurements for the proposed antenna confirm the improved impedance bandwidth and radiation properties. The use of a multiple feeding mechanism in this kind of antennas and the physical explanation of their behaviour by means of characteristic modes has been taken as a reference by other authors [84]-[104].

Finally, multiple feeding mechanisms are also useful to provide diverse polarizations in a radiating structure. When combined with a planar structure, wideband behaviour is obtained in addition to this ability.

Therefore, in the present chapter it has been demonstrated that the information provided by characteristic modes about resonance frequency and radiating bandwidth of a conducting structure is immensely useful for the antenna design. These modes provide a very clear physical insight into the behaviour of the radiating structure, hence facilitating the design process. The current distribution exhibited by the different modes provides very useful information regarding the optimal location and configuration of the feeding points.

Chapter 5

Modal analysis and design of wideband antennas with coupled resonators

“If you can't explain it simply, you don't understand it well enough”

Albert Einstein

5.1. Introduction

In the previous chapter, the excitation of characteristic modes in wire and planar antennas was investigated, and novel designs for wideband and multi-polarized antennas were proposed. In this chapter, the Theory of Characteristic Modes will be applied for the analysis and design of wideband planar antennas with a narrowband resonator embedded into the planar geometry. In this case, the coupling of the narrowband resonator produces some effect in the behaviour of the wideband structure, which will be investigated in the present chapter from a modal perspective.

Antennas with coupled resonators have been extensively used in the last decades for a great variety of applications. In particular, wireless communication terminals have long made use of antennas with coupled resonators to achieve multiple operating bands with a single compact antenna, to obtain circular polarization or to increase the impedance bandwidth of the antenna [2][3].

Figure 5.1 shows some examples of coupled resonators used in microstrip antennas. As it can be seen, coupled resonators can consist in a slot embedded into the planar surface of a patch antenna, in order to generate an additional resonance and obtain a dual-band antenna (Figure 5.1a) [113][114]. Moreover, a slit with some specific shape can be inserted into the planar structure, so as to generate two or more connected resonators of different size, creating multiple operating bands (Figure 5.1b) [115]-[117]. In addition, gap-coupled parasitic patches can be used to enhance the bandwidth of microstrip antennas, as shown in Figure 5.1c

[118]. In this case, the patches are designed to have slightly different resonant lengths. As a result, their resonances occur at frequencies close to each other and hence the operating frequency band is increased. It is possible to use not only parasitic patches, but also other driven patches, which can be coupled to increase the bandwidth, as shown in Figure 5.1d [119][120]. Furthermore, diverse coupled resonators can be combined within the same structure, as shown in Figure 5.1e, where two stacked patches with embedded slots are used to increase the number of operating bands [121].

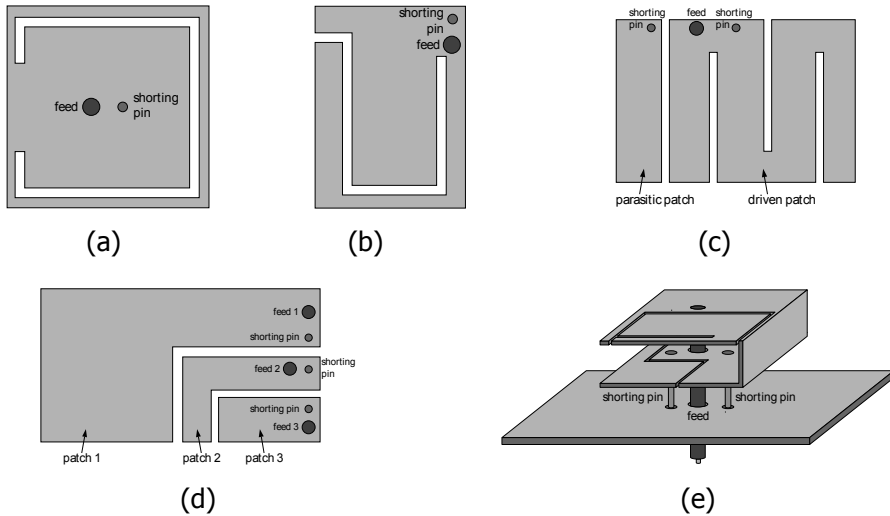


Figure 5.1 Traditional microstrip antennas with coupled resonators.

In consequence, it can be stated that the use of coupled resonators in narrowband antennas, such as microstrip antennas, has been extensively investigated. A comprehensive review of microstrip antennas with coupled resonators can be found in [2],[3] and [122].

In recent years, however, the use of narrowband resonators embedded in wide-band antennas has been significantly extended. More precisely, resonant slots embedded in wideband planar monopole antennas have focused much attention recently, due to the fact that the insertion of the narrowband slot has been proven to produce a frequency-notch feature in the antenna response [123]-[129].

This feature is especially interesting in planar monopole antennas used for Ultra-Wideband (UWB) systems. Planar monopole antennas have been found to be excellent candidates to operate in UWB systems, since they can cover the system's required frequency range (from 3.1 to 10.6 GHz) while presenting a low-cost and

very compact structure [130]. Moreover, this kind of antennas satisfactorily complies with the time-domain requirements of UWB systems. However, as observed in Figure 1.1 of chapter 1, several frequency bands for narrowband technologies have been allocated within the UWB frequency range, such as wireless LAN at the 5.2 GHz (5150 GHz-5350 MHz) and 5.8 GHz (5725–5825 MHz) bands, which might interfere with the UWB system. Hence, the possibility of providing a frequency-notched characteristic in the antenna itself to mitigate the unwanted interference from wireless LAN systems results extraordinarily attractive.

Several authors have recently proposed numerous designs of UWB antennas including this feature [123]-[129], which is usually accomplished by inserting an inverted-U-shaped resonant slot in the antenna planar geometry, and by properly adjusting its length in order to make it resonant at the desired filtering frequency, as discussed later. However, all the proposed designs provide only pure experimental results, with no detailed explanation about the coupling phenomena between the wideband and narrowband structure.

In order to physically explain the behaviour of these antennas and to provide some design guidelines, the present chapter is devoted to investigate this type of structures by means of the Theory of Characteristic Modes. The understanding of the behaviour of wideband antennas with narrowband embedded resonators will allow to propose novel designs based on controlling the excitation of the narrowband structure resonance. Therefore, a further step in the design of UWB antennas with band-notched characteristic may consist in using active devices to control these resonances. Part of this work was developed at IMST GmbH., whose experience in the use of miniaturized active devices was immensely valuable to initiate the proposals of planar monopoles with active devices.

In the next section, characteristic modes of a common planar monopole antenna with a narrowband resonator will be computed and analyzed. In addition, the modal excitation will be investigated, when exciting the structure with a single port. Based on the conclusions obtained from the modal analysis, a new slot shape and an electronic control of its excitation will be proposed to be used in an UWB antenna. A prototype of the antenna will be fabricated and measured to demonstrate the feasibility of the proposal. Finally, reactive loading will be proposed to control the coupled narrowband resonance. Not only frequency-domain but also time-domain measurements will be provided, in order to fully demonstrate the convenience of the proposed antenna for UWB applications.

5.2. Modal analysis of wideband planar monopole antennas with embedded resonators

In this section, the characteristic modes of a planar monopole antenna with a coupled resonator will be analyzed. For the analysis, a square planar monopole element is chosen due to its simple geometry, which is useful for a generalized modal study of this kind of antennas.

The geometry of the antenna is shown in Figure 5.2. As observed, a thin slot with an inverted-U shape is etched in the interior of the radiating element in order to generate an additional resonance in the structure. Dimensions of the antenna have been taken from [129], where a complete parametric study of the radiating element is provided. The response of the antenna has been calculated by means of an electromagnetic simulation tool based on the Method of Moments, which has been developed and implemented by the Electromagnetic Radiation Group of the UPV [17]. The computed return loss is depicted in Figure 5.3, where it is possible to observe that a rejected band is generated within the operating bandwidth of the antenna, due to the resonance of the embedded slot. Thus, the center frequency of the notched band is determined by the dimensions of the slot, as follows [129]:

$$f_{notch} = \frac{c}{4(l_1 + l_2/2 - t)}$$

where c is the speed of light. Therefore, by adjusting the dimensions of the slot the notched band can be shifted to the desired frequency.

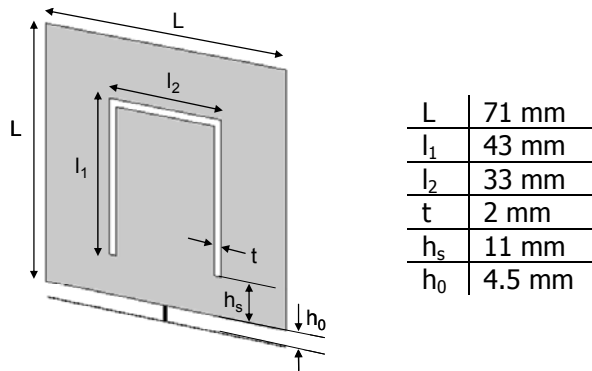


Figure 5.2 Geometry of the square planar monopole loaded with a resonant slot.

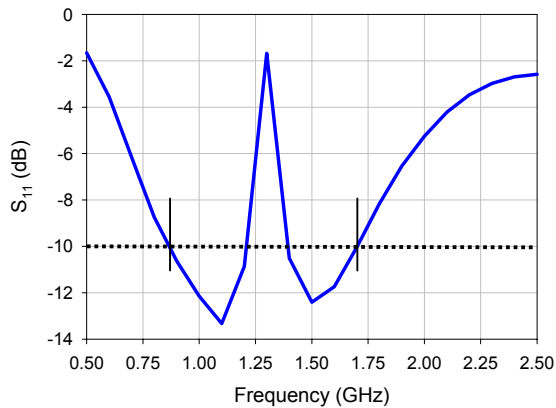


Figure 5.3 Return loss of the antenna shown in Figure 5.2, where the band notched behavior can be observed.

In existing literature, there exists a lack of rigorous analysis to investigate the effect of the slot embedded in the planar surface. However, the Theory of Characteristic Modes can provide an innovative approach to analyze this type of problems, and hence it has been applied to the structure shown in Figure 5.2. Thus, the objective is to obtain an in-depth physical insight into the behavior of the antenna, with the aim of improving its performance and functionality.

Figure 5.4 shows the normalized current distribution for the first five characteristic modes of the square planar monopole with a narrowband coupled resonator. In Figure 5.5, diagrams representing schematically the current distribution of these modes are depicted for better understanding. According to this figure, modes J_0 , J_1 , J_2 and J_3 present a current distribution very similar to that exhibited by the modes associated to the traditional square planar monopole antenna. For the sake of comparison, the first four modes of this latter structure are represented in Figure 5.6.

For the slotted antenna, the location of the slot has been optimized to minimize disturbance on the modal current distributions. Nevertheless, the presence of the slot produces an additional resonant mode in the structure, called *slot mode*, which is responsible for the degradation of the input impedance of the antenna at a certain frequencies, i.e. within the notched frequency band.

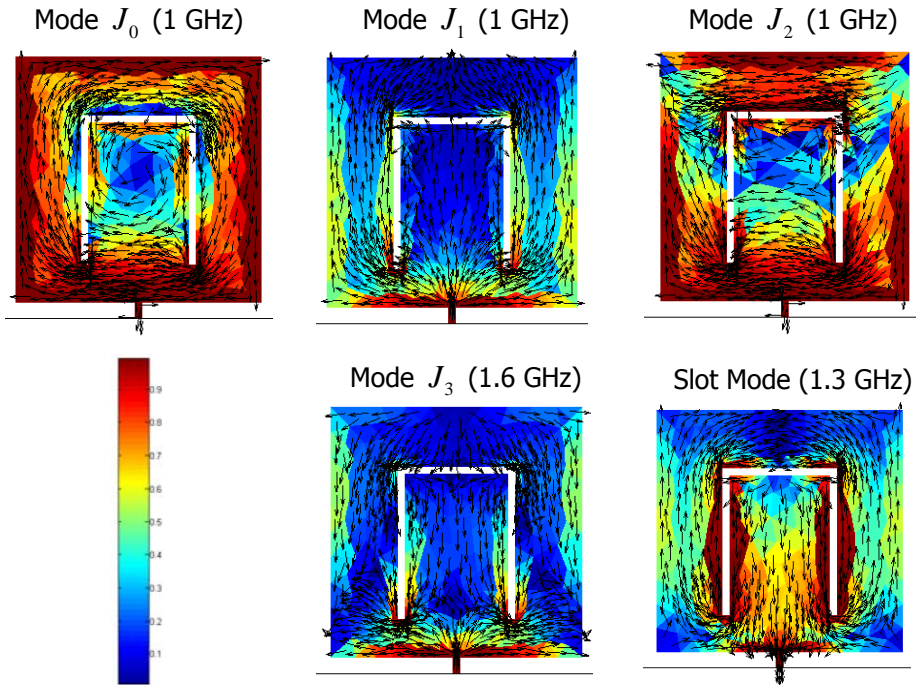


Figure 5.4 Normalized current distribution for the first five characteristic modes of the square planar monopole antenna loaded with a thin inverted-U shape slot, at a frequency near the resonance of each mode.

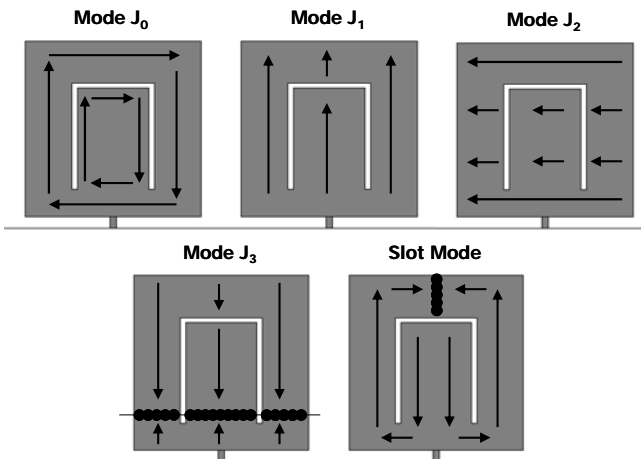


Figure 5.5 Diagrams of the modal current distributions in the square planar monopole antenna loaded with a thin inverted-U shape slot.

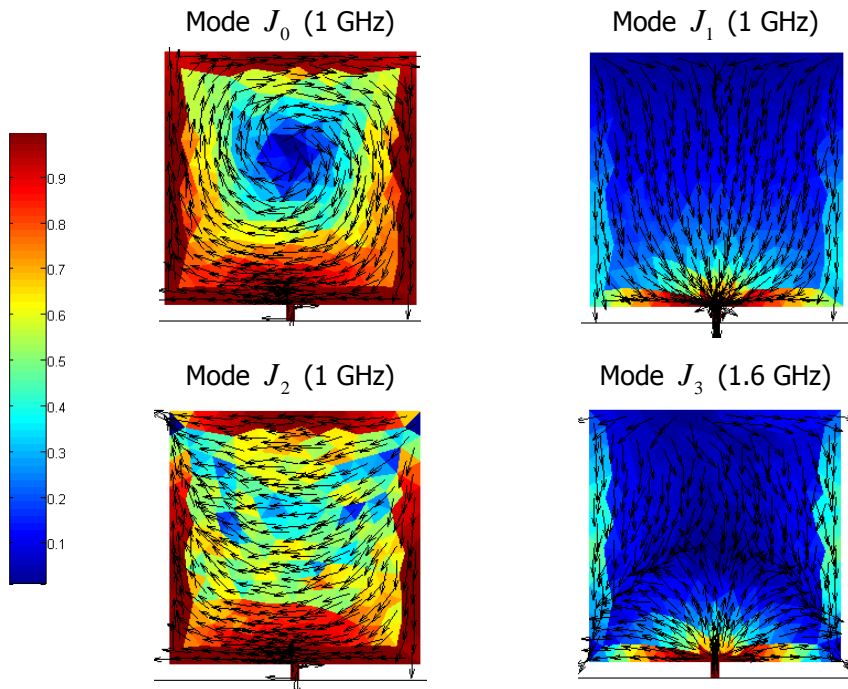


Figure 5.6 Normalized current distribution for the first four characteristic modes of the square planar monopole antenna without slots, at a frequency near the resonance of each mode.

In Figure 5.7, the characteristic angle variation with frequency for the first characteristic modes is represented, both for the slot-free and the slotted monopole. As observed, mode J_1 exhibits similar radiating behavior and resonant frequency in both monopoles. The same occurs for mode J_3 . From the current distribution of these modes in the two structures, it is possible to deduce that this is caused by the optimal location of the slot in a position within the structure, where the current is not significantly altered. The height of the slot, measured from the ground plane, is critical to avoid disturbing the current distribution of modes J_1 and J_3 excessively [131]. These modes present a very intense current at the base of the monopole, whose value decreases sharply as it flows away. In consequence, these modes are intensely affected by presence of the slot near the base of the monopole, and hence the effect of the notched band becomes stronger as seen in the parametric study carried out in [129].

Furthermore, as mode J_0 does not present a very intense current distribution at the central part of the planar surface, its behavior is not affected by the insertion of the slot. Nevertheless, the insertion of the slot affects the characteristic angle as-

sociated to mode J_2 . As observed in the figure, the resonant frequency of mode J_2 in the slotted structure decreases, due to the current meandering produced by the slot. In addition, this current meandering decreases moderately the radiating bandwidth of this mode.

Finally, the presence of the *slot mode* can clearly be noticed in the figure for the slotted structure. The curve of the characteristic angle associated to this mode presents a very steep slope, which confirms its narrowband behavior. Moreover, it can be also noted that its resonant frequency coincides with the center of the rejected band. Within the range of frequencies analyzed, only the first resonant mode of the slot appears. However, there exist higher order slot modes produced by the successive higher order resonances of the slot, which lie beyond this frequency range.

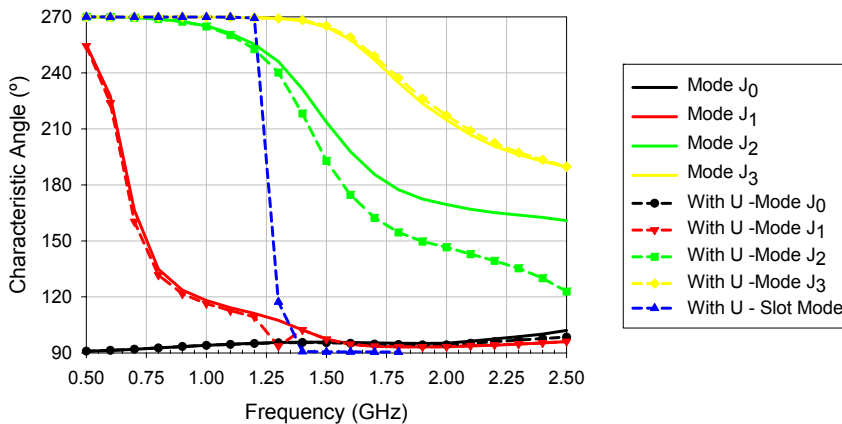


Figure 5.7 Characteristic angle variation with frequency for the first characteristic modes of the square planar monopole antenna, with and without slot.

Moreover, when the slotted monopole is fed at the center of its base by means of a voltage gap source, the modal admittances shown in Figure 5.8 are obtained. The total admittance calculated at the input port has also been represented in the figure, so as to facilitate the identification of the contribution of each mode to the total input admittance. As it can be seen, both in the real and imaginary parts of the admittances, mode J_1 dominates at lower frequencies, up to 1.2 GHz. Suddenly, at 1.3 GHz, the *slot mode* appears and provokes an abrupt anti-resonance, due to the strong inductive behavior exhibited by this mode after its resonance. As observed, since the slot mode presents a narrow band, its influence on the total admittance is reduced to a short range of frequencies. Finally, after the resonance of the *slot mode*, mode J_3 is excited.

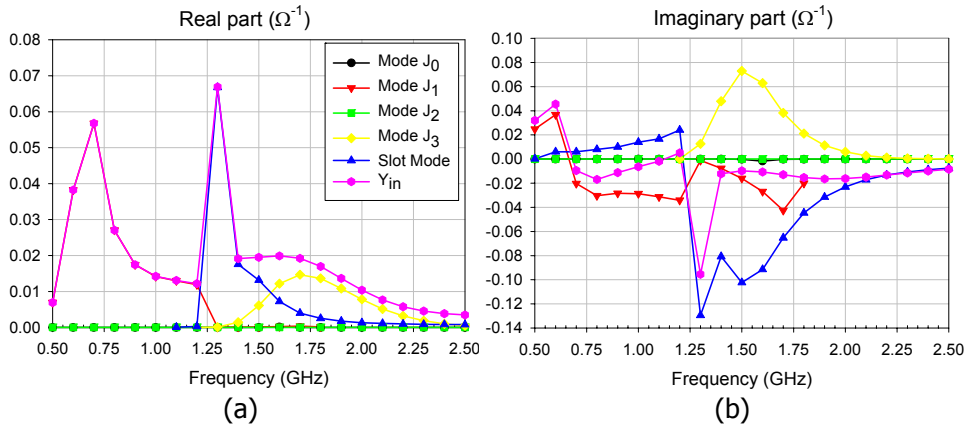


Figure 5.8 Contribution of the modal admittances Y_n to the input admittance Y_{in} for the square planar monopole antenna with two feeding ports. Legend is common to both plots.

Therefore, the sudden appearance of the narrowband *slot mode* provokes a strong perturbation in the curve of the input admittance, which leads to a mismatching in a frequency range near the resonant frequency of the *slot mode*. In Figure 5.9 a comparison of the input impedance of the antenna with and without slot has been depicted, clearly showing the effect of the *slot mode*. As observed, the resonance of the slot causes the resistance at the input port to suddenly decrease, due to the increment of current intensity produced by the slot resonance, and provokes a mismatching in the input impedance.

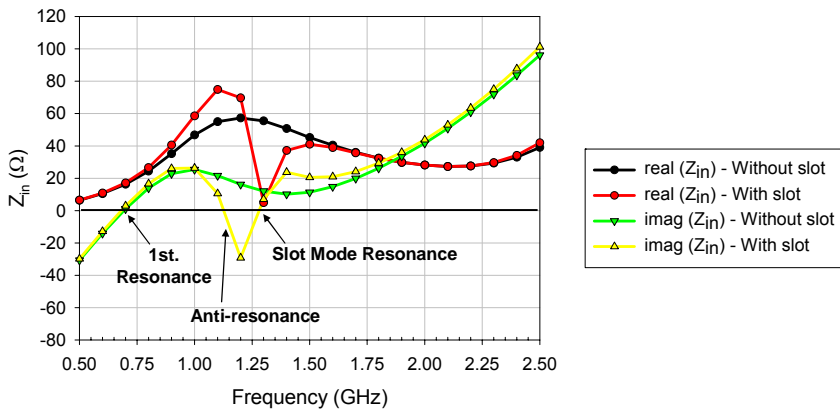


Figure 5.9 Comparison of the input admittance of the square planar monopole antenna with and without band-notched behavior.

5.3. Control of the slot mode excitation

As previously considered, the resonance of the slot embedded within the planar antenna is the responsible of its band-notched behavior. Usually, the slot takes an inverted-U shape, allowing this compact structure to achieve the rejection of lower frequencies within the operating band of the antenna.

In Figure 5.10(a), an alternative shape for the slot can be proposed, with the purpose of being able to control the excitation of the *slot mode*. In this case, the slot consists of a square ring with the dimensions shown in the figure (in mm). As portrayed in the figure, a strip has been inserted in the upper part of the slot ring, and thus the slot can be fed by allowing the pass of the current to the internal part of the slot. The VSWR (referred to 50Ω) obtained when the slot is fed is shown in Figure 5.10(b). This result has been simulated with CST Microwave Studio™, and a notched-band is obtained, as expected. In this case, the slot dimensions have been adjusted to introduce a band-notch around 5.5 GHz.

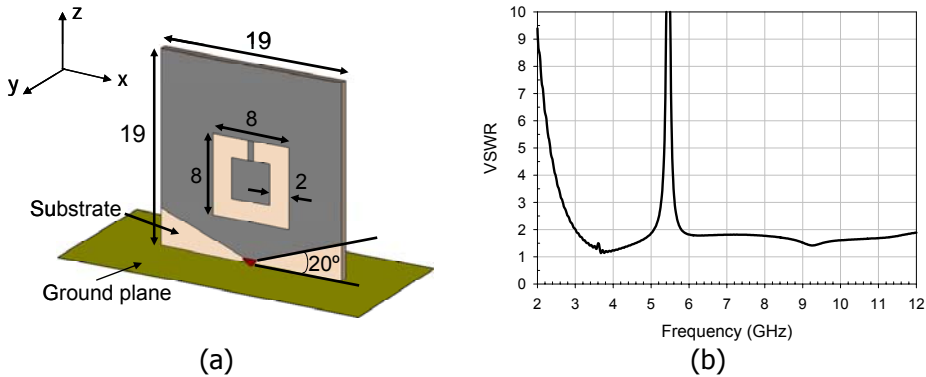


Figure 5.10 (a) Geometry of the beveled square planar monopole antenna with a quasi-square slot ring embedded in its planar surface. Dimensions are given in mm. (b) Simulated VSWR referred to 50Ω .

Nevertheless, if the strip accounting for the excitation of the slot is eliminated, the slot resonance is prevented, and hence no band-notched feature is produced. Figure 5.11 shows the geometry of the antenna for this case, together with the simulated VSWR. As it can be seen in the figure, the antenna presents a very high bandwidth for $VSWR \leq 2$, and since the *slot mode* resonance is prevented, no frequency band is rejected. Therefore, the excitation of the *slot mode* and conse-

quently its effect on the behavior of the wideband antenna can be controlled through the proposed technique.

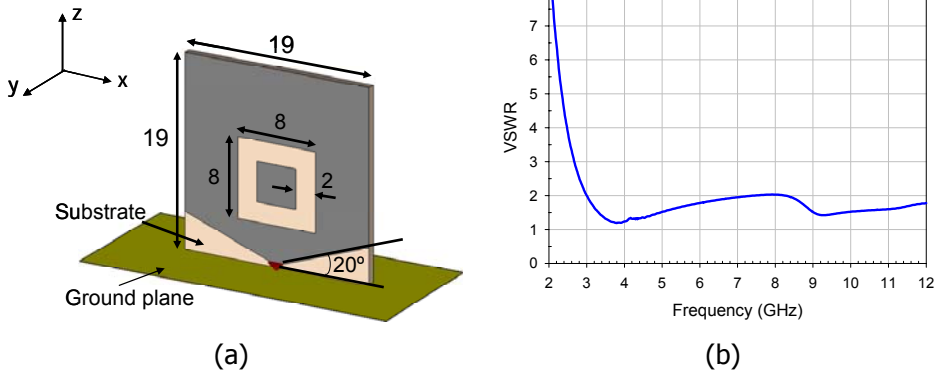


Figure 5.11 (a) Geometry of the beveled square planar monopole antenna with a square slot ring embedded in its planar surface. Dimensions are in given in mm. (b) Simulated VSWR referred to 50Ω .

Figure 5.12 shows the normalized current distribution obtained with CST Microwave Studio™, at 5.5 GHz, for the cases when the slot mode is fed and when it is not. As observed in Figure 5.12(b), when the strip is not inserted, the slot resonance, and hence the excitation of the slot mode, are prevented, and the normal surface current distribution of the planar monopole is practically not disturbed. On the other hand, when exciting the slot mode (Figure 5.12a), a strong resonance is provoked at 5.5 GHz, which alters the current distribution within the planar surface of the monopole, what in turn translates into a degradation of the input impedance.

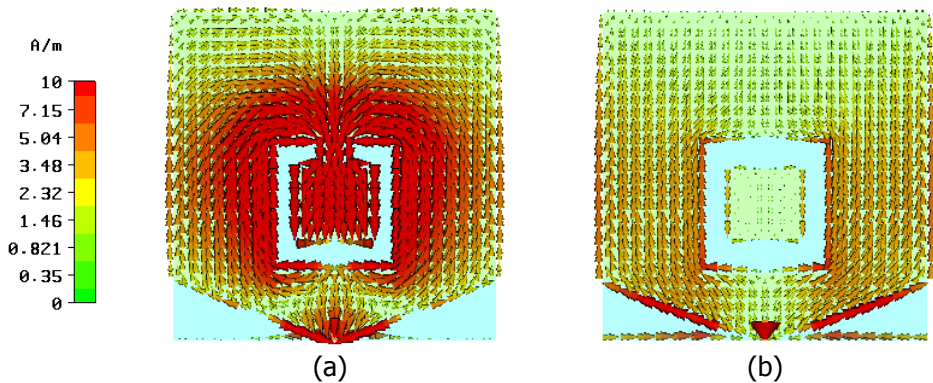


Figure 5.12 Normalized current distribution at 5.5 GHz obtained with CST Microwave Studio™, for a beveled square planar monopole antenna loaded with a square slot ring, where: (a) *slot mode* is fed; (b) *slot mode* is not fed.

It must also be noted that only the first resonance of the slot occurs, when the length of its external perimeter is $\lambda/2$ approximately. Nevertheless, higher order resonances of the slot are not coupled in the structure due to the symmetry imposed by the excitation of the planar monopole antenna. As the frequency increases, mode J_3 and successive higher order modes are excited in the monopole, but the current distribution of these modes prevents the coupling of higher order slot modes.

5.3.1. Insertion of active devices to control the slot mode excitation

Based on the previous analysis, it is clear that the functionality of wideband planar monopole antennas with band-notched behavior can be significantly improved if the excitation of the slot mode is electronically controlled.

Electronic control of the slot mode resonance can be accomplished, by means of an RF switching device that controls the flow of current to the inner part of the slot. Therefore, the antenna filtering capability can be further improved by making this band-notched behaviour switchable [131][132]. Since the existence of interfering systems depends on the antenna environment, the filtering function exhibited by planar monopoles with fixed band-notched behaviour might not be necessary in some cases. In this case, depending on whether interference from other systems is present or not, the antenna filtering feature can be activated at will.

The structure of the proposed antenna is shown in Figure 5.13(a), where the switching device has been inserted in the upper part of the slot, so as to minimize the effect over the antenna performance. On the one hand, when the switch is in ON state, and assuming an ideal shunt for this switching state, the antenna behavior is the same as that observed in Figure 5.10, where the slot mode is excited and a rejected band is generated (see Figure 5.13b). On the other hand, when the switch is in OFF state, the antenna is equivalent to that shown in Figure 5.11, and the band rejection is consequently prevented.

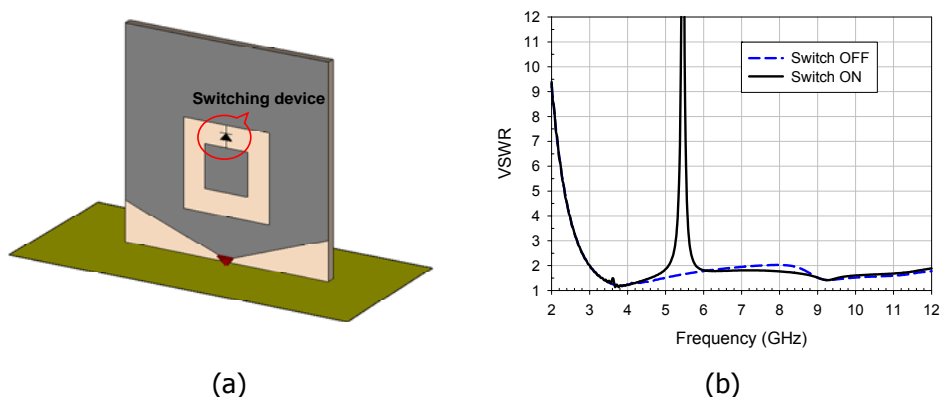


Figure 5.13 (a) Geometry of the beveled square planar monopole antenna with a square slot ring embedded in its planar surface, loaded with a switching device; (b) Simulated VSWR for both states of the switch.

5.3.1.1. Implementation of the switch by means of a PIN diode

In principle, the implementation of the RF switch can be carried out by means of a Micro-Electro-Mechanical System (MEMS) or a high frequency PIN diode. MEMS switches are becoming increasingly applied to antenna design [133]-[135], and constitute an appealing alternative, since they offer very low power consumption and very low ohmic losses [136]. However, their commercial cost is still prohibitive nowadays, so their use in this case is not an attractive option, if we consider their application in a very low cost antenna, such as a planar monopole. Therefore, the use of PIN diodes seems to be the best alternative for the application under study, due to their low-cost, reliability, compact size, and small resistance and capacitance in both the ON and OFF states. Several recent reconfigurable antennas based on the use of PIN diodes can be found in the literature, mainly dealing with slot antennas [137][138] and microstrip antennas [139][140].

Since PIN diodes require a DC bias current for polarization, the RF and DC signals must be isolated in the design. Figure 5.14 schematically shows the required setup for the switch connection and biasing. In the proposed configuration, the DC signal travels from the DC source to the anode of the diode through a resistance of $1\text{ k}\Omega$, which limits the current applied to the diode. Besides, the return of the DC signal to ground is provided by means of an inductance. A bias-T could alternatively be used to polarize the diode as in [141][142], but the proposed setup seems more general for its application in a real device. Considering the planar structure of the

antenna, which is etched on a substrate, a low-pass microstrip filter can be located on the opposite side of the substrate, in order to isolate the RF and DC signals. The structure of the RF-DC isolation circuit is depicted in Figure 5.15(a). Scattering parameters corresponding to this structure have been optimized with the Microwave Office™ simulation software and are represented in Figure 5.15(b). The structure is symmetric and, as observed, good isolation is obtained between RF and DC ports at 5.5 GHz.

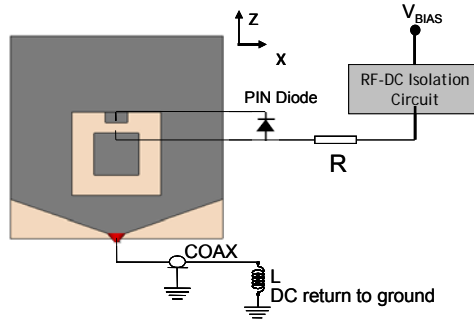


Figure 5.14 Setup diagram for the activation of the PIN diode switch.

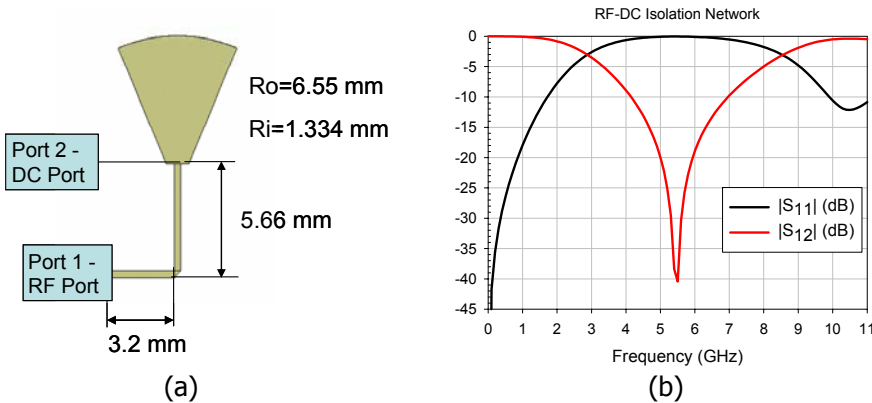


Figure 5.15 (a) Geometry of the RF-DC isolation microstrip circuit. (b) S-parameters simulated with Microwave Office™ (the structure is symmetric).

Therefore, the final geometry of the antenna with the RF-DC isolation network etched on the back side of the substrate is shown in Figure 5.16 (gray color corresponds to the back side of the antenna). The whole geometry has been simulated

with CST Microwave Studio™ in order to take into account possible coupling effects between the isolation network and the slotted planar monopole antenna. The dimensions of the slot have been adjusted to cause a band rejection at 5.5 GHz. Both sides of the substrate are connected by a metallic via located at the RF port shown in Figure 5.15.

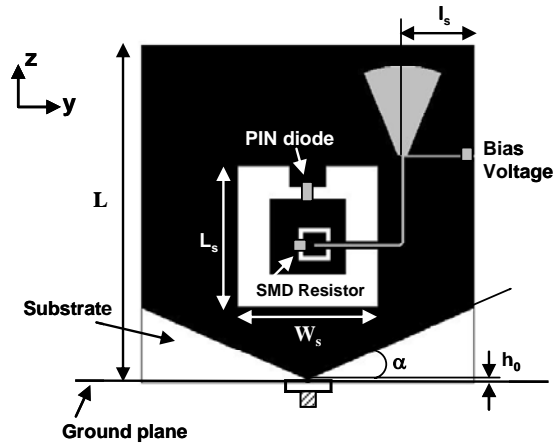


Figure 5.16 Geometry of the wideband planar monopole antenna with a rectangular slot ring loaded with a PIN diode, and the RF-DC isolation network ($L=19$ mm, $h_0=0.2$ mm, $\alpha=23^\circ$, $L_s=10.2$ mm, $W_s=9.2$ mm, $l_s=3.5$ mm, $l_1=5.1$ mm, $l_2=0.3$ mm). Gray color corresponds to the back side of the antenna.

5.3.2. Results for the reconfigurable antenna prototype

A prototype for the proposed wideband planar monopole antenna with switchable band-notched behavior was fabricated and is shown in Figure 5.17. In the front side view, the PIN diode in the upper part of the slot ring can be distinguished, as well as the $1\text{ k}\Omega$ resistance for limiting the current through the diode. A high frequency silicon PIN diode from Infineon Technologies (BAR50-02V) has been selected for the prototype. The compact size of the selected PIN diode simplifies its placement on the planar monopole surface, and the small resistance and capacitance in the ON and OFF states exhibited by the diode, together with its operative frequency range, have been essential parameters to consider for the diode selection.

In the back side view (Figure 5.17b), the RF-DC isolation circuit described in the previous section is observed, including the required wiring for the polarization of

the switch. As commented, both sides of the substrate are connected by a metallic via located at the center of the planar monopole.

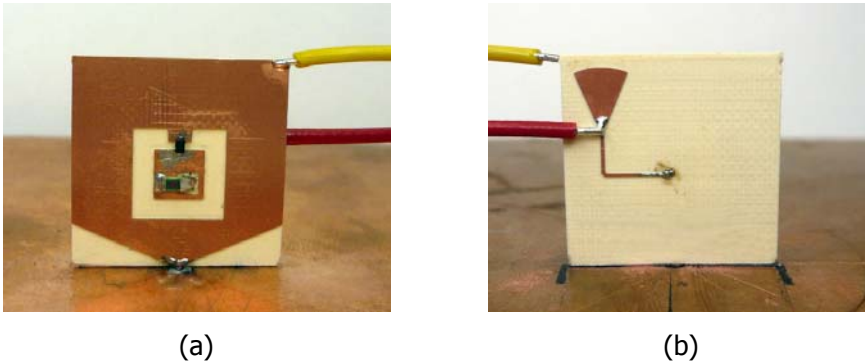


Figure 5.17 Fabricated prototype: (a) Front-side view; (b) Back-side view.

Figure 5.18 shows the return loss measured for different bias voltages applied to the PIN diode. As expected, filtering around 5.5 GHz only occurs when the diode is polarized forward ($V_{\text{BIAS}} \geq 0.95$ V); otherwise, the effect of the slot is practically negligible. However, the small resistance (around 3Ω) exhibited by the diode in the ON state considerably affects the intensity of the band rejection. As presented in [137] (Figure 8), the ON state resistance of the PIN diode notably influences the slot resonance and hence the filtering effect. It has been experimentally observed that the slot width can be increased to counteract the ON state resistance effect, leading to a better frequency rejection. The final prototype presented has been already optimized to avoid this effect. In the reverse state, the PIN diode exhibits a small capacitance (0.15 pF typically), which does not significantly affect the antenna response.

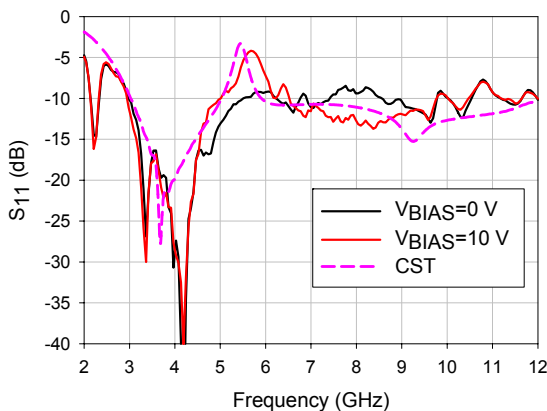
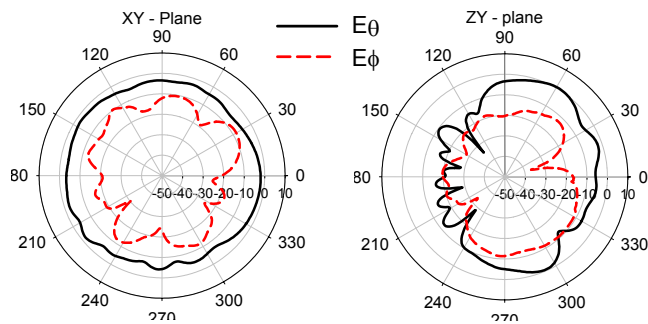


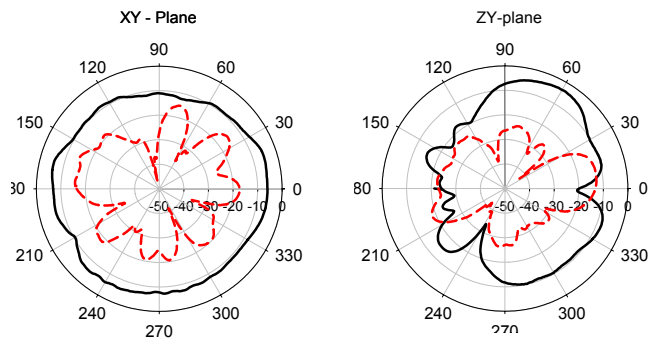
Figure 5.18 Measured return loss for different bias voltages and comparison with CST simulation.

Moreover, comparison with simulated results shows a rather good agreement. It can also be observed in the results that the notched band is rather mitigated than rejected, since active devices provide a rejection that is not as good as the one produced by a perfect shunt. This effect can be again attributed to the finite small resistance exhibited by the PIN diode in ON state. Usage of MEMS switches is expected to improve this behavior.

The measured radiation patterns at 4, 8 and 11 GHz for the XY and YZ planes are shown in Figure 5.19. As desired, nearly omnidirectional radiation patterns are obtained in the azimuth plane. Therefore, the insertion of the printed RF-DC isolation network on the back side of the antenna does not significantly alter the radiation patterns of the planar monopole antenna.



(a)



(b)

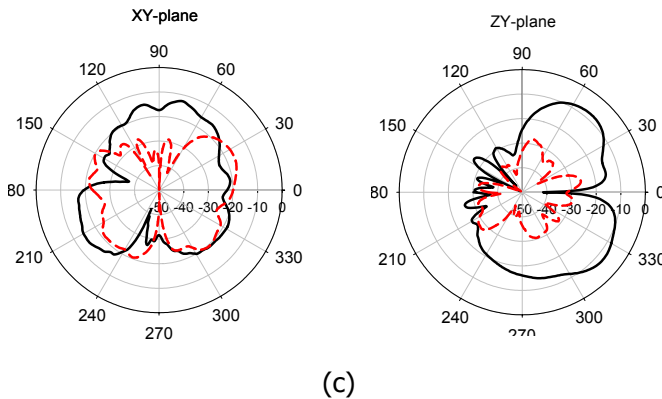


Figure 5.19 Measured radiation patterns in the XY and ZY plane for the proposed antenna, (a) at 4 GHz; (b) at 8 GHz and (c) at 11 GHz.

The provided results clearly show that electronically controlling the activation of the *slot mode* can notably increase the functionality of this kind of antennas. No design of this type applied to wideband planar monopole antennas has been found in the literature, except in [143], where a similar idea was developed in parallel to the present design. However, in this reference another concept is applied, based on the usage of a PIN diode not to feed the slot, but to change its length and generate a resonance outside the operating band. In this proposal, the normal behavior of the antenna is to produce a band rejection, which can be avoided when the diode is switched on. For practical applications, the opposite behavior would probably be more interesting, since interferences are more rarely to occur than otherwise. This is, in contrast, the behavior offered by the design proposed in this section.

5.4. Reactive loading to control the slot mode resonance

As discussed in chapter 4, reactive loading can be used to control the resonant frequency of characteristic modes. When discrete loads are strategically placed on the structure, the resonant frequency of some modes can be modified, while minimizing the effect over the rest of characteristic modes.

Accordingly, the resonant frequency of the slot mode can be adjusted by loading the slot with a reactance [61], while the rest of the modes of the planar monopole structure will not be modified significantly. Moreover, if a variable reactance is used, a much more precise control of the resonant frequency of the slot can be gained, and the rejected band can hence be tuned electronically. Consequently,

the functionality of the antenna can be notably increased, as in the design presented in the previous section.

Figure 5.20 shows the geometry of the previous antenna, although with the slot loaded in the upper part with a lumped capacitor. Figure 5.21 depicts the response of the antenna computed with CST Microwave Studio™ for different values of the capacitance (from 0.5 to 2.1 pF). Depending on the selected values, the resonant frequency of the embedded slot changes, allowing for adjustment of the band-rejection within the UWB frequency range. In order to control the capacitance value electronically, a varactor diode can be used [144][145].

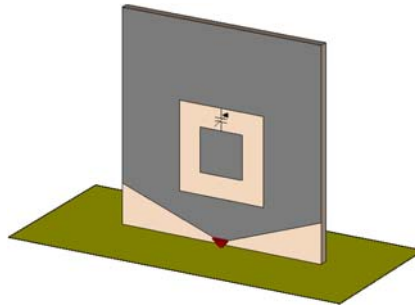


Figure 5.20 Geometry of the band-notched planar monopole antenna with a slot loaded with a variable capacitor.

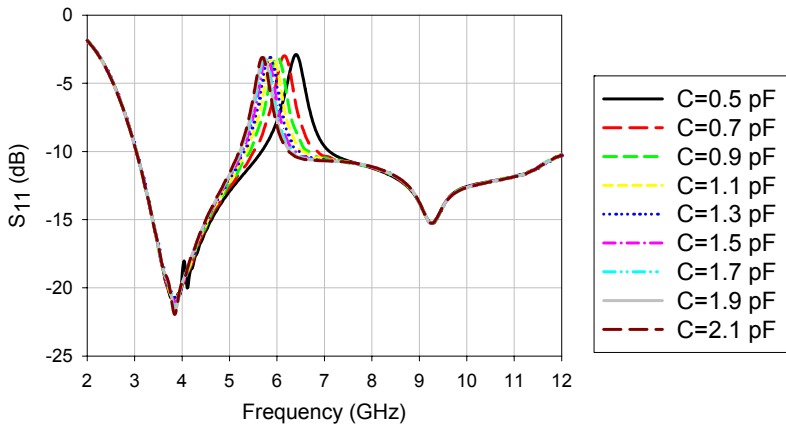


Figure 5.21 Simulated return loss with CST Microwave Studio for the proposed UWB antenna.

Therefore, a similar configuration to the one presented in the previous section can be used to obtain an UWB antenna with tuneable band-notched behaviour [146]. In this case, the PIN diode must be substituted by a varactor diode, and the applied reverse DC voltage is used to control the capacitance value. Figure 5.22 shows the geometry of the final design, which is very similar to the previous one. A prototype of the antenna has been fabricated, using a high quality varactor diode with a tuning range of 0.5 to 2.1 pF for $20 \text{ V} \geq V_{\text{DC}} \geq 0 \text{ V}$ (model MA46H200 from Tyco Electronics). The back-side printed circuit allows to achieve RF-DC isolation for a wide frequency range (see Figure 5.15b), as it is needed for the tuning frequency range of the antenna.

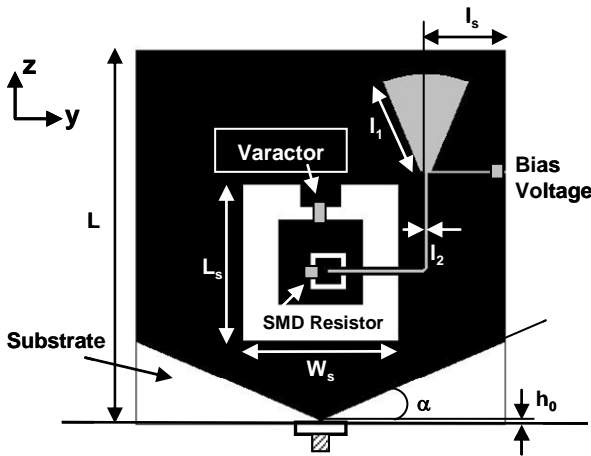


Figure 5.22 Geometry of the proposed UWB antenna ($L=19 \text{ mm}$, $h_0=0.2 \text{ mm}$, $\alpha=23^\circ$, $L_s=10.2 \text{ mm}$, $W_s=9.2 \text{ mm}$, $l_s=3.5 \text{ mm}$, $l_1=5.1 \text{ mm}$, $l_2=0.3 \text{ mm}$). Gray color corresponds to the back side of the antenna.

5.4.1. Results for the UWB tunable antenna prototype

The return loss of the prototype measured for different bias voltages is depicted in Figure 5.23. As observed, the filtering frequency can electronically be tuned by adjusting the reverse bias voltage applied to the varactor. By increasing the DC bias voltage from 0 to 20 V, the capacitance value decreases and the notch band is shifted up from 4.6 GHz to 6.2 GHz. The tuning range for the rejected frequency obtained is thus rather large, and it is even broader than expected from the simulated results.

Radiation patterns have also been measured, at different frequencies and for different bias voltages. Similar patterns to those depicted in Figure 5.19 have been obtained, for different control voltages. In particular, the radiation patterns measured for a tuned rejected band centered at 5.8 GHz can be found in [146]. Nearly omnidirectional radiation patterns in the XY plane are obtained within the whole frequency range.

Measurements of the antenna gain in the entire operating band have also been performed. Figure 5.24 shows the result obtained for a notched band tuned around 5.8 GHz. As observed, a sharp gain decrease is obtained at the tuned frequency, as desired.

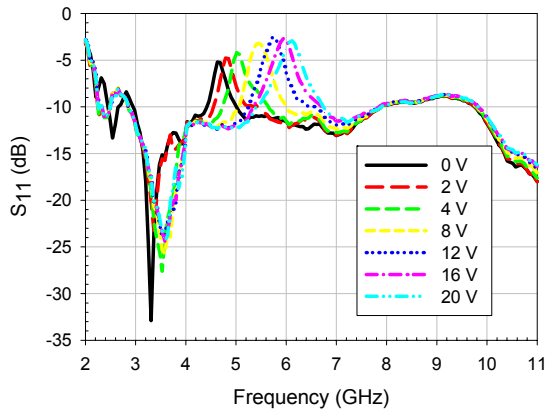


Figure 5.23 Measured return loss of the proposed antenna for different bias voltages.

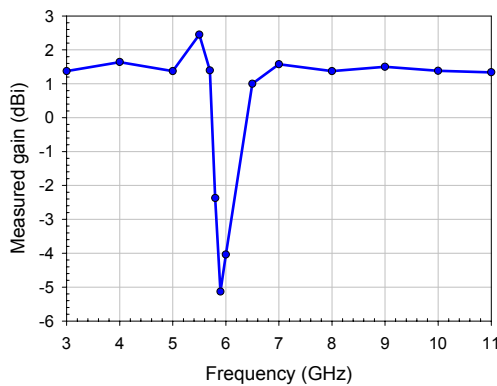


Figure 5.24 Measured gain (dBi) vs. frequency, for a notched band tuned to 5.8 GHz.

Finally, in order to guarantee the suitability of the antenna for UWB systems, time domain measurements have been carried out. Specifically, measurement of the group delay has been performed, since this parameter indicates the linearity of the far-field and provides information about the pulse distortion [127].

Therefore, in order to measure phase linearity, an experimental setup consisting of two identical antennas separated 100 mm has been used. Figure 5.25 shows the measurement setup, where the transmitted signal has been measured over a large range of frequencies by means of an HP8510C network analyzer.

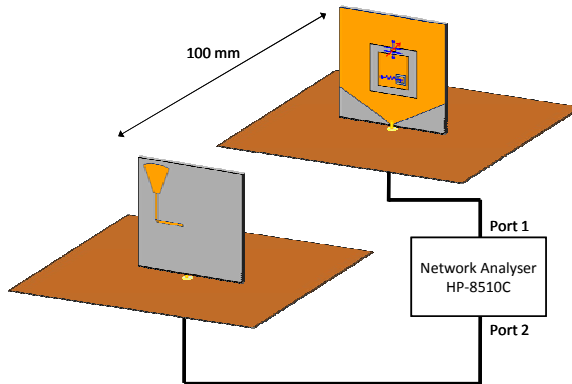


Figure 5.25 Measurement setup for the group delay measurement in the UWB antenna with tunable band-notched behavior prototype.

The measured phase of the transmitted signal when the rejected frequency is tuned to 5.8 GHz is depicted in Figure 5.26(a). As observed, the phase is linear within the whole operating band except at the notched frequency, where a non-linearity is found. The same behavior can be noticed in the group delay measurement, which is shown in Figure 5.26(b). The antenna exhibits a nearly constant group delay in the whole band except at the notched frequency. However, this result is as expected, and since the UWB antenna does not work at the rejected frequency, phase linearity in the rest of UWB frequencies is achieved. With these results, the suitability of the proposed antenna for UWB wireless communications is thus fully demonstrated [127].

Consequently, the use of an active device in a planar monopole antenna can be used to increase its functionality in UWB systems. In the proposed design, by means of a control signal, the notch band can easily be tuned within a wide range of frequencies, while maintaining good radiation performance. The phase linearity

of the radiated field is preserved, what guarantees the suitability of the antenna for UWB systems. Moreover, the idea of loading the slot with an active device to control the frequency rejection can be straightforwardly extended to those monopoles whose structure is coplanar to the ground plane and are hence more compact.

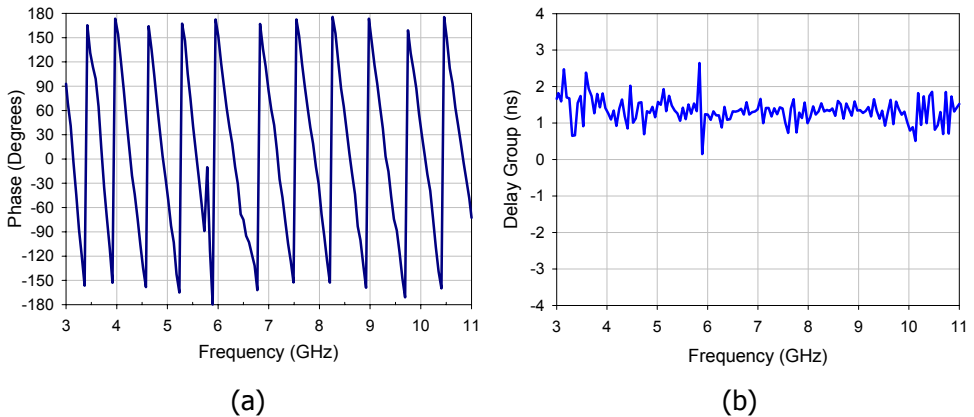


Figure 5.26 (a) Measured S_{21} phase (degrees) vs. frequency; (b) Measured group delay (ns) vs. frequency.

5.5. Conclusions

In the present chapter, characteristic modes have been used to analyze the behavior of a wideband antenna with a narrowband slot embedded in its planar geometry. In contrast to the pure experimental results provided by the references, a physical explanation of the effect of the slot resonance coupled to the antenna modes has been provided, by means of modal analysis and the study of the excitation of the different modes.

Next, the physical understanding of the effect of the coupled resonance has been used to propose a new type of slot, in which the excitation of its resonant mode can be controlled. By electronically controlling the excitation of the slot mode in the planar antenna, the functionality of the wideband antenna with band-notched behavior can be hugely increased.

Moreover, it has also been demonstrated that reactive loading can be used in the slot to control its resonant frequency. If a variable capacitor is inserted in the slot,

its resonant mode can be electronically controlled, in turn increasing the functionality of the antenna.

Thus, two novel antenna designs have been proposed for UWB applications. In the first case, a switching device has been used to implement an UWB antenna with switchable band-notched behavior. Depending on the presence or absence of interfering signals in the antenna operating environment, the filtering function in the antenna can be enabled or disabled electronically. In the second case, a varactor diode has been inserted in the slot, so as to electronically control the value of the reactive loading, and hence implementing an UWB antenna with tunable band notched behavior. In case of inaccuracies during the fabrication process of the antenna or in case of unexpected interferences, the band-notched filter integrated in the antenna can be tuned to the desired frequency.

Prototypes of the two antennas have been fabricated and measured, obtaining excellent results. Indeed, as the antenna is devoted to UWB systems, time domain measurements have been reported for the first time for UWB antennas with active devices. Time-domain measurements confirm the feasibility of using active devices for this application.

Chapter 6

Design of antennas for mobile terminals using the PCB resonant modes

"The most exciting phrase to hear in science, the one that heralds new discoveries, is not 'Eureka!' (I found it!) but 'That's funny...'"

Isaac Asimov

6.1. Introduction

In chapter 4, the excitation of characteristic modes in planar structures was investigated. The study was focused on planar monopole antennas, since this kind of antennas have attracted increasing interest during the last years. Due to their capability to fulfill the sometimes stringent requirements of current wireless standards, planar monopole antennas have been analyzed by means of the Theory of Characteristic Modes. Moreover, novel feeding configurations have been proposed in order to optimize the behavior of the antenna by properly exciting certain modes.

Following with the analysis of planar monopole antennas, chapter 5 has dealt with the study of this kind of antennas when a narrowband resonant structure is coupled to them. Characteristic modes of planar monopole antennas with coupled resonators have been computed and their properties analyzed. Novel designs of reconfigurable antennas have been proposed by combining the information provided by the modal analysis with the use of active devices, therefore vastly increasing the functionality of this kind of antennas.

In the present chapter, however, modal analysis will be applied to mobile terminal antennas, since the design of this kind of antennas has been a very active research topic in recent years. Due to the development of electronics in the last decade, mobile terminals are becoming smaller and smaller, forcing the antennas employed in mobile terminals to have their dimensions reduced accordingly to meet minia-

turization requirements. Unfortunately, when the size of the antenna is decreased, its gain, bandwidth and/or efficiency usually degrade [147]. Additionally, as wireless communications evolve, demanding for increased handset functionality, it is required to simultaneously cover several frequency bands corresponding to the different worldwide wireless standards. Therefore, small dimensions and wideband or multi-band behavior are the main goals to achieve in antenna design for mobile terminals nowadays. Consequently, the design of this type of antennas has currently become extremely demanding.

Extensive research has been carried out in the last two decades to find mechanisms to reduce the size of resonant antennas, in order to make them fit within a given volume inside a handset [148]. This implies that either the antenna has to be electrically small or conformed to a certain shape adapted to the small volume available [149]. As known, the performance of compact antennas is limited by the well-known fundamental limits for small antennas [150][151]. Thus, a great variety of wire and planar antennas, such as IFAs (Inverted-F Antennas), PIFAs (Planar Inverted-F Antennas), monopoles, fractal antennas and slotted patch antennas, among others, have been proposed as broadband or multiband antennas with small dimensions [2]. However, in all these cases the achievable bandwidth is limited by the maximum dimension of the electrically small antenna.

Recently, a new design strategy that shifts away from traditional antenna design philosophies has been proposed for mobile terminals [152]. This new technique is based on considering the Printed Circuit Board (PCB) or chassis of the mobile terminal as part of the antenna. Thereby, the maximum dimension of the radiating structure increases and hence the achievable bandwidth. In [152], the performance of the antenna-PCB combination in mobile phone handsets was analyzed by means of an intuitive decomposition of the structure into two resonant wave-modes: the antenna-element wavemode and the chassis wavemode. Figure 6.1 shows the circuit model of the handset proposed in [152], where the coupling between these two modes is represented. The effect of the mobile chassis on the antenna performance has been investigated, and for the first time it was shown that the bandwidth of the antenna-PCB combination has an important dependency on the PCB resonant wavemode and on the coupling between those modes. Thereby, it was proved that the PCB of the mobile terminal radiates energy at some frequencies, and therefore dimensions of the coupling element could be reduced and radiating properties of the whole structure could improve, if the PCB was properly excited by the coupling element.

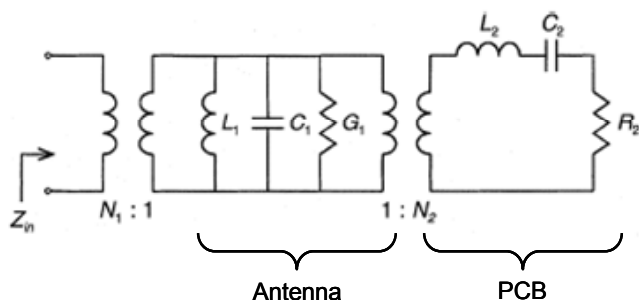


Figure 6.1 Circuit model of the combination of a single-resonant antenna and the mobile terminal PCB [152].

However, as we know from the modal analysis performed in chapter 4, the rectangular plate which shapes the handset PCB does not present a single resonant mode but several ones, which can be computed by means of the Theory of Characteristic Modes. As each resonant mode presents a different resonant frequency and distinct bandwidth properties, the information provided by each mode can be very helpful in the design process [153][154].

In this chapter, characteristic modes of a typical rectangular PCB will be analyzed. Based on the information provided by these modes, their excitation will be investigated, through usage of different topologies of planar elements coupled to the PCB. The suitability of different feeding configurations will also be analyzed, and some designs based on coupling element-PCB combinations will be proposed. The study will be focused not only in the design of handset antennas, but also in antennas for other kinds of devices, such as PDAs or PCMCIA cards for laptops, which can also be based on the use of the PCB or chassis to radiate. To conclude, a general design procedure will be sketched, which summarizes some important design considerations.

Some part of the work presented here was developed at the Department of Antennas & EM Modeling of IMST GmbH., a German research company very experienced in the design and development of antennas for mobile terminals. The aim of this collaboration was to connect research in the field of antenna design for mobile terminals with more practical aspects, in order to provide design methodologies and results according to market requirements. Moreover, the IMST professionals' wide experience in manufacturing and measurement techniques was very valuable to improve the fabrication method and measurement of different prototypes of mobile terminal antennas. Also the use of the FDTD-based commercial electromagnetic 3D simulator EMPIRE™, developed by IMST, was very useful to compare results with those obtained by means of other CAD tools.

6.2. Characteristic modes of a mobile handset rectangular PCB

Usually, the PCB of a mobile handset consists of a rectangular plate of some dimensions, typically $100 \times 40 \text{ mm}^2$. In chapter 4, the characteristic modes of a differently sized rectangular plate were computed, and the normalized current distributions of the first six modes were depicted in Figure 4.24. Also the associated characteristic angle was plotted in Figure 4.27.

If we consider a rectangular plate with different dimensions to those used in chapter 4, for example a PCB with the aforementioned typical dimensions of $100 \times 40 \text{ mm}^2$, similar current distributions are obtained for the characteristic modes, as discussed in [154]. Modal properties are also very similar, except for the resonant frequencies, which are obviously modified when dimensions change.

Figure 6.2 shows the characteristic angle associated to the eigenmodes of a rectangular PCB of $100 \times 40 \text{ mm}^2$ in free space, where the modes have been numbered according to the same numbering scheme of chapter 4. Thus, mode J_0 corresponds to the first special non-resonant mode, which forms a loop on the PCB surface; mode J_1 presents a full horizontal current distribution along the PCB, while mode J_2 presents a vertical current distribution along the shorter dimension of the PCB. Finally, mode J_3 presents horizontal and vertical current distribution with a null of current at the center of the PCB, while mode J_4 exhibits a horizontal current distribution with a null at the center of the chassis. As the length of the PCB is larger than that of the rectangular plate considered in chapter 4, the resonances of characteristic modes are consequently shifted down to lower frequencies. As it can be observed in the figure, horizontal current modes J_1 and J_4 have the lowest resonant frequency and exhibit very wide bandwidth, since their characteristic angle remains very close to 180° for a wide frequency range. On the other hand, modes J_2 and J_3 resonate at higher frequencies, whereas mode J_0 does not resonate.

Therefore, from the analysis of characteristic modes on the rectangular chassis it can be concluded that, due to the appealing behavior exhibited by the horizontal current modes, these will be in principle more suitable to be excited in the PCB in order to obtain optimum radiation behavior.

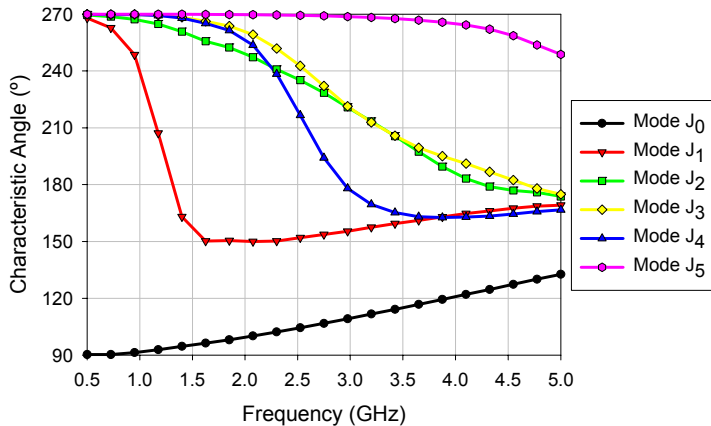


Figure 6.2 Characteristic angle variation with frequency for the current modes of a rectangular plate of $100 \times 40 \text{ mm}^2$ in free space.

Once the resonant modes of the handset PCB are extracted and its properties identified, the selection of an appropriate feeding or coupling mechanism to excite those modes having more interesting properties is crucial. This will be investigated in the following sections, where different experiments will be performed with coplanar and non-coplanar coupled elements in order to analyze the excitation of modes in the handset PCB. As a result, some design guidelines for the feeding of wideband antennas based on the use of the PCB resonances will be established.

6.3. Investigations in the excitation of the PCB characteristic modes

6.3.1. Experiments with coplanar resonant elements

Let us investigate the effect of the insertion of coplanar elements on the excitation of the PCB characteristic modes. As concluded in the previous section, horizontal current wavemodes are the best candidates to be excited in the PCB. Consequently, in order to excite these current modes, different types of coplanar structures may be coupled to the PCB. Depending on the arrangement of these coupling structures, different modes will be excited.

6.3.1.1. Insertion of two IFAs at the longer edges of the PCB

In the first case, two resonant Inverted-F Antennas (IFAs) will be placed at the longer edges of the PCB, in order to excite horizontal current modes in the ground plane [153]. The configuration is shown in Figure 6.3, where two resonant elements are used instead of a single one, so as to keep the symmetry of the structure with respect to the x -axis.

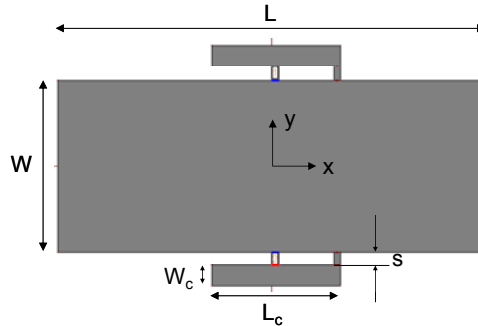


Figure 6.3 PCB with two coplanar IFAs designed to couple horizontal modes in the PCB ($L=100$ mm; $W=40$ mm; $L_c=30$ mm; $W_c=4.8$ mm; $s=3.2$ mm).

As discussed in chapter 5, the insertion of coupled resonators may somehow modify the properties of some of the isolated PCB characteristic modes [17][153]. Essentially, the location of the resonant IFAs will affect the properties of those modes whose current distribution is disturbed by the presence of the coupled structures. A comparative of the characteristic angle for the modes of the rectangular PCB with and without coupled IFAs is shown in Figure 6.4. As observed, modes J_0 , J_3 and J_6 (which exhibits a horizontal current distribution with two nulls of current along the PCB) remain mostly unaffected by the insertion of the coupling elements, whereas mode J_1 resonance is slightly shifted up in frequency and its radiating behavior degrades from 2.5 GHz on. Mode J_2 is slightly affected at lower frequencies, with a reduction in smoothness of the characteristic angle slope, but with no alteration of its resonant frequency. Finally, modes J_4 and J_5 are the most affected ones by the insertion of the coupling elements, since its resonant frequency is shifted down, due to the coupling of the IFAs and the proximity of their resonance, which manifests itself in the existence of an additional IFA mode. As seen, dimensions of the IFAs are designed to achieve resonance at 2.75 GHz ($L_c \approx \lambda/4$).

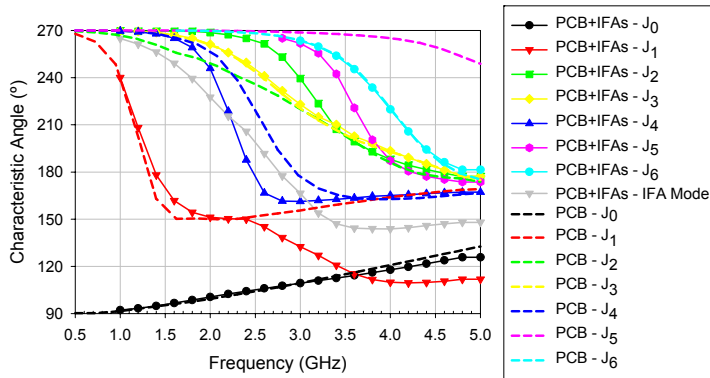


Figure 6.4 Characteristic angle variation with frequency for the current modes of the PCB with and without two coupled resonant IFAs, in free space.

Once the modal analysis has been performed, the next step is to analyze the excitation of the modes by means of the voltage probes inserted at the IFAs, as shown in Figure 6.3.

In Figure 6.5 the input impedance and the input admittance computed with Zeland IE3D™ at each of the IFA antennas are represented graphically. For each port, the input impedance has been computed by means of the simulated Z-parameters as:

$$Z_{in} = Z_{11} + Z_{12}$$

From the information presented in chapter 4, the input impedance or admittance plots, together with the total surface current distribution graphs at different frequencies, are very useful tools for the identification of the modes excited in the structure. For that purpose, the power radiated by each mode at every frequency can also be studied, alternatively to the modal admittances, as it allows for an easier identification of several contributions from different modes to the total current at any given frequency.

In Figure 6.6, the contribution of each mode to the total radiated power of the antenna has been computed. As observed, mode J_1 is excited from 1 GHz on, although its main contribution is around 3.4 GHz, due to the best coupling to the feeding probes there. Between 2 GHz and 2.6 GHz, mode J_4 is dominant, whereas mode J_5 dominates around 3.5 GHz. Therefore, as observed in the input admittance graph of Figure 6.5, mode J_4 and mode J_5 are combined with mode J_1 between 2 and 3.5 GHz, where good matching is achieved. After the resonance of mode J_5 , a higher order mode (mode J_7) –which exhibits horizontal current distribution with three nulls– starts to appear. Coupling of the *IFA Mode* is not observed.

Figure 6.7 depicts the total current distribution computed with IE3D in the surface of the structure, at six different frequencies. Arrows have been plotted in order to facilitate the identification of current distribution. As observed, the current distribution in the PCB at 1 GHz resembles that of mode J_{1i} , though the mode is not highly coupled at this frequency, as it does not resonate but presents an inductive behavior at the excitation port. At 2 GHz an anti-resonance occurs, and mode J_4 starts to appear, which couples immediately with mode J_5 . At 3.5 GHz the dominant mode in the PCB is the mode J_5 combined with mode J_1 . Above this frequency range, a higher order mode (mode J_7) presenting three nulls in the horizontal direction starts to appear, as observed in the current distribution at 4.4 GHz.

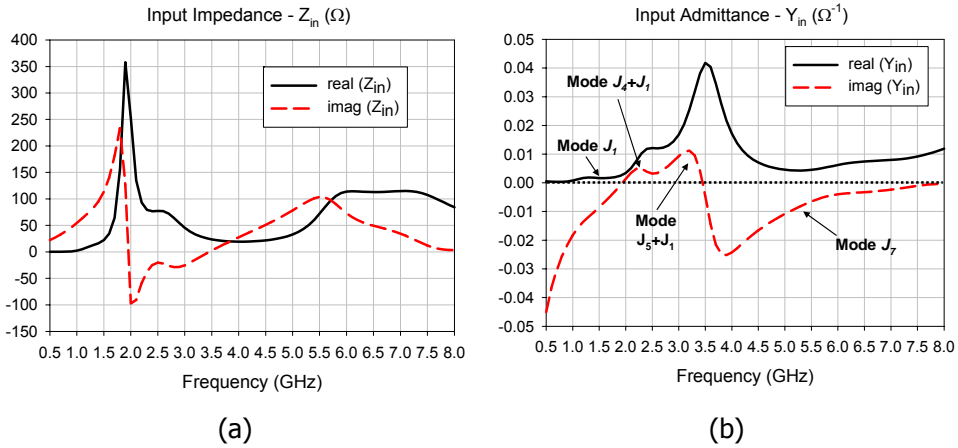


Figure 6.5 (a) Input impedance computed with IE3D at each of the IFA ports; (b) Input admittance with the contribution of each mode.

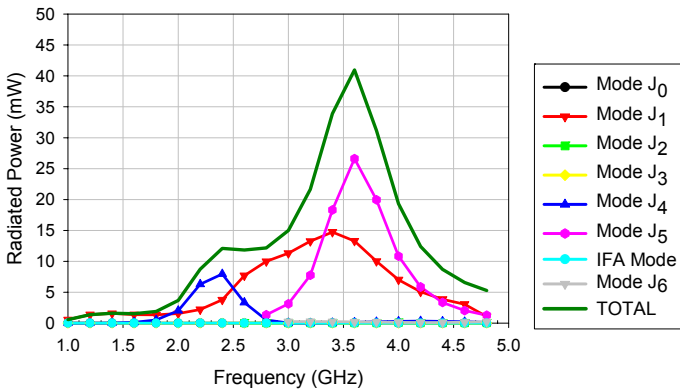


Figure 6.6 Contribution of the different modes to the total power radiated by the structure shown in Figure 6.3.

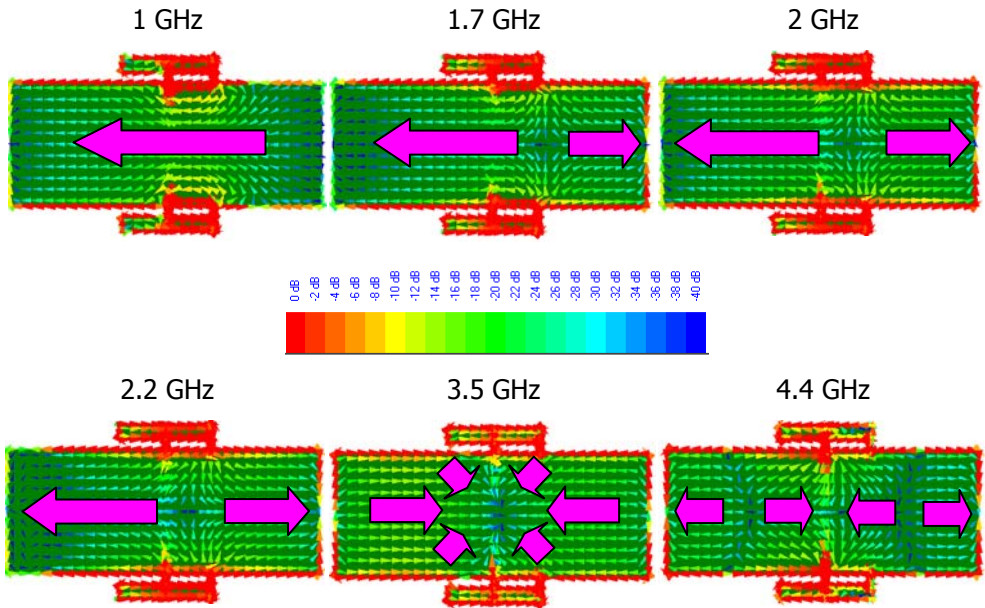


Figure 6.7 Total current distribution computed with IE3D in the structure shown in Figure 6.3, at different frequencies.

As observed in the input impedance plot, by means of the combination of PCB modes J_4 , J_5 and J_7 with mode J_{11} , the impedance bandwidth of the isolated resonant IFA antenna can be increased. Figure 6.8 represents the return loss obtained at each of the IFA ports, taking a reference impedance value of 50Ω . From the figure, it can be seen that a very wide impedance bandwidth of 53% is obtained, considering a maximum value for return loss of -6 dB, as usual for handset antennas. For the sake of comparison, the return loss obtained when the PIFA resonates at lower frequencies ($L_c=36 \text{ mm}$) is depicted as well in the figure.

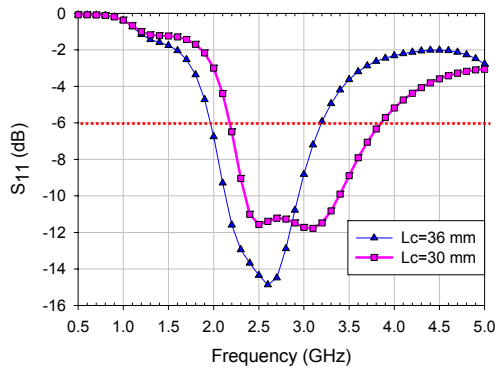


Figure 6.8 Return loss vs. frequency at each of the IFA ports, for an impedance reference value of 50Ω .

Therefore, it has been seen that due to the location of the coupled resonant structures, only modes J_1 , J_4 , J_5 and J_7 are excited in the PCB. These modes are combined satisfactorily obtaining good impedance matching around 3 GHz. However, due to the feeding configuration and location, the horizontal mode J_1 is not coupled appropriately in the PCB at lower frequencies. As observed in Figure 6.5(a), the impedance of this mode at lower frequencies is always inductive at the input ports, hence not resonating. Moreover, because of the symmetry of the feeding configuration, excitation of mode J_0 , mode J_2 and mode J_6 is prevented.

6.3.1.2. Insertion of a coplanar plate at the shorter edge of the PCB

In the previous case, excitation of mode J_1 was not achieved at lower frequencies, since the location of the feeding ports was not optimal to match the impedance of this mode at these frequencies. As seen in chapter 4, Figure 4.24, mode J_1 presents a very intense current at the longer edges of the PCB, what entails a very low level of impedance there. Therefore, although the feeding arrangement based on the use of two resonant IFA structures was suitable to force the current distribution of mode J_1 (see Figure 6.6), the real part of the input impedance at this point was too low, and no appropriate mode coupling was obtained.

In order to obtain a proper coupling to horizontal mode J_1 , another configuration based on a metallic plate placed in one of the shorter edges of the PCB has been investigated. The geometry of the structure is shown in Figure 6.9, where the overall structure is fed by means of a voltage gap generator between the PCB and

the plate. In contrast to the previous case, a metallic plate is used instead of an IFA antenna, in order to avoid the excitation of mode J_2 (vertical mode) in the PCB.

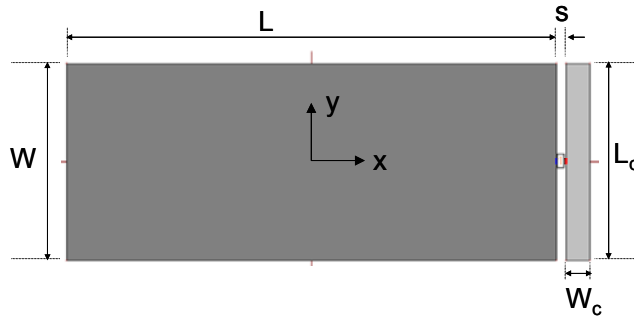


Figure 6.9 PCB with a coplanar metallic plate designed to couple horizontal modes in the PCB ($L=100$ mm; $W=L_c=40$ mm; $W_c=4.8$ mm; $s=2$ mm).

As in the previous case, the insertion of the metallic plate may modify some properties of the characteristic modes corresponding to the isolated PCB. In Figure 6.10, a comparative of the characteristic angle associated to the modes of the rectangular PCB with and without a coupled plate is shown. As observed, modes J_0 , J_2 , J_3 and J_5 are barely affected by the insertion of the conducting plate, whereas mode J_1 resonance is slightly shifted down in frequency and its bandwidth behavior degrades from 2.5 GHz on. Mode J_4 is affected to a large extent by the insertion of the coplanar plate, since its resonant frequency is considerably shifted down, and the same happens to mode J_6 , which exhibits a horizontal current distribution with two nulls of current along the PCB. This means that the coplanar plate acts similarly to a load for these modes, hence shifting their resonant frequency. Nevertheless, their radiating bandwidth remains wide, as observed in the figure. Finally, since the metallic plate resonates around 3.75 GHz ($L_c \approx \lambda/2$), an additional mode associated to the resonance of the plate appears, which is called *Plate Mode*.

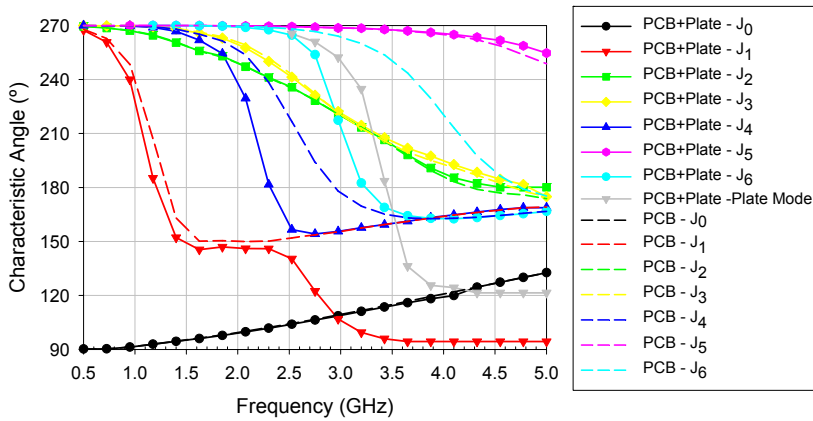


Figure 6.10 Characteristic angle variation with frequency for the current modes of the PCB with and without a coupled metallic plate, in free space.

In Figure 6.11, the input impedance and the input admittance computed with Zealand IE3D™ are represented graphically, in order to identify the modes excited in the structure. For this purpose, the information provided by the power radiated by each mode and the total radiated power at different frequencies, shown in Figure 6.12, is also used. As observed, mode J_1 is dominant in the structure up to 1.5 GHz, where mode J_4 starts to appear. A resonance is observed at 2.4 GHz, which is due to mode J_4 as observed in the plot associated to the radiated power and also in the current distribution graphs shown in Figure 6.13. Then mode J_6 , which exhibits two nulls of current along the PCB, is excited, whereas coupling of the *Plate Mode* is not observed. As shown in Figure 6.12, contribution of mode J_1 is important at 3.75 GHz, since at this frequency the coupling of the feeding probe to this mode is optimum.

The input impedance plot in Figure 6.11(a) shows that a constant level of resistance around 25Ω appears above 0.9 GHz, due to absence of strong anti-resonances. However, the reactance takes several values within a wide range, what prevents obtaining a good impedance matching within a wide range of frequencies. Figure 6.14 represents the return loss obtained for a reference value of 50Ω , showing a quite reduced bandwidth (below 1 GHz) for a reference value of -6dB .

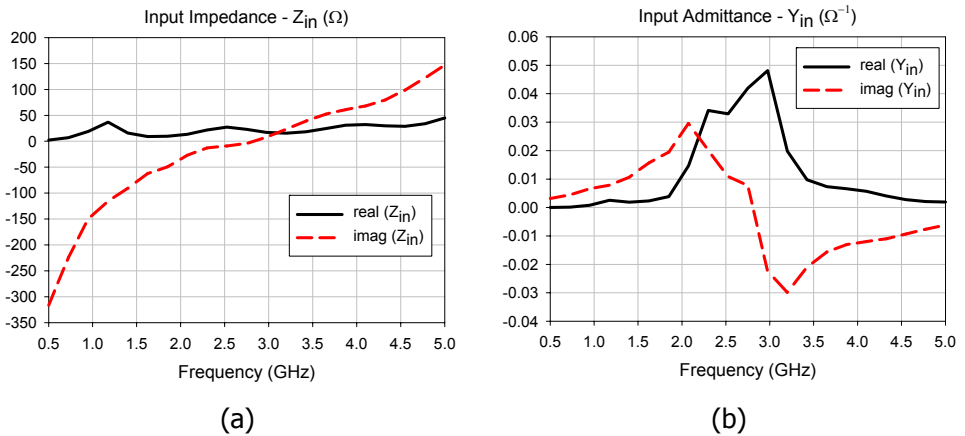


Figure 6.11 Results computed with IE3D: (a) Input impedance; (b) Input admittance, with the contribution of each mode.

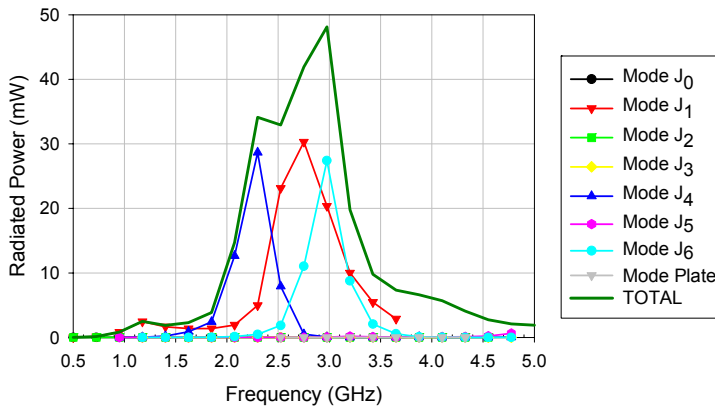


Figure 6.12 Contribution of the different modes to the total power radiated by the structure shown in Figure 6.9.

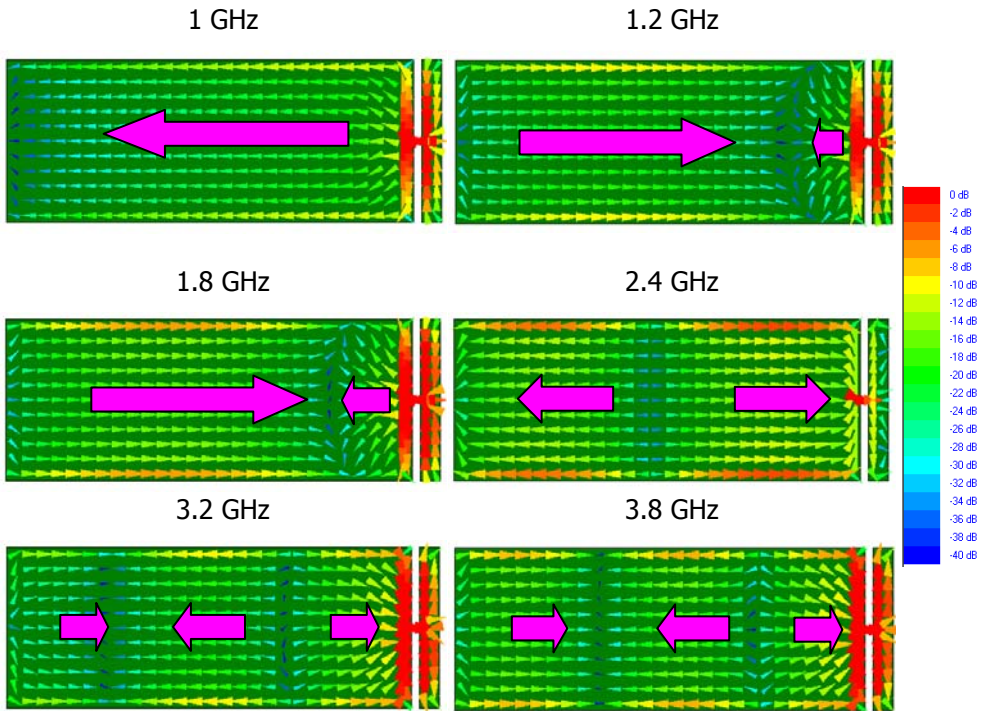


Figure 6.13 Total current distribution computed with IE3D in the structure shown in Figure 6.9, at different frequencies.

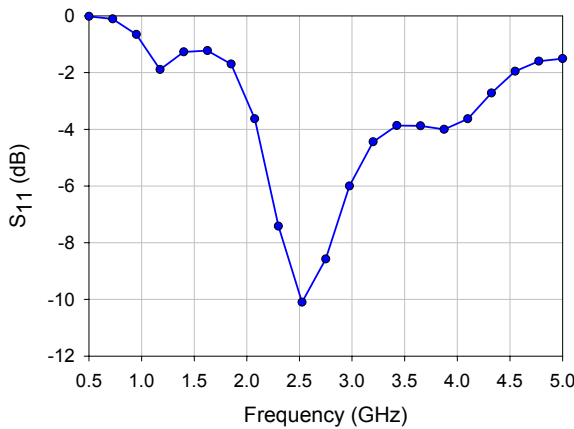


Figure 6.14 Return loss vs. frequency at the input port of the PCB with a coupled metallic plate, for an impedance reference value of 50Ω .

Therefore, although horizontal mode J_1 is fully excited with this structure and is better coupled in the PCB than in the previous case (obtaining higher resistance values when this mode is excited), optimal matching is not achieved for this mode at lower frequencies. As observed in the input impedance plot, mode J_1 presents capacitive behavior for its reactance at these lower frequencies.

In order to increase the excitation of mode J_1 , one possible solution would be using a pair of coplanar plates fed in opposite phase, as shown in Figure 6.15. Thereby, a strong excitation of horizontal current modes is forced in the PCB. This can be observed in the normalized total current distribution shown in Figure 6.16, where current associated to mode J_1 at lower frequencies is much intense than in the previous case. Moreover, it is observed that due to symmetrical excitation, only horizontal modes presenting even symmetry with respect to the y -axis are excited in the PCB.

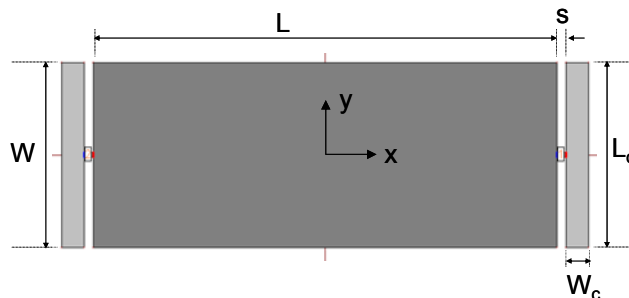


Figure 6.15 PCB with two coplanar metallic plates ($L=100$ mm; $W=L_c=40$ mm; $W_c=4.8$ mm; $s=2$ mm).

The input impedance at each of the input ports, computed as $Z=Z_{11}+Z_{12}$, is depicted in Figure 6.17, and it is compared with the input impedance obtained for the case of using a single plate coplanar to the PCB. Excitation of different modes can be appreciated in the input impedance plot as a series of peaks on the resistance curve. In conclusion, by means of the use of two plates, excitation of horizontal modes J_1 and J_6 increases, as higher values of resistance are obtained around their resonant frequency. Moreover, it is observed that excitation of odd mode J_4 is avoided when using two coplanar plates, because of the symmetry imposed by the feeding configuration.

Nevertheless, due to the fact that the feeding configuration type (voltage gap generators) and location has not changed, reactance values are very similar when using one or two coplanar plates. Although in both cases horizontal modes are excited in the PCB (as commented, more intensively with two plates), mode coupling is not optimal, since no good matching can be obtained, due mainly to the reactance values obtained at the input ports. Figure 6.18 shows the return loss

referred to 50Ω obtained for the structure with two coplanar plates, where the two bands provided by the excitation of mode J_1 and mode J_6 are distinguished. However, matching at the input ports is not enough to achieve an acceptable value for the return loss.

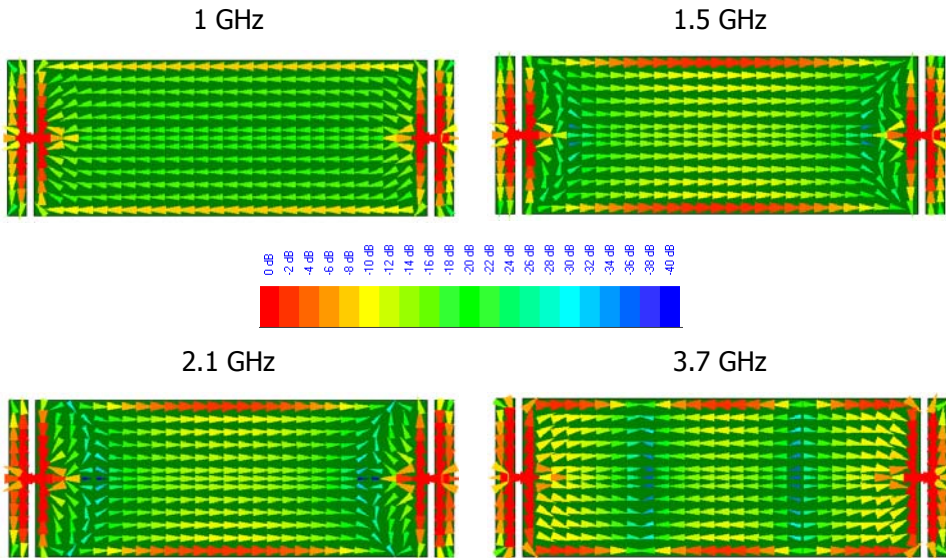


Figure 6.16 Normalized total current distribution computed with IE3D in the structure shown in Figure 6.15, at different frequencies.

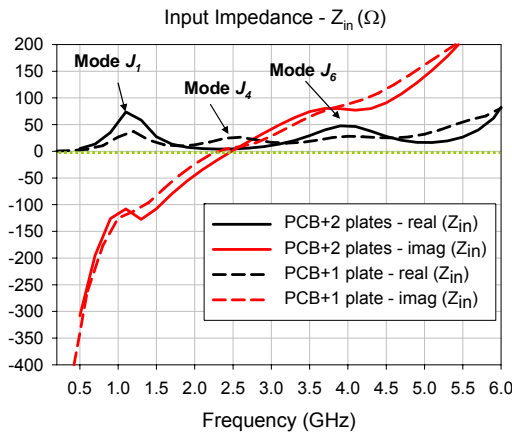


Figure 6.17 Input impedance at each of the input ports of the structure shown in Figure 6.15, with the contribution of each mode.

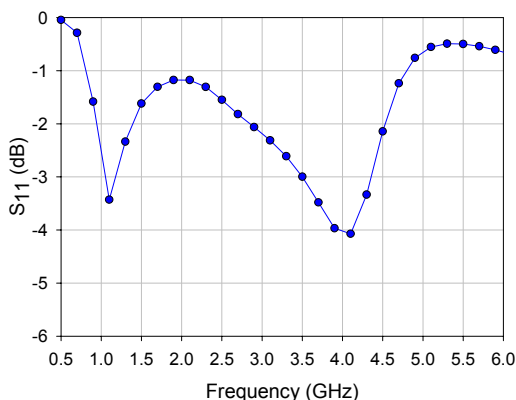


Figure 6.18 Return loss referred to 50Ω obtained for the structure shown in Figure 6.15.

As a conclusion of this section, it has been demonstrated that the placement and type of the coupling elements and the feeding configuration fully determines the excitation of the PCB characteristic modes. However, it has been observed that although the feeding arrangement forces the excitation of the desired modes, the impedance level obtained at the input ports is not always optimal, especially for reactance values. Therefore, together with the use of an optimal arrangement of coupling elements to force the excitation of desired modes, some additional mechanism to match impedance levels should be provided.

6.3.2. Experiments with non-coplanar coupling elements

In the present section, experiments concerning the use of non-coplanar coupled elements will be presented. The objective of using non-coplanar elements instead of coplanar elements is to provide a mechanism for adjusting the input impedance value of the antenna, so as to match the traditional 50Ω characteristic impedance of the feeding cable.

6.3.2.1. Use of a coupled plate at the shorter edge of the PCB

Let us insert a coupled plate at a certain height from the PCB, as depicted in Figure 6.19. The plate is located near the shorter edge of the PCB and its shape has been modified so as to efficiently couple to horizontal current modes, which present a maximum of current at the longer edges of the PCB. Only one coupling element has been used instead of two, since this is preferred for a practical implementation

of a mobile terminal antenna. Furthermore, the feeding mechanism has been implemented in this case by means of a strip connected to a voltage gap generator. As observed, the length of the strip (L_{feed}) can be modified conveniently to achieve optimal impedance levels.

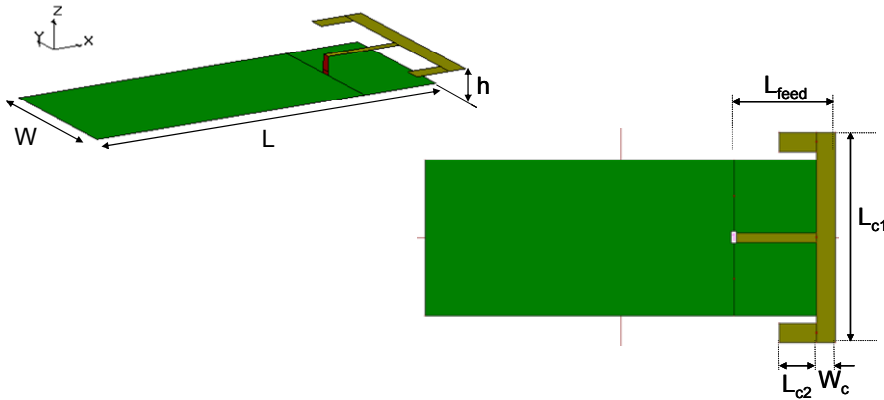


Figure 6.19 Perspective and top views of the PCB with a coupled plate ($L=100$ mm; $W=40$ mm; $h=5$ mm; $L_{c1}=53.6$ mm; $L_{c2}=9.6$ mm; $W_c=4.8$ mm; $L_{feed}=21$ mm).

The input impedance computed with IE3D for the structure shown in the previous figure is represented in Figure 6.20. As observed, in this case the strip length (L_{feed}) has been adjusted to obtain good impedance matching for mode J_1 , obtaining a resonance around 1 GHz. The return loss is plotted in Figure 6.21, where it can be seen that an operating band around the resonance of mode J_1 is obtained. The normalized total current distribution is depicted in Figure 6.22 for different frequencies. At 1.1 GHz, it is possible to appreciate the excitation of mode J_1 in the PCB, which presents very intense current because it is at resonance. At 1.5 GHz, mode J_4 starts to appear, which dominates until mode J_6 , which exhibits two nulls of current along the PCB, appears at 2.7 GHz. As observed in the input impedance, a strong anti-resonance occurs between the transition from mode J_4 to mode J_6 , what degrades the impedance bandwidth. Resonance of mode J_6 takes place around 4 GHz, and above this frequency, a higher order horizontal mode (J_7) presenting three nulls of current starts to appear in the PCB, producing a notable anti-resonance at 4.6 GHz, which degrades once again the bandwidth performance.

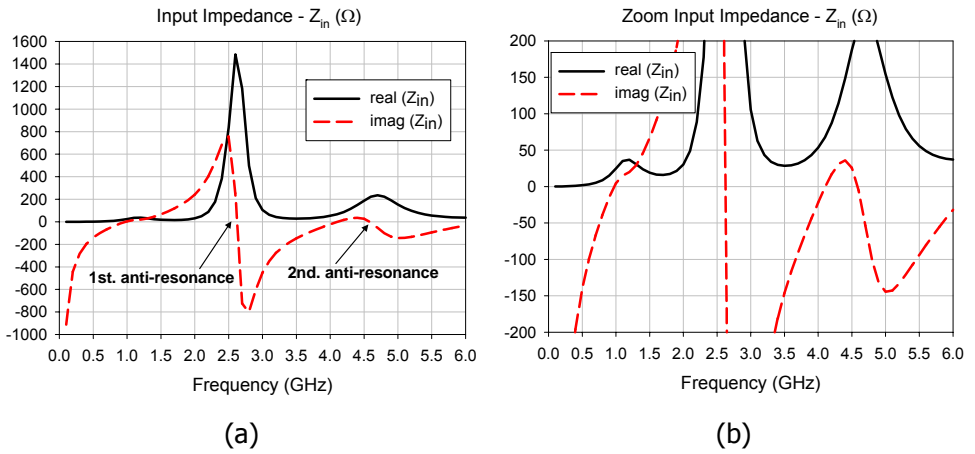


Figure 6.20 (a) Input impedance computed with IE3D, for the structure shown in Figure 6.19; (b) Zoom of the input impedance.

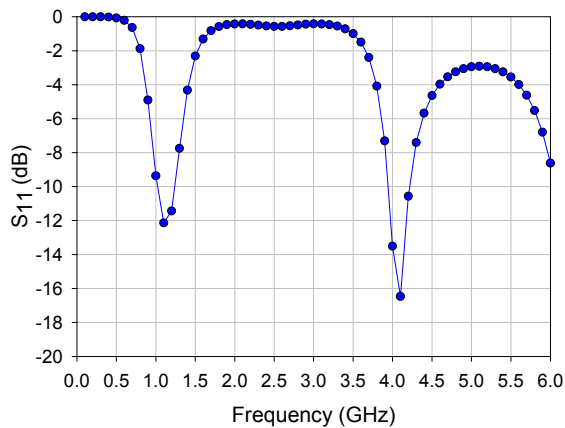


Figure 6.21 Return loss referred to 50Ω obtained for the structure shown in Figure 6.19.

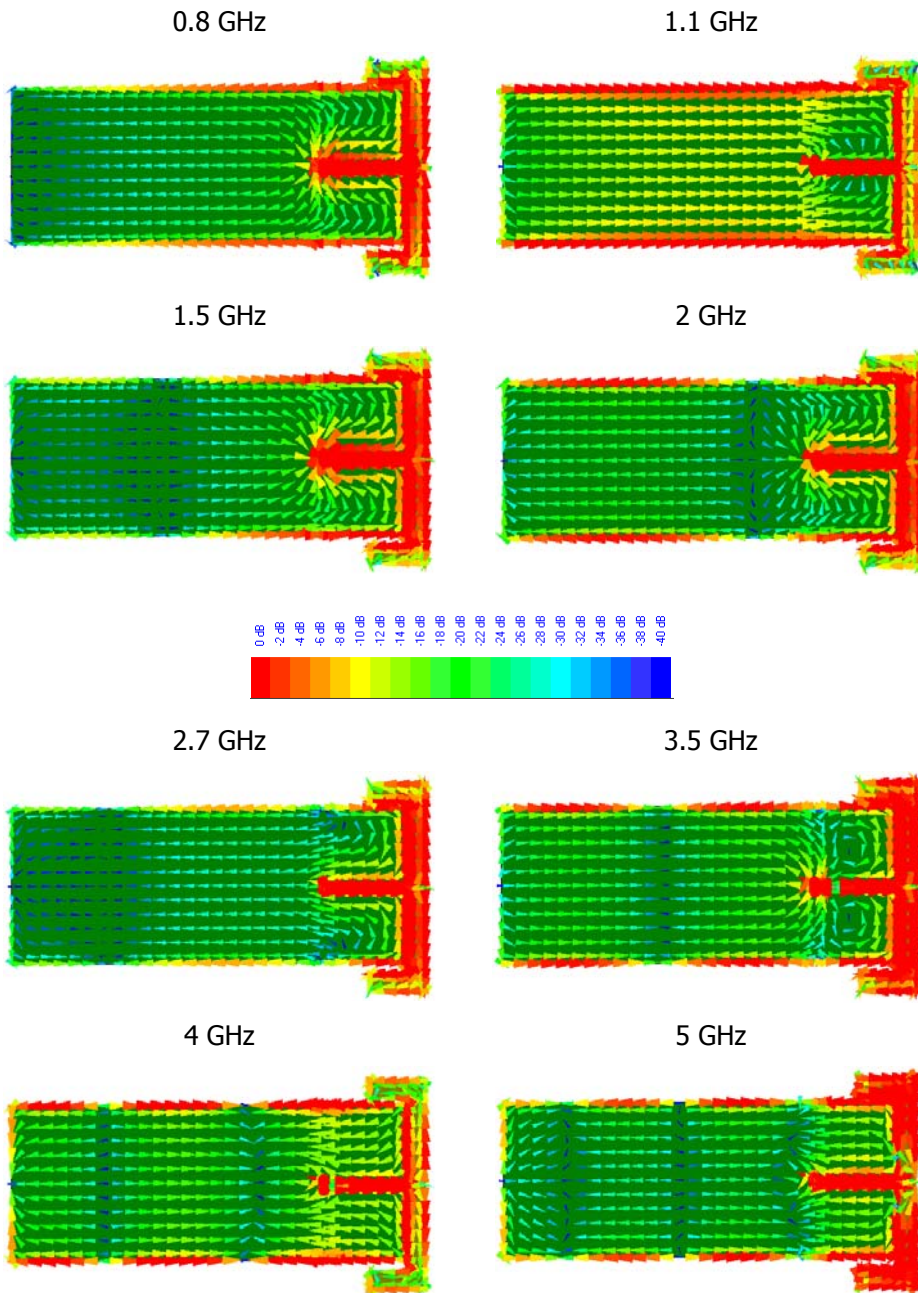


Figure 6.22 Normalized total current distribution computed with IE3D for the structure shown in Figure 6.19, at different frequencies.

Therefore, by means of a feeding mechanism that allows adjusting an appropriate input impedance level, optimal coupling to certain modes can be obtained. In Figure 6.23, the return loss vs. frequency computed for different values of L_{feed} is depicted. By varying this parameter, the impedance level at the input port changes, according to the variation of the modal current distributions. Note that modal currents are not uniform within the PCB. Thus, by adjusting parameter L_{feed} good matching for different modes can be obtained, as observed in the figure.

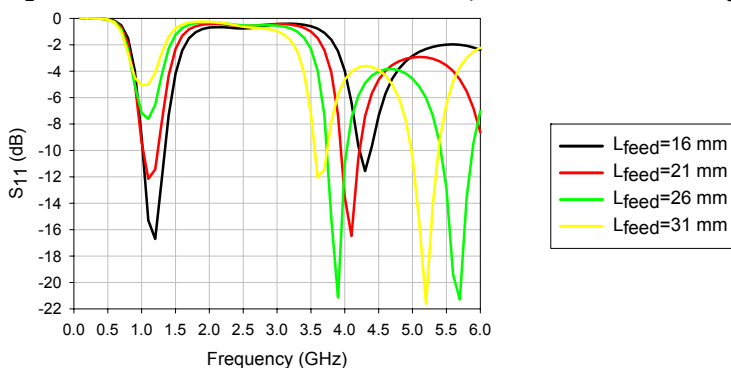


Figure 6.23 Return loss referred to 50Ω obtained for the structure shown in Figure 6.19, for different values of L_{feed} .

Consequently, not only the location of the coupling structures and the feeding symmetry is crucial to properly excite characteristic modes in the PCB, but also an appropriate input impedance matching is necessary to couple desired radiating modes, and take the most of the input power provided by the excitation source.

This is in accordance with the investigations carried out by Helsinki University of Technology (HUT) in [155]-[157], which propose the use of compact non-resonant coupling elements to optimally couple energy to the PCB modes, as a basis for the design of a circuit for matching the impedance of the coupling element-PCB combination at resonance. The knowledge of the current distribution of the PCB characteristic modes is crucial to determine the optimum location and shape of the coupling structures. Once the energy is efficiently coupled to the PCB mode(s), a matching circuit can be designed to match the input impedance at the desired frequency. If multiple bands must be covered, multiple matching circuits may be designed.

Nevertheless, it has been observed that some of the characteristic modes present very wideband radiating properties. It is expected that with the use of matching circuitry it would be difficult to achieve very wideband behavior, unless the circuit complexity is considerably increased. In the next section, strategies for increment-

ing the bandwidth of the PCB will be investigated, and other possible feeding techniques will be analyzed.

6.3.2.2. Use of a folded-PCB structure

In order to excite horizontal current wavemodes in the PCB, a radiating structure consisting of a folded PCB can be proposed. The geometry of the structure, resembling a PIFA with a shorting wall, is depicted in Figure 6.24. As observed in the side view of the structure, a probe-fed connecting the lower and upper plates is used to excite the structure.

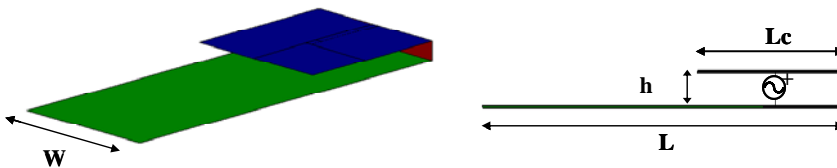


Figure 6.24 Perspective and side views of the folded PCB antenna ($L=100$ mm; $W=40$ mm; $L_c=49.15$ mm; $h=10$ mm).

In this case, folding the chassis implies modifying the geometry of the antenna and hence the properties of the characteristic modes of the PCB will be slightly modified, compared to those of the isolated chassis. Although the modal current distributions of the folded chassis are similar to those of the isolated chassis, the characteristic angle associated to the modes changes, especially for the first longitudinal mode, due to the capacitive effect generated by the folded section.

After folding the PCB, eigenmodes have been newly computed for this structure [17]. The resulting normalized current distribution at first resonance (1.1 GHz) for the first six characteristic modes is represented in Figure 6.25. Characteristic currents have been represented with arrows for a better understanding of the current flow. As depicted in the figure, modal current distributions are very similar to those of the isolated rectangular chassis analyzed in chapter 4. There are two modes, J_{01} and J_{02} , with currents forming closed loops, which are special non-resonant modes. Other modes, such as J_1 , J_3 and J_4 , exhibit longitudinal currents along the structure. Mode J_1 is again the fundamental mode, and it flows uninterrupted between the open ends on the upper and bottom plates. This fundamental mode resonates when the current path is approximately half a wavelength. Modes J_3 and J_4 are higher order longitudinal modes presenting one and two current nulls along the structure, respectively. Finally, mode J_2 is the only one that presents transverse currents.

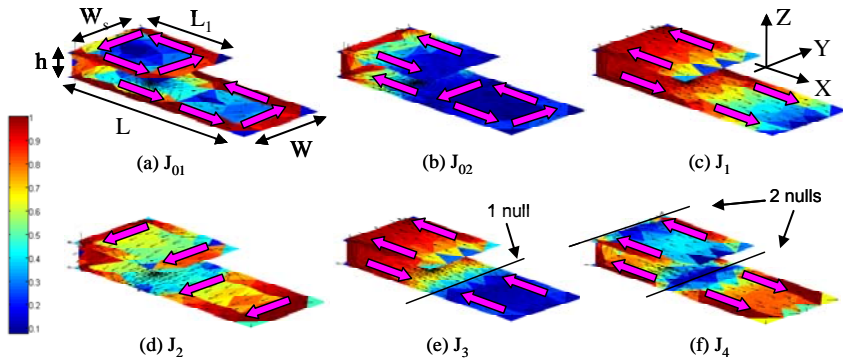


Figure 6.25 Normalized current distribution at first resonance ($f = 1.1$ GHz) of the first six characteristic modes J_n of a radiating folded PCB.

Figure 6.26 plots the characteristic angles associated to the current modes depicted in the previous figure as a function of frequency. As shown in the figure, the properties of characteristic angles change when compared to those of the isolated chassis shown in Figure 6.2. As in the rectangular chassis, modes J_{01} and J_{02} do not resonate and present inductive contribution at every frequency. Longitudinal current modes, J_1 , J_3 and J_4 resonate at 1.1 GHz, 1.7 GHz and 3.25 GHz, respectively, while the transverse mode J_2 resonates at 3.5 GHz. Note that modes J_1 and J_3 resonate at a lower frequency than in the isolated chassis, due to the effect of the capacitive coupling when the chassis is folded. Wide bandwidth is still obtained for mode J_3 , in contrast to mode J_1 , whose radiating behavior has become poorer, since it exhibits a characteristic angle curve with steep slope near 180° . Modes J_2 and J_4 are also good radiators and they resonate at higher frequencies. For modes J_1 and J_3 , currents in the parallel plate region flow with opposite phase at the lower and upper plates. This means that there exists some cancellation between these currents flowing similarly as in a transmission line. Conversely, the longitudinal current mode J_4 presents the broadest radiating bandwidth because its currents flow in phase in the parallel plate region, thereby reinforcing its radiation [17].

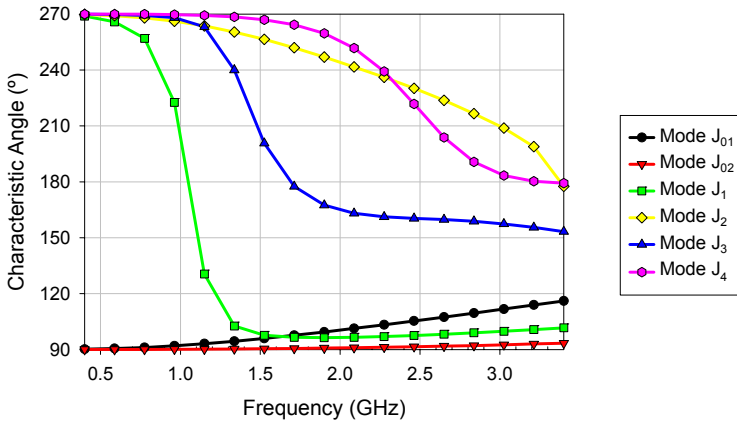


Figure 6.26 Characteristic angle variation with frequency for the first six characteristic modes of the radiating folded PCB.

Therefore, the main effect of folding the PCB is the decrease of the radiating bandwidth of mode J_1 . Figure 6.27 and Figure 6.28 show the input impedance, input admittance and the return loss computed with IE3D for the folded PCB shown in Figure 6.24. The total current distribution at different frequencies is also depicted in Figure 6.29, so as to facilitate the identification of the modes excited at different frequencies. These currents have been computed with electromagnetic simulator Zeland IE3D™.

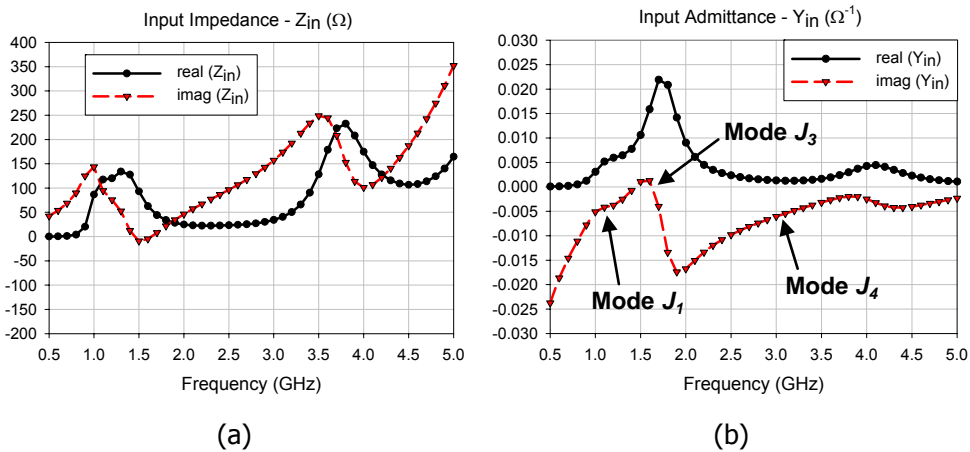


Figure 6.27 Results computed with IE3D for the folded PCB shown in Figure 6.24: (a) Input impedance (b) Input admittance.

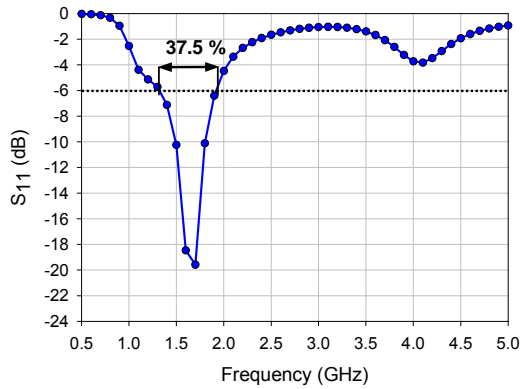


Figure 6.28 Return loss referred to 50Ω computed with IE3D for the folded PCB shown in Figure 6.24.

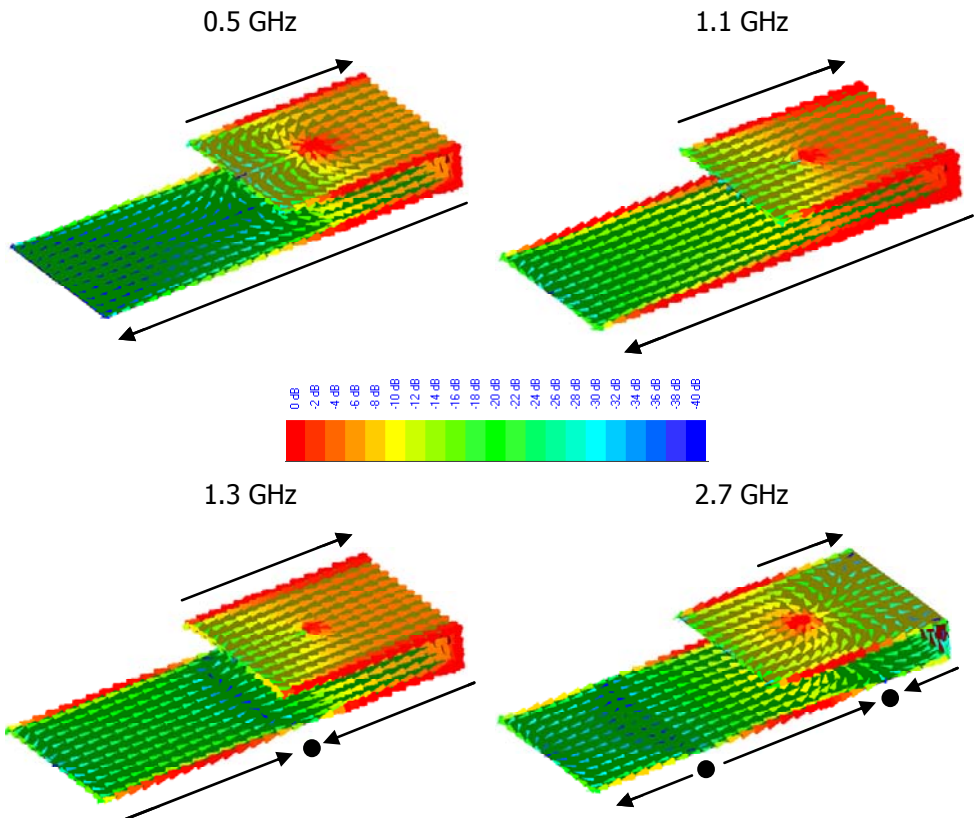


Figure 6.29 Total current distribution computed with IE3D for the structure shown in Figure 6.24, at different frequencies.

Figure 6.27 and Figure 6.29 show how mode J_1 is excited up to 1.2 GHz, which is the frequency where mode J_3 starts to appear, according to plots of the input admittance and total current distribution. Note that transitions between modes in the input impedance graph are barely noticeable in this case, hence rendering the input admittance plot enormously useful, since little changes can easily be appreciated there. As observed, mode J_1 is coupled to the PCB and although it does not resonate due to the inductive behavior produced by the feeding probe, high values of resistance are obtained in the transition to next excited mode J_3 (in the anti-resonance). This mode presents a resonance at 1.6 GHz, whereas mode J_4 becomes dominant at higher frequencies.

Through the use of a probe to excite the structure, moderate impedance bandwidth is obtained for the folded PCB antenna, as shown in Figure 6.28. The feeding arrangement couples modes J_1 and J_3 satisfactorily, and a good transition from mode J_1 to mode J_3 is obtained. Nevertheless, resistance values are too high for a good matching to reference value of $50\ \Omega$, whereas reactance values are also positive and relatively high, due to the inductive behavior of the probe-fed mechanism. Impedance bandwidth at lower frequencies can be improved if matching to other reference values of real impedance. Figure 6.30 plots the return loss computed for several values of impedance, showing different gains in impedance bandwidth when matching to other impedance values. In case more bandwidth is needed, an impedance matching network can be inserted to match these values to the standard $50\ \Omega$. Notice however that although impedance bandwidth is increased when matching to other impedance values, the operating bandwidth is shifted down in frequency.

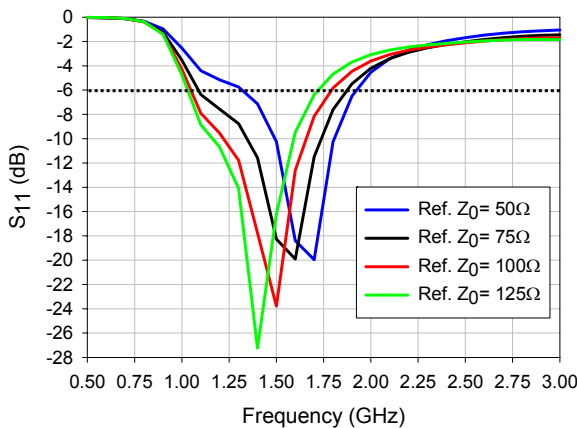


Figure 6.30 Return loss computed for different values of reference real impedance.

6.4. Wideband feeding of the mobile handset PCB

In order to excite the longitudinal current wavemodes in the PCB, a radiating structure consisting of a folded PCB has been proposed [154]. The loop effect of the geometry and the selected dimensions facilitate the excitation of longitudinal modes in the structure, as far as an adequate feeding configuration is selected.

In previous section, a common probe was used to feed the antenna. This feeding arrangement creates a voltage gap difference between the upper and lower plates of the PCB, which forces the excitation of horizontal modes that present wideband radiating behavior. With this design, moderate bandwidth is obtained, as the coupling of horizontal modes and their proper matching only occurs in a certain band at lower frequencies. As observed in Figure 6.27(a), above 2 GHz the inductive behavior at the input port increases with frequency, and consequently the impedance matching and coupling of higher order modes to the probe-feed is not satisfactory. Thereby, it can be concluded that the probe exhibits narrowband behavior and is not optimum to satisfactorily couple higher order horizontal modes, hence limiting the possibility to obtain a larger bandwidth.

Therefore, an optimum feeding configuration should produce a voltage difference in the structure so as to favor the appearance of the current distribution associated to longitudinal modes, and it should also present wide matching bandwidth in order to make the most of the behavior of mode J_1 and especially of the wideband modes J_3 and J_4 . Gradual transition to the successive resonant modes should be provided as well. Some references can be found in the literature, which propose the use of alternative feeding mechanisms for planar structures to increase the impedance bandwidth [158]-[161]. They consist basically in planar plates with different shapes, whose dimensions can be adjusted for wideband matching. These structures can therefore be considered as wideband feeding mechanisms. Figure 6.31 shows some examples of wideband feeding mechanisms for planar antennas.

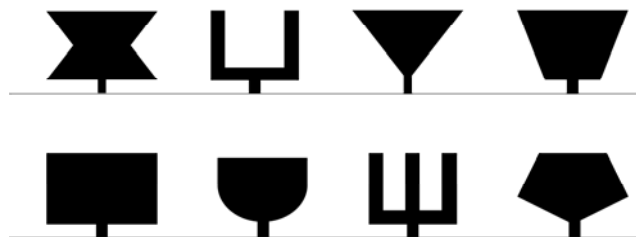


Figure 6.31 Different types of wideband feeding mechanism. The bottom lines represent ground plane connections.

In conclusion, use of a conventional coaxial probe feeding should be discarded for the folded PCB, since it yields narrowband matching and also degrades the current distribution of longitudinal modes through the increase of the transverse current component. In contrast, a wideband feeding mechanism, such as any of the ones shown in Figure 6.31, should be employed. Figure 6.32 shows the folded PCB proposed in the previous section fed by means of a planar square plate [154]. A detail of the wideband feeding, which consists of a square plate, is provided in the figure.

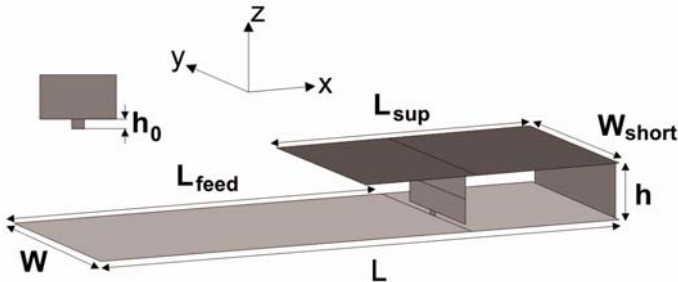


Figure 6.32 Geometry of the proposed folded PCB antenna, excited with a square planar plate. ($L=100$ mm; $W=40$ mm; $L_{\text{sup}}=49.15$ mm; $h=10$ mm; $L_{\text{feed}}=72.5$ mm; $h_0=0.5$ mm and $W_{\text{short}}=35$ mm and $W_{\text{feed}}=25$ mm). A detail of the feeding plate is provided.

The dimensions of the feeding square plate have been optimized to achieve optimum performance using the electromagnetic software Zeland IE3D™ and EM-PIRE™. Afterwards, a prototype of the antenna was constructed in order to validate simulations with real measurements. The prototype is shown in Figure 6.33.

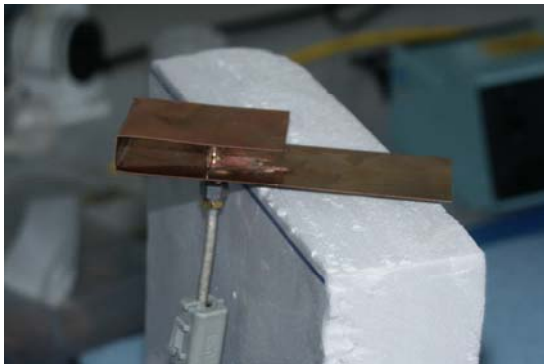


Figure 6.33 Fabricated prototype for the antenna shown in Figure 6.32.

Simulated and measured return losses of the antenna are plotted in Figure 6.34, showing a good agreement between them. By means of this optimized wideband feeding a much wider impedance bandwidth can be achieved for the folded PCB, ranging from 1 to 6 GHz, if a reference value of -6 dB is considered. Thus, the proposed antenna is capable of working simultaneously with several wireless standards, such as DCS1800, PCS, UMTS, IEEE 802.11b/g, IEEE 802.11a, and Bluetooth.

The square plate provides a sort of distributed voltage over the upper part of the folded chassis, which reinforces the excitation of longitudinal modes and avoids transversal modes that can degrade the response of the antenna, as happens in the probe-fed structure. Moreover, the square plate provides a kind of wideband matching mechanism to match the input impedance of horizontal modes. The input impedance of the folded PCB is depicted in Figure 6.35, where it is possible to clearly appreciate the wideband behavior of the feeding mechanism, which is capable to couple to the successive horizontal modes, providing at the same time a smooth transition from one mode to the next one. Consequently, strong anti-resonances that degrade the impedance bandwidth are avoided.

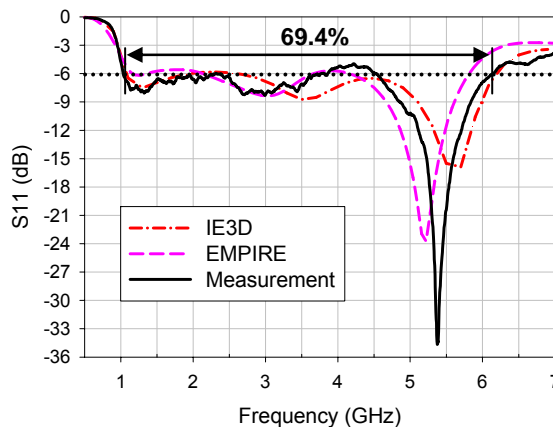


Figure 6.34 Simulated and measured return loss referred to 50 Ω , for the folded PCB antenna.

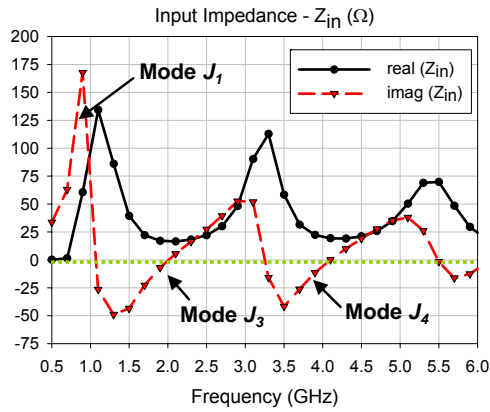


Figure 6.35 IE3D simulated input impedance for the folded PCB antenna.

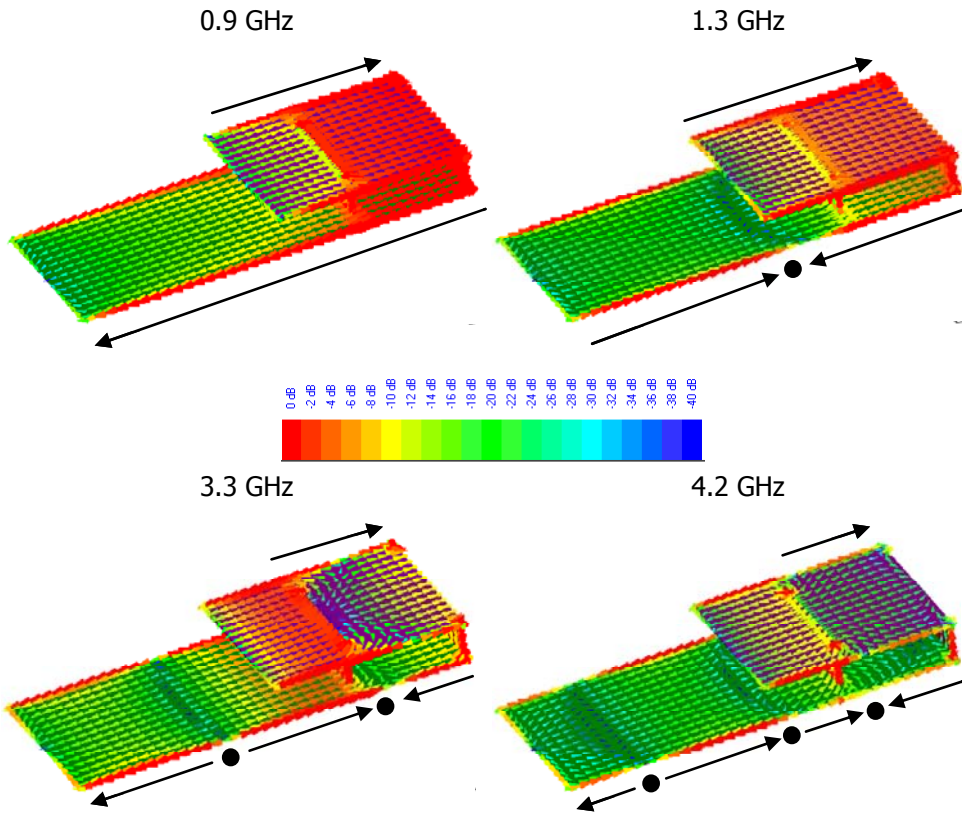


Figure 6.36 Total current distribution computed with IE3D for the structure shown in Figure 6.24, at different frequencies.

Figure 6.36 depicts the normalized total current distribution computed with IE3D for the folded-PCB structure, at different frequencies. According to the previous discussion, the information provided by the input impedance plot, together with the total current distribution, facilitates the identification of excited modes. Thus, at lower frequencies (0.9 GHz), mode J_1 is dominant, until 1.3 GHz, when mode J_3 starts to appear in the structure. Then, at 3.3 GHz mode J_4 appears and resonates around 4 GHz, coupling immediately to the next resonant higher order mode. This latter mode presents three nulls of current along the PCB structure, as shown in Figure 6.36. As it can be appreciated in the input impedance plot, the feeding location and type is optimum to couple satisfactorily to the different resonant modes of the structure, without producing strong anti-resonances in the transitions between them.

As the whole PCB is employed to radiate, very high radiation efficiency and good gain levels are obtained for this antenna. Figure 6.37 shows measurements for both the radiation efficiency and the antenna gain, performed at the IMST GmbH facilities at Kamp-Linfort, Germany. These values may be very difficult to achieve with traditional resonant small antennas. Moreover, Figure 6.38 illustrates the radiation patterns measured at the IMST anechoic chamber at three different frequencies within the impedance bandwidth. As observed, a satisfactory omnidirectional radiation behavior is obtained at all frequencies, as it is desirable in handset antennas.

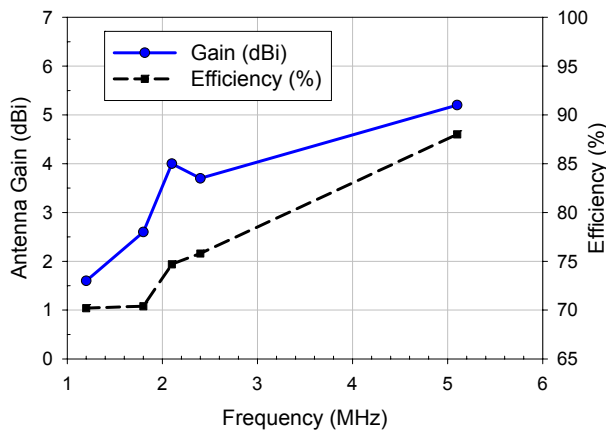


Figure 6.37 Gain (dBi) and efficiency (%) vs. frequency.

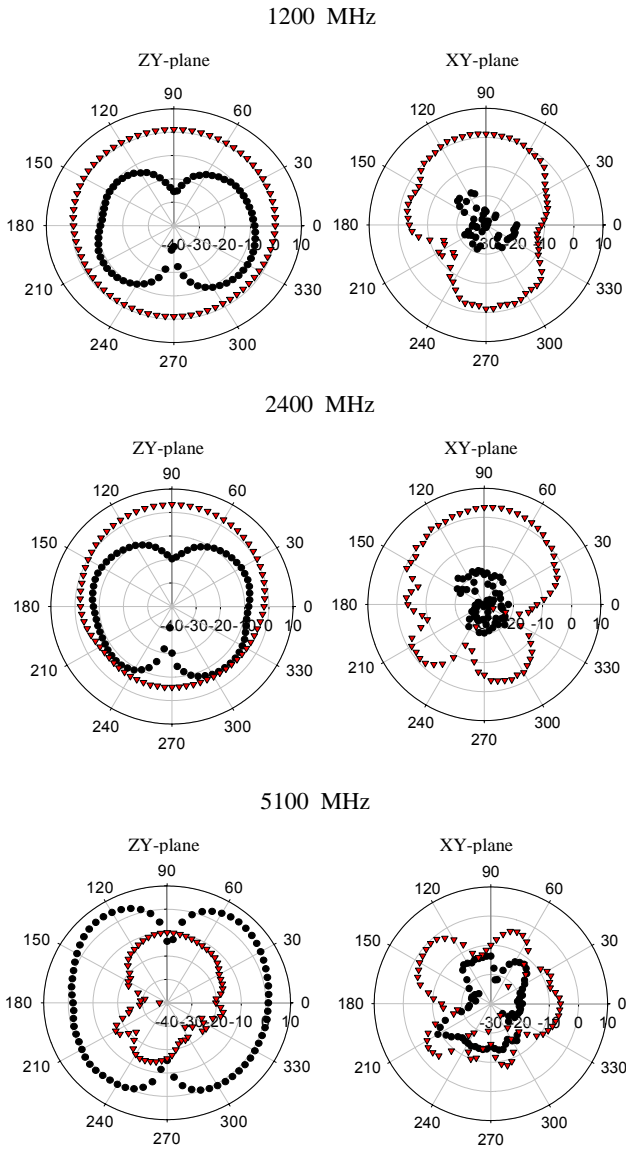


Figure 6.38 Measured radiation patterns in the ZY and XY planes for the proposed folded PCB antenna at 1.2, 2.4, and 5.1 GHz.

Moreover, in order to further improve the impedance matching level, some authors have proposed the insertion of slots in the PCB [162]-[163], as shown in Figure 6.39. This slot not only produce a meandering effect that contributes to reduce the resonant frequency of horizontal modes, but it also changes the current distribution of these modes near the excitation point, favoring the coupling between them and the feeding source. In Figure 6.40 the return loss obtained for the structure with and without slot is plotted. As observed, improved matching is obtained when inserting the slot in the lower plate. In [17] and [164], characteristic modes for the slotted structure were computed and their properties analyzed. Moreover, a prototype of the proposed antenna was fabricated and measured [17], obtaining very good agreement with the results presented in Figure 6.40.

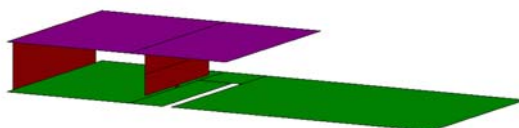


Figure 6.39 Geometry of a folded slotted PCB antenna, excited with a square planar plate.

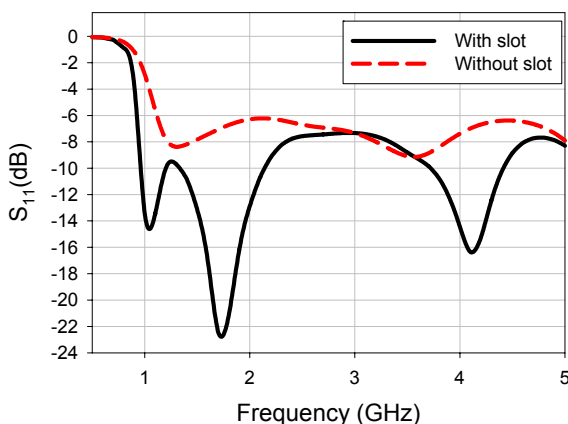


Figure 6.40 Return loss of the folded PCB antenna excited with a square planar plate, with and without the slot in the PCB.

6.5. Double folded PCB antenna

According to section 6.2, the lowest resonant frequency of the PCB is determined by its total length, when the way covered by the horizontal current mode J_1 is equal to half of a wavelength approximately.

Thus, if a mobile terminal must cover the GSM900 band, the total length of the PCB should be increased. Therefore, in order to cover the 900 MHz band and excite horizontal current modes in the structure, which provide wideband radiating properties, a modified structure consisting in a double folded PCB can be proposed. Its geometry is depicted in Figure 6.41, where dimensions have been optimized for good performance. The PCB considered is narrower than in the previous case, so as to prevent the excitation of transversal modes which could degrade the bandwidth of the antenna, when excited by a wire-probe feed.

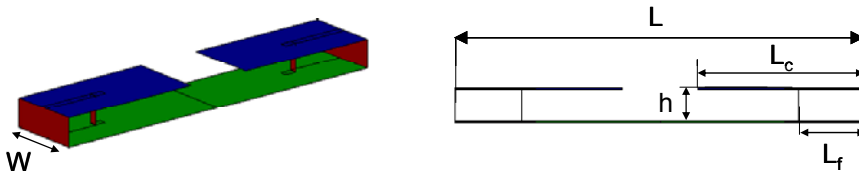


Figure 6.41 Perspective and side view of the double folded PCB antenna ($L=90$ mm; $W=20$ mm; $L_c=39.8$ mm; $h=8$ mm; $L_f=14.3$ mm).

Due to the modification of the PCB geometry, characteristic modes have been newly computed for this structure, in order to determine the effect on the modal behavior of the capacitance produced by the double folding. The current distribution of the first non-resonant mode (Mode J_0) and the first three horizontal current modes (modes J_1 , J_3 and J_4) are depicted in Figure 6.42, showing some similarities to the modal current distribution of the folded and isolated PCB.

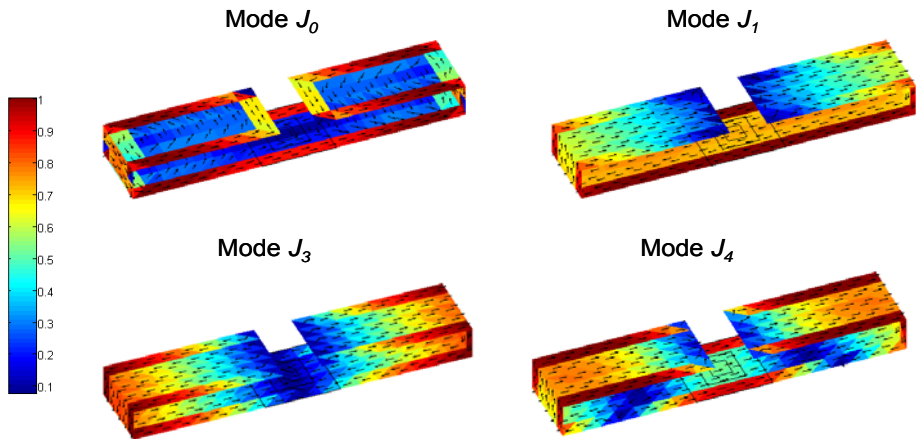


Figure 6.42 Normalized current distribution at first resonance ($f = 1.1$ GHz) of the first six characteristic modes J_n of a radiating double-folded PCB.

Nevertheless, the characteristic angle associated to these double-folded PCB modes, whose curves are plotted in Figure 6.43, presents some changes compared to those of the one side folded PCB. In the latter, the folding in one side of the rectangular PCB diminishes the radiation bandwidth of the full-horizontal current mode J_1 , as previously discussed. This is due to the fact that in the folded part, current flows in opposite directions in the upper and lower plates, producing a cancellation effect that contributes to decrease the overall radiation. In the double-folded PCB case, not only mode J_1 but also mode J_3 decrease their radiation bandwidths, as observed in Figure 6.43. When folding the other edge of the PCB and due to the location of a null of current in the center of the double-folded PCB, a cancellation of radiation in both folded parts of the structure is produced for mode J_3 . In contrast, mode J_4 still keeps a good radiation bandwidth, since the location of its two nulls of current below the folded plates reduces the current cancellation and consequently the drop in the radiated field. Nevertheless, due to the proximity of the resonant frequency of modes J_3 and J_4 , if a good transition between both modes is achieved, good impedance bandwidth can still be obtained by means of a proper feeding mechanism.

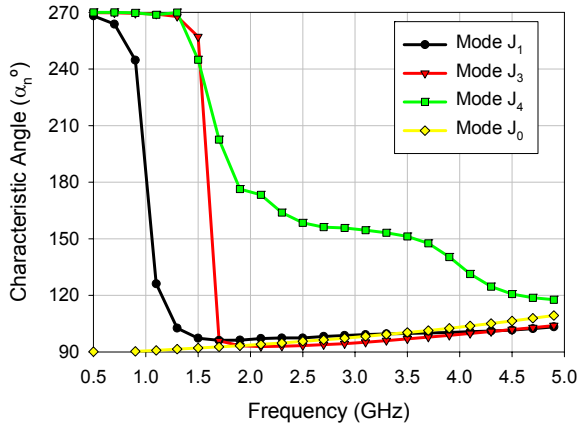


Figure 6.43 Characteristic angle variation with frequency for the previous four characteristic modes of the radiating double-folded PCB.

As observed in Figure 6.41, in order to excite horizontal modes two vertical strips that account for the probe feeds have been used to produce a voltage gap difference between the upper and lower plates. Moreover, the feeds will be in opposite phase so as to excite horizontal currents in the structure. In Figure 6.44 the input impedance and the return loss referred to 50Ω and computed with IE3D are represented. As it can be seen, neither the GSM900 band is covered nor a wide impedance bandwidth is obtained. Again, the inductive behavior of the feeding mechanism produces high values of positive reactance, as observed in the input impedance plot shown in Figure 6.44(a). A capacitive mechanism should hence be used to compensate the inductive behavior of the feeding probes [165].

Therefore, an alternative feeding mechanism based on the use of capacitive plates, which compensates the inductive behavior of the probes, has been used, leading to the structure shown in Figure 6.45. In this structure, two small horizontal plates are located at the end of the vertical probes, so as to compensate its inductive behavior. Furthermore, for the sake of a more practical implementation of the excitation mechanism, a balanced feeding is employed, placing the input port at the center of the PCB. Dimensions have been again optimized for an optimum behavior.

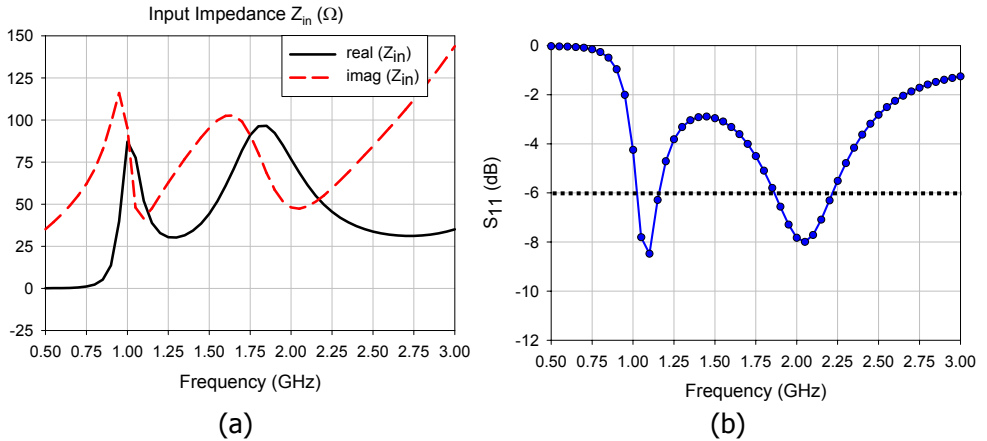


Figure 6.44 Results computed with IE3D for the double folded PCB shown in Figure 6.41: (a) Input impedance; (b) Return loss referred to 50 Ω .

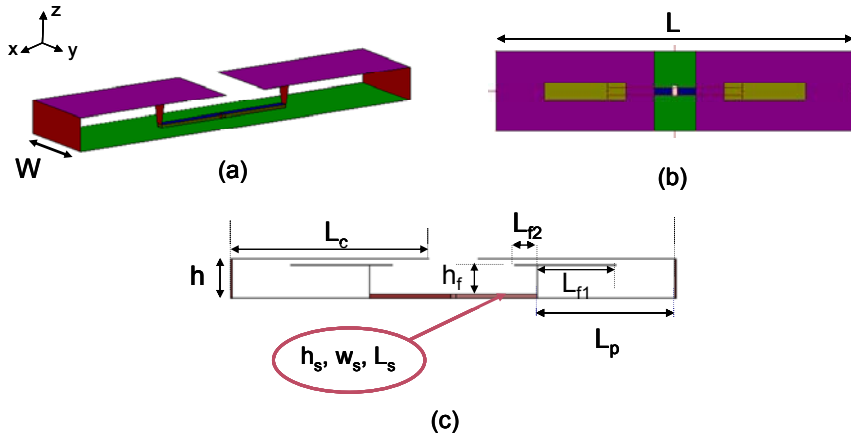


Figure 6.45 Double folded PCB antenna with a balanced feeding ($L=90$ mm; $W=20$ mm; $L_c=39.8$ mm; $h=8$ mm; $L_p=28$ mm; $h_f=6.8$ mm; $L_{f1}=15.9$ mm; $L_{f2}=4.6$ mm; $h_s=1.5$ mm; $w_s=1.78$ mm; $L_s=34$ mm): (a) Perspective view; (b) Top view (each color represents a different height); (c) Side view.

Input impedance and return loss for this alternative feeding configuration are shown in Figure 6.46. Taking a level of -6 dB as an acceptable return loss limit for wireless communication terminals, two operating bands are derived now from the proposed antenna. These bands cover the communication standards GSM900, DCS1800, PCS, UMTS and IEEE 802.11b with a relatively compact structure. As

observed, by means of the capacitive plates a good coupling to PCB mode J_2 (around 900 MHz) and mode J_4 (between 1.3 GHz and 2.5 GHz) is obtained, as implied by the total current distribution at different frequencies depicted in Figure 6.47. These currents have been obtained with electromagnetic simulator Zeland IE3D™. Since mode J_2 does not exhibit very wide radiating bandwidth, a narrow-band behavior is obtained when exciting this mode. As observed in Figure 6.47, the use of a balanced feeding prevents the excitation of mode J_3 , due to the symmetry imposed. However, mode J_4 provides enough bandwidth to obtain a wide-band matching between 1.23 and 2.49 GHz.

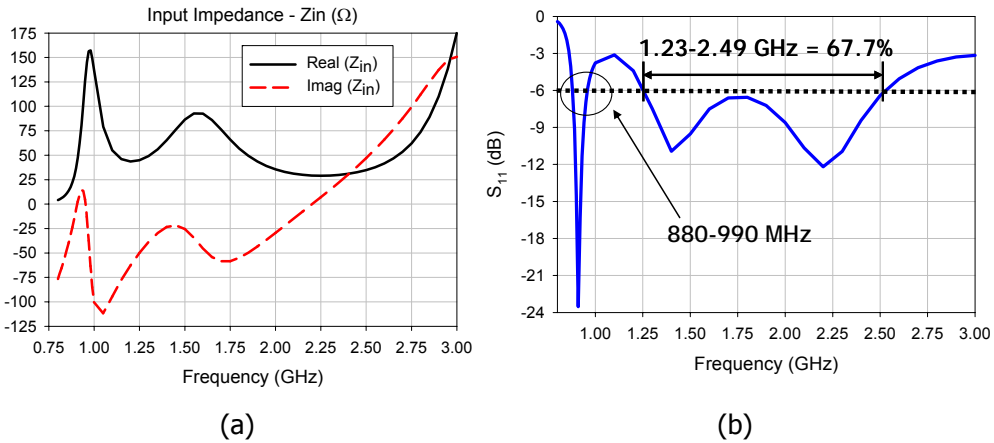
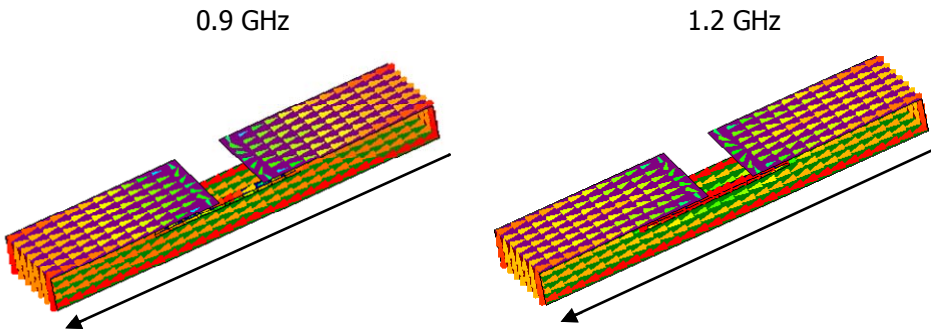


Figure 6.46 Results computed with IE3D for the double folded PCB shown in Figure 6.45: (a) Input impedance; (b) Return loss referred to 50 Ω.



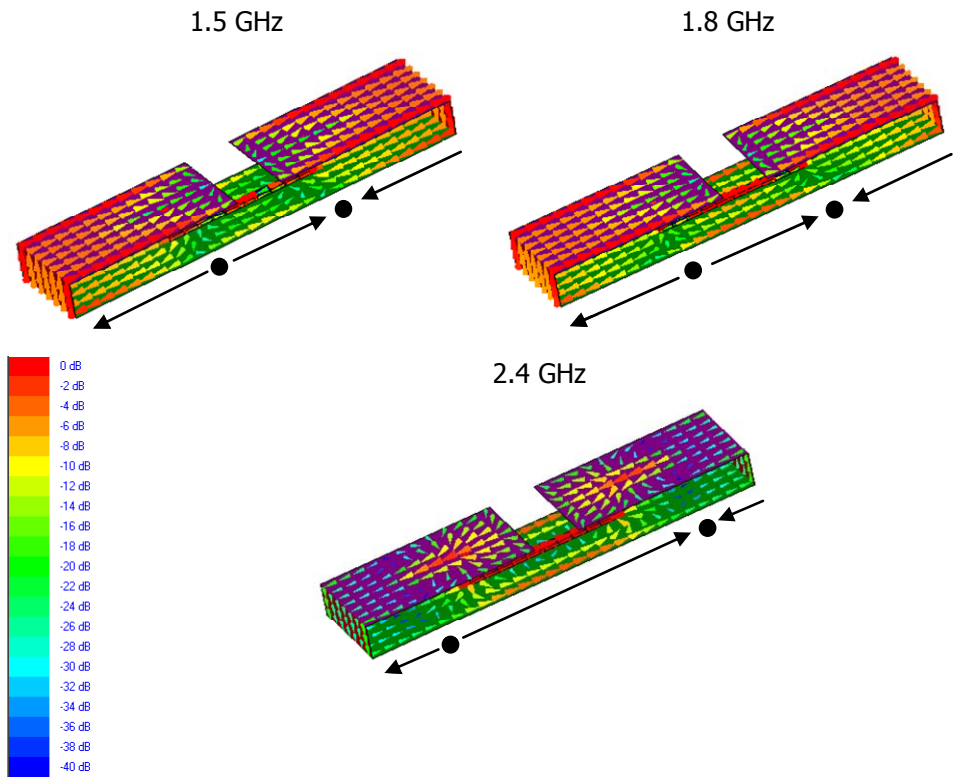


Figure 6.47 Total current distribution computed with IE3D for the structure shown in Figure 6.45, at different frequencies.

Finally, radiation patterns simulated for the proposed structure are plotted in Figure 6.48, for both the XZ and YZ planes, at 900 MHz, 1800 MHz and 2.4 GHz. As desired for wireless terminal antennas, an omnidirectional radiation pattern is obtained in the YZ plane, at all frequencies.

Therefore, it has been proved in the preceding sections that the analysis of the characteristic modes of the PCB is very useful as an initial step in the design of antennas for mobile handsets. Once the properties of the different PCB modes have been analyzed and those modes with more interesting properties identified, an appropriate feeding mechanism should be provided to excite these modes. It has been seen that location, shape, symmetry and impedance matching behavior are important parameters to consider for the selection of the feeding configuration.

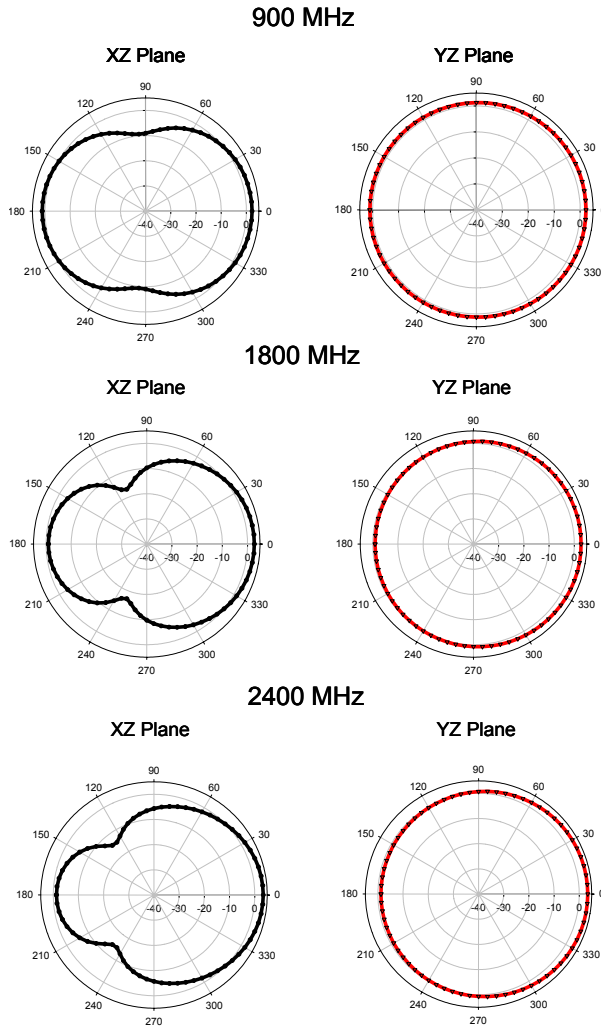


Figure 6.48 Measured radiation patterns in the XZ and YZ planes for the proposed double-folded PCB antenna, at 900, 1800, and 2400 MHz.

6.6. Notched radiating ground plane

The concept of using the ground plane or PCB as a radiating element can be extended to other types of mobile terminal antennas, and not only to handset antennas. For instance, antennas for PCMCIA cards or PDA terminals can also be designed using this philosophy. In this section, a radiating structure based on the use of a double-notched ground plane will be designed, starting from the information provided by characteristic modes.

Relatively large notch antennas have long been used in VHF and UHF applications [166], but when fabricated with microstrip technology, notch antennas can be implemented as very compact structures that can be effectively used for wireless communications [167]. Ideally, typical notch antennas consist in a quarter wavelength slot cut on the edge of a semi-infinite ground plane. They are commonly fed by a coaxial cable without the need of any balancing system. However, when a notch is cut on a finite ground plane of resonant dimension, the shape and size of the ground plane significantly affect the performance of the notch antenna [17]. Indeed, the insertion of notches in planar microstrip antennas can be used to increase their bandwidth [3], due to the additional resonances produced by the notch. Among this type of antennas, special attention has been given to the wide-band E-shaped patch antenna [167]-[171], which consists of a rectangular patch with two parallel notches inserted in its surface. The geometry is shown in Figure 6.49. Usually the microstrip E-shaped antenna is designed for IEEE 802.11 a/b/g WLAN applications, and a coaxial probe is usually employed to feed the antenna.

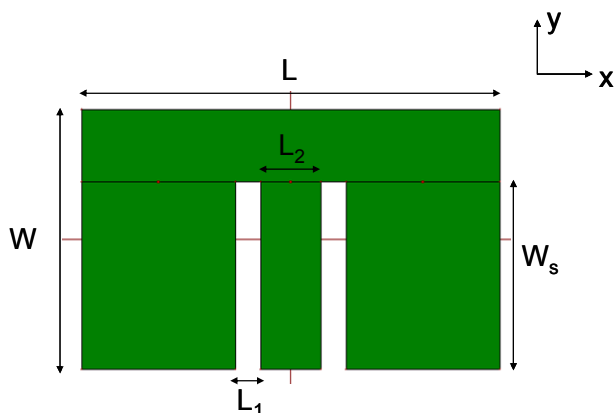


Figure 6.49 Geometry of the E-shaped antenna.

In this section, the E-shaped antenna will be used as a radiating ground plane for a PDA terminal, instead of a microstrip antenna, so as to increase the radiating efficiency and bandwidth. In [17] and [172], characteristic modes of an E-shaped radiating ground plane were analyzed. Based on the information provided by these modes, an alternative feeding mechanism for this type of antennas can be proposed. In next section, a review of the characteristic modes of an E-shaped plate in free space will be made, in order to further discuss the possible feeding mechanisms suitable to excite the desired modes.

6.6.1. Characteristic modes of a double-notched radiating ground plane

This section is aimed to review the properties of the characteristic modes of an E-shaped radiating ground plane, which were already analyzed in [17]. Afterwards, the information provided will be employed to select the optimum feeding mechanism for the antenna.

For the analysis, the ground plane considered is that of a typical PDA (in Figure 6.49: $L=105$ mm and $W=65$ mm) and dimensions of the notches are $W_s=47$ mm, $L_1=2$ mm and $L_2=6.5$ mm. Figure 6.50 shows the normalized current distribution at 1.1 GHz for the first six characteristic modes of the E-shaped radiating ground plane.

According to the figure, modes J_0 , J_1 , J_3 and J_4 present intense currents flowing around the notches. Unfortunately, these intense currents do not contribute to radiation as they are in opposite phase, like in a transmission line, and they cancel each other out along the notch. In contrast, in modes J_2 and J_5 the current flows in phase in the upper and lower notch, and hence these modes can be considered radiating modes or antenna modes.

Figure 6.51 plots the variation with frequency of the characteristic angle associated to the modes of Figure 6.50. Mode J_0 is one of the special non-resonant inductive modes, whose characteristic angle stays below 180° at every frequency. Mode J_4 exhibits the narrowest radiating bandwidth, while the rest of modes are all quite efficient radiators as their characteristic angles keep close to 180° in a wide range of frequencies. Regarding the resonant frequency, mode J_1 resonates at 1.1 GHz, mode J_2 at 2.85 GHz, mode J_3 at 2.45 GHz, mode J_4 at 2.42 GHz and mode J_5 at 3.9 GHz.

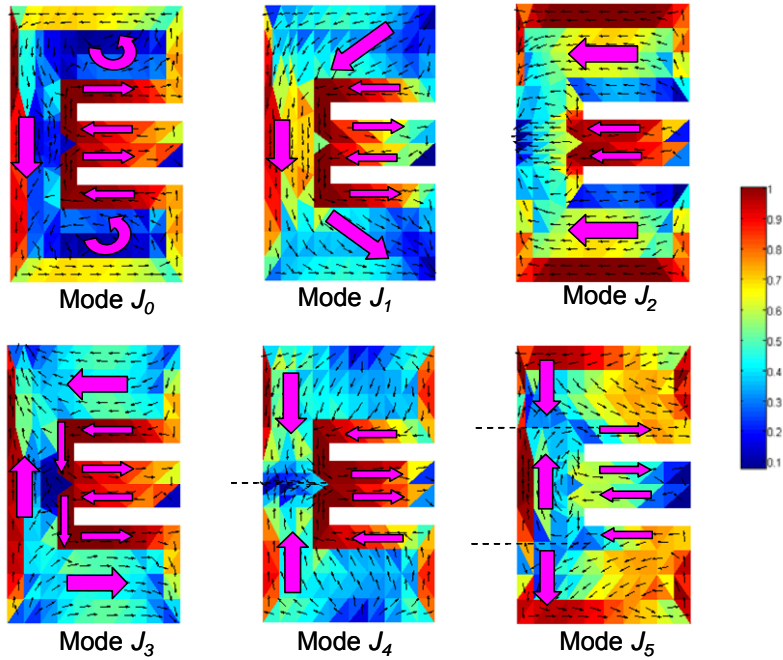


Figure 6.50 Normalized current distribution at 1.1 GHz for the first six modes of a double-notched radiating ground plane.

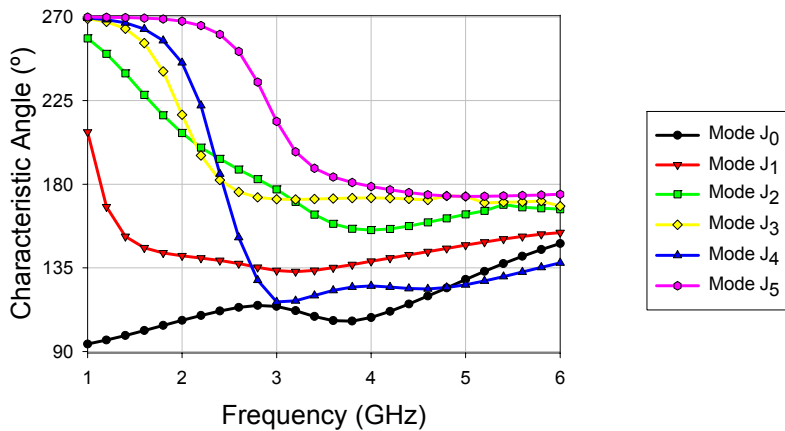


Figure 6.51 Characteristic angle vs. frequency associated to the current modes of Figure 6.50.

6.6.2. Modal excitation of a double-notched radiating ground plane

Once the properties of the characteristic modes of the double notched radiating ground plane have been analyzed, discussion on the feeding mechanism should be carried out.

As stated before, E-shaped microstrip antennas are usually fed by a coaxial probe at its centre [166], thereby exciting mainly mode J_2 and obtaining broad impedance bandwidth, even when using microstrip technology.

When using an E-shaped plate to radiate, if a voltage difference is created at each notch, thereby preserving the symmetry of the antenna, it will favour the appearance of transmission line currents flowing around the notches. As a result, modes presenting this type of currents, such as modes J_0 , J_1 , and J_3 , will couple to the excitation and will be excited. The contribution to radiation of mode J_0 will not be very important, since mode J_0 is a special non-resonant mode with inductive behaviour at every frequency. However, modes J_1 and J_3 , which resonate at 1.1 GHz and 2.45 GHz, respectively, present wideband radiating properties, as they radiate very efficiently in a broad range of frequencies.

In order to excite the wideband radiating modes J_1 and J_3 , a symmetrical (balanced) voltage can be used, thereby avoiding distorting modes that need non-symmetrical voltages (unbalanced). Thus, a dual port balanced feeding configuration as that shown in Figure 6.52(a) can be used to excite the structure, by placing two voltage gap generators at a distance $L_{feed}=38$ mm from the shorted end of the notches. In Figure 6.52(b), the input impedance at each of the input ports is plotted, showing that resistance and reactance remain constant in a wide range of frequencies. As commented in previous section, the input impedance plot, together with the normalized total current distribution, are very useful to identify the modes excited in the radiating ground plane.

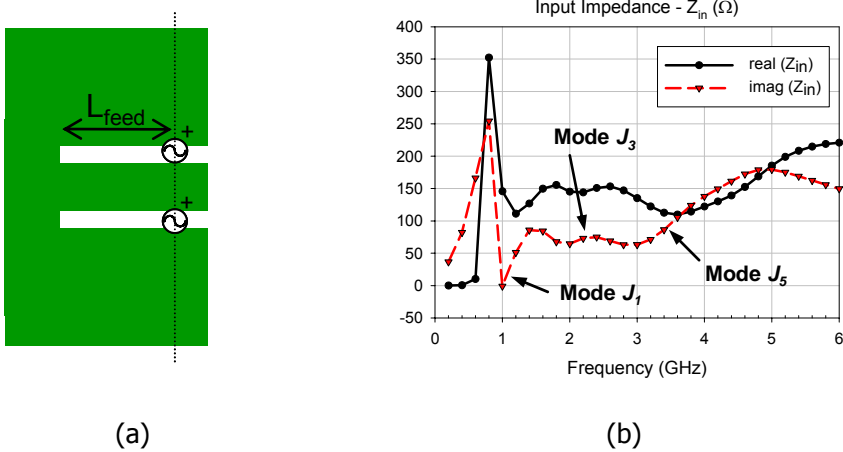


Figure 6.52 (a) Balanced feeding configuration employed to excite the double notched radiating ground plane; (b) Simulated input impedance at each of the input ports.

Figure 6.53 shows the resultant total current computed with IE3D at 0.4 GHz, 1 GHz, 2 GHz and 3 GHz, using this double excitation. At lower frequencies (0.4 GHz), it is observed that the current distribution is dominated by a non-resonant mode, since the current forms a loop in the surface of the planar structure. The presence of the non-resonant mode manifests itself in the inductive behaviour of the input impedance at lower frequencies. At 1 GHz, mode J_1 starts to appear, provoking a strong anti-resonance in the transition from the loop mode to mode J_1 . Due to the feed symmetry, at 1 GHz the current flowing through the centre of the plane is very weak. Moreover, because of the proximity of the two notches, current cancellation between them occurs. Then, at 2 GHz and 3 GHz there is an intense current flow on the feeding strips, favoring currents flowing on vertical direction, whereas transmission line currents are minimized. As observed in the input impedance plot, the transition from mode J_1 to mode J_3 is smooth, what improves the impedance bandwidth. Finally, mode J_5 starts to appear at higher frequencies. Radiation patterns produced by these currents over the structure are depicted in Figure 6.54, where it is observed the influence of each mode at the different frequencies. Omnidirectional patterns are obtained at the YZ plane for all frequencies.

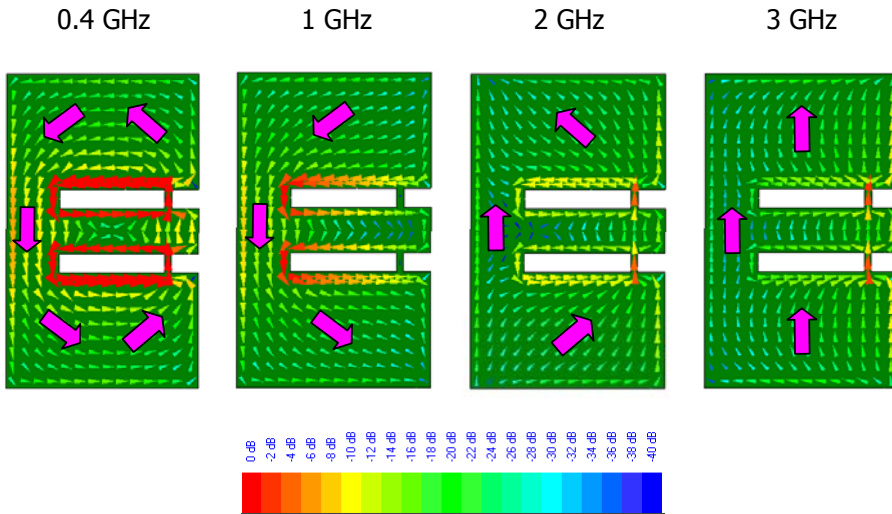
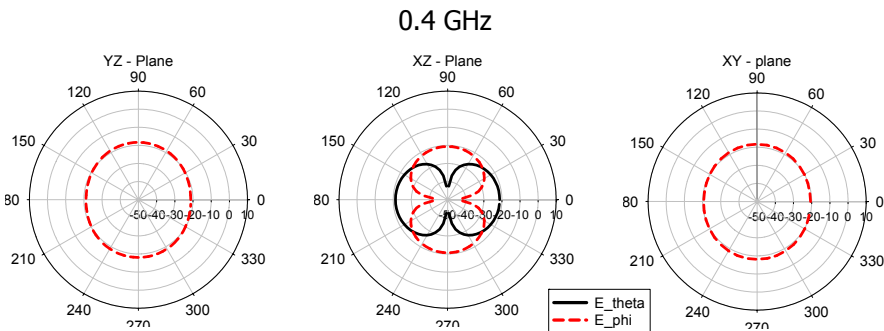


Figure 6.53 Total current distribution computed with IE3D for the structure shown in Figure 6.52, at different frequencies.

Consequently, using two balanced feed points the desired modes are excited, obtaining a good transition between the different excited modes and leading to a matching improvement. Figure 6.55 illustrates the return loss obtained with this balanced feeding for different reference values of characteristic impedance, showing a much better matching for an impedance value of 100Ω than of 50Ω . Thus, considering 100Ω as the reference value and an acceptable return loss value lower than -6 dB , an operating bandwidth ranging from 0.85 to 3.8 GHz is obtained for the proposed antenna. A wideband matching network is therefore needed to efficiently couple to the traditional 50Ω feeding cable. In next sections, the problem of physically implementing the feeding mechanism will be addressed.



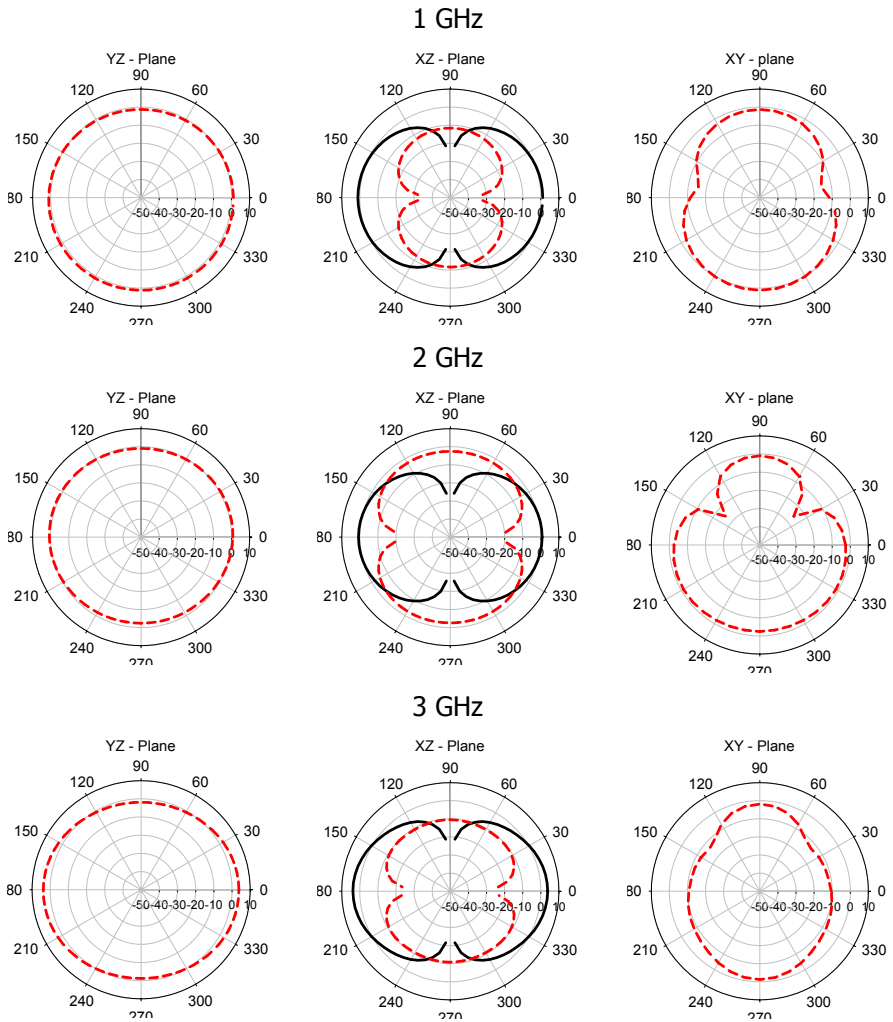


Figure 6.54 Radiation patterns for the structure shown in Figure 6.52(a), at different frequencies.

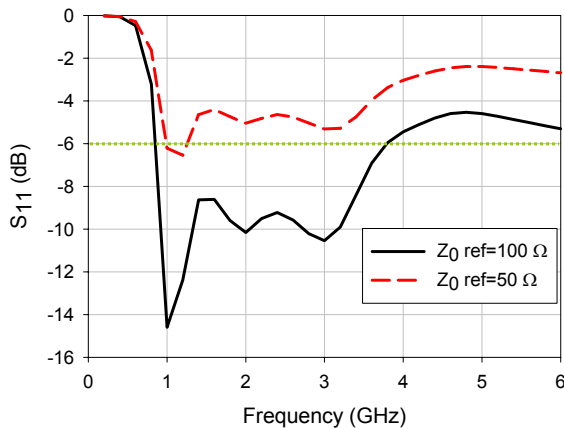


Figure 6.55 Return loss obtained for the structure shown in Figure 6.52(a).

6.6.2.1. Practical implementation of the feeding mechanism by means of transmission lines

A possible practical implementation of the feeding mechanism could consist of a power splitting network based on microstrip lines, which couples the energy efficiently to the notches at the feeding points [172]. The geometry of the proposed antenna with the feeding network is presented in Figure 6.56, where the power divider is printed in the back side of a substrate. The substrate employed has a height of $h=0.76$ mm and a permittivity of $\epsilon_r=3.2$. The length of the microstrip lines must be designed to ensure that both notches are fed in phase. As explained in chapter 4, the required bandwidth is provided by the microstrip power divider, since only the input reflection coefficient is considered. Moreover, the characteristic impedance of the output transmission lines is 100Ω , what is necessary for obtaining wide impedance matching, as discussed in the previous section.

A prototype of the proposed antenna was fabricated and is shown in Figure 6.57. Figure 6.58 represents the return loss for both simulation with IE3D and real measurements, with an acceptable agreement existing between them. Consequently, the antenna presents a matched bandwidth covering from 1.6 GHz to more than 5 GHz, when a return loss lower than -6 dB is considered. However, there are some differences with the results obtained in the previous section, when using two voltage gap generators, especially at lower frequencies. This is due to the fact that, although the feeding network excites both notches simultaneously, it is not completely equivalent to the feeding configuration previously used in Figure

6.52. The behavior of the feeding network within the impedance bandwidth is obviously different in both cases, affecting to the coupling of the different modes. Anyway, a very wide bandwidth is still obtained for this structure using the new feeding configuration, although the operating band is shifted up to higher frequencies. In next section, an alternative feeding mechanism based on the use of active devices is also proposed.

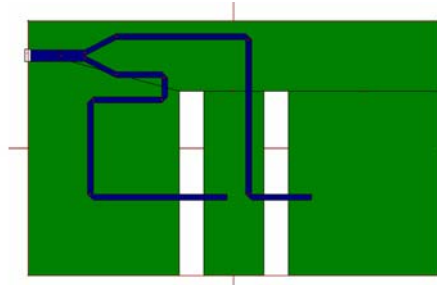
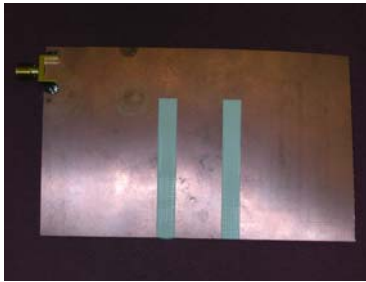
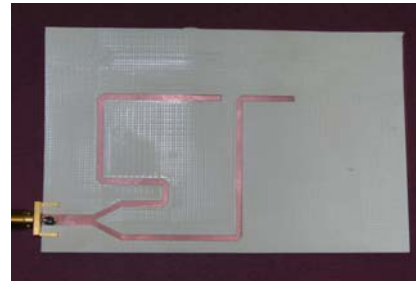


Figure 6.56 Double-notched radiating ground plane fed by means of a microstrip power divider. Each color corresponds to one of the sides of the substrate.



(a)



(b)

Figure 6.57 Prototype of the double-notched radiating ground plane fed by means of a microstrip power divider: (a) Front side; (b) Back side.

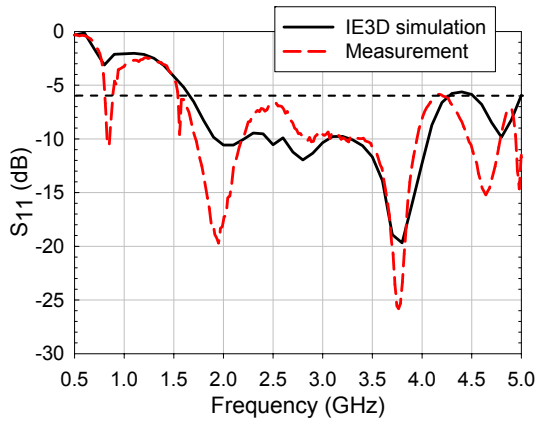


Figure 6.58 Simulated and measured return loss for the antenna prototype shown in Figure 6.57.

6.6.2.2. Practical implementation of the feeding mechanism by means of an active balance feeding

Another alternative to practically implement the double balanced feeding is to take advantage of the differential electronic configurations to directly produce balanced voltages, using appropriate symmetrically connected active devices, as illustrated in Figure 6.59. The implementation of this feeding mechanism has been possible as a result of a collaboration with the Technical University of Catalonia (UPC) [173], who are very experienced with the development and application of this feeding technique.

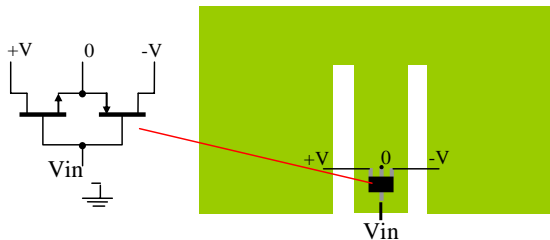


Figure 6.59 Active antenna feeding.

Conventional common-source transistors, which exhibit complex input impedance, can be used to implement the balanced feeding. To fit the previous double-notched radiating ground plane with the active balanced source and to get maximum power transference between both, it is necessary to fulfill the conjugate impedance matching condition [174]:

$$Z_{ant} = Z_{actdev}^*$$

where Z_{ant} is the impedance of the antenna at the feeding point and Z_{actdev} the input impedance of the active device.

A FET device presenting an input impedance value around $Z_{actdev} = 20 - j100 \Omega$ within the operating bandwidth of interest has been chosen for the feeding implementation. The FET device response can be more precisely modelled by a simplified circuit consisting of a combination of a resistance in series with a parallel RC circuit [173]. In order to fulfill the conjugate impedance matching condition, the feeding point on the antenna must be optimized consequently.

The input impedance of the double-notched ground plane changes with the position of the feeding along the notch (parameter L_{feed}), whereas the modes excited in the structure remain the same. Therefore, in order to find the optimum location for input impedance matching to the active feed, a parametric study has been performed, varying the input impedance of the antenna according to the different positions from the short circuit of the notch (parameter L_{feed}). Results are depicted in Figure 6.60. Optimum resistance values of input impedance should be around 20Ω , whereas the reactance should present an inductive behavior at the input port, around 100Ω . When approaching the short circuit, the real part decreases, being more appropriate for matching the active device. With respect to the imaginary part, it is usually inductive, what makes the device suitable for its connection to the capacitive reactance of the active device. In consequence, it seems possible to find proper locations of the feeding point to connect the active device directly to the antenna port, approaching the optimum matching condition and hence reducing system complexity, size and losses.

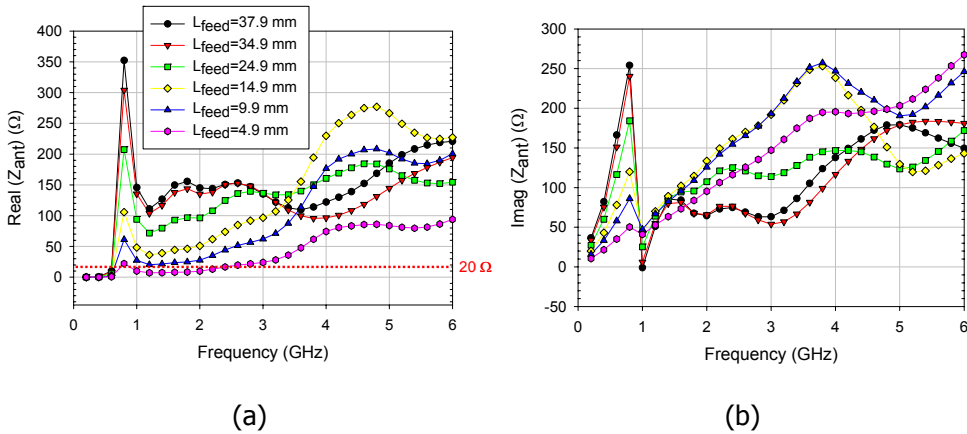


Figure 6.60 Input impedance of the radiating ground plane (Z_{ant}) for different values of L_{feed} : (a) Real part; (b) Imaginary part.

As complex impedances are currently being handled, the power transfer is estimated by the matching coefficient (C_a), which is defined as the relation between the actual power transferred (P_L) to the antenna and the maximum power available at the amplifier output (P_{Lmax}), as follows [174]:

$$P_L = P_{Lmax} \cdot C_a$$

$$C_a = 1 - |\rho|^2 = \frac{4 \cdot R_{ant} \cdot R_{amplifier}}{(R_{ant} + R_{amplifier})^2 + (X_{ant} + X_{amplifier})^2}$$

The matching coefficient obtained by fabricating and measuring the stand-alone radiating ground plane and the differential amplifier is depicted in Figure 6.61, where it has been verified that the power transferred from 800 MHz to 3.2 GHz is higher than 70% of the maximum.

The differential amplifier was integrated within the double-notched radiating ground plane geometry, obtaining the prototype depicted in Figure 6.62, fabricated by the UPC AntennaLab. The reflection coefficient at the input port was measured and it is shown in Figure 6.63(a). As observed, a wide bandwidth is obtained for a matching criteria of $S_{11} < -6\text{dB}$, which extends from 0.8 GHz to 2.9 GHz. This impedance bandwidth is far more similar to that obtained for the antenna with two voltage gap generators (Figure 6.55), being in turn more suitable for feeding the antenna than the transmission line feeding network used in previous section.

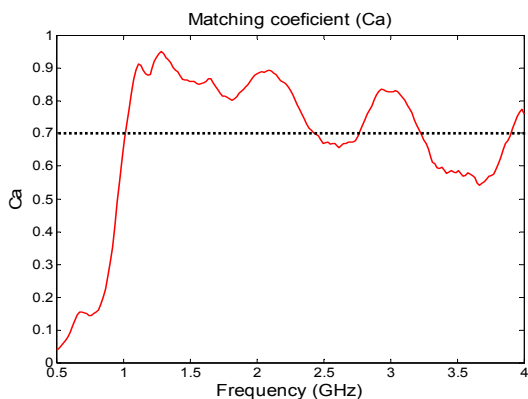
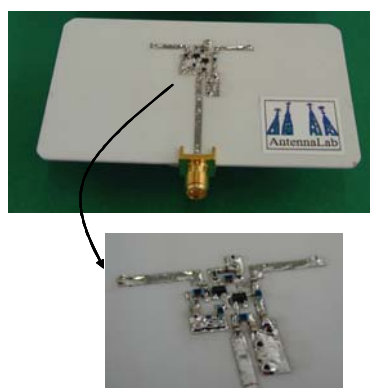


Figure 6.61 Simulated C_a for FET feeding.



(a)



(b)

Figure 6.62 Prototype of the wideband E-shaped antenna; (a) Front side view; (b) Back side view, with detail of the differential amplifier.

Finally, the gain has also been measured in the anechoic chamber at the UPC facilities, and it is compared with that of a reference dipole in Figure 6.63(b). As portrayed by the figure, a global gain 10 dB higher than the reference dipole is obtained within the operating bandwidth. However, at higher frequencies the gain deteriorates, due to the unavoidable narrower bandwidth when the input is matched at certain frequencies. Radiation patterns have also been measured, ob-

taining the desired omnidirectional pattern in the XZ plane and also good polarization purity [175].

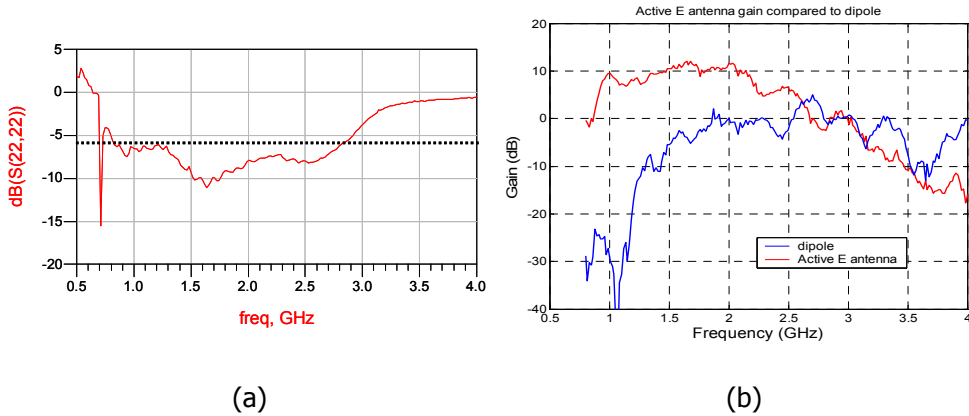


Figure 6.63 (a) Measured reflection coefficient at the input; (b) Measured active antenna gain compared to a reference dipole.

6.7. Conclusions

The present chapter has demonstrated the usefulness of characteristic modes to design mobile terminal antennas based on the use of the PCB or ground plane resonances. Once the characteristic modes of the PCB and their properties are known, different strategies to excite the most interesting eigencurrents in the PCB or ground plane of different mobile terminals have been investigated. Moreover, some practical designs of mobile terminal antennas based on this philosophy have been proposed.

From the different experiments carried out throughout the chapter, it can be concluded that the excitation of the PCB characteristic modes can be performed by means of one or more coupling elements, whose shape and location determine the type of current –and hence the modes– excited in the PCB. When using two or more coupling elements, certain symmetries for the current distribution can be imposed in the PCB, what can be employed to prevent the excitation of some modes. Moreover, either a resonant or a non-resonant coupling element can be used to excite modes in the PCB.

However, although the location, shape and symmetries imposed by the coupling element determine the modes excited in the PCB, the maximum energy is not always transferred from the feeding cable to the desired mode. If some mismatching

occurs at the excitation point near the resonant frequency of a specific desired mode, this mode would not be sufficiently excited in the PCB. Therefore, as exposed in section 6.3.2.1, some kind of impedance matching mechanism should be provided to match the modal impedance to the traditional $50\ \Omega$ of the input cable. This design method is summarized graphically in Figure 6.64. Some authors propose to implement the impedance matching mechanism by means of miniaturized electronic circuits, so that very compact antennas can be designed, also for multi-band operation [156].

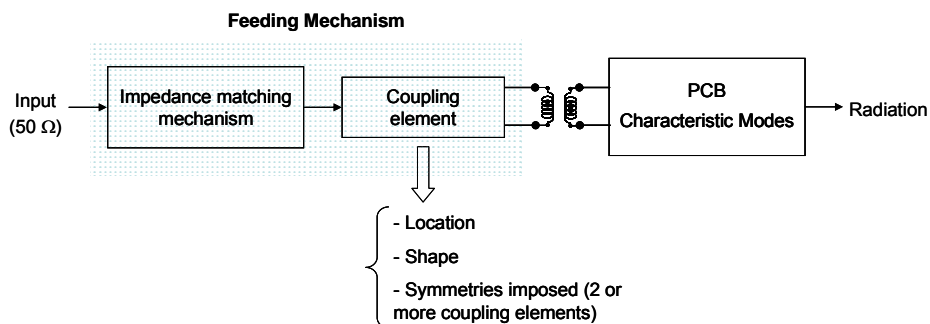


Figure 6.64 Excitation mechanism of the PCB characteristic modes.

The impedance matching mechanism and the coupling element can be joined into the same structure, as shown in sections 6.4, 6.5 and 6.6. Some wideband coupling structures that provide a wideband impedance matching mechanism within a unique planar element have been proposed. The location and geometry of the wideband feeding can be optimized to provide a good coupling to successive wideband resonant modes of the PCB. Impedance bandwidth never achieved before for this type of structures can be obtained. Other types of feeding mechanisms, based on transmission lines and active devices, have been presented to accomplish optimum coupling to the PCB modes within a wide range of frequencies. It has been demonstrated that the input impedance can be optimized to match other types of impedance, for instance, complex impedances required by active devices. Adjusting the excitation point on the antenna, the power transferred from the active device to the antenna can be optimized.

Chapter 7

Conclusions and further work

“What appears to be the end may really be a new beginning.”

Anonymous

7.1. Conclusions

The main objective of this Thesis has been to provide a general method for the design of antennas for wireless communications systems, based on the modal analysis of open conducting structures. The utility of the proposed method has been fully demonstrated, providing several antenna designs that cover different applications.

The proposed design procedure should start by performing a computation of the surface modal currents on the radiating structure. Once the properties of these modes have been analyzed, an appropriate feeding mechanism must be provided for a suitable excitation of modes and for a proper matching to the traditional $50\ \Omega$ feeding line.

In the first chapters, different modal techniques applicable to the analysis of conducting structures were discussed. It was shown that either complex current vector wave functions or real characteristic modes can be defined over the surface of the conducting body and computed. Both types of modes have been proven to present similar properties, except for the real nature of characteristic modes, what makes them more suitable for being used in design problems.

Moreover, in the initial chapters, an analytical method for the extraction of vector wave functions and characteristic modes of planar structures has been presented, which is based on the interpretation of the planar structure as a deformation of three-dimensional structures whose surfaces coincide with one of the eleven basic curvilinear coordinate systems. Thus, closed-form expressions for vector wave

functions and characteristic modes of an infinite planar strip were presented for the first time, both for the TM and TE case. The provided characteristic functions could be used as entire-domain basis functions in problems including rectangular surfaces, since it has been demonstrated that they are a generalization of the traditionally used Chebyshev polynomials. Moreover, as the proposed functions are frequency dependent, they can be used to accelerate the convergence to the solution of these problems when a broad frequency range is considered.

Real characteristic modes can be numerically computed for bodies of arbitrary shape, as explained in the literature. Therefore, the first step in the design of the antenna should be performing a computation of the real eigencurrents or characteristic modes of the structure. After obtaining these modes, characteristic values associated to the different eigencurrents provide valuable information about the resonant frequency and radiating bandwidth of each mode. Furthermore, due to the small size required for wireless communications antennas, only few modes will contribute to the radiation of the antenna.

Once the modes with more interesting properties have been identified, the next step is selecting the location and configuration of the feeding mechanism. This feeding mechanism is crucial to obtain an optimum behavior of the antenna, since the excitation of the modes depends mainly on the coupling between the source and the modal current.

Excitation of modes in the conducting structure can be analyzed by means of the modal admittance parameter. Thus, the total admittance at each input port of the antenna can be expressed as a superposition of the modal admittances corresponding to the different modes. Concepts of resonance and anti-resonance have also been revisited and connected with the excitation of characteristic modes. Starting from the observation of the total input admittance and the total current distribution on the surface of the antenna, it has been proven that a straightforward identification of the excited modes can be carried out in most cases.

Different excitation mechanisms have been investigated throughout the Thesis. It has been demonstrated that the excitation of a specific mode depends on the magnitude of its current at the location of the source, and that the use of multiple sources increases the control over the excitation of modes, since different symmetry conditions can be imposed. Additionally, multiple feeding points can also be used to reinforce the excitation of specific modes in the structure, for instance in the case of the square planar monopole antenna, where a double feeding mechanism has been proven to considerably increase the impedance bandwidth. The analysis presented for this type of antennas, based on the properties of the characteristic modes and their excitation, has attracted a lot of interest by many au-

thors. Some similar designs based on the ideas presented for the square planar monopole antenna can be found in the literature, as commented in chapter 4.

Moreover, combining the phases of multiple sources, antennas with polarization agility can be provided. A further enhancement of this concept enables the design of MIMO antennas by using multiple feeding points, due to the orthogonality of the radiation patterns produced by the eigencurrents.

Furthermore, it has been emphasized that although the source configuration and its location determine the excitation of the modes, this does not necessarily imply to achieve impedance matching to the traditional $50\ \Omega$ feeding line. If the mode has a high radiating bandwidth, it will be near resonance in a wide frequency range. Thus, the input impedance would be real, but not necessarily $50\ \Omega$. Therefore, some kind of wideband impedance matching mechanism is sometimes required to take the most of the excited modes, and to compensate the influence of the excitation source.

Usage of reactive loads in the structure has been also presented as a method to control the resonance of the modes. To some extent, the feeding mechanism could also include a reactance matching, so as to force modes to resonate at any desired frequency. This is especially interesting for narrowband applications.

Afterwards, modal analysis has also been applied for the first time to wideband antennas with an embedded narrowband resonator. The effect of this element over the antenna behavior has been explained by means of characteristic modes, which provide a very clear physical insight. Once the effect of the interaction between the resonances of the narrowband and wideband resonators has been clarified, new configurations for the narrowband slots can be proposed. As a result, a novel structure that allows to control the excitation of the slot resonance, and consequently its effect over the wideband antenna, has been proposed. Moreover, it has been demonstrated that the excitation of this resonance can be electronically controlled by means of active devices, thereby notably incrementing the functionality of the antenna. Furthermore, if the slot is reactively loaded with a variable capacitance, electronic tuning of the resonance of the slot can be obtained.

Prototypes for UWB antennas with a switchable and tunable band-notched behavior have thus been presented, together with real measurements that confirm the desired behavior. Moreover, not only frequency domain but also time domain results have been provided, confirming the suitability of active devices for UWB applications.

Then, the design method has been applied to the design of antennas for mobile terminals, based on the use of the PCB or ground plane of the terminal to radiate. Different feeding mechanisms have been investigated for the excitation of characteristic modes in the PCB and similar conclusions to that commented previously can be extracted for a general design of this kind of structures. Additionally, wideband feeding mechanisms have been proposed, which basically consist of a planar plate with a specific shape. Thereby, very good coupling to different modes can be achieved for a broad bandwidth, since strong anti-resonances are avoided. This novel proposal of applying characteristic modes to the analysis of the PCB resonances has attracted a lot of interest from other authors and even from some mobile phone manufacturers, as it provides important details about the best location and type of the feeding mechanisms.

In addition, other types of feeding configurations based on transmission lines and active devices have been presented to achieve an optimum coupling to the PCB modes, within a wide range of frequencies. It has been demonstrated that the input impedance can be optimized to match any other desired impedance, for instance, the complex impedances required by active devices. By adjusting the excitation point on the antenna, the power transferred from the active device to the antenna can be optimized. This has allowed for the design of antennas not only for mobile handsets but also for other devices, including mobile terminals such as PDAs and PCMCIA cards.

Therefore, it can be concluded that the use of modal techniques for antenna design may greatly assist in the design of antennas for wireless communications systems, as it provides a clear physical insight into the radiation phenomena taking place in the antenna. Some guidelines regarding the location, number and type of excitation mechanisms has been provided, which will be helpful to design the antenna. The proposed design method and guidelines have been successfully applied to antennas for different applications: generic wideband antennas as well as antennas for handheld devices and more specific systems, including both UWB and Multiple-Input Multiple-Output (MIMO) systems. Prototypes for the antennas have been provided and measured, yielding satisfactory results in all cases. Therefore, this proves the suitability of the design procedure to accomplish a final design with the required performance.

7.2. Further work

The design procedure presented has demonstrated its effectiveness for the design of small antennas for wireless communication systems, as it provides a clearer physical insight into the antenna performance. Some important guidelines to be

considered in the feeding configuration to excite the desired modes in the radiating structure have been presented, which may help the design process. Nevertheless, the final optimization of the feeding structure in conjunction with the radiating structure must be done in most cases manually.

As a consequence, one further working line would be the implementation of an automatic optimization tool capable of interacting with the code that computes characteristic modes, in order to improve the feeding mechanism and the coupling to the modes, avoiding an excessive degradation of the radiating properties of the modes. It must be noted that modifications in the geometry of the antenna sometimes produce important modifications into the radiating behavior of characteristic modes, what should be avoided when integrating the feeding mechanism.

Moreover, it has been shown that the use of reactive loading can be used to control the resonances of modes. This can be combined with the use of multiple sources to implement a multimode MIMO antenna. By properly combining the phases of the sources, different orthogonal modes can be excited, as previously discussed, whose resonances can be further adjusted by means of reactive loads, so as to force them to operate at the same frequency. When modes presenting a high radiating bandwidth are selected, even a broadband MIMO antenna may be designed.

The use of multiple feeding sources has been presented as an effective technique to control the excitation of modes in any structure. Practical implementation of this feeding configuration must be addressed in further work, as it increases the complexity of the antenna.

In chapter 6, the excitation of different radiating modes over the PCB of a mobile terminal has been investigated from a modal perspective. Different experiments with coupling elements have been performed, in order to show the dependence of the PCB modes with the coupling element/s location. Consequently, it would be very interesting to extend this investigation to comprehensively analyze the field radiated by the PCB eigencurrents and study their excitation, investigating the optimum shape and location of the coupling element by means of the field coupling.

Additionally to the applications presented, design of antennas for other systems can also be accomplished through application of the proposed guidelines. Thus, design of compact antennas for emergent DVB-H (*Digital Video Broadcast-Handheld*) standards may constitute an interesting new line of research, as well as antennas for sensor networks.

In the first part of the Thesis, diverse planar structures were analyzed using vector wave functions, yielding closed-form expressions for the modal surface currents over the conducting object. In fact, complex analytical functions for the modal currents over an infinite planar strip have been provided. Similarly to cavity coupling in microwave networks, these entire-domain functions may be used to analyze discontinuities in planar surfaces, from a modal point of view. Therefore, these modes will provide more physical insight into the radiation and coupling phenomena between lines at the two sides of the discontinuity, what may significantly assist in systematically designing radiating structures with discontinuities embedded within the planar surface. This may in turn open the possibility to design antennas with a beforehand determined response.

References

- [1] L.C. Godara, "Handbook of antennas in Wireless Communications", CRC Press, 2002.
- [2] K.L. Wong, "Planar Antennas for Wireless Communications", Wiley-Intersc., John Wiley & Sons, 2003.
- [3] K.L. Wong, "Compact and Broadband Microstrip Antennas", John Wiley & Sons, 2002.
- [4] Y. Rahmat-Samii and E. Michielssen, "Electromagnetic Optimization by Genetic Algorithms", New York: Wiley, 1999.
- [5] R.L. Haupt and D.H Werner, "Genetic Algorithms in Electromagnetics", Wiley-IEEE Press, April 2007.
- [6] J. Robinson and Y. Rahmat-Samii, "Particle Swarm Optimization in Electromagnetics," IEEE Trans. Antennas Propagat., vol. 52, Iss. 2, Feb. 2004, pp. 397 – 407.
- [7] J.R. Pérez and J. Basterrechea, "Comparison of Different Heuristic Optimization Methods for Near-Field Antenna Measurements", IEEE Trans. Antennas and Propagat., vol. 55, no. 3, pp.549-555, March 2007.
- [8] C. Christodoulou, M. Georgiopoulos, C. Christopoulos, "Applications of Neural Networks in Electromagnetics," Artech House, 2001.
- [9] R.F. Harrington, "Time-Harmonic Electromagnetic Fields", Wiley-IEEE Press, September 2001.
- [10] J.J Bowman, T.B.A Senior and P.L.E Uslenghi, "Electromagnetic and acoustic scattering by simple shapes", Hemisphere Pub., 1969.
- [11] J.A Stratton, "Electromagnetic Theory (Pure & Applied Physics)", McGraw-Hill, Inc., 1941.
- [12] C.E. Baum, "On the singularity expansion method for the solution of electromagnetic interaction problems," AFWL Interaction Notes 88, December 1971.
- [13] R.J Garbacz, "A generalized expansion for radiated and scattered fields", Ph.D. Dissertation, Ohio State University, Columbus, OH, 1968.
- [14] R.J Garbacz, R. Turpin, "A generalized expansion for radiated and scattered fields", IEEE Trans. Antennas and Propagat., vol. AP-19, no. 3, May 1971, pp.348-358.
- [15] R. F. Harrington and J. R. Mautz, "Theory of Characteristic Modes for Conducting Bodies", IEEE Trans. Antennas and Propagat., vol. AP-19, no. 5, pp.622-628, Sept. 1971.

- [16] R. F. Harrington and J. R. Mautz, "Computation of Characteristic Modes for Conducting Bodies", *IEEE Trans. Antennas and Propagat.*, vol. AP-19, no. 5, pp.629-639, Sept. 1971.
- [17] M. Cabedo Fabrés, "Systematic design of antennas using the Theory of Characteristic Modes", PhD. Dissertation, Universidad Politecnica de Valencia, Feb. 2007.
- [18] P.M Morse and H. Feshbach, "Methods of theoretical physics", McGraw-Hill, Inc., 1953.
- [19] L.J Chu, "Physical limitations of omnidirectional antennas", *Journal of Applied Physics*, vol. 19, pp. 1163-1175, Dec. 1948.
- [20] L.W Li, X.K Kang and M.S Leong, "Spheroidal Wave Functions in Electromagnetic Theory", John Wiley and Sons, Inc., 2002.
- [21] R. Janaswamy, "A note on the TE/TM decomposition of electromagnetic fields in three dimensional homogeneous space", *IEEE Trans. Antennas and Propagat.*, vol. 52, no. 9, pp.2474-2476, Sept 2004.
- [22] S. Zhang and J. Jin, "Computation of Special Functions", Wiley Interscience, 1996.
- [23] M. Abramowitz and I.A. Stegun, "Handbook of mathematical functions", Courier Dover Pub, 1965.
- [24] W.J. Thompson, "Spheroidal wave functions", *Computing in Science & Engineering*, Vol. 1, Iss. 3, pp.:84 – 87, May-June 1999.
- [25] J.C Sten and E. Marengo, "Transformation formulas for spherical and spheroidal multipole fields", *International Journal of Electronics and Communications (AEU)*, Vol. 61, p. 262-269, 2007.
- [26] Le-Wei Li, Zhong-Cheng Li and Mook-Seng Leong, "Closed-form eigenfrequencies in prolate spheroidal conducting cavity", *IEEE Trans. on Microwave Theory and Techniques*, Vol. 51, Iss. 3, pp.: 922- 927, Mar 2003.
- [27] G. F. Ricciardi and W. L. Stutzman, "A Near-Field to Far-Field Transformation for Spheroidal Geometry Utilizing an Eigenfunction Expansion", *IEEE Trans. Antennas and Propagat.*, vol. 52, no. 12, pp.3337-3349, Dec 2004.
- [28] I. R. Capoglu and G. S. Smith, "The Input Admittance of a Prolate-Spheroidal Monopole Antenna Fed by a Magnetic Frill", *IEEE Trans. Antennas and Propagat.*, vol. 54, no. 2, pp.572-585, February 2006.
- [29] J.C Gutierrez-Vega, "Notes on the theory and numerical analysis of the Mathieu functions", Photonics and Mathematical Optics Group, Monterrey, NL, Mexico, March 2003.
- [30] N.W. McLachlan, "Theory and application of Mathieu functions", Oxford Press, London, 1951.
- [31] L. B. Felsen and N. Marcuvitz, "Radiation and scattering of waves", 2nd Edition, *IEEE Series on Electromagnetic Wave Theory*, John Wiley & Sons, Inc., 1994.

-
- [32] J.G. Van Bladel, "Electromagnetic Fields", IEEE/OUP Series on Electromagnetic Wave Theory, 2nd Edition, June 2007.
- [33] H. Uberall and G. C. Gaunaurd, "The physical content of the singularity expansion method," *Appl. Phys. Lett.*, vol. 39, pp. 362-364, 1981.
- [34] G. C. Gaunaurd, H. Uberall, and A. Nagl, "Complex-frequency poles and creeping-wave transients in electromagnetic-wave scattering," *Proc. IEEE*, Vol. 71, pp. 172-174, 1983.
- [35] E. Heyman and L. B. Felsen, "Creeping waves and resonances in transient scattering by smooth convex objects," *IEEE Trans. Antennas Propagat.*, vol. AP-31, pp. 426-437, 1983.
- [36] Y. Wang, I. D. Longstaff and C. J. Leat, "Measurement of complex natural resonances of targets in free space and lossy media", *Progress In Electromagnetics Research*, PIER 29, 221-230, 2000.
- [37] R.F. Harrington, "Field computation by Moment Methods", Wiley-IEEE Press, 1995.
- [38] J. Chauveau, N. Beaucoudrey and J. Saillard, "Selection of contributing natural poles for the characterization of perfectly conducting targets in resonance region", *IEEE Trans. Antennas Propagat.*, vol. 55, no. 9, pp. 2610-2617, Sept. 2007.
- [39] L. Li and C.H Liang, "Generalized system function analysis of exterior and interior resonances of antenna and scattering problems", *IEEE Trans. Antennas Propagat.*, vol. 52, no. 8, pp. 2064-2072, August 2004.
- [40] L. Li and C.H Liang, "Analysis of resonance and quality factor of antenna and scattering systems using complex frequency method combined with model-based parameter estimation", *Progress In Electromagnetics Research*, PIER 46, 165-188, 2004.
- [41] S. Licul and W.A Davis, "Unified frequency and time-domain antenna modeling and characterization", *IEEE Trans. Antennas Propagat.*, vol. 53, no. 9, pp. 2882-2888, Sept. 2005.
- [42] R.C Hall and H. Steyskal, "Wideband scattering of microstrip patches using natural modes", *IEEE Trans. Antennas Propagat.*, vol. 43, no. 10, pp. 1140-1143, Oct. 1995.
- [43] W.Sun, K.M Chen, D.P Nyquist and E.J. Rothwell, "Determination of the natural modes for a rectangular plate", *IEEE Trans. Antennas Propagat.*, vol. 38, no. 5, pp. 643-652, May 1990.
- [44] T.H. Shumpert, L.S. Riggs and J.M. Lindsey, "Singularity expansion method analysis of regular polygonal loops", *IEEE Trans. Antennas and Propagat.*, Vol. 38, no. 8, pp. 1302 - 1306, Aug. 1990.
- [45] M. Cabedo Fabrés, E. Antonino-Daviu, A. Valero-Nogueira and M. Ferrando-Bataller, "Systematic antenna design using the Theory of Characteristic Modes", *JINA 2004*, 13th International Symposium on Antennas, Nice (France), November 2004.
-

- [46] K.Y. Kabalan, R.F Harrington, H.A. Auda and J.R. Mautz, "Characteristic Modes for Slots in a Conducting Plane, TE Case", *IEEE Trans. Antennas Propagat.*, vol. AP-35, no. 2, pp. 162-168, Feb. 1987.
- [47] K.Y. Kabalan, R.F Harrington, J.R. Mautz and H.A. Auda, "Characteristic Modes for a Slot in a Conducting Plane, TM Case", *IEEE Trans. Antennas Propagat.*, vol. AP-35, no. 3, pp. 331-335, March 1987.
- [48] M. Davidovitz, "Continuous Spectrum and Characteristic Modes of the Slot Line in Free Space", *IEEE Trans. Microwave Theory and Tech.*, vol. 44, no. 2, pp. 340-341, Feb. 1996.
- [49] G. Amendola, G. Angiulli and G. Di Massa, "Numerical and analytical characteristic modes for conducting elliptic cylinders", *Microwave and Optical Tech. Letters*, Vol. 16, no. 4, pp. 243-249, Nov. 1997.
- [50] D. Erricolo, "Acceleration of the Convergence of Series Containing Mathieu Functions Using Shanks Transformation", *IEEE Antennas and Wireless Propagat. Lett.*, Vol. 2, pp. 58-61, 2003.
- [51] M. Mongiardo and T. Rozzi, "Continuous Spectrum, Characteristic Modes, and Leaky Waves of Open Waveguides", *IEEE Trans. Microwave Theory and Tech.*, vol. 41, no. 8, pp. 1329-1335, August 1993.
- [52] T. Itoh, "Numerical Techniques for Microstrip and Millimeter-Wave Passive Structures", New York: Wiley, 1989.
- [53] C. Hechtman, H. Zmuda and D. Gabbay, "A Frequency-Dependent Basis Function Applied to Microstrip", *IEEE Trans. Microwave Theory and Tech.*, vol. 39, no. 5, pp. 893-896, May 1991.
- [54] M. Cabedo-Fabres, E. Antonino-Daviu, A. Valero-Nogueira and M. Ferrando-Bataller, "Controlled antenna design method based on the use of characteristic modes", *Progress in Electromagnetics Research Symposium PIERS 2004. Pisa (Italy)*. March 2004.
- [55] A.D. Yaghjian and S.R. Best, "Impedance, bandwidth, and Q of antennas", *IEEE Trans. Antennas Prop.*, vol. 53, pp. 1298 - 1324, April 2005.
- [56] D. Gesbert, M. Shafi, D-S Shiu, P. Smith and A. Naguib, "From Theory to Practice: An Overview of MIMO Space-Time Coded Wireless Systems", *IEEE Journal on Selected Areas in Communications*, vol. 21, no. 3, April 2003.
- [57] T. Svantesson, "Correlation and Channel Capacity of MIMO Systems Employing Multimode Antennas", *IEEE Trans. on Vehicular Techn.*, vol. 51, no. 6, pp. 1304-1312, Nov. 2002.
- [58] C. Waldschmidt, and W. Wiesbeck, "Compact Wide-Band Multimode Antennas for MIMO and Diversity," *IEEE Trans. Antennas Propagat.*, vol. 52, no. 8, pp. 1963-1969, August 2004.
- [59] R. F. Harrington and J. R. Mautz, "Control of Radar Scattering by Reactive Loading," *IEEE Trans. Antennas Propagat.*, vol. AP-20, no. 4, pp. 446-454, July 1972.

-
- [60] R. F. Harrington and J. R. Mautz, "Pattern Synthesis for Loaded N-port Scatterers," *IEEE Trans. Antennas Propagat.*, vol. AP-22, no. 2, pp. 184-190, March 1974.
- [61] C.S. Hong, "Small annular slot antenna with capacitor loading", *Electronics Letters*, Vol. 36, Is. 2, pp: 110-111, 20 Jan. 2000.
- [62] J.Y. Sze, C.I.G. Hsu and S.C. Hsu, "Design of a Compact Dual-Band Annular-Ring Slot Antenna", *IEEE Antennas and Wireless Propag. Let.*, Vol. 6, pp.:423-426, 2007.
- [63] S. Nikolaou; R. Bairavasubramanian, C. Lugo, I. Carrasquillo, D.C. Thompson, G.E. Ponchak, J. Papapolymerou and M.M. Tentzeris, "Pattern and frequency reconfigurable annular slot antenna using PIN diodes", *IEEE Trans. Antennas Propagat.*, vol. 54, no. 2, Part 1, pp. 439 - 448, Feb. 2006.
- [64] M.K. Fries, M. Grani and R. Vahldieck, "A reconfigurable slot antenna with switchable polarization", *IEEE Microwave and Wireless Comp. Let.*, Vol. 13, Is. 11, pp: 490-492, Nov. 2003.
- [65] G. McFeeters, M.A.J. Weldon and M. Okoniewski, "Aperture-fed patch antenna with planar reactive load", *Antennas and Wireless Propag. Let.*, Vol. 3, Iss.1, pp.: 182-185, 2004.
- [66] S.-W. Qu, C.-L. Ruan, B.-Z. Wang and Q. Xue "Planar Bow-tie Antenna Embedded in Circular Aperture within Conductive Frame", *Antennas and Wireless Propag. Lett.*, Vol. 5, Iss. 1, pp.: 399-401, Dec. 2006.
- [67] M. Lee, B.A. Kramer, C.C. Chen and J.L. Volakis, "Distributed Lumped Loads and Lossy Transmission Line Model for Wideband Spiral Antenna Miniaturization and Characterization", *IEEE Trans. Antennas Propagat.*, vol. 55, no. 10, pp. 2671-2678, Oct. 2007.
- [68] C.A. Balanis, "Antenna Theory: Analysis and design, 2nd Edition", Wiley, 2005.
- [69] S. Honda, M. Ito, H. Seki, and Y. Jingo, "A disc monopole antenna with 1:8 impedance bandwidth and omnidirectional radiation pattern", *Proc. Int. Sym., Antennas Propagat.*, Sapporo, Japan, September 1992, pp 1145-1148.
- [70] M. J. Ammann, "Impedance bandwidth of the square planar monopole," *Microwave Opt. Technol. Lett.*, vol. 24, no. 3, pp. 185-187, February 2000.
- [71] Z.N. Chen and M.Y.W. Chia, "Impedance characteristics of EMC triangular planar monopoles", *Electronics Letters*, vol. 37, Iss. 21, pp.1271 - 1272, 11 Oct 2001.
- [72] N. P. Agrawall, G. Kumar, and K. P. Ray, "Wide-band planar monopole antennas", *IEEE Trans. Antennas Prop.*, vol. 46, pp. 294-295, February 1998.
- [73] M. J. Ammann, "The pentagonal planar monopole for digital mobile terminals; bandwidth considerations and modelling," *Eleventh International Conference on Antennas and Propagation*, No. 480, vol. 1, pp. 82-85, April 2001.
- [74] M. Cabedo, M. Ferrando and A. Valero, "A wideband arrowhead planar monopole antenna for multi-service mobile systems", *Microwave and Optical Technology Letters*, vol. 37, Iss. 3, pp. 188-190, 5 May 2003.
-

- [75] Z.N. Chen, "Impedance characteristics of planar bow-tie-like monopole antennas", *Electronics Letters*, vol. 36, Iss. 13, pp.1100 – 1101, 22 June 2000.
- [76] M. J. Ammann, "Control of the impedance bandwidth of wideband planar monopole antennas using a beveling technique", *Microwave and Opt. Technol. Lett.*, vol. 30, no. 4, pp. 229-232, August 2001.
- [77] M. J. Ammann and Z.N. Chen, "A wide-band shorted planar monopole with bevel," *IEEE Trans. Antennas Propagat.*, vol. 51, no. 4, pp. 901-903, April 2003.
- [78] M. J. Ammann and Z.N. Chen, "Wide-band monopole antennas for multi-band wireless systems," *IEEE Antennas & Propagat. Magazine*, vol. 45, no. 2, pp. 146-150, April 2003.
- [79] M. Cabedo-Fabres, E. Antonino-Daviu, A. Valero-Nogueira and M. Ferrando-Bataller, "On the use of characteristic modes to describe patch antenna performance", *IEEE Antennas and Propag. Society International Symposium*, Vol. 2, pp. 712-715, 22-27 June 2003.
- [80] M. Cabedo, A. Valero, J. I. Herranz and M. Ferrando, "A discussion on the Characteristic Mode Theory limitations and its improvements for the effective modeling of antennas and arrays," *2004 AP-S/URSI Symposium*, Monterey, California, July 2004.
- [81] E. Antonino-Daviu, M. Cabedo-Fabres, M. Ferrando-Bataller and A. Valero-Nogueira, "Efecto de las discontinuidades en la radiación de estructuras planas", *XIX Simposium Nacional de la URSI*, Barcelona, Sep. 2004.
- [82] E. Antonino-Daviu, M. Cabedo-Fabres, A. Valero-Nogueira and M. Ferrando-Bataller "A discussion on the feed configuration of planar monopole antennas to obtain ultra wide band performance", *IEEE Antennas and Propag. Society International Symposium*, Vol. 2, pp. 1867-1870, 20-25 June 2004.
- [83] E. Antonino-Daviu, M. Cabedo-Fabres, M. Ferrando-Bataller and A. Valero-Nogueira, "Wideband double-fed planar monopole antennas", *Electronics Letters* , Vol. 39, Iss.: 23, pp.: 1635-1636, 13 Nov. 2003.
- [84] K.L. Wong, C.H. Wu and S.W. Su, "Ultrawide-band square planar metal-plate monopole antenna with a trident-shaped feeding strip", *IEEE Trans. Antennas Propagat.*, vol. 53, no. 4, pp. 1262-1269, April 2005.
- [85] J. Jung, H. Lee and Y. Lim, "Broadband flexible meander line antenna with vertical lines", *Microwave and Opt. Technol. Lett.*, vol. 49, no. 8, pp. 1984-1987, May 2007.
- [86] Z.N. Chen, T.S.P. See and X. Qing, "Small Printed Ultrawideband Antenna With Reduced Ground Plane Effect", *IEEE Trans. Antennas Propagat.*, vol. 55, no. 2, pp. 383-388, Feb. 2007.
- [87] J. Jung, W. Choi and J. Choi, "A Compact Broadband Antenna with an L-Shaped Notch", *IEICE Transactions on Communications*, Vol. E89-B, no. 6, pp. 1968-1971, 2006.

-
- [88] S.W. Su, K.L. Wong and C.L. Tang, "Ultra-wideband square planar monopole antenna for IEEE 802.16a operation in the 2-11-GHz band", *Microwave and Opt. Technol. Lett.*, vol. 42, no. 6, pp. 463-466, July 2004.
- [89] Z.N. Chen, M.J. Ammann, X. Qing, X.H. Wu, T.S.P. See and A. Cai, "Planar antennas", *IEEE Microwave Magazine*, Vol. 7, Iss. 6, pp.:63-73, Dec. 2006.
- [90] Z.N. Chen and M.Y.W. Chia, "Broadband Planar Antennas: Design and Applications", Ed. Wiley. December 2005.
- [91] S.B. Park, J.M. Park, B.C. Ahn and K.S. Kim, "Parametric Studies for the Optimum Design of a Hexagonal Plate Monopole Antenna", *Journal of the Korea Electromagnetic Engineering Society* 2006, vol.6 No.1, 2006.
- [92] X. L. Bao and M. J. Ammann, "Investigation on UWB printed monopole antenna with rectangular slitted groundplane", *Microwave and Opt. Technol. Lett.*, vol. 49, no. 7, pp. 1585-1587, April 2007.
- [93] D. Valderas, J. Meléndez and I. Sancho, "Some design criteria for UWB planar monopole antennas: Application to a slotted rectangular monopole", *Microwave and Opt. Technol. Lett.*, vol. 46, no. 1, pp. 6-11, May 2005.
- [94] J. Jung, W. Choi and J. Choi, "A small wideband microstrip-fed monopole antenna", *IEEE Microwave and Wireless Components Letters*, vol. 15, no. 10, pp. 703-705, Oct. 2005.
- [95] K.L. Wong, S.W. Su and C.L. Tang, "Broadband omnidirectional metal-plate monopole antenna", *IEEE Trans. Antennas Propagat.*, vol. 53, no. 1, pp. 581-583, January 2005.
- [96] A.A. Eldek, "Numerical analysis of a small ultra wide band microstrip-fed tap monopole antenna", *Progress In Electromagnetics Research*, PIER 65, 59-69, 2006.
- [97] D.C. Chang, J.C. Liu and M.Y. Liu, "A novel tulip-shaped monopole antenna for UWB applications", *Microwave and Opt. Technol. Lett.*, vol. 48, no. 2, pp. 307-312, Dec. 2005.
- [98] J. Liang, C.C. Chiau, X. Chen and C.G. Parini, "Study of a printed circular disc monopole antenna for UWB systems", *IEEE Trans. Antennas Propagat.*, vol. 53, no. 11, pp. 3500-3504, Nov. 2005.
- [99] S.W. Su, K.L. Wong, Y.T. Cheng and W.S. Chen, "Finite-ground-plane effects on the ultra-wideband planar monopole antenna", *Microwave and Opt. Technol. Lett.*, vol. 43, no. 6, pp. 535-537, Oct. 2004.
- [100] J. Liang, C.C. Chiau, X. Chen and C.G. Parini, "Printed circular disc monopole antenna for ultra-wideband applications", *Electronics Letters*, Vol. 40, Iss. 20, pp.: 1246-1247, 30 Sept. 2004.
- [101] C.Y. Huang and W.C. Hsia, "Planar elliptical antenna for ultra-wideband communications", *Electronics Letters*, Vol. 41, Iss. 6, pp.: 296-297, March 2005.
- [102] J. Liang, C.C. Chiau, X. Chen and C.G. Parini, "Analysis and design of UWB disc monopole antennas", *IEE Seminar on Ultra Wideband Communications*
-

- Technologies and System Design, University of London, pp: 103-106, July 2004.
- [103] S. Gupta, M. Ramesh and A.T. Kalghatgi, "Design of optimized CPW fed monopole antenna for UWB applications", *Microwave Conference Proceedings*, 2005. APMC 2005. Asia-Pacific Conference Proceedings, Vol. 4, Dec. 2005.
- [104] Z.N. Chen and X. Qing, "Research and development of planar UWB antennas", *Microwave Conference Proceedings*, 2005. APMC 2005. Asia-Pacific Conference Proceedings, Vol. 1, Dec. 2005.
- [105] S.C.K. Ko and R. Murch, "Compact Integrated Diversity Antenna for Wireless Communications", *IEEE Trans. Antennas Propagat.*, vol. 49, no. 6, pp. 954-960, June 2001.
- [106] N. Belmar-Moliner, A. Valero-Nogueira, M. Cabedo-Fabres and E. Antonino-Daviu, "Simple design for cost-effective diversity antennas", *Microwave and Optical Technology Letters*, Volume: 49, No. 4, pp.:994-996, April 2007.
- [107] M. Cabedo Fabr s, E. Antonino-Daviu, A. Valero-Nogueira, J. M. Molina-Garcia-Pardo, and L. Juan-Ll cer, "Compact Slitted Planar Monopoles for MIMO Systems", *IEEE Antennas and Propagat. Soc. Int. Symposium 2007*, Honolulu (EEUU). 10-15 June 2007.
- [108] S. Blanch, J. Romeu and I. Corbella, "Exact representation of antenna system diversity performance from input parameter description", *Electronics Letters*, Vol. 39, pp. 705-707, 2003.
- [109] J-M. Molina-Garc a-Pardo, J-V. Rodr guez and L. Juan-Llacer "Indoor MIMO Measurements for WiFi", in COST 273, TD(05)081, Leuven, Belgium, June 2005.
- [110] E. Antonino-Daviu, M. Cabedo-Fabres, M. Ferrando-Bataller and A. Valero-Nogueira, "Design of very wide-band linear-polarized antennas", *JINA, 13th International Symposium on Antennas*, Nice (France), November 2004.
- [111] M. Manteghi and Y. Rahmat-Samii, "Multiport characteristics of a wide-band cavity backed annular patch antenna for multipolarization operations", *IEEE Trans. Antennas Propagat.*, vol. 53, no. 1, pp. 466-474, January 2005.
- [112] Y. Yao and Z. Feng, "Novel switched sector beam planar UWB antenna", *Microwave and Optical Technology Letters*, Volume: 49, No. 5, pp.: 1185-1187, May 2007.
- [113] Y. Shin, B. Kim, W. Kwak and S. Park, "GSM/DCS/IMT-2000 triple-band built-in antenna for wireless terminals", *Antennas and Wireless Propagation Letters*, vol. 3, Iss. 1, pp.104 - 107, 2004.
- [114] D.M Nashaat, H.A Elsadek, H. Ghali, "Single Feed Compact Quad-Band PIFA Antenna for Wireless Communication Applications", *IEEE Trans. Antennas and Propagat.*, vol. 53, no. 8, part 2, pp. 2631 - 2635, Aug. 2005.

-
- [115] W.-I. Kwak, S.O Park and J.S Kim, "A Folded Planar Inverted-F Antenna for GSM/DCS/Bluetooth Triple-Band Application", *Antennas and Wireless Propag. Lett.*, vol. 5, no. 1, pp. 18-21, Dec. 2006.
- [116] K.L. Wong; Y.C. Lin and T.C. Tseng, "Thin internal GSM/DCS patch antenna for a portable mobile terminal," *IEEE Trans. Antennas Propagat.*, vol. 54, no. 1, pp. 238 - 242, Jan. 2006.
- [117] M. Martinez-Vazquez, M. Geissler, D. Heberling, A. Martinez-Gonzalez, and D. Sanchez-Hernandez, "Compact dual-band antenna for mobile handsets," *Microwave and Opt. Technol. Lett.*, vol. 32, no. 2, pp. 87-88, Jan. 2002.
- [118] M. K. Kärkkäinen, "Meandered multiband PIFA with coplanar parasitic patches", *IEEE Microwave and Wireless Components Letters*, vol. 15, no. 10, pp.630-632, Oct. 2005.
- [119] Y. Guo, M.Y.W Chia, Z.N. Chen, "Miniature built-in multiband antennas for mobile handsets", *IEEE Trans. Antennas and Propagat*, vol. 52, no. 8, pp.1936-1944, August 2004.
- [120] S.H. Wi, Y.S. Lee and J.G. Yook, "Wideband Microstrip Patch Antenna With U-Shaped Parasitic Elements", *IEEE Trans. Antennas and Propagat.*, vol. 55, no. 4, pp. 1196 - 1199, April 2007.
- [121] P. Ciaisi, R. Staraj, G. Kossivas, C. Luxey, "Design of an internal quad-band antenna for mobile phones", *IEEE Microwave and Wireless Components Letters*, vol. 14, no. 4, pp.148 - 150, April 2004.
- [122] A. Byndas, R. Hossa, M.E. Bialkowski and P. Kabacik, "Investigations into Operation of Single- and Multi-Layer Configurations of Planar Inverted-F Antenna", *IEEE Antennas and Propag. Magazine*, Vol. 49, Is. 4, pp. 22 - 33, Aug. 2007.
- [123] Y. Kim and D.-H. Kwon, "CPW-fed planar ultra wideband antenna having a frequency band notch function," *Electron. Lett.*, vol. 40, no. 7, Apr. 2004.
- [124] K. Chung, J. Kim and J. Choi, "Wideband microstrip-fed monopole antenna having frequency band-notch function", *IEEE Microwave and Wireless Comp. Lett.*, Vol. 15, Is. 11, pp. 766 - 768, Nov. 2005.
- [125] W.-S. Lee, W.-G. Lim and J.-W. Yu, "Multiple band-notched planar monopole antenna for multiband wireless systems", *IEEE Microwave and Wireless Components Letters*, vol. 15, Iss. 9, pp. 576-578, Sept. 2005.
- [126] W.S. Lee, D.Z. Kim, K.J. Kim and J.W. Yu, "Wideband planar monopole antennas with dual band-notched characteristics", *IEEE Trans. Microwave Theory and Tech.*, vol. 54, Iss. 6, Part 2, pp. 2800 - 2806, June 2006.
- [127] Y.J. Cho, K.H. Kim, D.H. Choi, S.S. Lee and S.O. Park, "A miniature UWB planar monopole antenna with 5-GHz band-rejection filter and the time-domain characteristics", *IEEE Trans. on Antennas and Propag.*, vol. 54, Is. 5, pp. 1453-1460, May 2006.

- [128] C.-Y. Hong, C.-W. Ling, I.-Y. Tarn and S.-J. Chung, "Design of a Planar Ultrawideband Antenna With a New Band-Notch Structure", *IEEE Trans. on Antennas and Propag.*, vol. 55, Is. 12, pp. 3391 - 3397, Dec. 2007.
- [129] A. Kerkhoff and H. Ling, "A parametric study of band-notched UWB planar monopole antennas", *IEEE Antennas and Propag. Soc. Int. Symp. 2004*, Vol: 2, pp: 1768- 1771, 20-25 June 2004.
- [130] H. Schantz, "The Art and Science of Ultrawideband Antennas," Artech House, Norwood, MA, 2005.
- [131] E. Antonino, M. Ferrando, M. Cabedo and C.A. Suarez, "Ultra-wideband antenna with switchable band-notched behaviour", 1st European Conference on Antennas and Propagation, Nice (France). November 2006.
- [132] E. Antonino, M. Cabedo, M. Ferrando and M. Baquero, "Novel UWB antennas with switchable and tunable band-notched behavior", *IEEE Antennas and Propagation Society International Symposium 2007*, Honolulu (EEUU). 10-15 June 2007.
- [133] N. Kingsley, D. E. Anagnostou, M. Tentzeris and J. Papapolymerou, "RF MEMS Sequentially Reconfigurable Sierpinski Antenna on a Flexible Organic Substrate With Novel DC-Biasing Technique", *Journal of Microelectromechanical systems*, Vol. 16, No. 5, Oct. 2007.
- [134] D. E. Anagnostou et al., "Design, fabrication, and measurements of an RF-MEMS-based self-similar reconfigurable antenna," *IEEE Trans. Antennas Propag.*, vol. 54, no. 2, pt. 1, pp. 422–432, Feb. 2006.
- [135] B. Cetiner, J. Qian, H. Chang, M. Bachman, G. Li, and F. DeFlaviis, "Monolithic integration of RF MEMS switches with a diversity antenna on PCB substrate," *IEEE Trans. Microw. Theory Tech.*, vol. 51, no. 1, pp. 332–334, Jan. 2003.
- [136] C. Goldsmith, J. Randall, S. Eshelman, T. H. Lin, D. Denniston, S. Chen, and B. Norvell, "Characteristics of micromachined switches at microwave frequencies," in *IEEE Microwave Theory and Techniques Symp. Dig.*, vol. 2, 1996, pp. 1141–1144.
- [137] D. Peroulis, K. Sarabandi and L. P. B. Katehi, "Design of Reconfigurable Slot Antennas", *IEEE Trans. Antennas Propagat.*, vol. 53, no. 2, pp. 645-654, February 2005.
- [138] N. Symeon, R. Bairavasubramanian, C. Lugo, I. Carrasquillo, D.C. Thompson, G.E. Ponchak, J. Papapolymerou, M.M. Tentzeris, "Pattern and frequency reconfigurable annular slot antenna using PIN diodes", *IEEE Trans. Antennas Propag.*, vol. 54, no. 2, pt. 1, pp. 439-448, Feb. 2006.
- [139] S.H. Chen, J.-S. Row, K.L. Wong, "Reconfigurable Square-Ring Patch Antenna With Pattern Diversity", *IEEE Trans. Antennas Propag.*, vol. 55, no. 2, pp. 472-475, Feb. 2007.

-
- [140] W.L. Liu, T.R. Chen, S.H. Chen and J.S. Row, "Reconfigurable microstrip antenna with pattern and polarisation diversities", *Electronics Letters*, Vol. 43, Is. 2, pp: 77 – 78, Jan. 18 2007.
- [141] H. Scott and V.F. Fusco, "Electronic beam tilting using a single reactively loaded circular wire loop antenna", *IEE Proc. Microwaves, Antennas and Propagation*, Vol. 149, Is. 56, pp.: 271- 274, Oct/Dec 2002.
- [142] E. Öjefors, S. Cheng, K. From, I. Skarin, P. Hallbjörner and A. Rydberg, "Electrically steerable single-layer microstrip traveling wave antenna with varactor diode based phase shifters", *IEEE Trans. Antennas Propag.*, vol. 55, no. 9, pp. 2451-2460, Sep. 2007.
- [143] V.A Shameena, M.N. Suma, K. Raj Rohith, P.C. Bybi and P. Mohanan, "Compact ultra-wideband planar serrated antenna with notch band ON/OFF control", *Electronics Letters*, Vol. 42, Is. 23, pp:1323-1324, 9 Nov. 2006.
- [144] N. Behdad, and K. Sarabandi, "A Varactor-Tuned Dual-Band Slot Antenna", *IEEE Trans. Antennas Propag.*, vol. 54, no. 2, pp. 401-408, Feb. 2006.
- [145] B.R. Holland, R. Ramadoss, S. Pandey and P. Agrawal, "Tunable coplanar patch antenna using varactor", *Electronics Letters*, Vol. 42, Is. 6, pp: 319-321, 16 March 2006.
- [146] E. Antonino-Daviu, M. Cabedo-Fabres, M. Ferrando-Bataller and A. Vila-Jimenez, "Active UWB Antenna with tuneable band-notched behaviour", *Electronics Letters*, Vol. 43, Is. 18, pp.: 959-960, 31 Aug. 2007.
- [147] R. F. Harrington, "Effect of Antenna Size on Gain, Bandwidth and Efficiency," *Journal of Research of the National Bureau of Standards - D. Radio Propagation*, 64D, January-February 1960, pp. 1-12.
- [148] R. Mittra and S. Dey, "Challenges in PCS antenna design", *IEEE Antennas and Propag. Soc. Int. Symposium*, 1999. Vol. 1, pp.:2751 – 2754, 11-16 July 1999.
- [149] M. Martínez-Vázquez, M. Geissler and D. Heberling, "Volume Considerations in the Design of Dual-Band Handset Antennas", *IEEE Antennas and Propagation Society Symposium*, Boston (Massachusetts, USA), July 2001.
- [150] R. C. Hansen, "Fundamental limitations in antennas," *Proc. IEEE*, vol. 69, pp. 170–182, Feb. 1981.
- [151] J. S. McLean, "A Re-Examination of the Fundamental Limits on the Radiation Q of Electrically Small Antennas," *IEEE Transactions on Antennas and Propagation*, AP-44, May 1996, pp. 672-676.
- [152] P. Vainikainen, J. Ollikainen, O. Kivekäs, and I. Klander, "Resonator-based analysis of the combination of mobile handset antenna and chassis," *IEEE Trans. on Antennas and Propag.*, Vol. 50, No. 10, pp. 1433–1444, Oct. 2002.
- [153] E. Antonino-Daviu, M. Cabedo-Fabres, M. Ferrando-Bataller and J.I. Herranz-Herruzo, "Analysis of the coupled chassis-antenna modes in mobile handsets", *IEEE Antennas and Propag. Soc. Int. Symposium*, 2004. Vol. 3, pp.:2751 – 2754, 20-25 June 2004.

- [154] E. Antonino-Daviu, C.A. Suarez-Fajardo, M. Cabedo-Fabres and M. Ferrando-Bataller, "Wideband antenna for mobile terminals based on the handset PCB resonance," *Microwave and Optical Technology Letters*, Vol. 48, No. 7, pp. 1408-1411, July 2006.
- [155] J. Villanen, J. Ollikainen, O. Kivekäs, and P. Vainikainen, "Coupling element based mobile terminal antenna structures," *IEEE Trans. on Antennas and Propag.*, Vol. 54, No. 7, pp. 2142–2153, July 2006.
- [156] J. Villanen, C. Icheln, and P. Vainikainen, "A coupling element-based quad-band antenna structure for mobile terminals," *Microwave and Optical Technology Letters*, vol. 49, no. 6, pp. 1277 - 1282, June 2007.
- [157] P. Vainikainen, J. Villanen, J. Holopainen and C. Icheln, "Development trends of small antennas for mobile terminals," *Antennas and Propagation Society International Symposium*, 2007.
- [158] F.S. Chang and K.L. Wong, "A broadband probe-fed planar patch antenna with a short probe pin and a conducting cylinder transition", *Microwave and Optical Technology Letters*, vol.31, no. 4, pp. 282-284, Nov 2001.
- [159] Z. N. Chen and M.Y.W Chia, "A feeding scheme for enhancing the impedance bandwidth of a suspended plate antenna," *Microwave and Optical Technology Letters*, vol.38, no. 1, pp. 21-25, July 5 2003.
- [160] R. Feick, H. Carrasco, M. Olmos and H.D. Hristov, "PIFA input bandwidth enhancement by changing feed plate silhouette," *Electronics Letters*, vol.40, no. 15, pp. 921-922, 22 July 2004.
- [161] J.-H. Jung, H. Choo, I. Park, "Small broadband disc-loaded monopole antenna with probe feed and folded stripline", *Electronics Letters*, vol.41, no. 14, pp. 788-789, 7 July 2005.
- [162] R. Hossa, A. Byndas, and M. E. Bialkowski, "Improvement of Compact Terminal Antenna Performance by Incorporating Open-End Slots in Ground Plane", *IEEE Microwave and Wireless Components Letters*, vol. 14, no.6, pp. 283-285, June 2004.
- [163] P. Kabacik, R. Hossa, A. Byndas, "Broadening the bandwidth in terminal antennas by tuning the coupling between the element and its ground", *IEEE Antennas and Propagation Society International Symposium*, 2005, Vol. 3A, pp: 557 – 560, July 2005.
- [164] M. Cabedo-Fabrés, A. Valero-Nogueira, E. Antonino-Daviu and M. Ferrando-Bataller, "Modal analysis of a radiating slotted PCB for mobile handsets", *1st European Conference on Antennas and Propagation*, Nice (France). November 2006.
- [165] E. Antonino, M. Cabedo, M. Ferrando, A. Valero and M. Martínez-Vazquez, "Novel antenna for mobile terminals based on the chassis-antenna coupling", *IEEE Antennas and Propag. Soc. Int. Symposium*, 2005. Vol. 1A, pp.:503 – 506, 3-8 July 2005.

-
- [166] R. A. Burberry, "VHF and UHF Antennas", IEEE Electromagnetic Waves Series, P. Peregrinus, March 1993.
- [167] F. Yang, X.X. Zhang, X. Ye and Y. Rahmat-Samii, "Wide-band E-shaped patch antennas for wireless communications", IEEE Trans. on Antennas and Propag., Vol. 49, No. 7, pp. 1094 - 1100, July 2001.
- [168] A.A. Deshmukh and G. Kumar, "Compact broadband E-shaped microstrip antennas", Electronics Letters, vol.41, no. 18, pp. 989-990, 1 Sept. 2005.
- [169] Y. Ge, K.P. Esselle and T.S. Bird, "Compact diversity antenna for wireless devices", Electronics Letters, Vol. 41, No. 2, pp. 52-53, Jan. 2005.
- [170] D. Caratelli, R. Cicchetti, G. Bit-Babik and A. Faraone, "A Perturbed E-Shaped Patch Antenna for Wideband WLAN Applications", IEEE Trans. on Antennas and Propag., Vol. 54, No. 6, pp. 1871 - 1874, June 2006.
- [171] Y. Ge, K.P. Esselle and T.S. Bird, "A compact E-shaped patch antenna with corrugated wings", IEEE Trans. on Antennas and Propag., Vol. 54, No. 8, pp. 2411-2413, August 2006.
- [172] M. Cabedo-Fabres, E. Antonino-Daviu, A. Valero-Nogueira, and M. Ferrando-Bataller; "Notched radiating ground plane analyzed from a modal perspective" Frequenz, Vol. 61, No. 3-4, pp. 66-70, March-April 2007.
- [173] R. Serrano, A. Aguasca, J. Romeu, S. Blanch, L. Jofre, M. Cabedo, E. Antonino, A. Valero, M. Ferrando, "Active balanced feeding for compact wideband antennas", Proc. APS Symp., 9-15 June 2007, pp.:2829-2832.
- [174] D. Pozar, "Microwave Engineering", 3rd Edition, John Wiley & Sons, 2004.
- [175] Antenna Centre of Excellence, Deliverable ACE 2.2.D2, "Small antennas technologies", December 2007.

Appendix A

Coordinate Systems

A.1. Spherical coordinate system

Spherical coordinates are a system of curvilinear coordinates that are natural for describing positions on a sphere. Any point of space is described in spherical coordinates by three values (ϕ, θ, r) , where ϕ is the azimuthal angle in the xy -plane defined from the x -axis with $0 \leq \phi \leq 2\pi$, θ is the polar angle defined from the z -axis with $0 \leq \theta \leq \pi$, and r is the distance (radius) from the point to the origin. Figure A.1 shows the commonly used spherical coordinate system.

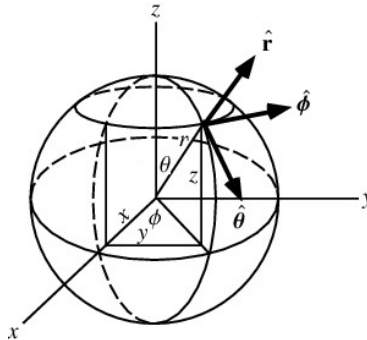


Figure A.1 Spherical coordinate system.

A.2. Oblate spheroidal coordinate system

Prolate and oblate spheroidal coordinate systems are formed by rotating the two-dimensional elliptic coordinate system, consisting of confocal ellipses and hyperbolas, about the major and minor axes of the ellipses, respectively.

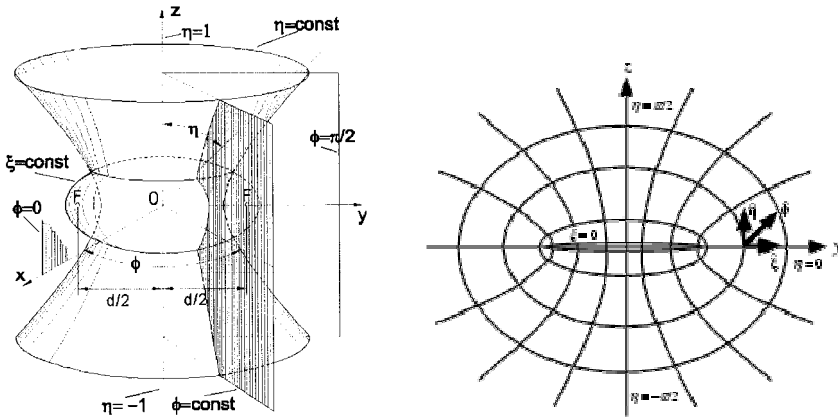


Figure A.2 Oblate spheroidal coordinate system

The oblate spheroidal coordinates shown in Figure A.2 are related to the rectangular coordinates by the following transformations:

$$\begin{aligned}
 x &= \frac{d}{2} \sqrt{(1-\eta^2)(\xi^2+1)} \cos \phi \\
 x &= \frac{d}{2} \sqrt{(1-\eta^2)(\xi^2+1)} \sin \phi \\
 z &= \frac{d}{2} \eta \xi
 \end{aligned}
 \tag{A.2.1}$$

where

$$-1 \leq \eta \leq 1, \quad 0 \leq \xi < \infty, \quad 0 \leq \phi \leq 2\pi
 \tag{A.2.2}$$

In an oblate spheroidal system, the surface at $\xi = \text{constant} > 0$ forms a flattened ellipsoid of revolution with a major axis of length $d\sqrt{\xi^2+1}$ and minor axis of length $d\xi$. The degenerated surface at $\xi = 0$ is a circular disk of radius $a = \frac{d}{2}$ which lies in the XY plane and is centered at the origin. The surface at $|\eta| = \text{constant} < 1$ is a hyperboloid of revolution of one sheet with an asymptotic cone whose generating line passes through the origin and is inclined at the angle $\theta = \cos^{-1} \eta$ to the z axis. The degenerate surface at $|\eta| = 1$ is the z axis. The

surface at $\phi = \text{constant}$ is a plane through the z axis forming the angle ϕ with respect to the XZ plane.

The oblate spheroidal coordinate system is also a curvilinear orthogonal system. Its metric coefficients are given by

$$\begin{aligned} h_\eta &= \frac{d}{2} \sqrt{\frac{\xi^2 + \eta^2}{1 - \eta^2}} \\ h_\xi &= \frac{d}{2} \sqrt{\frac{\xi^2 + \eta^2}{\xi^2 + 1}} \\ h_\phi &= \frac{d}{2} \sqrt{(1 - \eta^2)(\xi^2 + 1)} \end{aligned} \tag{A.2.3}$$

The coordinates (η, ξ, ϕ) form a right-handed system. In the limit where the inter-focal distance d becomes zero or the ξ approaches infinity (while $\eta = \text{constant}$), the oblate spheroidal coordinate system reduce to the ordinary spherical system.

A.2.1. Spheroidal scalar wave functions

With the use of the expression for the Laplacian ∇^2 in orthogonal curvilinear coordinates, the scalar wave equation

$$\nabla^2 \psi + k^2 \psi = 0 \tag{A.2.4}$$

is expressed in the oblate spheroidal coordinate system as

$$\begin{aligned} &\left[\frac{\partial}{\partial \eta} (1 - \eta^2) \frac{\partial}{\partial \eta} + \frac{\partial}{\partial \xi} (\xi^2 + 1) \frac{\partial}{\partial \xi} + \frac{\xi^2 + \eta^2}{(\xi^2 + 1)(1 - \eta^2)} \frac{\partial^2}{\partial \phi^2} \right] \psi + \\ &+ c^2 (\xi^2 + \eta^2) \psi = 0 \end{aligned} \tag{A.2.5}$$

where $c = \frac{1}{2} kd$.

The prolate and oblate systems are two of the eleven coordinate systems in which the scalar wave equations are separable. By the usual procedure of the separation of variables, eigenfunctions of the solutions of equation (A.2.5) may be obtained in the form of the Lamé products:

$$\psi_{mn} = S_{mn}(-ic, \eta) \cdot R_{mn}^{(i)}(-ic, i\xi) \cdot \begin{cases} \cos m\phi \\ \sin m\phi \end{cases} \quad (\text{A.2.6})$$

for oblate spheroidal coordinates.

The functions $S_{mn}(-ic, \eta)$ and $R_{mn}^{(i)}(-ic, i\xi)$ satisfy the following ordinary differential equations respectively:

$$\frac{\partial}{\partial \eta} \left[(1-\eta^2) \frac{\partial}{\partial \eta} S_{mn}(-ic, \eta) \right] + \left[\lambda_{mn} + c^2 \eta^2 - \frac{m^2}{1-\eta^2} \right] S_{mn}(-ic, \eta) = 0 \quad (\text{A.2.7})$$

$$\frac{\partial}{\partial \xi} \left[(\xi^2 + 1) \frac{\partial}{\partial \xi} R_{mn}^{(i)}(-ic, i\xi) \right] - \left[\lambda_{mn} + c^2 \xi^2 - \frac{m^2}{\xi^2 + 1} \right] R_{mn}^{(i)}(-ic, i\xi) = 0 \quad (\text{A.2.8})$$

The separation constants λ_{mn} and m , known as eigenvalues, are the same in these equations. These values can be determined by five different methods [20].

The spheroidal angular functions $S_{mn}(-ic, \eta)$ can be represented as a series of associated Legendre functions of different orders. The relations between angular spheroidal functions of the first and second kinds and associated Legendre functions of different orders are given for the prolate spheroidal coordinate as follows:

- for the first kind:

$$S_{mn}^{(1)}(-ic, \eta) = \sum_{r=0,1}^{\infty} d_r^{mn}(-ic) P_{m+r}^m(\eta) \quad (\text{A.2.9})$$

- for the second kind:

$$S_{mn}^{(2)}(-ic, \eta) = \sum_{r=-\infty}^{\infty} d_r^{mn}(-ic) Q_{m+r}^m(\eta) \quad (\text{A.2.10})$$

In equations (A.2.9) and (A.2.10), $P_n^m(x)$ is the associated Legendre function of the first kind (range within $-1 < x < 1$), and $Q_n^m(x)$ is the associated Legendre function of the second kind (range within $|x| \geq 1$), and the prime over the summation sign indicates that the summation is over only even values of r when $n - m$ is

even, and over only odd values of r when $n - m$ is odd. Also power series representation of angular spheroidal functions can be obtained [20].

The intermediate parameter $d_r^{mn}(-ic)$ is an important quantity used frequently in the formulation of the oblate angular (or radial) spheroidal harmonics of various kinds.

The radial spheroidal functions of the first to fourth kinds can be expressed by

$$R_{mn}^{(i)}(-jc, \xi) = \frac{1}{\sum_{r=0,1}^{\infty} d_r^{mn}(-jc) \frac{(2m+r)!}{r!}} \left(\frac{\xi^2 + 1}{\xi^2} \right)^{m/2} \cdot \sum_{r=0,1}^{\infty} i^{r+m-n} d_r^{mn}(-jc) \frac{(2m+r)!}{r!} z_{m+r}^{(i)}(c\xi) \tag{A.2.11}$$

where $z_n^{(i)}(x)$ is the i th kind of spherical Bessel functions of order n (i.e., $z_n^{(1)}(x) = j_n(x)$, $z_n^{(2)}(x) = n_n(x)$, $z_n^{(3)}(x) = h_n^{(1)}(x)$ and $z_n^{(4)}(x) = h_n^{(2)}(x)$, respectively). Since $h_n^{(1)}(x) = j_n(x) + in_n(x)$ and $h_n^{(2)}(x) = j_n(x) - in_n(x)$, thus

$$R_{mn}^{(3)}(-ic, \xi) = R_{mn}^{(1)}(-ic, \xi) + iR_{mn}^{(2)}(-ic, \xi) \tag{A.2.12}$$

$$R_{mn}^{(4)}(-ic, \xi) = R_{mn}^{(1)}(-ic, \xi) - iR_{mn}^{(2)}(-ic, \xi) \tag{A.2.13}$$

A.3. Elliptical-cylindrical coordinate system

Let us consider an ellipse in the plane (x, y) whose equation reads $(x/a)^2 + (y/b)^2 = 1$, where $a > b$. The semifocal distance f is given by $f^2 = a^2 - b^2$, and the eccentricity e is $e = f/a$, $e \in [0, 1]$. The ellipse is defined by any pair of parameters selected from $\{a, b, f, e\}$.

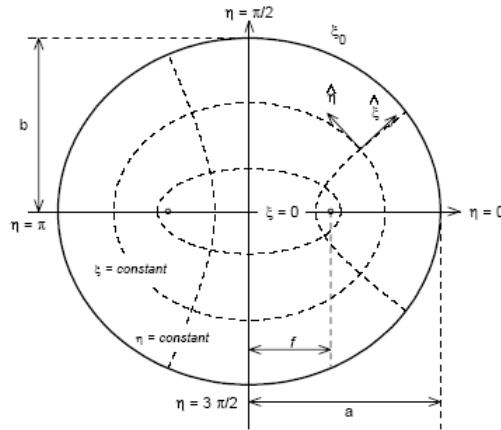


Figure A.3 Elliptical-cylinder coordinate system [29].

The elliptic coordinates (ξ, η, z) are defined according to the equivalence:

$$\begin{aligned} x &= f \cdot \cosh \xi \cdot \cos \eta \\ y &= f \cdot \sinh \xi \cdot \sin \eta \\ z &= z \end{aligned} \tag{A.3.1}$$

where ξ works as a radial coordinate and takes the values $\xi \in [0, \infty)$, the coordinate η is an angular coordinate taking the range $\eta \in [0, 2\pi)$, and $z \in (-\infty, \infty)$. The surface $\xi = \xi_0$ reduces to the elliptic cylinder with semi-major axis $a = f \cdot \cosh \xi_0$, and semi-minor axis $b = f \cdot \sinh \xi_0$. The surface $\eta = \eta_0$ reduces to an hyperbolic cylinder that crosses the x-axis at $\pm f \cdot \cos \eta_0$ and has asymptotes $y = \pm (\tan \eta_0) x$.

The two families of conics are confocal, intersect orthogonally, and each intersection (ξ, η) corresponds to a point in the plane (x, y) defined by equation (A.3.1). Observe in Figure A.3 that for $\eta = 0$ the hyperbola degenerates to the line segment $y = 0, x \geq f$. For $\eta = \pi$ the hyperbola degenerates to the line segment $y = 0, x \leq -f$. For $\eta = \pi/2$, the hyperbola becomes the positive y-axis, whereas $\eta = 3\pi/2$ becomes the negative y-axis.

In Figure A.3 we appreciate that confocal ellipses collapse to a segment of straight line joining the two foci when $\xi = 0$. The focal points $(x, y) = (\pm f, 0)$ are located in the elliptic plane on $(\xi, \eta) = (0, 0)$ and $(0, \pi)$. Finally the origin of the coordinate system can be specified with $(\xi, \eta) = (0, \pi/2)$ or $(0, 3\pi/2)$.

The description of the elliptic coordinate system is not complete without introducing the corresponding scale factors:

$$\begin{aligned} h &\equiv h_\xi = h_\eta = f \sqrt{\cosh^2 \xi - \cos^2 \eta} \\ h_z &= 1 \end{aligned} \tag{A.3.2}$$

Scale factors are necessary to write the gradient, divergence and curl in elliptic coordinates, as follows:

- Gradient:

$$\nabla f = \hat{\xi} \cdot \frac{1}{h_\xi} \cdot \frac{\partial f}{\partial \xi} + \hat{\eta} \cdot \frac{1}{h_\eta} \cdot \frac{\partial f}{\partial \eta} + \hat{z} \cdot \frac{\partial f}{\partial z} \tag{A.3.3}$$

- Divergence:

$$\nabla \cdot \vec{A} = \frac{1}{h_\eta h_\xi} \cdot \left[\frac{\partial}{\partial \xi} (A_\xi h_\eta) + \frac{\partial}{\partial \eta} (A_\eta h_\xi) + \frac{\partial}{\partial z} (A_z h_\xi h_\eta) \right] \tag{A.3.4}$$

- Curl:

$$\nabla \times \vec{A} = \frac{1}{h_\eta h_\xi} \cdot \begin{vmatrix} h_\xi \hat{\xi} & h_\eta \hat{\eta} & \hat{z} \\ \frac{\partial}{\partial \xi} & \frac{\partial}{\partial \eta} & \frac{\partial}{\partial z} \\ h_\xi A_\xi & h_\eta A_\eta & A_z \end{vmatrix} \tag{A.3.5}$$

A.3.1. Helmholtz equation in elliptic coordinates

With the elliptic coordinates introduced in last section, we can express the scalar-wave equation

$$\left[\nabla^2 + k^2 \right] \cdot \psi(\vec{r}) = 0 \quad (\text{A.3.6})$$

in elliptic coordinates and apply the Method of Separation of Variables (SoV) to divide it into three ordinary differential equations. In general, for cylindrical systems the Laplacian operator takes the form $\nabla^2 = \nabla_t^2 + \partial^2/\partial z^2$, then assuming a spatial solution $\psi(\vec{r}) = U_t(\vec{r}_t) \cdot Z(z)$ we can separate equation (A.3.6) into:

$$\left[\frac{d^2}{dz^2} + k_z^2 \right] Z(z) = 0 \quad (\text{A.3.7})$$

$$\left[\nabla_t^2 + k_t^2 \right] \cdot U_t(\vec{r}_t) = 0 \quad (\text{A.3.8})$$

where k_z^2 is the constant of separation and $k_t^2 = k^2 - k_z^2$. Equation (A.3.7) is the Harmonic equation whose solutions are $Z(z) = \exp(\pm i k_z z)$, whereas equation (A.3.8) is the two-dimensional Helmholtz equation. In elliptic coordinates this equation reads as:

$$\left[\frac{\partial^2}{\partial \xi^2} + \frac{\partial^2}{\partial \eta^2} + \frac{f^2 k_t^2}{2} (\cosh 2\xi - \cos 2\eta) \right] \cdot U_t(\xi, \eta) = 0 \quad (\text{A.3.9})$$

Applying again the technique of SoV we assume a solution of the form $U_t(\xi, \eta) = R(\xi) \cdot \Theta(\eta)$. Substitution of U_t into equation (A.3.9) yields

$$\left[\frac{d^2}{d\xi^2} - (a - 2s \cosh 2\xi) \right] R(\xi) = 0 \quad (\text{A.3.10})$$

$$\left[\frac{d^2}{d\eta^2} + (a - 2s \cos 2\eta) \right] \Theta(\eta) = 0 \quad (\text{A.3.11})$$

where a is the constant of separation, and s is a dimensionless parameter related to the transverse propagation constant k_t by

$$s = \frac{f^2}{4} k_t^2 \quad (\text{A.3.12})$$

Observe that equation (A.3.11) transforms into equation (A.3.10), and vice versa, if η is replaced by $\pm i\xi$. Equations (A.3.10) and (A.3.11) are known as the *Radial Mathieu Equation* (RME), and the *Angular Mathieu Equation* (AME) respectively. Their solutions are the *Radial Mathieu Functions* (RMFs) and the *Angular Mathieu Functions* (AMFs). They are also referred to in Mathematics as *Modified* and *Ordinary Mathieu Equations*, respectively, but we will use the Radial and Angular terminology by virtue of its physical meaning in relation with wave propagation.

Angular Mathieu Equation

In order to solve AME, physical considerations are usually such that AME equation (A.3.11) has periodic solutions with period π or 2π . The values of a which satisfy this condition are known as *characteristic values (eigenvalues)*, and they generate an infinite set of real values which have the property $a_0 < a_1 < a_2 < \dots$. When the solutions $\Theta(\eta)$ are even with respect to $\eta = 0$, the characteristic values are denoted as $a_m(s) : m \in \{0, 1, 2, \dots\}$, whereas for odd solutions they are represented as $b_m(s) : m \in \{1, 2, 3, \dots\}$. The characteristic values play an important role since they define the stability of the solutions. When the eigenvalues a belong to a discrete set, the solutions are called of *integral order*, otherwise they are of *fractional order*. The functions of integral order are always stable, but those of fractional order can be stable or unstable.

Since AME (A.3.11) is a second-order differential equation, there are two families of independent solutions:

- First kind solutions, which are periodic:
 - $Se_m(\eta; s)$, cosine-elliptic type
 - $So_m(\eta; s)$, sine-elliptic type
- Second kind solutions, which are non periodic:
 - $fe_m(v; s)$
 - $ge_m(v; s)$

Because of their periodicity, only first kind solutions are usually of importance in real applications.

As we mentioned above, the constant a in equation (A.3.11) is not given a priori, and we have to consider how it is to be determined. In most of the physical prob-

lems, equation (A.3.11) describes the angular dependence of a physical quantity (e.g. electric or magnetic field), and therefore its solutions must be periodic with period 2π . These periodic solutions can be expressed by using the Fourier series, and they fall into four classes, according to their symmetry or antisymmetry, about $\eta = 0$ and $\eta = \pi/2$:

$$\text{Class I: } Se_{2n}(\eta; s) = \sum_{j=0}^{\infty} A_{2j}(s) \cdot \cos(2j\eta), \quad : (a_{2n}) \quad (\text{A.3.13})$$

$$\text{Class II: } Se_{2n+1}(\eta; s) = \sum_{j=0}^{\infty} A_{2j+1}(s) \cdot \cos[(2j+1)\eta], \quad : (a_{2n+1}) \quad (\text{A.3.14})$$

$$\text{Class III: } So_{2n+2}(\eta; s) = \sum_{j=0}^{\infty} B_{2j+2}(s) \cdot \sin[(2j+2)\eta], \quad : (b_{2n+2}) \quad (\text{A.3.15})$$

$$\text{Class IV: } So_{2n+1}(\eta; s) = \sum_{j=0}^{\infty} B_{2j+1}(s) \cdot \sin[(2j+1)\eta], \quad : (b_{2n+1}) \quad (\text{A.3.16})$$

where $n \in \{0, 1, 2, \dots\}$, and the symbols in the right column denote the corresponding characteristic values. The Fourier coefficients A and B depends on the parameter s , and can be obtained by recurrence relations, which are exposed in [29]. Also in this reference, the procedure for the calculation of the characteristic values a_m and b_m is provided.

Functions Se_m and So_{m+1} are orthogonal, due to the orthogonality property of the sine and cosine series. According to the McLachlan normalization [30], the Angular Mathieu functions satisfy the following relations:

$$\int_0^{2\pi} Se_m(\eta; s) \cdot Se_p(\eta; s) \cdot d\eta = \int_0^{2\pi} So_m(\eta; s) \cdot So_p(\eta; s) \cdot d\eta = \begin{cases} \pi, & \text{if } m = p \\ 0, & \text{if } m \neq p \end{cases} \quad (\text{A.3.17})$$

We can also obtain the following normalization relations for the Fourier coefficients,

$$2A_0^2 + \sum_{j=1}^{\infty} (A_{2j})^2 = \sum_{j=0}^{\infty} (A_{2j+1})^2 = \sum_{j=0}^{\infty} (B_{2j+2})^2 = \sum_{j=0}^{\infty} (B_{2j+1})^2 = 1 \quad (\text{A.3.18})$$

This equation assures that all coefficients are bounded such that $|A_j| \leq 1$ and $|B_j| \leq 1$.

Finally, if $s < 0$ the ordinary solutions of AME can be found by using the properties of symmetry of the angular Mathieu solutions, namely:

$$\begin{aligned}
 Se_{2n}(\eta; -s) &= (-1)^n Se_{2n}(\pi/2 - \eta; s) \\
 Se_{2n+1}(\eta; -s) &= (-1)^n So_{2n+1}(\pi/2 - \eta; s) \\
 So_{2n+2}(\eta; -s) &= (-1)^n So_{2n+2}(\pi/2 - \eta; s) \\
 So_{2n+1}(\eta; -s) &= (-1)^n Se_{2n+1}(\pi/2 - \eta; s)
 \end{aligned}
 \tag{A.3.19}$$

Radial Mathieu Equation

The Radial Mathieu equation (A.3.10) plays in elliptic coordinates a similar role as the Bessel equation in circular coordinates. In this sense, for each Bessel function $[J, N, I, K]$ there exists a Radial Mathieu function, however the presence of even and odd versions in the elliptic case leads to eight RMFs. The Mathieu solutions with $s > 0$ are related to the solutions of the Ordinary Bessel equation $[J, N]$, whereas Mathieu solutions with $s < 0$ are connected with the solutions of the Modified Bessel equation $[I, K]$.

Since AME (A.3.11) is transformed into RME (A.3.10) by writing η for $i\xi$, we can derive a set of solutions of the RME by applying this transformation to equations (A.3.13)-(A.3.16), namely

$$\text{Class I: } \quad Re_{2n}^{(1)}(\xi; s) = Se_{2n}(i\xi; s) = \sum_{j=0}^{\infty} A_{2j}(s) \cdot \cosh(2j\xi) \tag{A.3.20}$$

$$\text{Class II: } \quad Re_{2n+1}^{(1)}(\xi; s) = Se_{2n+1}(i\xi; s) = \sum_{j=0}^{\infty} A_{2j+1}(s) \cdot \cosh[(2j+1)\xi] \tag{A.3.21}$$

$$\text{Class III: } \quad Ro_{2n+2}^{(1)}(\xi; s) = -i \cdot So_{2n+2}(i\xi; s) = \sum_{j=0}^{\infty} B_{2j+2}(s) \cdot \sinh[(2j+2)\xi] \tag{A.3.22}$$

Class IV: $Ro_{2n+1}^{(1)}(\xi; s) = -i \cdot So_{2n+1}(i\xi; s) = \sum_{j=0}^{\infty} B_{2j+1}(s) \cdot \sinh[(2j+1)\xi]$ (A.3.23)

Numerically speaking, the rate of convergence of these hyperbolic series decreases rapidly with increasing ξ , and they are consequently inconvenient for computation. Fortunately, these series can be expressed in terms of summations of Bessel functions, or summations of product of Bessel functions, which do not have these defects. The series involving Bessel functions converge absolutely and uniformly for all finite values of ξ . The rate of convergence of those involving products of Bessel function increases with increasing ξ .

If we first define

$$v_1 \equiv \sqrt{s} \exp(-\xi) \text{ and } v_2 \equiv \sqrt{s} \exp(\xi), \tag{A.3.24}$$

$$u \equiv v_2 - v_1 = 2\sqrt{s} \sinh(\xi) \text{ and } w \equiv v_1 + v_2 = 2\sqrt{s} \cosh(\xi) \tag{A.3.25}$$

the first kind RMF can be written as

$$Re_{2n}^{(1)}(\xi; s) = \frac{Se_{2n}(0; s)}{A_0} \sum_{j=0}^{\infty} A_{2j}(s) \cdot J_{2j}(u) \tag{A.3.26}$$

$$Re_{2n+1}^{(1)}(\xi; s) = \frac{Se_{2n+1}(0; s)}{\sqrt{s}A_1} \coth(\xi) \sum_{j=0}^{\infty} (2j+1) A_{2j+1}(s) \cdot J_{2j+1}(u) \tag{A.3.27}$$

$$Ro_{2n+2}^{(1)}(\xi; s) = \frac{So'_{2n+2}(0; s)}{sB_2} \coth(\xi) \sum_{j=0}^{\infty} (2j+2) B_{2j+2}(s) \cdot J_{2j+2}(u) \tag{A.3.28}$$

$$Ro_{2n+1}^{(1)}(\xi; s) = \frac{So'_{2n+1}(0; s)}{\sqrt{s}B_1} \sum_{j=0}^{\infty} B_{2j+1}(s) \cdot J_{2j+1}(u) \tag{A.3.29}$$

where the prime denotes the derivative with respect to ξ .

Furthermore, the second kind of RMF solutions can be obtained by taking advantage of the fact that J and N Bessel functions satisfy the same differential equation and recurrence formulae [9]. We can take the Bessel series representation for the functions $Re^{(1)}$ and $Ro^{(1)}$ in equations (A.3.26)-(A.3.29), replace therein J by

N , and transform to Bessel functions product expansions [30]. The results are given by:

$$\text{Re}_{2n}^{(2)}(\xi; s) = \frac{P_{2n}}{A_0^2} \sum_{j=0}^{\infty} (-1)^j A_{2j}(s) \cdot J_j(v_1) \cdot N_j(v_2) \quad (\text{A.3.30})$$

$$\text{Re}_{2n+1}^{(2)}(\xi; s) = -\frac{P_{2n+1}}{\sqrt{s}A_1^2} \sum_{j=0}^{\infty} (-1)^j A_{2j+1}(s) \cdot [J_j(v_1) \cdot N_{j+1}(v_2) + J_{j+1}(v_1) \cdot N_j(v_2)] \quad (\text{A.3.31})$$

$$\text{Ro}_{2n+2}^{(2)}(\xi; s) = -\frac{S_{2n+2}}{sB_2^2} \sum_{j=0}^{\infty} (-1)^j B_{2j+2}(s) \cdot [J_j(v_1) \cdot N_{j+2}(v_2) - J_{j+2}(v_1) \cdot N_j(v_2)] \quad (\text{A.3.32})$$

$$\text{Ro}_{2n+1}^{(2)}(\xi; s) = \frac{S_{2n+1}}{\sqrt{s}A_1^2} \sum_{j=0}^{\infty} (-1)^j B_{2j+1}(s) \cdot [J_j(v_1) \cdot N_{j+1}(v_2) - J_{j+1}(v_1) \cdot N_j(v_2)] \quad (\text{A.3.33})$$

where the coefficients read as

$$p_{2n} \equiv Se_{2n}(0; s) \cdot So_{2n}\left(\frac{\pi}{2}; s\right) \quad (\text{A.3.34})$$

$$p_{2n+1} \equiv Se_{2n+1}(0; s) \cdot Se'_{2n+1}\left(\frac{\pi}{2}; s\right) \quad (\text{A.3.35})$$

$$s_{2n+2} \equiv So'_{2n+2}(0; s) \cdot So'_{2n+2}\left(\frac{\pi}{2}; s\right) \quad (\text{A.3.36})$$

$$s_{2n+1} \equiv So'_{2n+1}(0; s) \cdot So_{2n+1}\left(\frac{\pi}{2}; s\right) \quad (\text{A.3.37})$$

where the prime in Se' and So' denotes the derivative of Se and So with respect to ξ .

Similar expressions for the first and second RMF for $s < 0$ (Ie, Io, Ke and Ko) can be easily obtained and they can be found in [29].

Finally, the complete solution of integral order for the RME for $s > 0$ will read as:

$$R(\xi) = \sum_{m=0}^{\infty} R_m(\xi) = \sum_{m=0}^{\infty} \begin{cases} A_m Re_m^{(1)}(\xi; s) + B_m Re_m^{(2)}(\xi; s), & a \in a_m \\ C_{m+1} Ro_{m+1}^{(1)}(\xi; s) + D_{m+1} Ro_{m+1}^{(2)}(\xi; s), & a \in b_{m+1} \end{cases} \quad (\text{A.3.38})$$

where A_m, B_m, C_m, D_m are arbitrary constants.

For $s < 0$ the complete solution of integral order for the RME will be written as:

$$R(\xi) = \sum_{m=0}^{\infty} R_m(\xi) = \sum_{m=0}^{\infty} \begin{cases} A_m Ie_m(\xi; -s) + B_m Ke_m(\xi; -s), & a \in a_m \\ C_{m+1} Io_{m+1}(\xi; -s) + D_{m+1} Ko_{m+1}(\xi; -s), & a \in b_{m+1} \end{cases} \quad (\text{A.3.39})$$

Analogous to Hankel functions $H_m^{(1),(2)}$ occurring in Bessel equations and circular cylinder coordinates, also exist the Mathieu-Hankel functions of the first and second kind:

$$\begin{aligned} Re_m^{(3)}(\xi; s) &= Re_m^{(1)}(\xi; s) + i Re_m^{(2)}(\xi; s), & a \in a_m \\ Re_m^{(4)}(\xi; s) &= Re_m^{(1)}(\xi; s) - i Re_m^{(2)}(\xi; s), & a \in a_m \\ Ro_m^{(3)}(\xi; s) &= Ro_m^{(1)}(\xi; s) + i Ro_m^{(2)}(\xi; s), & a \in b_{m+1} \\ Ro_m^{(4)}(\xi; s) &= Ro_m^{(1)}(\xi; s) - i Ro_m^{(2)}(\xi; s), & a \in b_{m+1} \end{aligned} \quad (\text{A.3.40})$$

As it occurs in circular cylinder coordinates, the Mathieu-Hankel functions are used to represent incoming and outgoing waves.

Finally, the general solution of the scalar wave equation in elliptic coordinates will be written as:

$$\psi(\xi, \eta, z) = R(\xi) \cdot \Theta(\eta) \cdot \exp(\pm i k_z z) \quad (\text{A.3.41})$$

Related publications

Book chapters

M. Martinez-Vazquez, E. Antonino-Daviu, M. Cabedo-Fabres, "Design considerations for integrated handset antennas", in book "Multiband integrated antennas for 4G terminals", Artech House Publishers. To appear in July 2008.

JCR indexed journals and magazines

- [1] E. Antonino-Daviu, M. Cabedo-Fabres, M. Ferrando-Bataller and A. Valero-Nogueira, "Wideband double-fed planar monopole antennas", *Electronics Letters*, Vol. 39, Issue: 23, pp.: 1635-1636, 13 Nov. 2003.
- [2] E. Antonino-Daviu; C. Suarez-Fajardo; M. Cabedo-Fabres and M.; Ferrando-Bataller, "Wideband antenna for mobile terminals based on the handset PCB resonance", *Microwave and Optical Technology Letters*, Vol. 48, No. 7, pp.:1408-1411, July 2006.
- [3] N. Belmar-Moliner, A. Valero-Nogueira, M. Cabedo-Fabres and E. Antonino-Daviu, "Simple design for cost-effective diversity antennas", *Microwave and Optical Technology Letters*, Volume: 49, No. 4, pp.:994-996, April 2007.
- [4] M. Cabedo-Fabres, E. Antonino-Daviu, A. Valero-Nogueira, and M. Ferrando-Bataller; "Notched radiating ground plane analyzed from a modal perspective" *Frequenz*, Vol. 61, No. 3-4, pp. 66-70, March-April 2007.
- [5] E. Antonino-Daviu, M. Cabedo-Fabres, M. Ferrando-Bataller and A. Vila-Jimenez, "Active UWB Antenna with tuneable band-notched behaviour", *Electronics Letters*, Vol. 43, Issue: 18, pp.: 959-960, 31 August 2007.
- [6] M. Cabedo-Fabres, E. Antonino-Daviu, A. Valero-Nogueira, and M. Ferrando-Bataller, "The Theory of characteristic modes revisited: A contribution to the design of antennas for modern applications", *IEEE Antennas and Propagation Magazine*, Vol. 49, no. 5, pp. 52-68, Oct. 2007.

International conferences

- [1] M. Cabedo-Fabres, E. Antonino-Daviu, A. Valero-Nogueira and M. Ferrando-Bataller, "Analysis of wide band planar monopole antennas using characteristic modes", Antennas and Propagation Society International Symposium, 2003. IEEE, Vol.: 3, pp.: 733 – 736, 22-27 June 2003.
- [2] M. Cabedo-Fabres, E. Antonino-Daviu, A. Valero-Nogueira and M. Ferrando-Bataller, "On the Use of Characteristic Modes to Describe Patch Antenna Performance", Antennas and Propagation Society International Symposium, 2003. IEEE, Vol.: 2, pp.: 712 – 715, 22-27 June 2003.
- [3] M. Ferrando, A. Valero, M. Cabedo and E. Antonino, "Design of ultra-wide band antennas using characteristic modes", INICA/COST 284 Workshop, Berlin (Germany), Oct. 2003.
- [4] M. Cabedo-Fabres, E. Antonino-Daviu, A. Valero-Nogueira and M. Ferrando-Bataller, "Controlled antenna design method based on the use of characteristic modes", Progress in Electromagnetics Research Symposium PIERS 2004. Pisa (Italy). March 2004.
- [5] E. Antonino-Daviu, M. Cabedo-Fabres, A. Valero-Nogueira, and M. Ferrando-Bataller, "Resonant modes in antenna handsets", INICA/COST 284 Workshop, Gothenburg (Sweden), June 2004.
- [6] M. Cabedo-Fabres, E. Antonino-Daviu, A. Valero-Nogueira and M. Ferrando-Bataller, "Optimization of the polarization of reflectarrays using characteristic modes", IEEE Antennas and Propagation Society Symposium, 2004, Vol. 1, pp.:13 – 16. , 20-25 June 2004.
- [7] E. Antonino-Daviu, M. Cabedo-Fabres, A. Valero-Nogueira, and M. Ferrando-Bataller, "A discussion on the feed configuration of planar monopole antennas to obtain ultra wide band performance", IEEE Antennas and Propagation Society Symposium 2004, Vol.: 2, pp.:1867 – 1870, 20-25 June 2004.
- [8] E. Antonino-Daviu, M. Cabedo-Fabres, M. Ferrando-Bataller and J.I Herranz-Herruzo, "Analysis of the coupled chassis-antenna modes in mobile handsets", IEEE Antennas and Propagation Society Symposium 2004, Vol.: 3, pp:2751 – 2754, 20-25 June 2004.
- [9] E. Antonino-Daviu, M. Cabedo-Fabres, M. Ferrando-Bataller and A. Valero-Nogueira, "Design of small antennas for mobile terminals", INICA/COST 284 Workshop, Barcelona, September 2004.
- [10] E. Antonino-Daviu, M. Cabedo-Fabres, M. Ferrando-Bataller and A. Valero-Nogueira, "Design of very wide-band linear-polarized antennas", JINA, 13th International Symposium on Antennas, Nice (France), November 2004.

- [11] M. Cabedo-Fabres, M. Ferrando-Bataller, E. Antonino-Daviu and A. Valero-Nogueira, "Systematic antenna design using the theory of characteristic modes", JINA, 13th International Symposium on Antennas, Nice (France), November 2004.
- [12] M. Cabedo-Fabrés, E. Antonino-Daviu, A. Valero-Nogueira and M. Ferrando-Bataller, "Wideband Radiating Ground Plane with Notches", IEEE Antennas and Propagation Society International Symposium, 2005. Washington (EEUU) pp.:560 – 563, vol. 2B, 3-8 July 2005.
- [13] E. Antonino-Daviu, M. Cabedo-Fabres, M. Ferrando-Bataller, A. Valero-Nogueira, M. Martinez-Vazquez, "Novel antenna for mobile terminals based on the chassis-antenna coupling", IEEE Antennas and Propagation Society International Symposium, 2005. Washington (EEUU), pp.:560 – 563, vol. 2B, 3-8 July 2005.
- [14] M. Ferrando, M. Cabedo, E. Antonino and A. Valero, "Overview of planar monopole antennas for UWB applications", 1st European Conference on Antennas and Propagation, Nice (France). November 2006.
- [15] E. Antonino, M. Ferrando, M. Cabedo and C.A. Suarez, "Ultra-wideband antenna with switchable band-notched behaviour", 1st European Conference on Antennas and Propagation, Nice (France). November 2006.
- [16] M. Bonnedal, E. Angelopoulos, E. Antonino, P. Balling, K. Chan, R. Erickson, I. Lager, M. Mazanek, W. Sörgel, E. Ubeda, A. Yarovoy, "Activities in ACE WP 2.3-1 on wideband and multiband radiators", 1st European Conference on Antennas and Propagation, Nice (France). November 2006.
- [17] M. Cabedo, A. Valero, E. Antonino and M. Ferrando, "Modal analysis of a radiating slotted PCB for mobile handsets", 1st European Conference on Antennas and Propagation, Nice (France). November 2006.
- [18] C.A Suarez, M. Ferrando, E. Antonino and F. Vico, "Circular Arrays for GSM-UMTS applications", 1st European Conference on Antennas and Propagation, Nice (France). November 2006.
- [19] E. Antonino, M. Cabedo, M. Ferrando and M. Baquero, "Novel UWB antennas with switchable and tunable band-notched behavior", IEEE Antennas and Propagation Society International Symposium 2007, Honolulu (EEUU). 10-15 June 2007.
- [20] M. Cabedo Fabrés, E. Antonino-Daviu, A. Valero-Nogueira, J. M. Molina-Garcia-Pardo, and L. Juan-Llácer, "Compact Slitted Planar Monopoles for MIMO Systems", IEEE Antennas and Propagation Society International Symposium 2007, Honolulu (EEUU). 10-15 June 2007.

- [21] R. Serrano, A. Aguasca, J. Romeu, S. Blanch, L. Jofre, M. Cabedo, E. Antonino, A. Valero and M. Ferrando, "Active Balanced Feeding for Compact Wide-band Antennas", IEEE Antennas and Propagation Society International Symposium 2007, Honolulu (EEUU). 10-15 June 2007.
- [22] C. Tarin, L. Traver, P. Marti, N. Cardona, J.A Diaz and E. Antonino, "UWB Channel Measurements for Hand-Portable Devices: A comparative Study", 8th Annual IEEE Int. Symp. on Personal, Indoor and Mobile Radio Comm.-PIMRC'07, Athens, Sept. 2007.
- [23] M Cabedo-Fabrés, E Antonino-Daviu, D Sánchez-Escuderos, V M Rodrigo-Peñarrocha, "On the Application of Characteristic Modes for the Analysis of Large Scale Antenna Problems", 2nd European Conference on Antennas and Propagation, Edinburgh (UK). November 2007.
- [24] E Antonino-Daviu, M Cabedo-Fabrés, M Ferrando-Bataller, V M Rodrigo-Peñarrocha, "Active UWB Antenna with Tunable Band-Notched Behaviour", 2nd European Conference on Antennas and Propagation, Edinburgh (UK). November 2007.

National conferences

- [1] E. Antonino-Daviu, M. Cabedo-Fabrés, A. Valero-Nogueira and M. Ferrando-Bataller, "Diseño de monopolos planos con alimentación múltiple a partir de la Teoría de Modos Característicos", XVIII Symposium Nacional de la URSI. A Coruña. Septiembre 2003.
- [2] E. Antonino-Daviu, M. Cabedo-Fabrés, A. Valero-Nogueira and M. Ferrando-Bataller, "Nueva antena de banda ancha y polarización dual", XVIII Symposium Nacional de la URSI. A Coruña. Septiembre 2003.
- [3] M. Cabedo-Fabrés, E. Antonino-Daviu, A. Valero-Nogueira and M. Ferrando-Bataller, "Modos característicos de estructuras planas de forma arbitraria", XVIII Symposium Nacional de la URSI. A Coruña. Septiembre 2003.
- [4] E. Antonino-Daviu, M. Cabedo-Fabrés, M. Ferrando-Bataller and A. Valero-Nogueira, "Efecto de las discontinuidades en la radiación de estructuras planas", XIX Symposium Nacional de la URSI. Barcelona. Septiembre 2004.
- [5] E. Antonino-Daviu, M. Cabedo-Fabrés, M. Ferrando-Bataller and A. Valero-Nogueira, "Acoplamiento de modos resonantes en terminales móviles", XIX Symposium Nacional de la URSI. Barcelona. Septiembre 2004.

- [6] M. Cabedo-Fabrés, E. Antonino-Daviu, A. Valero-Nogueira and M. Ferrando-Bataller, "Estudio modal de resonadores abiertos acoplados", XIX Symposium Nacional de la URSI. Barcelona. Septiembre 2004.
- [7] M. Cabedo-Fabrés, E. Antonino-Daviu, A. Valero-Nogueira and M. Ferrando-Bataller, "Diseño de antenas de hendidura en plano de masa finito", XIX Symposium Nacional de la URSI. Barcelona. Septiembre 2004.
- [8] C.A. Suarez, M. Ferrando, M. Chulia y E. Antonino, "Antena PIFA para aplicaciones en UWB", XX Symposium Nacional de la URSI, Gandia, Septiembre 2005.
- [9] E. Antonino, M. Cabedo, F.Vico y C.A. Suarez, "Nueva antenna multibanda para terminales moviles basada en la generacion de resonancias en el plano de masa del terminal", XX Symposium Nacional de la URSI, Gandia, Septiembre 2005.
- [10] M. Cabedo, E. Antonino, D.Sanchez and M. Ferrando, "On the influence of the shape of planar monopole antennas in the impedance bandwidth performance", XX Symposium Nacional de la URSI, Gandia, Septiembre 2005.
- [11] N. Belmar, A. Valero, M. Cabedo and E. Antonino, "Diseño de una antena compacta para sistemas MIMO", XX Symposium Nacional de la URSI, Gandia, Septiembre 2005.
- [12] E. Antonino, M. Ferrando, M. Cabedo y C.A. Suarez, "Monopolo plano de banda ancha con filtro notch conmutable", XXI Symposium Nacional de la URSI, Oviedo, Septiembre 2006.
- [13] M. Cabedo, E. Antonino, V.M. Rodrigo y C.A. Suarez, "Análisis modal de un plano de masa radiante doblado y con una ranura para terminales móviles", XXI Symposium Nacional de la URSI, Oviedo, Septiembre 2006.

Other publications

JCR indexed journals and magazines

- [1] A. Valero-Nogueira, J.I Herranz-Herruzo, E. Antonino-Daviu and M. Cabedo-Fabres, "Linearly Polarized Radial Line Slot Array Antenna With Wideband Return Loss Performance Using a Multisleeve Coaxial Transition", *IEEE Antennas and Wireless Propagation Letters*, Vol. 3, Is. 1, pp:348-350, 2004.
- [2] A. Valero-Nogueira, J.I Herranz-Herruzo, E. Antonino-Daviu and M. Cabedo-Fabres, "Evaluation of the input impedance of a top-loaded monopole in a parallel plate waveguide by the MoM/Green's function method", *IEEE Trans. on Microwave Theory and Techniques*, Vol. 53, Is. 3, Part 1, pp.: 868 – 873, March 2005.

International conferences

- [1] A. Valero-Nogueira, J.I. Herranz-Herruzo, M. Ferrando-Bataller and E. Antonino-Daviu, "Radial-line slot-array antenna equivalent network model for fast design and optimization", *IEEE Antennas and Propagation Society Symposium*, 2004. Vol.: 1, June 20-25, 2004, pp.:535 – 538.
- [2] "Dual linearly polarized single layer radial-line slot-array antenna", *IEEE Antennas and Propagation Society International Symposium*, 2005. Washington (EEUU), 3-8 July 2005 Page(s):560 - 563 vol. 2B.
- [3] F. Vico, M. Ferrando, M. Baquero, M. and E. Antonino, "A new 3D fast physical optics method", *IEEE Antennas and Propagation Society International Symposium 2006*, Albuquerque (EEUU). 9-14 July 2006, pp.: 1849 – 1852.
- [4] D. Sanchez, M. Baquero, J.I Herranz and E. Antonino, "High resolution in currents reconstruction applying the extrapolation matrix and spectrum replies", *IEEE Antennas and Propagation Society International Symposium 2007*, Honolulu (EEUU), June 2007.

National conferences

- [1] A. Valero-Nogueira, J.I. Herranz-Herruzo, M. Ferrando-Bataller and E. Antonino-Daviu, "Modelo equivalente de array de ranuras en guía radial para el diseño rápido de la sonda de alimentación", XIX Simposium Nacional de la URSI. Septiembre 2004. Barcelona.
- [2] E. Antonino-Daviu, M. Cabedo-Fabrés, A. Valero-Nogueira and M. Ferrando-Bataller, "Nueva antena de banda ancha y polarización dual", XVIII Simposium Nacional de la URSI. A Coruña. Septiembre 2003.

